

KIT SCIENTIFIC REPORTS 7690

# **Analytical investigations concerning the performance of vane separators and experimental validation of droplet separation efficiency**

Hans Kristian Koopman



Hans Kristian Koopman

**Analytical investigations concerning the performance of vane separators and experimental validation of droplet separation efficiency**

Karlsruhe Institute of Technology  
**KIT SCIENTIFIC REPORTS 7690**

# **Analytical investigations concerning the performance of vane separators and experimental validation of droplet separation efficiency**

by  
Hans Kristian Koopman

Report-Nr. KIT-SR 7690

Dissertation, Karlsruher Institut für Technologie (KIT)  
Fakultät für Maschinenbau, 2014  
Tag der mündlichen Prüfung: 22. Dezember 2014

#### Impressum



Karlsruher Institut für Technologie (KIT)  
KIT Scientific Publishing  
Straße am Forum 2  
D-76131 Karlsruhe

KIT Scientific Publishing is a registered trademark of Karlsruhe  
Institute of Technology. Reprint using the book cover is not allowed.

[www.ksp.kit.edu](http://www.ksp.kit.edu)



*This document – excluding the cover – is licensed under the  
Creative Commons Attribution-Share Alike 3.0 DE License  
(CC BY-SA 3.0 DE): <http://creativecommons.org/licenses/by-sa/3.0/de/>*



*The cover page is licensed under the Creative Commons  
Attribution-No Derivatives 3.0 DE License (CC BY-ND 3.0 DE):  
<http://creativecommons.org/licenses/by-nd/3.0/de/>*

Print on Demand 2015

ISBN 978-3-7315-0331-6

DOI: 10.5445/KSP/1000045141





# **Analytical investigations concerning the performance of vane separators and experimental validation of droplet separation efficiency**

Zur Erlangung des akademischen Grades  
DOKTOR DER INGENIEURWISSENSCHAFTEN

der Fakultät für Maschinenbau  
Karlsruher Institut für Technologie (KIT)

genehmigte  
DISSERTATION

von  
Ir. Hans Kristian Koopman

Tag der mündlichen Prüfung:	22. Dezember 2014
Hauptreferent:	Prof. Dr.-Ing. T. Schulenberg
Korreferent:	Prof. Dr.-Ing. X. Cheng



# Abstract

Separation of particles or droplets from gaseous flows can be performed by wave separators, which use the inertia of the droplets to separate them from the main flow. Over half a century of research has been done into the separation efficiency of these separators. In the last decade the use of Computational Fluid Dynamics (CFD) has increasingly become the preferred investigative method, since it is regarded as cheaper and quicker than experiments. Being popular before, the use of analytical methods, has become more scarce.

This study focuses on analytical methods for the prediction of vane separator efficiency and aims to enhance such methods with the implementation of additional physical phenomena. An existing equation based upon diminishing droplet concentration, was modified by introducing the effect of straight channel parts on the separation efficiency of the vane separator. Different orientations of the vane separator in the gravity field, as well as in the velocity field, were included in the analytical model. Non-orthogonal velocity fields constitute simultaneously a positive and a negative impact on separation efficiency, caused by an increasing effective path length and an increasing effective channel width, respectively. The net result of these effects depends mainly on the total bend angle of the vane separator. It was shown that the gravitational contributions to the separation efficiency inside the bends cancel and only the straight channel sections effectively contribute to droplet separation. These contributions increase with droplet size and decrease with gas velocity and the optimum does not necessarily correspond to orthogonal flow conditions. For vane separators with high performance at low Stokes numbers, gravitational effects can be neglected. The orientation in the gravity field becomes significant under conditions of poor separation, e.g. at low velocities in wide flow channels.

Non-uniform velocity profiles are accounted for through a simplified model representing a low-velocity region near the outer wall. This allows for the computation of a limit escape diameter, below which droplets would not be separated. Identifying the corresponding modified terminal radial droplet velocity, the separation efficiency is adjusted. The result reflects the near-zero efficiency for droplet sizes below the escape diameter, as well as an increased efficiency for larger droplets, due to the higher gas velocity on the inside of the bend under incompressible conditions. An adjustment of the droplet concentration near the outer wall is suggested, to account for the non-uniform droplet distribution after a bend. The resulting modification of the separation efficiency is equivalent to a decrease of the effective wall length, dependent on a remixing factor and the Reynolds number.

Relevant physical phenomena, not represented explicitly in the analytical model, and their significance for the separation of droplets are discussed. These phenomena include liquid film flow, re-entrainment mechanisms and pressure drop. The expected carry-over of liquid film into subsequent vane separator stages is quantified by identifying the theoretical limits of liquid film thickness and gravitational drainage, in combination with the film flow angle. By setting these limits equal, a method of computing the average film height emerges, alternative to computing the Nusselt film height. The impact of liquid film carry-over on the overall vane separator efficiency is visualized and compared to a theoretical result with perforated wall sections, which significantly improves film drainage. A discussion of different re-entrainment mechanisms shows the disadvantage of sharp

inner corners with regard to film detachment. A large range of theoretical critical film and gas velocities from different authors are discussed. Experimental critical gas velocities of 5 - 8 m/s are reported most often, for water droplets immersed in air flow through vane separator channels.

The analytical model presented in this paper is benchmarked against several numerical, as well as experimental results from existing literature. The model is in very reasonable agreement with most sources. It is shown that straight type vane separators are represented well by the model and that accounting for non-uniform velocity profiles can lead to better predictions. Results from the analytical model are also compared with experiments performed by the Institute of Fluid Mechanics (LSTM) of the Friedrich-Alexander University in Erlangen, on a vane separator of simplified geometry, manufactured for this purpose. The experimental separation efficiencies, computed from the measured liquid mass balances, are significantly below the model predictions, which are arbitrarily close to unity. This difference is attributed to re-entrainment by film detachment from the edge of the last stage of the vane separator. After adjustment for re-entrainment effects, through the application of a cut-off filter to the outlet droplet size spectra, the experimental and theoretical outlet Sauter mean diameters show very good agreement. An analysis of the pressure drop reveals that the model by *Wilkinson* [70] represents the data well, although his proposed regime change for higher Reynolds numbers derogates the comparison. No dependence of pressure drop on liquid mass fraction is detected.

Based on the conclusions from previously discussed relevant geometrical aspects, a novel vane separator design is introduced, which incorporates features expected to improve efficiency. An engineering method for quantifying the geometrical parameters of the novel design is introduced, by means of a specific example in the form of the application of vane separators in a Moisture Separator & Reheater. Numerical computations on the resulting geometry performed by Siemens AG Corporate Research & Technology in Moscow reveal an increased separation efficiency at low gas velocities, as compared to the analytical model, thought to be related to the increased gas velocities caused by the variable channel width. For gas velocities beyond 4 m/s the numerical and analytical models are in good agreement. Experimental results from the novel vane separator geometry are compared with results from the simplified geometry. The separation efficiencies based on the recorded liquid mass flow balances are very similar for both geometries, although, based on an analysis of the outlet droplet size spectra, the novel design performs better. It is concluded that re-entrainment effects cloud the performance of the novel design and that the perforations in the wall sections are not very effective. Pressure drop measurements performed on both geometries show that the pressure drop for the novel design is higher by a factor of almost two, but remains below 300 Pa for gas velocities up to 8 m/s. A numerical investigation performed by Steinmüller GmbH, comparing the novel design with a commercial vane separator featuring pick-off hooks, reveals that the separation efficiency increases with the gas velocity for the novel design, while it is almost constant for the commercial design. The separation efficiencies cross at about 4 m/s, signaling the advantages of the novel vane separator design in the intended operating regime at higher gas velocities.

# Kurzfassung

Partikel oder Tropfen können, durch Ausnutzung deren Trägheit mittels eines Wellenabscheiders, von einer gasförmigen Hauptströmung getrennt werden. Nach Abscheidungsgraden der Wellenabscheider wird bereits seit über einem halben Jahrhundert geforscht, wobei der Einsatz von rechnerischen Methoden (CFD) als bevorzugte Mittel im letzten Jahrzehnt vermehrt angewandt werden, da diese im Gegensatz zu Experimenten als eine schnellere und kostengünstigere Variante angesehen werden. Obwohl vorher weitverbreitet, sind analytische Ansätze deshalb immer seltener vorzufinden.

Diese Arbeit konzentriert sich auf analytische Ansätze zur Berechnung des Wirkungsgrades und beabsichtigt diese unter Berücksichtigung zusätzlicher physikalischer Phänomene zu erweitern. Eine bereits bekannte, auf abnehmender Tröpfchenkonzentration basierende Formel, wurde mit dem Einfluss von geraden Kanalsegmenten auf den Abscheidungsgrad ergänzt. Unterschiedliche Ausrichtungen der Wellenabscheider, mit Bezug auf die Schwerkraft und auf die Gasgeschwindigkeit, wurden in ein analytisches Modell eingearbeitet. Ein schiefwinkliger Geschwindigkeitsvektor erzeugt sowohl einen positiven als einen negativen Effekt auf den Abscheidungsgrad, verursacht von einer Verlängerung der effektiven Weglänge beziehungsweise einer Verbreiterung der effektiven Kanalbreite, wobei das Nettoergebnis der beiden Effekte hauptsächlich vom Umlenkwinkel abhängt. Es wurde gezeigt, dass die Beiträge der Schwerkraft am Abscheidungsgrad innerhalb der Krümmen sich aufheben und nur die Beiträge innerhalb der geraden Kanalsegmente zum Abscheidungsgrad beitragen. Der Effekt nimmt mit steigendem Tropfendurchmesser zu, wobei das Optimum nicht unbedingt mit geradewinkligen Strömungsverhältnisse zusammenfällt. In Wellenabscheidern mit hohen Abscheidungsgraden bei niedrigen Stokeszahlen kann die Schwerkraft vernachlässigt werden, aber bei niedrigen Abscheidungsgraden, z.B. bei niedriger Geschwindigkeit in breiten Kanälen, ist der Beitrag signifikant.

Ein Modell wird ermittelt in welchen ungleichmäßigen Geschwindigkeitsprofilen vereinfacht mit einem niedrig-Geschwindigkeitsbereich an der äußeren Wand abgebildet werden, was die Berechnung eines limitierenden Tropfendurchmesser, unterhalb dessen keine Tropfen abgeschieden werden können, erlaubt. Mit der einhergehenden Anpassung der Fallgeschwindigkeit der Tropfen werden sowohl die sehr geringen Abscheidungsgrade für Tropfendurchmesser über den limitierenden Tropfendurchmesser als auch die, wegen der (unter Inkompressibilität) höheren Gasgeschwindigkeit am inneren Wand, höhere Abscheidungsgrade für Tropfendurchmesser oberhalb der limitierenden Tropfendurchmesser, reproduziert. Die ungleichmäßige Tropfenverteilung stromabwärts eines Krümmers wird mittels einer Modifizierung der Tropfenverteilung nahe der äußeren Wand berücksichtigt. Die daraus resultierende Anpassung des Abscheidungsgrades gleicht eine Reduzierung der effektiven Weglänge, abhängig vom Mischungsfaktor und der Reynoldszahl.

Nicht explizit in dem Modell enthaltene relevante physikalischen Phänomene, wie flüssige Filmströmung, dem Mitreißen von Tropfen in die Hauptströmung und Druckverlust, und deren Signifikanz für den Abscheidegrad werden diskutiert. Die theoretische Limits der Filmhöhe und gravitative Entwässerung werden in Zusammenhang mit dem Strömungswinkel untersucht, wodurch die Übertragung eines flüssigen Films in nachfolgenden Abscheiderstufen quantifiziert werden kann.

Alternativ zur Nusselt Filmhöhe, erlaubt eine Gleichstellung dieser Limits die Errechnung der durchschnittlichen Filmhöhe. Der Einfluss der Filmübertragung auf den Abscheidegrad wird visualisiert und das Ergebnis mit dem theoretischen Ergebnis unter Berücksichtigung von Wandperforationen verglichen, was die Entwässerung wesentlich verbessert. Der Nachteil schärferer innerer Krümmen mit Bezug auf Lösung der flüssigen Schichtströmung wird diskutiert. Obwohl theoretische Werte für kritische Film- und Gasgeschwindigkeit von unterschiedlichen Autoren sich sehr unterscheiden, werden in Experimenten mit Wassertropfen in Luftströmung durch Wellenabscheiderkanäle, Werte von 5 - 8 m/s ermittelt.

Ein Benchmark des in dieser Arbeit dargestellten analytischen Modells mit unterschiedlichen, numerischen sowie experimentellen Werten aus der Literatur, zeigt mit den meisten Quellen eine gute Übereinstimmung. Es wurde gezeigt, dass gerade Wellenabscheider gut vom Modell abgebildet werden und dass die Berücksichtigung ungleichmäßiger Geschwindigkeitsprofile bessere Abschätzungen herbeiführen kann. Modellergebnisse werden zusätzlich durch Experimente mit einem für dieses Ziel gefertigten Wellenabscheider in vereinfachter Form verglichen. Die Experimente wurden vom Lehrstuhl für Strömungsmechanik (LSTM) der Friedrich-Alexander Universität in Erlangen durchgeführt. Die mittels der Massenbilanz ermittelten experimentellen Abscheidegrade zeigten sich wesentlich unter den Modellprognosen, welche beliebig nahe bei 100% sind. Dieser Unterschied wurde der Filmlösung vom Rand der letzten Abscheiderstufe zugeschrieben. Nach Justierung für diese Filmlösung, durch Anwendung eines Filters auf Tropfengrößenverteilung am Austritt, stimmen die experimentellen und theoretischen Sauter Durchmesser am Austritt sehr gut überein. Eine Untersuchung des Druckverlustes zeigt, dass das Modell von *Wilkinson* [70] die experimentellen Werte gut reproduzieren kann, obwohl die von ihm vorgeschlagene Modellanpassung für den Bereich höherer Reynoldszahlen der Übereinstimmung nicht zu gute kommt. Es wurde keine Abhängigkeit des Druckverlustes vom flüssigen Massenanteil gefunden.

Basierend auf den Schlussfolgerungen aus den vorher diskutierten relevanten geometrischen Aspekten, wird eine neue Auslegung für Wellenabscheider introduziert, welche Merkmale die den Abscheidegrad verbessern sollten einbezieht. Mittels des Einsatzes von einem Wellenabscheider in einem Wasserabscheider/Zwischenüberhitzer als spezifisches Beispiel, wird eine Auslegungsmethodik zur Quantifizierung der geometrischen Parameter der neuen Auslegung dargestellt. Die resultierende Geometrie wurde von der Siemens AG Corporate Research & Technology in Moskau durchgerechnet. Die Ergebnisse zeigen, im Vergleich zum analytischen Modell, einen erhöhten Abscheidegrad bei niedriger Gasgeschwindigkeit, was der erhöhten Gasgeschwindigkeit durch die variable Kanalbreite zugeschrieben wird. Für Gasgeschwindigkeiten über 4 m/s stimmen numerisches und analytisches Modell gut überein. Ein Vergleich der experimentellen Ergebnisse für die neue Auslegung mit dem für die vereinfachte Geometrie zeigt sehr vergleichbare Werte basierend auf der Massenbilanz, aber in der Analyse der Tropfengrößenverteilungen am Austritt schneidet die neue Auslegung jedoch besser ab. Hieraus wird festgestellt, dass das Mitreißen von Flüssigkeit aus der Film den eigentlich besseren Abscheidegrad der neuen Auslegung verhüllt und die Wandperforationen nicht sehr effektiv sind. Druckverlustmessungen an beiden Geometrien ermitteln einen Druckverlust der neuen Auslegung, der im Vergleich zur vereinfachten Form fast um das zweifache höher ist, sich aber immer noch unterhalb von 300 Pa für Gasgeschwindigkeiten bis 8 m/s befindet. In einer numerischen Untersuchung vergleicht die Steinmüller GmbH die neue Auslegung mit einer mit Abfangrinnen

ausgestatteten kommerziellen Auslegung, und berichtet für die neue Auslegung eine Verbesserung des Abscheidegrades mit der Gasgeschwindigkeit, im Gegensatz zu nahezu konstanten Werte für den kommerziellen Wellenabscheider. Die Abscheidegrade der beiden Geometrien schneiden sich bei etwa 4 m/s, was die Vorteile der neuen Auslegung im anvisierten Betrieb bei höheren Gasgeschwindigkeiten hervorhebt.



# Acknowledgements

The theoretical and conceptual foundations underlying this paper were part of a research project carried out by Siemens AG Power Generation in Erlangen, who funded the droplet separation experiments, as well as part of the work leading to this paper. Mr. Berkant Mertkaya M.Sc., Dr.-Ing. Martin Meister and Dr.-Ing.habil. Nikolay Kolev cooperated in the design of the improved vane separator geometry, and Dr.rer.nat. Sergiy Khodyachykh and Dr.-Ing. Pietro Botazzoli assisted in the supervision of the experiments carried out at the Institute of Fluid Mechanics (LSTM) of the Friedrich-Alexander University (FAU) in Erlangen. I am particularly grateful for the intellectual support and advise provided by Dr.-Ing.habil. Nikolay Kolev throughout the project, without whom this paper would not have been realized.

I wish to thank the Karlsruhe Institute of Technology (KIT) and the Institute for Nuclear and Energy Technologies (IKET) for accepting this dissertation and in particular Prof.Dr.-Ing. Thomas Schulenberg for accepting me as his student and for his guidance and support. I am thankful to Prof.Dr.-Ing. Xu Cheng for accepting a position in the dissertation committee and to Prof.Dr.-Ing. Hans-Jörg Bauer for presiding the committee.

The experiments were performed at the Institute of Fluid Mechanics (LSTM) of the Friedrich-Alexander University (FAU) in Erlangen. I wish to thank Mr. Çağatay Köksoy M.Sc., Dr.-Ing. Özgür Ertunç, Dipl.-Ing. Hermann Lienhart, Mr. Heinz Hedwig and Prof.Dr.-Ing.habil. Antonio Delgado for the design and the construction of the experimental facility, for performing the measurements and recording the data, and in general for the very pleasant cooperation.

Dr. Viacheslav Schuchkin of Siemens AG Corporate Research & Technology in Moscow provided a CFD analysis of the new vane separator design, as did independently Dr.-Ing. Waldemar Hoffmann of Steinmüller Engineering GmbH, who also provided the numerical comparison with the commercial vane separator geometry (refer to chapter 6.3).

They are all gratefully acknowledged.

Special thanks also goes to my wife, for her understanding and her patience.

Forchheim, January 2015

Hans K. Koopman



*Aan Katja en aan de kleine...*



# Table of contents

<b>1</b>	<b>Introduction</b> .....	<b>1</b>
1.1	<b>Industrial relevance of vane separators in power plants</b> .....	<b>2</b>
1.1.1	Moisture content .....	2
1.1.2	Application in nuclear power plants.....	3
1.2	<b>Vane separator types</b> .....	<b>4</b>
1.3	<b>Vane separator efficiency</b> .....	<b>5</b>
1.3.1	Definitions .....	5
1.3.2	An introduction to cyclone separation efficiency .....	6
1.3.3	A cyclone separation model applied to vane separators .....	8
1.3.4	Droplet relaxation time constant.....	9
<b>2</b>	<b>State of the art</b> .....	<b>11</b>
2.1	<b>Analytical approaches</b> .....	<b>11</b>
2.2	<b>CFD approaches</b> .....	<b>16</b>
2.3	<b>Parametric and empirical approaches</b> .....	<b>17</b>
2.4	<b>Motivation and structure of the thesis</b> .....	<b>18</b>
<b>3</b>	<b>An analytical model for vane separator efficiency</b> .....	<b>21</b>
3.1	<b>Droplet flow path analysis and vane separator geometry</b> .....	<b>21</b>
3.1.1	Forces on droplets .....	21
3.1.2	Lagrangian particle tracking .....	27
3.1.3	Results for a wavy vane separator with straight channel sections .....	30
3.1.4	Separation efficiency in straight channel sections.....	31
3.2	<b>Gravitational influence on separation efficiency</b> .....	<b>33</b>
3.2.1	Gravitational influence in curved vane separator sections .....	34
3.2.2	Gravitational influence in straight vane separator sections .....	37
3.2.3	Grade efficiency under the influence of gravity .....	38
3.3	<b>Non-orthogonal gas flow</b> .....	<b>40</b>
3.3.1	Non-orthogonal flow in curved vane separator sections.....	41
3.3.2	Non-orthogonal flow in straight vane separator sections.....	44
3.3.3	Gravitational influence for non-orthogonal flow .....	47
3.4	<b>Non-uniform velocity field</b> .....	<b>51</b>
3.4.1	Velocity profiles.....	51
3.4.2	Significance to separation efficiency .....	52
3.5	<b>Non-uniform droplet distribution and remixing</b> .....	<b>56</b>
3.6	<b>Droplet size distributions and grade efficiency</b> .....	<b>59</b>
3.6.1	Characterization of droplet size distributions.....	59
3.6.2	Droplet size distributions in power plants .....	60
3.6.3	Evaluation of total separation efficiency from grade efficiencies .....	62
3.6.4	Total grade efficiency .....	64
<b>4</b>	<b>Film flow, re-entrainment and pressure drop</b> .....	<b>65</b>
4.1	<b>Film separation, carry-over and re-entrainment</b> .....	<b>65</b>
4.1.1	Liquid film formation .....	65
4.1.2	Liquid film carry-over.....	71
4.1.3	Film detachment .....	78
4.1.4	Droplet re-entrainment .....	80

4.1.5	Experimental critical gas velocities.....	84
<b>4.2</b>	<b>Pressure drop, pick-off hooks and drainage channels.....</b>	<b>89</b>
4.2.1	Pressure drop .....	89
4.2.2	Pick-off hooks and drainage channels .....	93
<b>5</b>	<b>Model validation.....</b>	<b>97</b>
<b>5.1</b>	<b>Experiments from literature .....</b>	<b>97</b>
5.1.1	Single stage vane separators.....	97
5.1.2	Multiple stage vane separators .....	99
5.1.3	Discussion.....	103
<b>5.2</b>	<b>Comparison with CFD results .....</b>	<b>104</b>
<b>5.3</b>	<b>Experiments on a wavy vane separator .....</b>	<b>108</b>
5.3.1	Research goals .....	108
5.3.2	Experimental setup .....	109
5.3.3	Results .....	114
5.3.4	Discussion.....	119
<b>5.4</b>	<b>Pressure drop.....</b>	<b>121</b>
<b>6</b>	<b>Optimizing vane separator design.....</b>	<b>123</b>
<b>6.1</b>	<b>Introduction .....</b>	<b>123</b>
<b>6.2</b>	<b>Optimizing vane separator geometry .....</b>	<b>124</b>
6.2.1	General considerations .....	124
6.2.2	Optimizing the flow channel .....	125
6.2.3	Boundary conditions.....	126
6.2.4	Design optimization.....	126
<b>6.3</b>	<b>CFD results of the novel design .....</b>	<b>129</b>
6.3.1	Comparison with the analytical model.....	129
6.3.2	Comparison with a commercial geometry .....	130
<b>6.4</b>	<b>Experimental results of the novel design .....</b>	<b>131</b>
6.4.1	Research goals and experimental setup .....	131
6.4.2	Results .....	132
6.4.3	Discussion.....	134
6.4.4	Pressure drop .....	135
<b>7</b>	<b>Conclusion.....</b>	<b>137</b>
<b>8</b>	<b>Summary.....</b>	<b>139</b>
8.1	Summary of scientific results .....	141
8.2	Proposal for future work .....	142
<b>A.I</b>	<b>Determination of droplet radial velocity in straight sections.....</b>	<b>145</b>
<b>A.II</b>	<b>Gravitational influence on efficiency in inlet and outlet sections .....</b>	<b>147</b>
<b>A.III</b>	<b>Quantitative analysis of gravitational influence on efficiency .....</b>	<b>149</b>
A.III-a	Geometrical and gravitational variations.....	149
A.III-b	Variation of physical parameters.....	152
<b>A.IV</b>	<b>Physical parameters of an air-water system .....</b>	<b>155</b>
<b>A.V</b>	<b>Experimental results for a wavy vane separator .....</b>	<b>157</b>
A.V-a	Varying liquid mass fraction .....	157
A.V-b	Varying gas velocity .....	158

---

<b>A.VI Experimental results for the novel vane separator design .....</b>	<b>159</b>
<b>A.VI-a Varying liquid mass fraction .....</b>	<b>159</b>
<b>A.VI-b Varying gas velocity .....</b>	<b>160</b>
<b>Nomenclature .....</b>	<b>161</b>
<b>Abbreviations .....</b>	<b>165</b>
<b>List of figures.....</b>	<b>167</b>
<b>List of tables .....</b>	<b>173</b>
<b>Bibliography.....</b>	<b>175</b>



# 1 Introduction

Vane separators are a specific type of separator widely used in industry, inter alia in the mining industry, the oil & gas industry, the chemical industry and in power generation. Their function is to separate solid particles or liquid droplets from gaseous flows and their application ranges from the elimination of dust or harmful substances (e.g. to protect equipment from erosion or corrosion), the separation of pollutants (e.g. to meet emission restrictions), and the recovery of valuable substances (e.g. in chemical processes), to drying steam or other saturated gases by separating the condensed matter (e.g. in power plants). Their use can be environmental or economical, with the goal of purification, separation and/or protection. Vane separators derive their name from their corrugated plates, installed in parallel to create curved flow channels. As the gas propagates through these curved channels, the droplets' inertia in combination with centrifugal forces directs the droplets' trajectories towards the channel wall, where they coalesce and form a liquid film, which is then extracted from the main gas flow. In case of separation of particles, pockets and channels are necessary for the transportation of the separated particles. In power plants, vane separators are used to mechanically dry the process steam in order to protect the equipment from erosion as well as increase thermodynamic efficiency. In most cases the larger droplets (40-200  $\mu\text{m}$ ) have already been separated from the flow by coarse separators; the vane separators are often classified as fine separators and are used for the separation of droplets down to a few micrometer in size.

The efficiency of vane separators depends on several physical parameters, including the size of the particles or droplets, the densities and viscosities of the different media and the flow velocity. In general, the separation efficiency of vane separators increases with gas velocity and droplet size, but decreases with pressure (in single component mixtures, because the ratio of liquid-to-gas density decreases) and viscosity (because the drag increases). Re-entrainment of droplets from the liquid film and turbulent effects also play a major role, especially at higher gas velocities. Apart from the physical properties of the flow medium, the efficiency of vane separators is also largely dependent on geometrical factors, i.e. on its design. Secondary boundary conditions also play an important role: for instance the physical space available for installation of the equipment, the corrosivity of the substances and hence the material selection, the relevance of pressure loss in the process, the importance of maintenance and accessibility, the production costs, and/or exposure to very high or very low temperatures. Until the 1960s, the application of different types of separators was largely based on experience and empirical data, most of which were gathered by manufacturers who protected their know-how. Most theoretical work until that time was centered around particle separation from gases [53, p. 1107]. Early authors researching the physical background of droplet separation, producing valuable experimental data as well as physical and empirical relations to describe separation efficiency, include *Regehr* [53], *Brauer* [7]<sup>1</sup> and *Bürkholz* [10].

---

<sup>1</sup> Refer to *Kall* [29, p. 15].

## **1.1 Industrial relevance of vane separators in power plants**

### **1.1.1 Moisture content**

About 90% of the world's electricity is generated through the use of steam engines in a Rankine cycle [69], in which saturated steam enters the turbine and a mixture of vapor and droplets exits the turbine. Steam expansion in low pressure (LP) turbines is so rapid that under-cooling below the saturation line occurs, often exhibiting exit moisture contents of several percent. Condensation effects significantly reduce the efficiency of steam turbines, mainly due to the following reasons:

- condensation limits steam expansion, causing reduced velocities through the turbine stages and thus reducing the driving force of the turbine,
- the inertia of the droplets cause a mechanical impact on the turbine blades which reduce the rotational momentum of the rotor,
- droplets on the surface of the blades increase friction, turbulence and pressure loss across the stages, and
- droplets released from the blades are entrained back into the steam flow at lower velocities, thus reducing the kinetic energy of the steam flow.

In addition to a reduction of thermal efficiency, droplet impingement causes liquid-impact-induced-erosion on the turbine blades and thus severely shortens their lifetime. For high and intermediate pressure turbines, this is an issue mainly because of the elevated steam temperatures; for low pressure turbines, mainly because of the high steam velocities. Especially on the last stage blades of low pressure steam turbines, where the moisture content as well as steam and blade velocities are largest, provisions must be made to minimize erosion. Preventive measures include condensate drainage on casings and/or hollow blades, blade heating, increasing the axial distance between rotor and stator blades, use of erosion resistant blade materials, blade edge hardening, applying protective layers and using protective shields on leading blade edges. Erosion-corrosion is also a common cause of failure for other components in steam power plants, e.g. for piping and valves, especially at locations of high turbulence. Reduction of moisture content is thus not only relevant to steam turbines, but to the entire steam cycle. Measures to reduce moisture content in saturated steam should be applied as far upstream as possible; ideally shortly downstream of the source of droplet generation.

The most straightforward way to eliminate moisture content in steam is by superheating. In modified Rankine cycles with reheating loops, condensation takes place at the heat sink only, thus largely exempting the turbine from the effects described above. Furthermore, since the Carnot efficiency increases with the average temperature of heat input (at equal temperature of heat output), the process of superheating steam increases the thermodynamic efficiency of the cycle. In conventional nuclear power plants, however, the thermodynamic properties of the main steam and thus the possibility of superheating are limited by some important characteristics of the power plant itself, which is why, as far as fossil power plants are concerned, mechanical separation of moisture is most relevant in these types of plants. The main causes of these limitations in nuclear power plants are the following:

1. The coolant is evaporated through pool boiling (the heat source is submerged);

in Boiling Water Reactors (BWRs) the cooling water is evaporated directly by the energy released from the reactor fuel pins and in Pressurized Water Reactors (PWRs) by the heat transferred from the primary coolant. In both cases the heat source is (almost entirely) submerged and superheating does not occur on a significant scale. The saturated steam rises up and is mechanically dried by separators installed in the upper part of the Reactor Pressure Vessel (RPV) or steam generator. As a result, the steam admitted to the high pressure turbine is always in a saturated state.

2. The primary heat source is not easily accessible;

In most fossil power plants the heat source is the exhaust gas produced by a combustion process (e.g. natural gas, diesel, coal, biomass or waste combustion). The Heat Recovery Steam Generator (HRSG), in which the heat from the exhaust gas is transferred to the coolant, is a large piece of equipment at near ambient pressure. It can accommodate much heat exchanger piping and its walls are easily penetrable. Reactor Pressure Vessels and nuclear steam generators have to withstand very high pressures and their designs are at the limit of the technical possibilities in terms of forging and wall thickness. Reintroducing steam into these vessels for the purpose of superheating is both technically and commercially not feasible. The practical consequence is that in nuclear power plants superheating must be done by cannibalizing steam from higher pressure parts of the steam cycle.

### **1.1.2 Application in nuclear power plants**

By far the most common type of (commercial) nuclear power plant is the PWR, in which steam drying is applied at several stages of the water steam cycle. The steam generator usually contains moisture separators in its upper head to supply the high pressure (HP) turbine with high quality steam. The first reheating stages were implemented in the 1970's to increase the thermo-dynamic efficiency. Also during this time, the importance of external (to the turbine) separation of droplets was discussed and the physical background of droplet separation was under investigation (e.g. [21], [29]). As a result, the reheating stages were fitted with their own moisture separators, thus becoming Moisture Separator & Reheaters (MSRs). The loss of mass flow through mechanical separation of droplets is compensated by the fact that evaporation of moisture content in the HP steam turbine exhaust steam either requires the sacrifice of additional valuable high pressure steam, which reduces the thermal power output of the HP steam turbine, or causes a lower temperature output of the MSR, which reduces the power output of the low pressure (LP) steam turbines. But the main reason for the application of mechanical separation of droplets, as preferred to evaporation, is that it helps protect the downstream components (most notably the reheating pipe bundles) from the erosion-corrosion effects described in the previous section. Replacement of reheating pipe bundles can significantly be reduced by installing (or retrofitting) moisture separators.

Mechanical separation of droplets also takes place in wet cooling towers, in which the condensate from the condenser is released into a stream of ambient air. In the case of natural convection cooling towers, the temperature increase of the air causes an upward air flow through which the condensate is effectively cooled as it falls downward and is collected at the bottom. Droplets below a certain size, however, will be carried upward by the air, which reduces the chimney effect of the cooling tower

and increases the need for make-up cooling water. The latter disadvantage can be very important in arid areas<sup>2</sup>. For these reasons, air dryers (often in the form of vane separators) are usually installed at a location directly above the condensate spray lines.

## 1.2 Vane separator types

The channels of a vane separator, through which the gaseous medium swerves from left to right, thereby alternately accelerating the immersed droplets towards one wall or the other, can be of a zigzag form, with very sharp corners, or of a sinusoidal shape with rounded bends. Most vane separators contain some type of pocket for the collection of the separated moisture. The evolution of vane separators has been towards inventing ever more efficient ways to collect the droplets and *pick off* the liquid film building on the vanes, while minimizing pressure loss. This has led to many different types of vane separators, featuring single or multiple pockets per stage, perforated walls and shielded drainage channels.

Basic types of vane separators have been investigated by *Bürkholz* [10] (Fig. 1.1). With the exception of type *R*, which incorporates roughened wall sections that promote separation by inducing a turbulent boundary layer, all depicted vane separators have some type of hook or pick-off channel. types *N*, *P* and *Q* can be characterized as wavy type vane separators, type *O* is a zig-zag or straight type vane separator and types *R* and *S* are intermediate forms. Types *N*, *R*, *T*, *U* and *V* can be characterized as single stage vane separators, although in types *N*, *R* and *V* there are effectively several sections contributing to the separation of droplets.

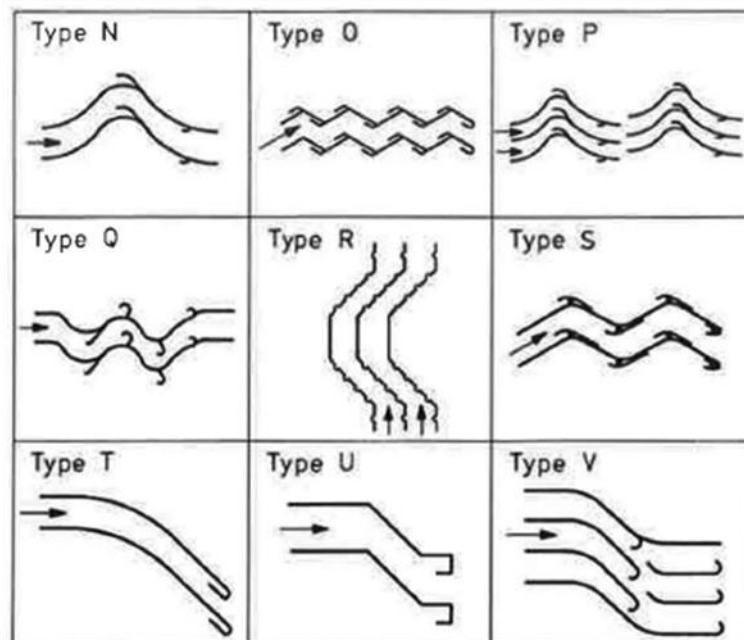


Fig. 1.1 Schematic views of different types of vane separators<sup>3</sup>

<sup>2</sup> In very arid areas with almost no access to water, dry cooling towers with a closed cooling water cycle will be the main choice.

<sup>3</sup> Reprinted from [10, p. 101]. Copyright Wiley-VCH Verlag GmbH & Co. KGaA. Reproduced with permission.

A more detailed vane separator geometry is discussed by *Kall* [29], according to whom the relevant geometrical parameters that characterize a wavy type vane separator include the channel width, the bend angle, the wavelength, the inner and outer radii of curvature, and the channel offset. The latter is defined by the lateral distance between subsequent inner bends, which should be positive, so that an 'optical' pathway through the separator channel does not exist. This would allow an easy passage for heavy droplets, referred to by *Kall* [29, p. 44] as *Durchschlagen*, which will henceforth be translated as *strike through*.

*Kolev* [34, p. 357] lists several industrial vane separators that exhibit more complex geometries. Most of these vane separators can be classified as either wavy or straight type vane separators and many also feature some type of pick-off hook, in some cases combined with a drainage channel.

## 1.3 Vane separator efficiency

### 1.3.1 Definitions

In a practical sense, the vane separator efficiency is defined by the droplet mass flow at the exit of a vane separator, divided by the inlet droplet mass flow. This definition incorporates all phenomena affecting droplet mass inside the vane separator, including possible phase transitions (evaporation or condensation) and re-entrainment effects, and it is applied when discussing experimental results. For theoretical purposes other definitions are applied. Phase transitions are almost always neglected (as will be done throughout this paper) and, with some exceptions (as will be discussed in the following chapters), CFD models usually do not account for re-entrainment of droplets. Theoretical vane separator efficiencies are often defined by the mass of droplets hitting the walls, divided by the inlet droplet mass flow. According to this definition, droplet re-entrainment is non-existent, liquid drainage is irrelevant, and all that matters is the droplet movement inside the vane separator channel. This is driven mainly by drag and centrifugal forces. As will become clear, the main physical parameters influencing the droplet separation efficiency, are the droplet diameter  $D_d$ , the droplet density  $\rho_d$ , the (homogeneous) gas velocity  $v_g$  and the dynamic gas viscosity  $\mu_g$ . The most important geometrical parameters are the channel width  $\delta_R$  and the bend angle  $\varphi$ . All but the bend angle are incorporated in the dimensionless Stokes number  $St$ , which results from a balance of drag and centrifugal forces:

$$St = \frac{\rho_d v_g D_d^2}{18 \mu_g \delta_R} \quad (1.1)$$

The Stokes number will be derived at the end of this chapter, but first the basic physics is explained as it applies to *cyclone* separators. Although droplet separation in wave separators is often attributed to the inertia of the droplets, in the case of wavy-type separators, the description of centrifugal forces acting on the droplets is perfectly equivalent. Under the assumption that the droplet distribution remains spatially uniform, vane separator separation theory emerges from the same basic equations.

### 1.3.2 An introduction to cyclone separation efficiency

A simple model to compute the separation efficiency of cyclone separators<sup>4</sup> is constructed, to serve as an introductory starting point for the analysis of the vane separator efficiency in the next section. A cylindrical cyclone separator is considered of length  $H$  and radius  $R_{out}$ , with a cylindrical solid inner body of radius  $R_{in}$  and attached to it a swirler in the form of a propeller (Fig. 1.2).

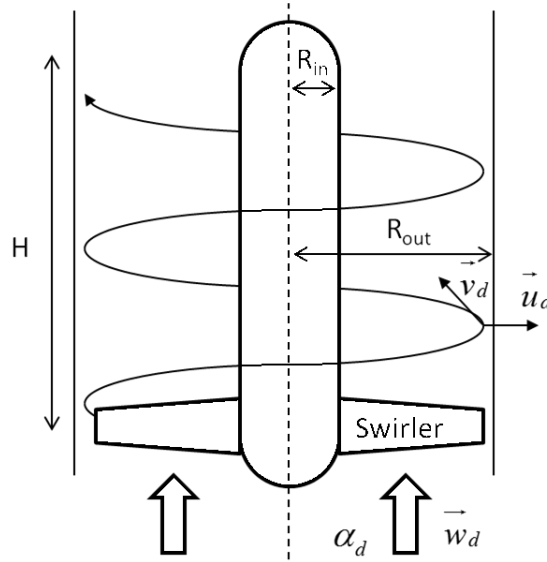


Fig. 1.2 Schematic model of a cyclone separator

If a uniformly distributed droplet volume fraction  $\alpha_d$  is assumed in the flow, moving with an axial velocity of  $w_d$  into the cyclone, then the moisture mass flow entering in axial direction into the control volume  $\pi(R_{out}^2 - R_{in}^2)d\theta dz / 2\pi$  equals

$$\dot{m}_d = \alpha_d w_d \rho_d \pi (R_{out}^2 - R_{in}^2) d\theta / 2\pi \quad (1.2)$$

in which  $\theta$  and  $z$  are the radial and axial coordinates respectively. The moisture mass flow deposited on the wall section  $R_{out}d\theta dz$  of the control volume equals

$$d\dot{m}_d = -\alpha_d u_d \rho_d R_{out} d\theta dz \quad (1.3)$$

in which  $u_d$  is the radial droplet velocity. The separation efficiency is defined as the ratio of the separated moisture mass flow and the moisture inlet mass flow, leading to

$$\frac{d\dot{m}_d}{\dot{m}_d} \equiv d \ln \dot{m}_d = -\frac{u_d}{w_d} \frac{2R_{out}}{(R_{out}^2 - R_{in}^2)} dz \quad (1.4)$$

<sup>4</sup> The cyclone separation model presented here, and many similar ones, can be found in a number of publications, partly dating back several decennia. The model presented here is a close representation of the one introduced by Kolev [34, pp. 363-366].

To obtain the radial droplet velocity  $u_d$ , the simplified radial momentum equation for incompressible fluids is employed. The conservation of momentum is given by

$$\rho \left( \frac{\partial \vec{v}}{\partial t} + \nabla \cdot \vec{v}\vec{v} \right) = -\nabla p + \nabla \cdot \vec{\tau} + \rho \vec{g} \quad (1.5)$$

For industrial-sized cyclone separators the flow velocities are usually very high and thus centrifugal forces are much larger than gravitational and pressure gradient forces. Therefore, the pressure gradient, as well as the gravitational influences, are neglected. Assuming perfectly laminar flow and considering Stokes drag only<sup>5</sup> (i.e. the ratio of liquid and gas viscosity is very large and the droplets, being very small and having constant density, can be approximated by rigid spheres), the two-dimensional radial momentum equation reduces to

$$M_d \left( \frac{du_d}{dt} - \frac{v_d^2}{r} \right) + c_{gd}^d \frac{A_d}{2} \rho_g (u_d - u_g) |u_d - u_g| = 0 \quad (1.6)$$

in which  $M_d$  is the mass of the droplet,  $A_d$  is the area of the frontal projection of the droplet and  $c_{gd}^d$  is the drag coefficient. In addition, the following assumptions are made:

- there is a no-slip condition in the circumferential direction ( $v_d = v_g$ ),
- the droplets reach their terminal radial velocity before they hit the cyclone wall ( $\frac{du_d}{dt} = 0$ ),
- the radial velocity component of the gas can be neglected ( $u_g = 0$ ).

These assumptions reduce equation (1.6) to a balance of centrifugal and drag force:

$$\rho_d \pi \frac{D_d^3}{6} \frac{v_g^2}{r} = c_{gd}^d \frac{\pi D_d^2}{8} \rho_g u_d^2 \quad (1.7)$$

The drag coefficient for Stokes flow is defined as

$$c_{gd}^d = \frac{24 \mu_g}{\rho_g D_d u_d} \quad (1.8)$$

The radial droplet velocity at the wall is then given by the following equation:

$$u_d = \frac{1}{18} \frac{\rho_d}{\mu_g} D_d^2 \frac{v_g^2}{R_{out}} \quad (1.9)$$

<sup>5</sup> For sufficiently small droplets in laminar flow with small velocities, the Reynolds number is below unity. The drag coefficient and the validity of the Stokes regime is discussed further in section 3.1.1.

Inserting equation (1.9) into equation (1.4) and integrating over the height of the cyclone separator leads to the following equation for the liquid mass flow:

$$\dot{m}_{d,out} = \dot{m}_{d,in} \exp\left(-\frac{\rho_d v_g^2 D_d^2}{18w_d \mu_g (R_{out}^2 - R_{in}^2)} H\right) \quad (1.10)$$

Dividing the separated liquid mass flow by the inlet liquid mass flow gives an expression for the separation efficiency  $\eta$  of the cyclone separator:

$$\eta = 1 - \exp\left(-\frac{\rho_d v_g^2 D_d^2}{18w_d \mu_g (R_{out}^2 - R_{in}^2)} H\right) = 1 - \exp\left(-\frac{\rho_d v_g^2 D_d^2}{18w_d \mu_g (R_{out}^2 - R_{in}^2)} H\right) \quad (1.11)$$

### 1.3.3 A cyclone separation model applied to vane separators

A wave separator functions similar to a small cyclone in the sense that separation of droplets onto the vane surfaces is governed by centrifugal and drag forces. Analogous to the previous section, the vane separator is modeled as a series of consecutive two-dimensional circular bends (also referred to as stages), each of which acts as a small cyclone. Because the velocities in vane separators are much smaller as compared to cyclone separators, the gravitational force may not be negligible, but by assuming a vertical orientation of the vanes its impact vanishes<sup>6</sup>. The third dimension represents the height of the vanes. Each channel of a vane separator, enclosed by two vane plates, is defined by an inner radius  $R_{in}$ , an outer radius  $R_{out}$ , a channel width  $\delta_R$ , a total stage angle  $\varphi$ , a height  $H$  and the number of stages  $n$  (Fig. 1.3).

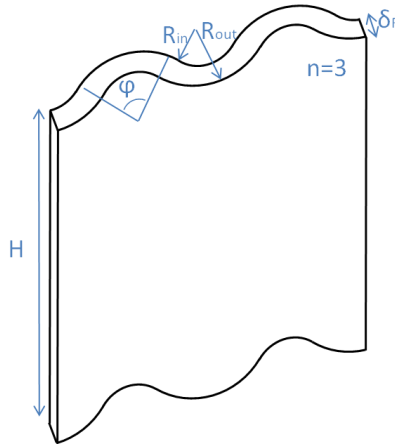


Fig. 1.3 Schematic view of a vane separator channel

The mass flow entering the control volume  $\pi(R_{out}^2 - R_{in}^2)d\theta dz / 2\pi$  (from the side in Fig. 1.3) is then given by

$$\dot{m}_d = \alpha_d v_d \rho_d \delta_R dz \quad (1.12)$$

<sup>6</sup> The gravitational influence on vane separator efficiency will be discussed in section 3.2.

in which  $v_d$  is the droplet velocity into the control volume. The moisture mass flow deposited on the wall section  $R_{out}d\theta dz$  equals

$$d\dot{m}_d = -\alpha_d u_d \rho_d R_{out} d\theta dz \quad (1.13)$$

This now leads to

$$d \ln \dot{m}_d = -\frac{u_d}{v_d} \frac{R_{out}}{\delta_R} d\theta \quad (1.14)$$

Inserting equation (1.9) for the terminal radial velocity and assuming a no slip condition for the droplets in the direction of flow along the channel ( $v_d = v_g$ ) results in

$$d \ln \dot{m}_d = -\frac{\rho_d v_g D_d^2}{18\mu_g \delta_R} d\theta = -St d\theta \quad (1.15)$$

from which the relevance of the Stokes number has become clear. Analogous to equation (1.11), but integrating over the total angular path  $n\varphi$  of the wave separator<sup>7</sup>, in which  $\varphi$  is the total bend angle and  $n$  is the number of stages, this leads to the following expression for the separation efficiency of the vane separator:

$$\eta = 1 - \exp\left(-\frac{\rho_d v_g D_d^2}{18\mu_g \delta_R} n\varphi\right) = 1 - \exp(-St \cdot n\varphi) \quad (1.16)$$

This result was already reported by *Jackson & Calvert* [26], although in their case  $n$  is defined as the number of 360° turns (refer to chapter 2.1). The analysis represented here equals the one by *Kolev* [34, pp. 375-376], arriving at the identical result.

#### 1.3.4 Droplet relaxation time constant

Equations for droplet separation efficiency are often simplified by inserting the droplet relaxation time constant  $\Delta\tau_{gd}$ , which scales with the inertia of the droplet and the viscosity of the surrounding flow, thus representing a measure of how quickly the droplet adjusts itself to the surrounding flow<sup>8</sup>. For Stokes flow, equation (1.8) is valid and the droplet relaxation time constant is given by

$$\Delta\tau_{gd} = \frac{\rho_d D_d^2}{18\mu_g} \quad (1.17)$$

<sup>7</sup> By performing this integration it is implicitly assumed that, analogous to the cyclone separator, the droplets always travel with the terminal radial velocity near the wall and that the entire wall is effective in the separation of the droplets. This corresponds to the limit of droplets without inertia in an infinitesimally narrow channel. Non-uniformity of droplet distributions will be discussed further in later sections.

<sup>8</sup> See for instance *Galletti et al.* [17] or *James et al.* [27] for different forms of droplet relaxation time constants.

This is the definition of the droplet relaxation time constant that will be used throughout this paper, unless explicitly stated otherwise. The Stokes number can now also be written as the product of the gas velocity and the droplet relaxation time constant under Stokes conditions, divided by the channel width  $\delta_R$ :

$$\text{St} = \frac{v_g \rho_d D_d^2}{18 \mu_g \delta_R} = \frac{v_g \Delta \tau_{gd}}{\delta_R} \quad (1.18)$$

The droplet separation efficiency of vane separators can thus alternatively be written as

$$\eta = 1 - \exp(-\text{St} \cdot n\varphi) = 1 - \exp\left(-\frac{\Delta \tau_{gd} v_g}{\delta_R} n\varphi\right) \quad (1.19)$$

## 2 State of the art

Before the 1990s, the number of publications on vane separators and specifically on their separating performance could be called meager, especially as compared to their extensive industrial application [10, p. 103]. But since then, many numerical and experimental studies dealing with the separation efficiency of vane separators have been published. Amongst other authors, *Verlaan* [64], *James et al.* [27] and *Galletti et al.* [17] have performed experiments or used existing data to validate their numerical models. These were based on a simplified equation of motion for the droplets in a gas velocity field in which gravity, lift forces, virtual mass forces, droplet deformation and droplet-droplet interaction was neglected and only one-way-coupling was considered. Much attention was paid to the modeling of turbulence, driven by the fact that models without turbulence often under-predict the separation efficiency, especially for small droplet sizes [17].

### 2.1 Analytical approaches

*Regehr* [53, p. 1108] considers the maximum radial migration distance of droplets as they traverse a vane separator bend, represented by the droplet entering the bend at a radius  $R_{d,0}$  and just reaching the outer wall at  $R_{out}$  as it exits the bend. He defines the separation efficiency  $\eta$  of a vane separator bend as the ratio of this maximum radial droplet migration distance ( $R_{out} - R_{d,0}$ ) and the channel width  $\delta_R$  :

$$\eta = \frac{R_{out} - R_{d,0}}{R_{out} - R_{in}} = \frac{R_{out} - R_{d,0}}{\delta_R} \quad (2.1)$$

This representation is sensible when considering a uniform spatial distribution of identical droplets at the inlet. All droplets beyond the initial radius  $R_{d,0}$  become separated and none within (Fig. 2.1).

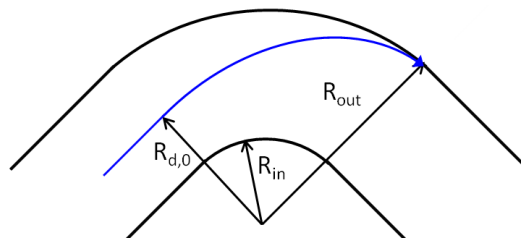


**Fig. 2.1** Droplet path through a bend with inner radius  $R_{in}$ , outer radius  $R_{out}$  and initial droplet starting radius  $R_{d,0}$

Other analytical approaches were supported early on by the formulation of the earlier discussed Stokes number. *Jackson & Calvert* [26], for instance, analyze the separation efficiency of packed bed separators. Assuming uniform flow they provide a very simple expression for the separation efficiency:

$$\eta = \pi nK \quad (2.2)$$

in which  $n$  is the number of  $360^\circ$  turns the droplet experiences and the *inertial impaction parameter*  $K$  is a dimensionless ratio between the droplet's inertial force and the force resisting motion (e.g. drag). By assuming a continuous mixing of droplets throughout the flow path, as well as a homogeneous circumferential gas velocity  $V_g$ , the authors arrive at a differential equation for the number of droplets per flow volume  $C$ , as a function of the flow angle  $\theta$  around an obstacle. Solving this equation and equating it to the initial number concentration  $C_0$  leads them to

$$\frac{C(\theta)}{C_0} = \exp\left(-\frac{u_{term}}{V_g} \frac{R_{out}\theta}{\delta_R}\right) \quad (2.3)$$

Balancing drag and inertial forces and solving for the droplet terminal radial velocity  $u_{term}$  leads to the following expression for the separation efficiency:

$$\eta = 1 - \exp(-\pi n K) \quad (2.4)$$

in which

$$K = \frac{\rho_d v_g D_d^2 \theta}{18 \mu_g \delta_R} = St \theta \quad (2.5)$$

Although the objects of investigation were packed bed separators, this equation shows much resemblance to the droplet separation efficiency of vane separators as defined in the last chapter (equation (1.16)).

*Calvert et al.* [11] provide a theoretical relation for the separation efficiency of zigzag baffles, which are arranged as  $n$  stages of simple straight wall sections of length  $L$ , at a lateral spacing  $s$  and at an angle  $\phi$  with respect to the gas flow direction (Fig. 2.2).

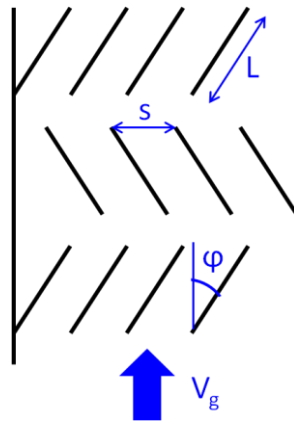


**Fig. 2.2** Packed bed separator as parametrized by *Calvert et al.* [11]

Based on inertial mechanisms, the separation efficiency for a terminal droplet velocity  $v_{term}$  (not further defined) and a homogeneous gas velocity  $V_g$  is<sup>9</sup>:

$$\eta = 1 - \exp\left(-\frac{v_{term}}{V_g} \frac{nL\varphi}{s \tan \varphi}\right) \quad (2.6)$$

*Bürkholz* [9] investigates wired mesh eliminators and derives from a dimensional analysis what he calls the separation parameter  $\psi_A$ , which is a function of droplet density  $\rho_d$ , gas density  $\rho_g$ , dynamic gas viscosity  $\mu_g$ , pressure loss  $\Delta p$ , impact body width  $D$  (given by the wired mesh thickness) and droplet diameter  $D_d$ :

$$\begin{aligned} \psi_A &= \frac{1}{4} \left( \rho_d \rho_g^{-1/3} \mu_g^{-4/3} \right) \left( \Delta p^{2/3} D^{-2/3} D_d^2 \right) \\ &= \frac{9}{2} \left( \frac{\rho_d v_g D_d^2}{18 \mu_g D} \right) \left( \frac{\rho_g v_g D}{\mu_g} \right)^{1/3} \left( \frac{\Delta p}{\rho_g v_g^2} \right)^{2/3} = \frac{9}{2} \text{St Re}^{1/3} \text{Eu}^{2/3} \end{aligned} \quad (2.7)$$

in which Re and Eu are the Reynolds and Euler number respectively. For effective use of the separation parameter, *Bürkholz* [9] also assumes an *effective* impact body width  $\bar{D}$ , which in the case of vane separators equals  $\bar{D} = \delta_R a^*$  with  $a^* = 0.13$ . Given that for vane separators  $D = \delta_R$  in equation (2.7), the separation efficiency is given as a function of a single parameter  $x$ :

$$\eta = x(1 - \exp(-1/x)), \quad x = 0.003 \psi_A^2 a^{*-4/3} \quad (2.8)$$

Equation (2.8) considers droplet impingement on baffle-type vane separators. *Bürkholz* [10] later investigated vane separators of several different types. The equation by *Regehr* [53] is refined by defining the radial droplet migration distance as the product of the time of passage  $t_d$  through the bend and the terminal radial droplet velocity  $u_{term}$  under Stokes conditions [10, p. 104]<sup>10</sup>:

$$R_{out} - R_{d,0} = u_{term} t_d = \frac{\rho_d v_g^2 D_d^2}{18 \mu_g R_g} \frac{\varphi R_g}{v_g} \quad (2.9)$$

in which  $R_g$  is the radius of curvature of the gas flow. By dividing this equation by the channel width, *Bürkholz* [10] arrives at a separation efficiency for a single stage vane separator, defined by the Stokes number, multiplied with the bend angle  $\varphi$ :

$$\eta = \frac{\rho_d v_g D_d^2}{18 \mu_g \delta_R} \varphi = \text{St} \varphi \quad (2.10)$$

<sup>9</sup> The erroneous minus sign outside the brackets in the original relation by *Calvert et al.* [11] is corrected here.

<sup>10</sup> The square of the droplet velocity was omitted by *Bürkholz*, although his subsequent analysis is correct. A correction is made here for this printing error.

The same result is reported by *Leber* [40, p. 65], specifically for a 90° deflection. *Bürkholz* [10] subsequently adjusts both the Stokes number and the channel width, to account for flow effects behind the bend and a consequent narrowing of the effective channel width, which accelerates the flow. This adjustment contains an empirical function of channel width and gas velocity and is represented by  $Re^{2/3}$ . An empirical parameter  $C_2$  is included, to fit the data with experimental data, which ultimately leads to the following equation for the separation efficiency of a single stage:

$$\eta = \frac{\rho_d v_g D_d^2}{18 \mu_g \delta_R} \varphi Re^{2/3} C_2 = St Re^{2/3} C_2 \varphi = \psi_e \varphi \quad (2.11)$$

in which  $\psi_e = St Re^{2/3} C_2$  is the *effective separation parameter*. The value adopted by *Bürkholz* [10, p. 108] for the empirical parameter  $C_2$  is 0.003<sup>11</sup>. In comparison with equation (2.7), the Euler number, and with it a representation of the pressure drop, has apparently been dropped. To arrive at separation efficiencies for multiple stage vane separators with  $n$  number of stages, the following equation is used [10, p. 113]:

$$\eta = 1 - (1 - \psi \varphi)^n \quad (2.12)$$

in which the *separation parameter*  $\psi$  can be represented by the Stokes number or by the *effective separation parameter*  $\psi_e$ . The term  $\psi \varphi$  can also be represented by an experimental value for the separation efficiency for a certain number of stages, in order to arrive at separation efficiencies for larger numbers of stages of the same shape. A uniform initial droplet distribution is considered, which is inaccurate for consecutive bends, depending on how much the droplet distribution is skewed towards one side after the first bend, thus increasing the radial distance of the bulk of the droplets to the effective inertial wall. This sub-optimal remixing of droplets deteriorates the separation efficiency in subsequent stages. *Verlaan* [64, p. 56] (citing *Gardner* [18]) accounts for this effect by including an additional power  $m$  in equation (2.12):

$$\eta = 1 - (1 - \psi \varphi)^{mn} \quad (2.13)$$

The magnitude of the power  $m$  usually lies between 0.5 for bad remixing and 1 for perfect remixing (as in the case of [10]).

*Wilkinson* [70] also applies a mixing factor to account for the uneven droplet distribution upstream of the first bend, but uses it to adjust the separation efficiency of each bend directly. Differentiating between the first bend and consecutive bends, he arrives at the following relation:

$$\eta = 1 - (1 - St \varphi)(1 - f_m St \varphi)^{n-1} \quad (2.14)$$

---

<sup>11</sup> This number is given without reference to his previous work. It is interesting that it coincides with the number included in the parameter  $x$  in equation (2.8).

The form of the *mixing factor*  $f_m$  is based on the transverse droplet migration distance  $y$  across the channel, for which the r.m.s. turbulent transverse gas velocity is the driving force. Assuming Stokes drag and a constant transverse gas velocity  $c_{pb}cV_g\delta_R/4L$ , in which  $c$  is an empirical constant,  $c_{pb} = 2\Delta p_b/\rho_g V_g^2$  is the pressure loss coefficient in the mitre bend,  $V_g$  is the homogenous circumferential gas velocity,  $\delta_R$  is the channel width and  $L$  is the length of the mitre bend, the transverse droplet migration distance equals  $y = Lc_{pb}c/18St$ . Assuming complete mixing for  $y = \delta_R$ , leading to  $f_m = 1$ , and assuming no mixing for  $y = 0$ , leading to  $f_m = 0$ , the following mathematical relation for the mixing factor is proposed:

$$f_m = 1 - \exp\left(-\frac{y}{L(\delta_R - y)}L\right) = 1 - \exp\left(\frac{c_{pb}c}{c_{pb}c - 18St\delta_R/L}\right) \quad (2.15)$$

The empirical pressure drop coefficient  $c_{pb}$  is given by *Wilkinson* [70] as

$$c_{pb} = \left(0.0649 + \frac{22.3}{\sqrt{\text{Re}}}\right)\varphi \quad (2.16)$$

with

$$\text{Re} = \frac{\rho_g V_g \delta_R}{\mu_g} \quad (2.17)$$

Based on experimental data, the empirical constant  $c$  is suggested to be 0.257 [70, p. 269].

*Verlaan* [64, p. 56] also bases the separation efficiency on the ratio of radial droplet displacement and effective channel width, a similar approach to *Bürkholz* [10]. In his case the effective channel width is derived by a simple trigonometric adjustment defined by the bend angle. He arrives at the following separation efficiency, in which also the virtual mass force is accounted for:

$$\eta = \frac{(\rho_d - \rho_g)v_g D_d^2}{18\mu_g} \frac{2\varphi}{\delta_R (\cos\varphi)^2} \quad (2.18)$$

The virtual mass force (as well as the pressure force) becomes significant below droplet-to-gas density ratios of 100 only [64, p. 53]<sup>12</sup>. Rewriting equation (2.18) in terms of the droplet diameter, he arrives at an expression for the droplet diameter  $D_d^{100}$  at which the separation efficiency reaches unity:

$$D_d^{100} = \sqrt{\frac{\mu_g \delta_R (\cos\varphi)^2}{(\rho_d - \rho_g)v_g \varphi}} \quad (2.19)$$

<sup>12</sup> Forces on droplets are elaborated in chapter 3.1.1.

Based on numerical results for the influence of certain physical and geometrical parameters, *Verlaan* [64, p. 59] then revises this equation to reach the following relation:

$$D_d^{100} = K \sqrt{\frac{\mu_g \delta_R^2}{(\rho_d - \rho_g) v_g \varphi^3}} \quad (2.20)$$

in which  $K$  is an empirical parameter. Most notably the influence of channel width and bend angle have been strongly increased. It is noted that a formulation of  $D_d^{100}$  is possible because of the non-exponential form of equation (2.18). Separation efficiencies of the form of equation (2.8) display asymptotic behavior at unity, thus arriving at an infinite droplet diameter for 100% separation efficiency. Being linear functions of the gas velocity and quadratic functions of the droplet size, equations (2.10) and (2.18) quickly result in values for the separation efficiency that are much greater than unity. A clear advantage of exponential equations for the separation efficiency is that they do not show this unphysical behavior.

*Kolev* [34] investigates separation efficiencies of cyclones and extends this analysis to the separation efficiency of vane separators. His analysis has been discussed in detail in chapters 1.3.2 and 1.3.3.

## 2.2 CFD approaches

Much research on vane separators deals with numerical models for the evaluation of droplet separation efficiency. Often, existing CFD codes like *Fluent* [2], *CFX* [1] or *Phoenix* [12] are used. *Galletti et al.* [17] provide an overview of numerical models used by different authors, many of which make use of some form of the droplet time relaxation constant. It is applied to a solution of the two-dimensional momentum equation, which represents the basic equation for droplet motion in the numerical code which tracks the droplet paths. The droplets are usually uniformly distributed across the vane separator channel entrance and are removed from the flow as soon as they cross the boundary of the wall. This method was for instance used by *Verlaan* [67]. A similar approach was used by *Wang & James* [64], including the pressure force and the virtual mass force in the description of droplet motion.

Some form of turbulence is often added to the model. Two different turbulence models (as available in the CFD package employed by these authors) are discussed and compared by *Wang & James* [67]. These are the STD  $k - \varepsilon$  model and the low Reynolds  $k - \varepsilon$  model, the first of which uses wall functions where the latter is capable of resolving flows near solid boundaries [67, p. 981]. *Wang & James* [68] and *James et al.* [27] use a basic eddy interaction model, which applies a three-dimensional randomly oriented offset to the gas velocity, based on the eddy length and time scales. The velocity fluctuations, the eddy interaction time and the eddy length scale can be updated only after the eddy interaction time has elapsed, or updated each time a control volume boundary has been traversed, i.e. when the mean velocity is updated. These models are referred to as *Constant Eddy Interaction Model* (Const EIM) and *Varied Eddy Interaction Model* (Varied EIM), respectively [68, p. 693]. The applied random number is in both cases updated only after the eddy interaction time has elapsed. This seemingly insignificant detail can produce very different results, as shown by these authors. The Varied EIM is employed by *James et al.* [27].

## 2.3 Parametric and empirical approaches

*Kall* [29, pp. 23-25] describes the outlet wetness of a vane separator as a function dependent on 16 variables. A dimensional analysis reduces this to thirteen characteristic coefficients, in terms of which he describes all relevant physical parameters in dimensionless form (i.e. Reynolds number, Weber number, Froude number, inlet wetness, outlet wetness, separation efficiency, density ratio, viscosity ratio and six ratios of length). Apart from also noting the relation reported by *Regehr* [53] (equation (2.1)), *Kall* [29] does not report a physical formulation for the separation efficiency based on his dimensional analysis.

*Zamora & Kaiser* [72] spend much effort on fitting numerical data. Without further physical background, they propose the following equation for the separation efficiency:

$$\eta = \frac{1}{1 + \exp\left(-\frac{P_i - P_0}{\lambda}\right)} \quad (2.21)$$

in which  $P_i = \rho_d v_g D_d^2 / (\mu_g L)$  is called the *inertial parameter*<sup>13</sup> and  $P_0$  and  $\lambda$  are adjustment functions of the form  $a \exp(-b\Lambda)$ .  $L$  is the geometrical length of the vane separator (not accounting for deflections) and the empirical constants  $a$  and  $b$  are defined for different aspect ratios  $\delta_R/L$ . The *removal geometric parameter*  $\Lambda$  is defined as

$$\Lambda = \left(\frac{L_w}{L}\right)^2 \sum_{i=1}^n \varphi_i \quad (2.22)$$

in which  $L_w$  is the wetted length, i.e. the total length of all wall sections. The sum over  $\varphi_i$  produces the total angle of all  $n$  deflections (stages). *Zamora & Kaiser* [72] reach near perfect fits of their numerical data, which can be attributed to the arbitrary choice of equation (2.21) as well as the extensive use of empirical constants.

*Zhao et al.* [73] use results from a CFD model to investigate the correlation between separation efficiency and five geometrical parameters and operating conditions. The CFD model is validated against experimental results reported by *Lang et al.* [38] for a single stage separator. In what they term *response surface methodology*, the authors employ statistical software to fit response surfaces, defined by the response of the separation efficiency to changes in two different dependent parameters. A function including linear, quadratic and cross terms of the dependent parameters is applied for the fitting. The resulting regression coefficients provide insight into which terms cause significant responses. *Zhao et al.* [73] arrive at the following function for the separation efficiency:

<sup>13</sup> According to *Zamora & Kaiser* [72, p. 1234] the inertial parameter equals the Stokes number multiplied by a factor 18. The Stokes number, however, considers the channel width  $\delta_R$ , whereas these authors make use of the total vane separator length  $L$ . Compare also the *inertial impaction parameter* by [26] discussed earlier in this chapter.

$$\eta = 1.95539 + 0.004491(\pi - \varphi) + 0.001046H_1 - 0.02186H_2 - 0.0074\delta_R + 0.182297V_g - 0.00004(\pi - \varphi)^2 - 0.000043(\pi - \varphi)\delta_R - 0.00047(\pi - \varphi)V_g \quad (2.23)$$

in which  $H_1$  is the length of the identical in- and outlet sections and  $H_2$  the distance between the in- and outlet sections (which is a measure for the length of the bend). Unfortunately, the absence in the analysis, of the response of the separation efficiency to the droplet diameter<sup>14</sup>, prevents a general application of equation (2.23).

## 2.4 Motivation and structure of the thesis

As discussed in chapter 1.1, the separation efficiency of vane separators is of major importance for the preservation of downstream equipment. Poor design of vane separators can lead to poor separation efficiencies, which can cause serious damage and constitutes a bad investment. Malfunctioning vane separators can significantly accelerate the erosion of piping, valves, reheater tubes and/or turbine blades. In addition, vane separator behavior during large liquid loading transients can be relevant for the integrity of some components and even for the safety of the plant. For instance, certain accident scenarios cause a sudden pressure drop in parts of the system connected to condensate tanks. This can lead to sudden evaporation in the condensate tank, which can push large amounts of water-steam mixture back into the steam system and can cause major damages and prolonged outages. This phenomenon is known as condensate back-flashing. If the two-phase mixture passes through moisture separators, it is relevant to know their (dys)functional behavior during such extreme conditions. This is a factor that is often neglected.

Vane separators are available for many applications, and it is important to know which aspects are significant for them to function correctly, to be able to optimize the design for the specific boundary conditions, and to reliably predict the separation efficiency for different operational loads and failure conditions. Being able to do this analytically minimizes the need for CFD analyses to validation purposes only, leading to a reduction of development time and costs. Furthermore, it allows for a basic analysis of vane separator behavior during conditions that are difficult and/or expensive to reproduce in experiments. Another major advantage of a reliable analytical solution for separation efficiency is that it allows for direct implementation in nuclear CFD codes used for the dynamic analysis of larger parts of the steam cycle (1D or 3D, porous media or boundary fitted code), without impairing calculation speed. Especially CFD codes with modular capabilities, encompassing physically large, possibly coupled systems<sup>15</sup>, such as those used for the analysis of the entire primary cycle of a PWR or the entire water-steam cycle of a BWR, cannot afford to handle all the physical and geometrical details contained in these systems. Vane separators are often not contained in these codes as a building block. An analytical representation of the separation efficiency of vane separators, based on relevant geometrical input parameters and dependent on the relevant physical parameters supplied by the code for each timestep, represents an easy, straightforward and valuable addition to the analysis.

---

<sup>14</sup> In all cases a constant droplet diameter of 50  $\mu\text{m}$  was considered.

<sup>15</sup> Examples of such codes are TRACE and RELAP5, developed by the United States Nuclear Regulatory Committee (NRC), ATHLET, developed by the Gesellschaft für Anlagen- und Reaktorsicherheit (GRS), and Skythia, developed by Kolev ([31]- [34]).

These first two chapters have already shown that an important factor that influences the separation efficiency is the specific geometry of the flow channel. Separation efficiencies have been reported accounting for several relevant geometrical parameters, e.g. bend angle, channel width and number of stages, often used for a comparison with experimental data. Some authors investigate and compare different geometries ( [49], [10, pp. 105-109]), but are often not very systematic in their comparison or specific about their results. For instance, *Verlaan* [64] lists the correlation between several geometrical parameters and the separation efficiency, but only reports a positive, negative or no net effect: he does not quantify his results. A more extensive analysis is given by *Kolev* [34, p. 376], who introduces a dimensionless 'vane number', as well as a 'vane geometry number', of which the separation efficiency is an exponential function. Nonetheless, the specific impact of geometrical parameters on separation efficiency has, to the opinion of this author, not sufficiently been explored.

This paper intends to identify the most significant geometrical parameters of a vane separator and analytically quantify their impact on separation efficiency, by relaxing traditional assumptions and introducing additional aspects to the analytical model for separation efficiency. These aspects include the integration of the straight channel parts between bends, the non-uniformity of the droplet distribution and of the velocity field, the effect of gravity and the effect of non-orthogonal flow conditions. Additional circumstantial effects influencing vane separator efficiency are discussed. The resulting analytical model is compared with empirical data from existing literature, as well as with novel experimental data provided by the Institute of Fluid Mechanics (LSTM) of the Friedrich-Alexander University in Erlangen-Nuremberg. Based on the experimentally validated analytical approach and incorporating relevant findings from the foregoing discussions in this paper, an exemplary industrial application is worked out, arriving at a novel vane separator design. This novel design was also experimentally tested by the Institute of Fluid Mechanics (LSTM) of the Friedrich-Alexander University in Erlangen-Nuremberg. The resulting data is compared to the simplified design in order to determine the effectiveness of the novel design features.



## 3 An analytical model for vane separator efficiency

### 3.1 Droplet flow path analysis and vane separator geometry

If an analytical model for the evaluation of vane separator efficiencies is to arrive at realistic results for broader application ranges, additional factors influencing the droplet flow path must be accounted for. In this section, forces on droplets are discussed in general, after which a simple Lagrangian particle tracking method is introduced to be applied as a straight-forward method for investigating droplet paths through the vane separator channel.

#### 3.1.1 Forces on droplets

*Maxey & Riley* [44] derive an equation of motion for small rigid spheres in a non-uniform flow field, which, applied to spherical droplets, after some rearrangement, assumes the following form:

$$\rho_d \frac{d\vec{v}_d}{dt} - \rho_g \frac{D\vec{v}_{gd}}{Dt} = (\rho_d - \rho_g) \vec{g} + \frac{1}{2} \rho_g \left\{ \left( \frac{d\vec{v}_{gd}}{dt} - \frac{d\vec{v}_d}{dt} \right) + \frac{1}{10} r_d^2 \frac{d\nabla^2 \vec{v}_{gd}}{dt} \right\} - \frac{9\mu_g}{2r_d^2} \left( \vec{v}_d - \vec{v}_{gd} - \frac{1}{6} r_d^2 \nabla^2 \vec{v}_{gd} \right) - \frac{9\mu_g}{2r_d} \int_0^t \frac{d/d\tau \left( \vec{v}_d - \vec{v}_{gd} - \frac{1}{6} r_d^2 \nabla^2 \vec{v}_{gd} \right)}{\sqrt{\pi\nu_g(t-\tau)}} d\tau \quad (3.1)$$

In this equation,  $\vec{v}_{gd}$  is the undisturbed gas velocity defined at the centre of the droplet,  $r_d$  is the droplet radius,  $d/dt$  is the time derivative of the gas velocity (following the moving droplet) and  $D/Dt$  is the time derivative using the undisturbed gas velocity as the convective velocity (such that  $D\vec{v}_{gd}/Dt$  is the acceleration of the gas as observed at the instantaneous center of the droplet [44, p. 883]). The terms on the right-hand side of equation (3.1) represent the effects of gravity (or buoyancy), virtual mass, Stokes drag and history, respectively [45, p. 1212]. The lift force is not accounted for in equation (3.1), because according to *Maxey & Riley* (citing *Bretherton* [8]) there is no such force in the Stokes regime [44, p. 884]. *McLaughlin* [45, p. 1212] accounts for the lift force by adding an additional term to the right side of equation (3.1), which in this context takes the form of

$$[F_{lift}] \Rightarrow 4.845 \frac{\mu_g}{\pi r_d} \sqrt{\frac{1}{\nu_g} \left| \frac{dv_g}{dy} \right|} (\vec{v}_d - \vec{v}_g) \quad (3.2)$$

These terms represent the basic specific forces on (rigid spherical) droplets. The history term (the last term in equation (3.1)) in fact represents the Basset force, if the gas flow is considered spatially uniform. This force accounts for the temporal viscous boundary layer effects caused by acceleration of the droplets. It can be significant at high acceleration rates of bodies through fluids, but is often neglected for practical reasons. It will be neglected here, because liquid fluid flows are not considered. The drag force, virtual mass force and lift force will be discussed here. In chapter 3.2, a more detailed analysis is devoted to the impact of gravity.

### 3.1.1.1 Virtual mass force

The second term in equation (3.1) is connected with the virtual mass of the droplet. For relatively small droplets and low Reynolds numbers the so-called Faxén correction term [15] drops out, which then leaves

$$\frac{1}{2}\rho_g \left( \frac{d\vec{v}_{gd}}{dt} - \frac{d\vec{v}_d}{dt} \right) \quad (3.3)$$

The factor of  $\frac{1}{2}$  in this equation is called the virtual mass coefficient and will here be written as  $c_{gda}^{vm}$ . Accounting for the virtual mass (in radial direction only) in equation (1.6) leads to

$$\left( \rho_d + c_{gda}^{vm} \rho_g \right) \pi \frac{D_d^3}{6} \frac{du_d}{dt} - \rho_d \pi \frac{D_d^3}{6} \frac{v_d^2}{r} + c_{gda}^{vm} \frac{\pi D_d^2}{8} \rho_g u_d^2 = 0 \quad (3.4)$$

Because the virtual mass force is related to the droplet's *acceleration*, the *terminal* radial droplet velocity is not influenced by it. Therefore, virtual mass is not included in the analysis for the separation efficiency. The added inertia of the droplets can, however, be relevant for droplet path calculations. *Zaichik* [71]<sup>16</sup> proposes to include the virtual mass coefficient in the droplet relaxation time constant as follows:

$$\Delta\tau_{cd} = \left( \rho_d + c_{gda}^{vm} \rho_g \right) D_d^2 / (18\mu_g\psi) \quad (3.5)$$

A value of  $1/2$  is common for the virtual mass coefficient, although different relations for it exist. These depend on droplet shape, deformity or volume fraction. The virtual mass drag coefficient  $c_{gda}^{vm}$  along the principal axis  $a$  of a droplet with a shape defined by the three principal axes  $a$ ,  $b$  and  $c$  is given by [6, p. 730]

$$c_{gda}^{vm} = \frac{\alpha_0}{2 - \alpha_0} \quad (3.6)$$

where

$$\alpha_0 = abc \int_0^\infty \frac{d\lambda}{(a^2 + \lambda) \sqrt{(a^2 + \lambda)(b^2 + \lambda)(c^2 + \lambda)}} \quad (3.7)$$

For a spherical droplet  $a = b = c$  and thus  $c_{gda}^{vm} = c_{gdb}^{vm} = c_{gdc}^{vm} = 1/2$ . Droplets of small diameters are of interest in this paper and because they are approximated by rigid spherical bodies (as discussed in chapter 1.3.2), the value of  $\frac{1}{2}$  will be taken for the virtual mass coefficient when droplet paths are described.

<sup>16</sup> As cited in *Kolev* [34, p. 386].

### 3.1.1.2 Drag force

The third term in equation (3.1) represents Stokes drag. Eliminating the Faxén correction term and multiplying with the volume of a sphere, one arrives at the Stokes drag force:

$$-6\pi r_d \mu_g (\vec{v}_d - \vec{v}_{gd}) \quad (3.8)$$

Equating this force with the centrifugal force in radial coordinates led to the droplet relaxation time constant in the form of equation (1.17). A more general form of the droplet relaxation time constant was already introduced in equation (3.5):

$$\Delta\tau_{gd} = (\rho_d + c_{gd}^{vm} \rho_g) D_d^2 / (18\mu_g \psi) \quad (3.9)$$

The parameter  $\psi$  in equation (3.9) accounts for different droplet flow regimes and is given as

$$\psi = \begin{cases} 1, & \text{Re}_{gd} < 24 \\ 1 + 0.15 \text{Re}_{gd}^{0.687}, & 24 \leq \text{Re}_{gd} < 1000 \\ 0.11 \text{Re}_{gd} / 6, & \text{Re}_{gd} \geq 1000 \end{cases} \quad (3.10)$$

in which

$$\text{Re}_{gd} = \rho_g |V_d - V_g| D_d / \mu_g \quad (3.11)$$

is the droplet Reynolds number. The first regime in equation (3.10) corresponds to the assumptions made in the previous section and is equivalent to taking the Stokes drag coefficient (equation (1.8)) until its value is down to unity:

$$c_{gd}^d = \frac{24\mu_g}{\rho_g D_d u_d} = 24/\text{Re}_{gd}, \quad \text{Re}_{gd} < 24 \quad (3.12)$$

The second regime was originally proposed by *Schiller & Naumann* [59] and the third regime simply states the commonly known constant drag coefficient of 0.44, valid for the Newton regime:

$$c_{gd}^d = (24/\text{Re}_{gd})(0.11 \text{Re}_{gd} / 6) = 0.44, \quad \text{Re}_{gd} \geq 1000 \quad (3.13)$$

For no-slip conditions, the relative velocity between droplet and continuum is given by the terminal radial droplet velocity. The particle Reynolds number in equation (3.11) is in this case given by

$$\text{Re}_{gd} = \rho_g |V_d - V_g| D_d / \mu_g = \frac{\rho_g \Delta\tau_{gd} v_g^2 D_d}{\mu_g R_{out}} \quad (3.14)$$

The parameter  $\psi$  as defined by equation (3.10) is not continuous, consequently an analysis of the separation efficiency should be based on physical parameters that ensure validity *within* a certain

regime, because transgression into other regimes would cause discontinuous jumps in the results. To avoid these discontinuities and allow continuous analyses across flow regimes, the following transition regimes are proposed:

$$\psi = \begin{cases} 1, & \text{Re}_{gd} < 24 - \varepsilon_1 \\ F_1 + (1 - F_1)(1 + 0.15 \text{Re}_{gd}^{0.687}), & 24 - \varepsilon_1 \leq \text{Re}_{gd} < 24 + \varepsilon_1 \\ 1 + 0.15 \text{Re}_{gd}^{0.687}, & 24 + \varepsilon_1 \leq \text{Re}_{gd} < 1000 - \varepsilon_2 \\ F_2(1 + 0.15 \text{Re}_{gd}^{0.687}) + (1 - F_2)0.11 \text{Re}_{gd} / 6, & 1000 - \varepsilon_2 \leq \text{Re}_{gd} < 1000 + \varepsilon_2 \\ 0.11 \text{Re}_{gd} / 6, & \text{Re}_{gd} \geq 1000 + \varepsilon_2 \end{cases} \quad (3.15)$$

The transition functions  $F_{1,2}$  are given by

$$F_{1,2} = \frac{1}{2} \left[ 1 - \cos \left( \pi \frac{\text{Re}_{gd} - L_{1,2} + \varepsilon_i}{2\varepsilon_{1,2}} \right) \right] \quad (3.16)$$

in which  $L_1 = 24$ ,  $L_2 = 1000$  and  $\varepsilon_{1,2}$  are the selected bandwidths for the transition regime.

Transition regimes for  $\varepsilon_1 = \varepsilon_2 = 10$  are depicted in Fig. 3.1.

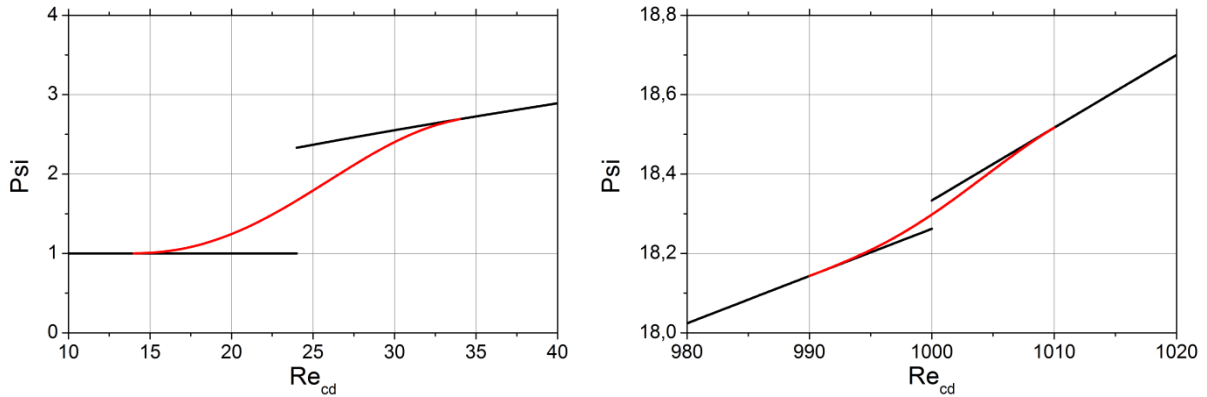


**Fig. 3.1** Transition functions (red) for  $\psi$

The droplet Reynolds number increases with the density of the gas, the droplet diameter and the droplet velocity relative to the flow. Considering water-steam applications, unless high pressures and large droplet sizes are present (also leading to large relative droplet velocities), the Stokes regime will normally be valid. Furthermore, for droplet Reynolds numbers greater than 24, the separation efficiency is often arbitrarily close to unity, with the exception of very poorly designed vane separators (e.g. with an extremely large channel width) and applications at very high pressures (for which  $\rho_d \gg \rho_g$  is no longer valid). The last two regimes of equation (3.10) are thus less relevant for the vane separator applications discussed here and equation (1.17) is a valid representation of the droplet relaxation time constant for the cases presented in this paper.

### 3.1.1.3 Lift force

The lift force is in principle the same force responsible for aerodynamic lift of planes, with the difference that the pressure gradient over the droplet is generated by the velocity gradient present in the flow field itself, instead of by the specific form of the wing generating an asymmetric flow field. The lift force is significant for droplets experiencing large velocity gradients on scales comparable to their diameter, e.g. due to the vicinity of a wall (Fig. 3.2).

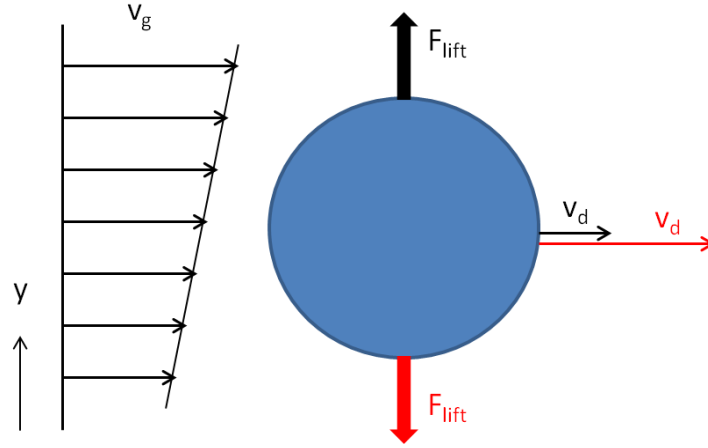


Fig. 3.2 Lift force acting on a droplet

*Saffman* ([56], [57]) derived for negligible particle rotation, low particle Reynolds numbers and small gradients of the gas velocity field the following lift force coefficient:

$$F_{lift} = -6.46\mu_g r_d^2 (\vec{v}_d - \vec{v}_g) \text{sign} \left( \frac{dv_g}{dy} \right) \sqrt{\frac{1}{\nu_g} \left| \frac{dv_g}{dy} \right|} \quad (3.17)$$

The velocity difference  $\vec{v}_d - \vec{v}_g$  is defined at the droplet center, the coordinate  $y$  is perpendicular to the gas velocity (as depicted in Fig. 3.2) and  $\nu$  is the kinematic viscosity. The inclusion of the sign of the gas velocity gradient ensures that if the gas velocity (at the droplet's center) exceeds the droplet velocity, the lift force will be directed in the direction of the gradient of the gas velocity (depicted with black arrows in Fig. 3.2). If the droplet velocity exceeds the gas velocity, it will be directed in the opposite direction (depicted with red arrows).

Alternatively, equation (3.17) can be written in the form proposed by *Jøsang* [28, p. 16]:

$$F_{lift} = 1.61\mu_g D_d \left| \vec{v}_g - \vec{v}_d \right| \sqrt{\text{Re}_{shear}} \quad (3.18)$$

in which

$$\text{Re}_{shear} = \frac{D_d^2}{\nu_g} \frac{du}{dy} \quad (3.19)$$

is the shear Reynolds number. As described by *Legendre & Magnaudet* [41, p. 82], the *Saffman* equation is valid for small rigid spheres in linear shear flows in the limits of small Reynolds numbers and large shear. According to *Wang et al.* [66, p. 751] the Reynolds number should be smaller than unity and in addition, the slip Reynolds number defined by  $Re_{slip} = (\vec{v}_d - \vec{v}_g) D_d / \nu_g$  should be smaller than the square root of the shear Reynolds number defined above. These authors also state that the *Saffman* equation is invalid in the vicinity of walls or other solid boundaries [66, p. 749]. Notwithstanding this statement, for the present work it is relevant to note that in the vicinity of a wall, the lift force will in general be directed towards the wall [66, p. 760]. This is related to the inertia of the droplets travelling from a high to a low velocity in the flow field, which results in a higher droplet velocity than the net gas velocity along its boundary (red arrows in Fig. 3.2). This increases the deposition rate for small droplets, causing the dependence of the deposition rate on the droplet relaxation time to increase when including the lift force in the analysis ([30], [66]). This effect is most pronounced for normalized droplet relaxation time constants of  $1 < \tau^+ = \rho_d D_d^2 u_{fr}^2 / (18 \rho_g \nu_g^2) < 10$ , in which  $\nu_g$  is the kinematic gas viscosity and  $u_{fr}$  is the friction velocity [30, p. 441]. The *Saffman* relation of the lift force was also simulated by *Jøsang*, who found no significant impact on droplet trajectories [28, p. 17]. This corresponds to the earlier statement by *Maxey & Riley* [44, p. 884].

### 3.1.1.4 Additional forces

#### 3.1.1.4.1 Pressure force

The pressure force results from a pressure gradient across the surface of a body. It drives the global gas flow from high to low pressure, but the droplets under consideration are too small to experience a net pressure gradient. For the purpose of describing droplet paths the pressure force on the droplets can be neglected.

#### 3.1.1.4.2 Magnus force

The magnus force is derived from rotating bodies. Its perhaps most commonly known effect is the curved path of a baseball or soccerball. The Magnus force is given by *Rubinow & Keller* ([55] as follows<sup>17</sup>:

$$F_{Magnus} = \frac{1}{2} \rho_g |\vec{v}_g - \vec{v}_d| C_{LR} A \frac{(\vec{v}_g - \vec{v}_d) \times \vec{\omega}_r}{\left| \vec{\omega}_d - \frac{1}{2} \nabla \times \vec{v}_g \right|} \quad (3.20)$$

in which  $C_{LR}$  is the lift coefficient due to rotation and  $\omega_r$  is the relative spin of the droplet with respect to the fluid, which has spin  $\omega_d$ . It can be shown that the Magnus effect, or rotational lift force, is at least an order of magnitude smaller than the shear lift force [30, p. 436]. It can therefore also be neglected for the purposes of this paper.

<sup>17</sup> As cited in *Jøsang* [28, p. 17].

### 3.1.1.4.3 Electro-magnetic forces

The application of electro-static forces for the separation of particles from gas flows is not uncommon. In gas power plants electro-static precipitators are used to electrically charge dust particles in the exhaust flow for subsequent filtration. Furthermore, possible electrical charges on particles can affect deposition mechanisms of the particle on the wall [45, p. 1213]. For water-steam applications, however, electro-magnetic forces are considered irrelevant for droplet paths and deposition rates.

## 3.1.2 Lagrangian particle tracking

Particle tracking methods can be used to evaluate droplet separation efficiency of vane separators, usually defined by the number of droplets that hit the wall, weighted with their size (if more than one droplet size was present in the initial distribution). Such methods were used for these purposes by for instance *Wang & James* [67], *James et al.* [27] and *Verlaan* [64]. In addition, particle tracking methods can be applied for a qualitative assessment of the droplet paths and thus provide valuable insights into the working mechanisms of vane separators. For this purpose, a simple Lagrangian particle tracking code was written, the basic equations of which are introduced in the following paragraphs.

### 3.1.2.1 Isotropic turbulence

A  $k - \varepsilon$  model for turbulence is introduced, in which the specific turbulent kinetic energy  $k$  is defined by

$$k = \frac{1}{2} (u_g'^2 + v_g'^2 + w_g'^2) \quad (3.21)$$

The velocity fluctuations, denoted by the accent, are defined as the difference between actual and average velocity:

$$\begin{aligned} u_g' &= u_g - \overline{u_g} \\ v_g' &= v_g - \overline{v_g} \\ w_g' &= w_g - \overline{w_g} \end{aligned} \quad (3.22)$$

For isotropic turbulence<sup>18</sup>  $u_c' = v_c' = w_c' \equiv V'$ , leading to

$$k = \frac{3}{2} V'^2 \Leftrightarrow V' = \sqrt{\frac{2}{3} k} \quad (3.23)$$

<sup>18</sup> Due to the large dimensional asymmetry for channel flow (one dimension being clearly bounded by the vane separator walls), it is likely that the turbulence is not completely isotropic. Because the purpose of the model is to provide a *qualitative* investigative method, the possible effects of anisotropic turbulence are nevertheless neglected.

After a mathematical analysis of the dissipation of turbulent kinetic energy  $\varepsilon$ , which is a function of the kinematic viscosity  $\nu$  and of average velocity fluctuations, *Taylor* [62] eventually found, for the isotropic dissipation of micro-turbulent kinetic energy:

$$\varepsilon = 15\nu \frac{\overline{V'^2}}{\ell_e^2} \quad (3.24)$$

Micro-turbulence deals with the very small-scale eddies, which play a small part in *diffusion* of kinetic energy, but are the principal agents for the *dissipation* of turbulent kinetic energy [62, p. 430]. The characteristic length  $\ell_e$  is described as a measure of the diameter of the smallest eddies, which do not break down further, but dissipate their energy into heat [62, p. 437]. It is defined as the ratio of the correlation of the velocities at two points along the  $y$ -axis and the square of their distance  $y$ , in the limit of neighboring points in space:

$$\frac{1}{\ell_e^2} = \lim_{y \rightarrow 0} \left( \frac{1 - \overline{V_o V_y} / \overline{V^2}}{y^2} \right) \quad (3.25)$$

From equation (3.23), if the micro-scale kinematic viscosity is defined as the product of the characteristic molecular velocity  $V'$  and the mean free path length  $\ell_e$ , an expression for  $\ell_e$  emerges that is called the Taylor micro-scale of turbulence [33, p. 52]:

$$\ell_e = \nu \sqrt{\frac{3}{2k}} \quad (3.26)$$

For large scale eddies equation (3.24) is written as [33, p. 52]

$$\varepsilon = C\nu^t \frac{V'^2}{\ell_e^2} \quad (3.27)$$

$C$  is an empirical constant in the order of unity, from which, in comparison with equation (3.24), it is clear that large scale eddies are dissipated less than micro-scale eddies. Estimating the turbulent viscosity  $\nu^t$  by its micro-scale counterpart [33, p. 52] and inserting it, along with equation (3.23), into equation (3.27), results in an expression for the large eddy length scale:

$$\ell_e = C \left( \frac{2}{3} \right)^{3/2} \frac{k^{3/2}}{\varepsilon} \equiv C_\ell \frac{k^{3/2}}{\varepsilon} \quad (3.28)$$

Representative for the eddy lifetime  $\tau_e$  is the time it takes a molecule to cross the eddie:

$$\tau_e = \frac{\ell_e}{V'} = C_\ell \frac{k^{3/2}}{\varepsilon V'} = \sqrt{\frac{3}{2}} C_\ell \frac{k}{\varepsilon} \equiv C_\tau \frac{k}{\varepsilon} \quad (3.29)$$

Commonly used values for the empirical constants are  $C_\tau = 0.201$  and  $C_\ell = 0.164$  [27], although *Zamora & Kaiser* [72] reach better results with  $C_\tau = 0.15$ <sup>19</sup>. To evaluate the turbulent kinetic energy, its net generated production per unit mass and time  $P^t$  can be set equal to its irreversible dissipation  $\varepsilon$  [33, p. 90]:

$$P^t = \frac{1}{2} \frac{\lambda_{fr}}{\ell_e} \bar{V}^3 \equiv \varepsilon = \frac{C}{\ell_e} \left( \frac{2}{3} k \right)^{3/2} \Leftrightarrow k = \left( \frac{\lambda_{fr}}{C} \right)^{2/3} \bar{V}^2 \quad (3.30)$$

Inserting the Blasius law for the friction factor ( $\lambda_{fr} = 0.079/\text{Re}^{1/4}$ ) leads to a final expression for the turbulent kinetic energy:

$$k = C_k \bar{V}^2 \text{Re}^{-1/6} \quad (3.31)$$

*Chandesris et al.* [13] suggest for the constant  $C_k$  a value of 0.0306 for flow in channels. These authors suggest for the eddy length scale the following equation:

$$\ell_e = D_h / \left( 1 - \gamma_{lim}^+ \sqrt{\lambda_{fr}/2} \right) \quad (3.32)$$

in which  $\gamma_{lim}^+$  is a measure for the thickness of the boundary layer. For channel flow  $\gamma_{lim}^+ = 8$  is suggested.

### 3.1.2.2 Governing equations for the flow

In analogy to equation (1.6), making the same assumptions as in section 1.3.2 (Stokes flow with no slip in angular direction), the simplified two-dimensional radial momentum equations read

$$\rho_d \frac{D_d^3}{6} \left( \frac{du_d}{dt} - \frac{v_d^2}{r} \right) = 3\mu_g D_d (u_d - u_g) \quad (3.33)$$

$$\rho_d \frac{D_d^3}{6} \left( \frac{dv_d}{dt} - \frac{u_d v_d}{r} \right) = 3\mu_g D_d (v_d - v_g) \quad (3.34)$$

For constant velocity of the continuum, the solution to this system of equations is provided by *Crowe & Pratt* [14]:

$$u_d = u_g - (u_g - u_{d,ini}) \exp(-\Delta\tau/\Delta\tau_{gd}) + [1 - \exp(-\Delta\tau/\Delta\tau_{gd})] \Delta\tau_{gd} v_d^2 / r \quad (3.35)$$

$$v_d = v_g - (v_g - v_{d,ini}) \exp(-\Delta\tau/\Delta\tau_{gd}) - [1 - \exp(-\Delta\tau/\Delta\tau_{gd})] \Delta\tau_{gd} v_d u_d / r \quad (3.36)$$

<sup>19</sup> The work of *Zamora & Kaiser* [72] is discussed in chapter 5.2.

For droplet motion in straight channel parts<sup>20</sup>, the simplified two-dimensional momentum equations reduce to

$$u_d = u_g - (u_g - u_{d,ini}) \exp(-\Delta\tau/\Delta\tau_{gd}) \quad (3.37)$$

$$v_d = v_g - (v_g - v_{d,ini}) \exp(-\Delta\tau/\Delta\tau_{gd}) \quad (3.38)$$

For known  $k$ , the velocity fluctuations are determined as follows:

$$u' = \pm\sqrt{2kn_u}, \quad v' = \pm\sqrt{2kn_v}, \quad w' = \pm\sqrt{2kn_w} \quad (3.39)$$

in which  $n_i$  are random numbers between -1 and 1, for which  $\sum_{i=u,v,w} |n_i| = 1$ . When the traversed

path exceeds the eddy length scale given by equation (3.32) or the elapsed time since the introduction of the last turbulent eddy exceeds the eddy lifetime given by equation (3.29), new velocity fluctuations are introduced for the particular droplet only. Droplets that encounter the channel wall are separated from the flow.

### 3.1.3 Results for a wavy vane separator with straight channel sections

It has thus far implicitly been assumed that the droplet distribution is uniform everywhere in the channel and the droplet separation rate is determined by the initial droplet volume fraction only. The droplet distribution in each but the first stage is, however, significantly skewed toward the outer bend of the previous stage. In other words, at the inlet of the stage, the droplet distribution is skewed toward the inner bend. The more turbulence is introduced into the channel (e.g. by pick-off hooks), the less significant this effect is expected to be. But for laminar flow through smooth channels at relatively low velocities, it is very likely that the stage separation efficiency is significantly impaired by the previous stage. For this reason, newer generations of vane separator geometries featured increased distances between the bends to produce a more effective geometry for separating droplets, an example of which is displayed in Fig. 3.3.

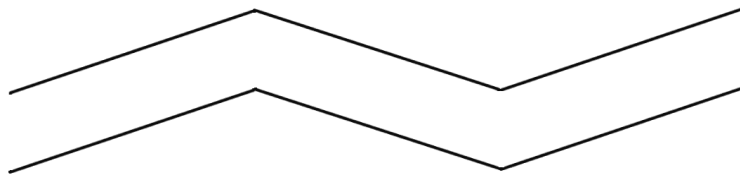


Fig. 3.3 Schematic view of a straight-type vane separator

The purpose of the straight sections is two-fold:

1. The relaxation of the flow in the straight sections helps to redistribute the droplets more uniformly as they enter the next bend.

<sup>20</sup> Straight channel sections will be discussed in the next section.

2. The straight sections effectively take part in the droplet separation process, because the droplets leave the bend maintaining their terminal radial velocity and their inertia will continue to drive them towards the wall of the straight section, at least until their radial velocity has reduced to zero<sup>21</sup>.

The latter can be visualized nicely with the use of the previously described particle tracking model, the result of which is depicted in Fig. 3.4<sup>22</sup>. The droplet paths continue to advance towards the outer wall, even after the droplets have passed from the curvilinear into the cartesian coordinate system, i.e. from the bend into the straight channel section. The straight sections of the channel path thus contribute to the overall separation efficiency of the channel.

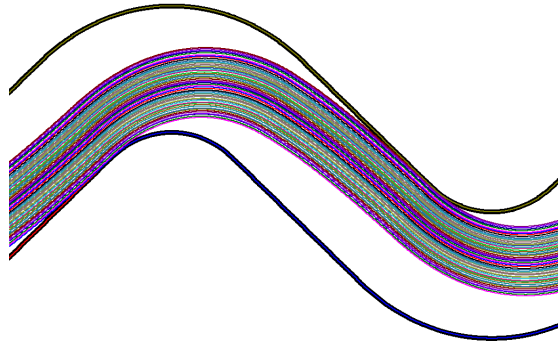


**Fig. 3.4** Droplet paths through a straight-type vane separator channel with rounded bends

### 3.1.4 Separation efficiency in straight channel sections

In chapter 1.3.3, the separation efficiency of each bend of the vane separator was computed by regarding each of these regions as a small cyclone separator. This analysis will be extended by including straight sections of the channel, in which a relaxation of the flow takes place. Assuming, as before, that the droplets move with the constant velocity of the continuum without slip, the time  $\Delta\tau$  it takes a droplet to reach a position  $s$  along the wall of the straight part, as measured from the exit of the preceding curved section, equals

$$\Delta\tau = s/v_g \quad (3.40)$$

According to equation (3.37), if the radial gas velocity is neglected ( $u_g = 0$ ), the radial velocity of the droplets in the straight section of the channel, as a function of the traversed length  $s$ , is given by

$$u_d(s) = u_{d,ini} \exp(-s/\Delta\tau_{gd}v_g) \quad (3.41)$$

<sup>21</sup> The term radial velocity is used here, although the straight sections are not described by curvilinear, but by cartesian coordinates. The radial velocity by definition transforms into a velocity vector perpendicular to the plane of the wall. As the straight section ends, the coordinate system reverts back into curvilinear. For clarity: this velocity will continuously be referred to as radial velocity, even where the velocity in straight sections is concerned.

<sup>22</sup> In the given example, the velocity fluctuations are relatively small, which is why hardly any redistribution of droplets takes place in the straight channel section. Furthermore, all depicted droplets have the same diameter, thus the paths do not cross.

Because the droplets reaching the wall and being separated in the straight section are already near to the outer wall as they leave the bend, the initial radial velocity of the droplets as they leave the bend can be approximated by the terminal radial velocity near the outer wall<sup>23</sup>:

$$u_{d,ini} \approx u_{d,term}(R_{out}) = \frac{\Delta\tau_{gd}v_g^2}{R_{out}} \quad (3.42)$$

This leads to the following expression for the radial velocity of the droplets in the straight sections:

$$u_d(s) \approx \frac{\Delta\tau_{gd}v_g^2}{R_{out}} \exp(-s/\Delta\tau_{gd}v_g) \quad (3.43)$$

The droplet mass flow deposited on the straight wall section  $d_s dz$  is then given by

$$d\dot{m}_d = -\alpha_d u_d(s) \rho_d d_s dz = -\alpha_d \rho_d \frac{\Delta\tau_{gd}v_g^2}{R_{out}} \exp(-s/\Delta\tau_{gd}v_g) d_s dz \quad (3.44)$$

Dividing equation (3.44) by the incoming mass flow leads to

$$d \ln \dot{m}_d = -\frac{\alpha_d \rho_d \frac{\Delta\tau_{gd}v_g^2}{R_{out}} \exp(-s/\Delta\tau_{gd}v_g) d_s dz}{\alpha_d v_d \rho_d \delta_R dz} = -\frac{\Delta\tau_{gd}v_g \exp(-s/\Delta\tau_{gd}v_g)}{R_{out} \delta_R} ds \quad (3.45)$$

Integrating equation (3.45) over the length  $L$  of the straight section then leads to the following separation efficiency  $\eta_S$  for the straight sections of the vane separator:

$$\eta_S = 1 - \frac{\dot{m}_{d,out}}{\dot{m}_{d,in}} \approx 1 - \exp\left(-\frac{(\Delta\tau_{gd}v_g)^2 (1 - \exp(-L/\Delta\tau_{gd}v_g))}{R_{out} \delta_R}\right) \quad (3.46)$$

The separation efficiency  $\eta_C$  in the curved sections of a vane separator is an exponential function of the Stokes number; the separation efficiency  $\eta_S$  in the straight sections of a vane separator, is an exponential function of the *square* of the Stokes number and an additional term that scales exponentially with the inverse of the Stokes number<sup>24</sup>. The ratio of separation efficiencies  $\eta_S/\eta_C$  as a function of the Stokes number ( $\{1 - \exp(-St^2(1 - \exp(-1/St)))\}/\{1 - \exp(-St)\}$ ) is plotted in Fig. 3.5, showing that with increasing Stokes number, the separation efficiency in the straight sections increases relative to that in the curved sections. The sharp decrease of  $\eta_S/\eta_C$  for small Stokes numbers is due to the double impact of decreasing terminal radial droplet velocity and faster

<sup>23</sup> The validity of this approximation is worked out in Appendix A.I.

<sup>24</sup> The *characteristic length* in the Stokes number is either represented by  $\delta_R$ ,  $R_{out}$  or  $L$ . These normally have the same order of magnitude. For simplicity, the bend angle  $n\phi$  is approximated by unity. This has no qualitative influences on the argument.

droplet relaxation in the straight sections. For roughly equal values of the characteristic lengths ( $\delta_R$ ,  $R_{out}$  and  $L$ ), the separation efficiency in straight sections reaches 50% of the separation efficiency in curved sections for a Stokes number of 0.5 and reaches nearly 100% of this value for Stokes numbers larger than 5.

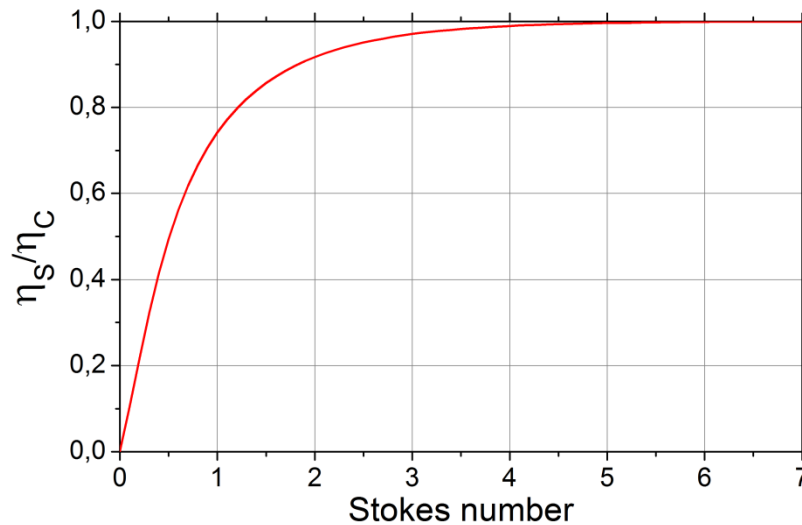


Fig. 3.5 The separation efficiency in a straight section, relative to that in a curved sections, as a function of the Stokes number

#### Quintessence

*With increasing Stokes numbers, the separation efficiency in straight sections increases relative to the separation efficiency in curved sections, but, for similar characteristic lengths, never exceeds it. For Stokes numbers beyond 0.5, straight sections can play a significant role in the droplet separation characteristics of vane separators.*

## 3.2 Gravitational influence on separation efficiency

For many applications of vane separators a vertical orientation is desirable, mainly for reasons of limiting the re-entrainment from the liquid film flow on the walls. In practice, this is not always attainable; for example in large horizontally arranged cylindrical pressure vessels, with a bottom-to-top or top-to-bottom cross-flow of saturated steam (Fig. 3.6). When vane separators are installed in such vessels, there is often not enough space to allow for a vertical orientation. In this section, the assumption of a vertically oriented installation is discarded and its gravitational influence on the separation efficiency is investigated.

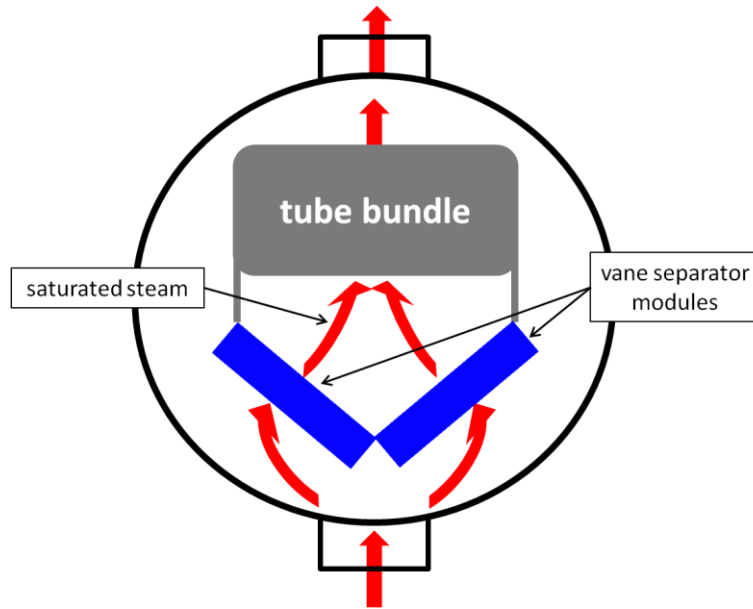


**Fig. 3.6** Schematic view of a horizontal pressure vessel with a reheater tube bundle and a non-vertical arrangement of vane separators

### 3.2.1 Gravitational influence in curved vane separator sections

To determine the influence of gravitational acceleration in the radial direction, the terminal radial velocity  $u_d$  of the particles must be re-evaluated. The assumption remains that all droplets have a radial velocity component in the local flow direction equal to the gas velocity:  $v_d = v_g$ . The radial velocity is computed from the simplified radial momentum equation (1.6), which now includes the radial component of gravity  $\vec{g} \cdot \hat{r}$ :

$$M_d \left( \frac{du_d}{dt} - \frac{v_d^2}{r} - \vec{g} \cdot \hat{r} \right) + c_{gd}^d \frac{A_d}{2} \rho_g (u_d - u_g) |u_d - u_g| = 0 \quad (3.47)$$

Making the same assumptions as in section 1.3.2 (droplets are approximated by rigid spheres, droplets hit the wall with radial terminal velocity, the gas velocity has no radial component and Stokes flow is valid), equation (3.47) reduces to

$$\rho_d \frac{\pi}{6} D_d^3 \left( \frac{v_g^2}{R_{out}} + \vec{g} \cdot \hat{r} \right) = \frac{24\mu_g}{\rho_g D_d u_d} \rho_g \frac{\pi}{8} D_d^2 u_d |u_d| \quad (3.48)$$

Solving this equation for  $u_d$  gives

$$u_d = \frac{1}{18} D_d^2 \left( \frac{v_g^2}{R_{out}} + \vec{g} \cdot \hat{r} \right) \frac{\rho_d}{\mu_g} \equiv \Delta\tau_{gd} \left( \frac{v_g^2}{R_{out}} + \vec{g} \cdot \hat{r} \right) \quad (3.49)$$

To evaluate the gravity component in equation (3.49), the orientation of the gravity vector in the vane separator coordinate system, must be formulated. A cartesian coordinate system is defined, in

which the  $z$ -axis aligns with the vanes (perpendicular to the  $\vec{u} - \vec{v}$  plane), the  $y$ -axis aligns with the central line of the vanes around which the vanes swirl (i.e. the macroscopic direction of flow from vane separator inlet to outlet) and the  $x$ -axis is perpendicular to both (it aligns with  $\vec{u}$  or  $-\vec{u}$  in the middle of each bend) (Fig. 3.7).

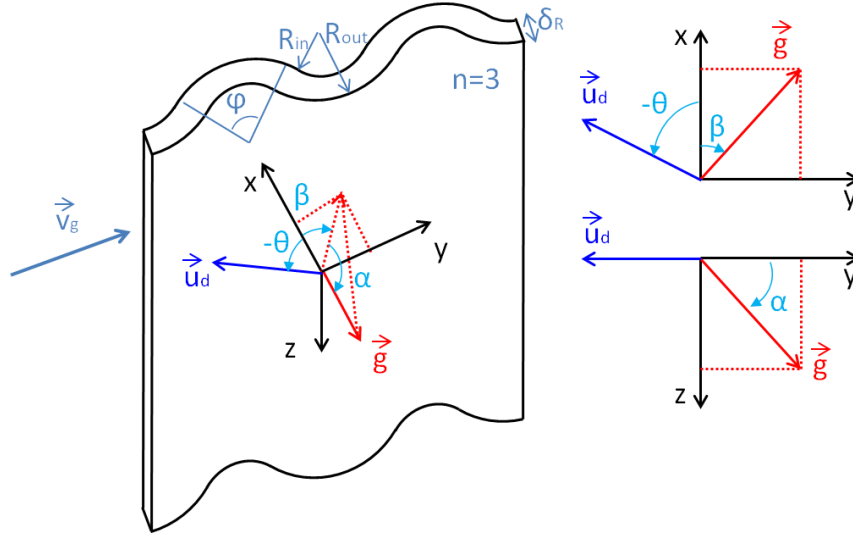


**Fig. 3.7 Cartesian coordinate system depicted with arbitrary gravity vector, with top view (upper right) and side view (bottom right)**

The gravity vector is defined by two angles: the angle  $\alpha$  describes the angle of the gravity vector with the  $\vec{u} - \vec{v}$  plane and the angle  $\beta$  describes the angle of the gravity vector component in the  $\vec{u} - \vec{v}$  plane with the  $x$ -axis (Fig. 3.7). To avoid any ambiguity with vane separator orientation, the following definitions shall apply:

- the  $y$ -axis aligns with the macroscopic direction of flow,
- the  $x$ -axis lies in the  $\vec{u} - \vec{v}$  plane and is positive where  $\alpha$  is smallest<sup>25</sup>, and
- $\beta$  defines the angle with the positive  $x$ -axis and runs from positive  $x$  towards positive  $y$ <sup>26</sup>.

The angle  $\theta$  describes the variable angle between the velocity vector  $\vec{u}$  and the  $x$ -axis, for which the following is valid<sup>27</sup>:

$$\begin{aligned} -\varphi/2 \leq \theta \leq \varphi/2, & \quad \text{bend at positive } x\text{-coordinate} \\ \pi - \varphi/2 \leq \theta \leq \pi + \varphi/2, & \quad \text{bend at negative } x\text{-coordinate} \end{aligned} \quad (3.50)$$

<sup>25</sup> This implies that the  $z$ -axis can be upward or downward. For  $\alpha = \pi/2$  the choice of positive  $x$ -direction is arbitrary.

<sup>26</sup> This directly implies  $-\pi/2 \leq \beta \leq \pi/2$ .

<sup>27</sup> Note that the positive direction of the angle  $\theta$  is defined in the same direction as the angle  $\beta$ , with  $\theta = 0$  aligning with the  $x$ -axis. To avoid unnecessary complexity, the following analysis will be defined for forward integration of  $\theta$  for both positive and negative  $x$ -coordinates. This does not affect the result.

Since  $\vec{u}$  changes its direction with respect to the cartesian coordinate system, the gravity component  $\vec{g} \cdot \hat{r}$ , which aligns with  $\vec{u}$ , is a function of  $\theta$ . It can be written as

$$\vec{g} \cdot \hat{r} = g \cos \alpha \cos(\beta - \theta) \quad (3.51)$$

Inserting equations (3.49) and (3.51) into equation (1.14) gives the following expression:

$$d \ln \dot{m}_d = -\frac{u_d}{v_d} \frac{R_{out}}{\delta_R} d\theta = -\frac{\Delta \tau_{gd}}{\delta_R} \left( v_g + \frac{R_{out}}{v_g} g \cos \alpha \cos(\beta - \theta) \right) d\theta \quad (3.52)$$

Integrating this equation between the limits  $\theta = -\varphi/2 \rightarrow \varphi/2$  leads to

$$[\ln \dot{m}_d]_{-\varphi/2}^{\varphi/2} + C = -\frac{\Delta \tau_{gd}}{\delta_R} \left[ \varphi v_g + \frac{2R_{out}}{v_g} g \cos \alpha \cos \beta \sin(\varphi/2) \right] \quad (3.53)$$

in which the following relation has been used:

$$\sin(\beta - \varphi/2) - \sin(\beta + \varphi/2) = -2 \cos \beta \sin(\varphi/2) \quad (3.54)$$

Equation (3.53) is solved for the droplet mass flow. Following the definition of the separation efficiency results in a separation efficiency  $\eta_+$  for bends with positive  $x$ -coordinates:

$$\eta_+ = 1 - \frac{\dot{m}_{3,out}}{\dot{m}_{3,in}} = 1 - \exp \left\{ -\frac{\varphi \Delta \tau_{gd} v_g}{\delta_R} - \frac{2 \Delta \tau_{gd} R_{out}}{\delta_R v_g} g \cos \alpha \cos \beta \sin(\varphi/2) \right\} \quad (3.55)$$

Alternatively, carrying out the integration of equation (3.52) between the limits  $\theta = \pi - \varphi/2 \rightarrow \pi + \varphi/2$  leads to a separation efficiency  $\eta_-$  for bends with negative  $x$ -coordinates:

$$\eta_- = 1 - \frac{\dot{m}_{3,out}}{\dot{m}_{3,in}} = 1 - \exp \left\{ -\frac{\varphi \Delta \tau_{gd} v_g}{\delta_R} + \frac{2 \Delta \tau_{gd} R_{out}}{\delta_R v_g} g \cos \alpha \cos \beta \sin(\varphi/2) \right\} \quad (3.56)$$

in which the following relation has been used:

$$\sin(\beta - \pi - \varphi/2) - \sin(\beta - \pi + \varphi/2) = 2 \cos \beta \sin(\varphi/2) \quad (3.57)$$

In general, the separation efficiency for curved sections  $\eta_C$  can thus be written as

$$\eta_C = 1 - \exp \left[ -\frac{\varphi \Delta \tau_{gd} v_g}{\delta_R} \mp \frac{2 \Delta \tau_{gd} R_{out}}{\delta_R v_g} g \cos \alpha \cos \beta \sin(\varphi/2) \right] \quad (3.58)$$

The  $\mp$ -sign defines the orientation of the curves<sup>28</sup>. In the limits  $g \rightarrow 0$  or  $\alpha \rightarrow \pm\pi/2$  equation (3.58) reduces to equation (1.16). In the limit  $\beta \rightarrow \pm\pi/2$  equation (3.58) also reduces to equation (1.16), because in this case the contributions of the gravity vector for  $-\varphi/2 \leq \theta < 0$  and  $0 < \theta \leq \varphi/2$  cancel<sup>29</sup>.

### 3.2.2 Gravitational influence in straight vane separator sections

The radial momentum equation in straight channel sections, accounting for gravity, reads

$$\rho_d \frac{\pi}{6} D_d^3 \left( \frac{du_d}{dt} - \vec{g} \cdot \frac{\vec{u}_d}{|u_d|} \right) = -\frac{24\mu_g}{\rho_g D_d u_d} \rho_g \frac{\pi}{8} D_d^2 u_d |u_d| \quad (3.59)$$

Keeping with equation (3.51), the gravitational component is defined as<sup>30</sup>

$$\vec{g} \cdot \frac{\vec{u}_d}{|u_d|} = \pm g \cos \alpha \cos(\beta \mp \varphi/2) \quad (3.60)$$

for straight sections that run from positive to negative  $x$ -coordinates and from negative to positive  $x$ -coordinates, respectively. Inserting equation (3.60) into equation (3.59) gives

$$\frac{du_d}{dt} = -\frac{u_d}{\Delta\tau_{gd}} \pm g \cos \alpha \cos(\beta \mp \varphi/2) \quad (3.61)$$

Equation (3.61) can be solved by making use of a Laplace transformation:

$$\begin{aligned} s\tilde{U} - u_{d,ini} &= -\frac{\tilde{U}}{\Delta\tau_{gd}} \pm \frac{g}{s} \cos \alpha \cos(\beta \mp \varphi/2) \\ \Rightarrow \tilde{U} &= \frac{g \cos \alpha \cos(\beta \mp \varphi/2)}{s(s + 1/\Delta\tau_{gd})} + \frac{u_{d,ini}}{s + 1/\Delta\tau_{gd}} \end{aligned} \quad (3.62)$$

This leads to the following equation for the radial droplet velocity:

$$u_d = \left\{ u_{d,ini} \mp \Delta\tau_{gd} g \cos \alpha \cos\left(\beta \mp \frac{\varphi}{2}\right) \right\} \exp\left(\frac{-\tau}{\Delta\tau_{gd}}\right) \pm \Delta\tau_{gd} g \cos \alpha \cos\left(\beta \mp \frac{\varphi}{2}\right) \quad (3.63)$$

<sup>28</sup> The convention throughout this chapter shall be that the upper part of any  $\pm$  or  $\mp$ -signs is valid for bends with positive  $x$ -coordinates, whereas the lower part is valid for bends with negative  $x$ -coordinates.

<sup>29</sup> This statement is also valid for the regions  $\pi - \varphi/2 \leq \theta < \pi$  and  $\pi < \theta \leq \pi + \varphi/2$ .

<sup>30</sup> The gravitational component was written in the last section as  $\vec{g} \cdot \hat{r}$ . The notation here is used because there is no radial coordinate in the straight section.

The initial radial droplet velocity  $u_{d,ini}$  is given by equation (3.49), while inserting equations (3.60) for the term  $\vec{g} \cdot \hat{r}$ . Inserting also  $\tau = s/v_g$  leads to

$$u_d = \Delta\tau_{gd} \left\{ \frac{v_g^2}{R_{out}} \exp(-s/\Delta\tau_{gd}v_g) \pm g \cos\alpha \cos(\beta \mp \varphi/2) \right\} \quad (3.64)$$

Rewriting equation (3.45) to account for the modified droplet velocity gives

$$d \ln \dot{m}_d = - \frac{\Delta\tau_{gd} \left\{ (v_g^2/R_{out}) \exp(-s/\Delta\tau_{gd}v_g) \pm g \cos\alpha \cos(\beta \mp \varphi/2) \right\}}{v_g \delta_R} ds \quad (3.65)$$

Integrating from  $s = 0 \rightarrow L$  and solving for the efficiency leads to the following relation for the separating efficiency in straight sections  $\eta_S$ :

$$\eta_S \approx 1 - \exp \left( - \frac{\Delta\tau_{gd}^2 v_g^2}{\delta_R R_{out}} \left( 1 - \exp \left( \frac{-L}{\Delta\tau_{gd} v_g} \right) \right) \mp \frac{\Delta\tau_{gd} L}{v_g \delta_R} g \cos\alpha \cos \left( \beta \mp \frac{\varphi}{2} \right) \right) \quad (3.66)$$

In the limits  $g \rightarrow 0$  or  $\alpha \rightarrow \pi/2$ , equation (3.66) reduces to equation (3.46).

### 3.2.3 Grade efficiency under the influence of gravity

The separation efficiency in curved sections, under the influence of gravity, was given by equation (3.58) and can be written in short as

$$\eta_C = 1 - \exp \left[ - \frac{\varphi \Delta\tau_{gd} v_g}{\delta_R} \mp \frac{2\Delta\tau_{gd} R_{out}}{\delta_R v_g} g \cos\alpha \cos\beta \sin \left( \frac{\varphi}{2} \right) \right] = 1 - e^{-C \mp G} \quad (3.67)$$

The coefficient  $C$  represents the contribution of the centrifugal force and the coefficient  $G$  the contribution of gravity:

$$C = \frac{\varphi \Delta\tau_{gd} v_g}{\delta_R} \quad (3.68)$$

$$G = \frac{2\Delta\tau_{gd} R_{out}}{\delta_R v_g} g \cos\alpha \cos\beta \sin \left( \frac{\varphi}{2} \right) \quad (3.69)$$

A similar simplification can be done for the general efficiency in straight sections:

$$\eta_S = 1 - e^{-S \mp H} \quad (3.70)$$

The coefficient  $S$  represents the contribution of the droplet's initial radial velocity and the coefficients  $H_-$  and  $H_+$  the contributions of gravity for straight sections from positive to negative  $x$ -coordinates and from negative to positive  $x$ -coordinates, respectively:

$$S = \frac{\Delta\tau_{gd}^2 v_g^2}{\delta_R R_{out}} \left( 1 - \exp\left(\frac{-L}{\Delta\tau_{gd} v_g}\right) \right) \quad (3.71)$$

$$H_{\mp} = \frac{\Delta\tau_{gd} L}{v_g \delta_R} g \cos\alpha \cos\left(\beta \mp \frac{\varphi}{2}\right) \quad (3.72)$$

It is recognized that in the limits  $G \rightarrow 0$  and  $H_{\mp} \rightarrow 0$ , equations (3.67) and (3.70) reduce to their 'gravitationless' counterparts (1.16) and (3.46). The grade efficiency of a vane separator with  $n$  stages can no longer be written according to equation (3.121): it differs for even and uneven numbers of stages and for different orientations of the inlet (toward or away from the half-plane of the gravity vector, i.e. toward positive or negative  $x$ ). This leads to four different equations for the grade efficiency. For a vane separator with an even number of stages, the gravitational contributions from the inlet and outlet sections cancel<sup>31</sup> and the grade efficiency can be written as

$$\begin{aligned} \eta_D &= 1 - \exp\left[-\left\{(n+1)C + (n-1)S + \frac{n}{2}G - \frac{n}{2}G \pm \frac{n}{2}H_{\pm} \mp \left(\frac{n}{2}-1\right)H_{\mp}\right\}\right] \\ &= 1 - \exp\left[-\left\{(n+1)C + (n-1)S \pm \frac{n}{2}H_{\pm} \mp \left(\frac{n}{2}-1\right)H_{\mp}\right\}\right] \end{aligned} \quad (3.73)$$

The gravitational contribution from the bends (including inlet and outlet sections) has thus fully vanished. The gravitational contributions in the straight sections remains, but still depends on the orientation of the inlet. For a vane separator with an uneven number of stages, the gravitational contributions of the inlet and outlet sections add up to equal a full bend<sup>32</sup> and the grade efficiency can be written as

$$\begin{aligned} \eta_D &= 1 - \exp\left[-\left\{(n+1)C + (n-1)S + \frac{n+1}{2}G - \frac{n+1}{2}G \pm \frac{n-1}{2}H_{\pm} \mp \frac{n-1}{2}H_{\mp}\right\}\right] \\ &= 1 - \exp\left[-\left\{(n+1)C + (n-1)S + \frac{n-1}{2}(H_+ - H_-)\right\}\right] \end{aligned} \quad (3.74)$$

It follows that in this case, the gravitational contribution from the curved sections always cancels; independent of the number of stages or the orientation of the vane separator. The three different grade efficiencies are listed in Table 1. The first two exponentials of each equation are always the same and represent the separation efficiency without the influence of gravity (according to equation (3.121)). The last exponential(s) represent(s) the influence of gravity on the grade efficiency.

<sup>31</sup> Inlet and outlet sections of equal size are considered (refer to chapter 3.6.4.1). For proof of this statement the reader is referred to Appendix A.II.

<sup>32</sup> See previous footnote. In addition, it is assumed that the inlet and outlet sections each equal one half of a full bend.

Table 1 Vane separator grade efficiencies under the influence of gravity

Number of stages	Orientation	Efficiency
Uneven	-	$\eta_d = 1 - e^{-C(n+1)} e^{-S(n-1)} e^{(H_+ - H_-)(n-1)/2}$
Even	inlet towards positive $x$	$\eta_d = 1 - e^{-C(n+1)} e^{-S(n-1)} e^{-H_-(n/2)} e^{H_+(n/2-1)}$
	inlet towards negative $x$	$\eta_d = 1 - e^{-C(n+1)} e^{-S(n-1)} e^{H_+(n/2)} e^{-H_-(n/2-1)}$

A quantitative analysis of the significance of different geometrical and physical parameters, with regard to the influence of gravity on the separation efficiency, is performed in appendix A.III. The main conclusions are:

1. The relative impact of gravity increases for  $\alpha \rightarrow 0$ .
2. The relative impact of gravity increases for  $\beta \rightarrow 90^\circ$ .
3. The relative impact of gravity increases for  $\varphi \downarrow 0^\circ$ .
4. The relative impact of gravity decreases for  $n \rightarrow \infty$ .
5. The relative impact of gravity decreases for  $v_g \rightarrow \infty$ .
6. The relative impact of gravity decreases for  $D_d \rightarrow \infty$ .
7. The three different configurations in Table 1 show significantly different results.

The first two points imply that gravity is most significant for purely horizontal vane separator orientations. The next two points signify that for increasing efficiency of the curved sections, the relative contribution from gravity decreases. Points 5 and 6 signify the same for an increasing centrifugal force, which usually corresponds to increasing Stokes numbers.

#### **Quintessence**

*The contribution from gravity to the separation efficiency can be significant under circumstances with low Stokes numbers and where centrifugal forces are small. The spatial orientation of a vane separator can thus be of interest when relatively poor separation efficiencies are to be expected: e.g. for small droplets in slow-moving media, passing few stages of small bend angles.*

### **3.3 Non-orthogonal gas flow**

Vane separators are designed to perform under conditions of orthogonal gas flow; where the gas velocity vector is perpendicular to the inlet surface. For most applications this is a realistic assumption. There are situations, however, where the gas flow does not enter the vane separator modules under optimum conditions. Typically, this is the case when vane separator modules are installed inside large vessels, for example inside a Moisture Separator and Reheater (MSR) (Fig. 3.8). In the depicted MSR, steam with a certain moisture content enters the bottom head of the MSR, in which a cyclone separation stage is installed. After a  $90^\circ$  deflection, the steam enters the cylindrical mid-section of the vessel, where the decreasing cross-sectional area gradually forces the steam through the second separation stage (the vane separator modules) toward the outlet. Locally,

especially near the bottom and top sections of the vessel, the steam does not propagate through the vane separator modules in a perpendicular angle. This is visualized by the CFD flow analysis in the right part of Fig. 3.8, from which it is clear that the gas velocity vectors are tilted upward with respect to the vane separator modules. The impact on separation efficiency of non-orthogonal gas flow is investigated in the following sections.

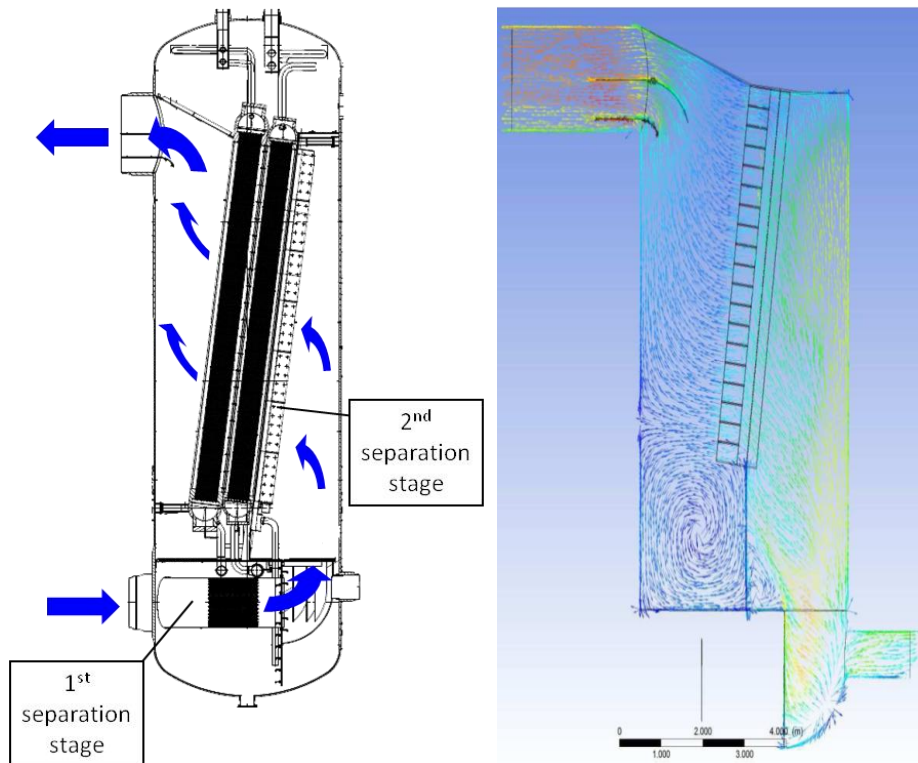


**Fig. 3.8** Schematic view of steam flow through a MSR (left) and gas velocity vectors through a MSR (right)<sup>33</sup>

### 3.3.1 Non-orthogonal flow in curved vane separator sections

Because rotation of the gas velocity vector is confined by the parallel vanes to two dimensions, variations of the direction of flow will be treated in the plane parallel to the vanes only (Fig. 3.9). A re-orientation of the gas velocity vector will be equivalently evaluated through an altered description of the geometry itself, by determination of the *effective* radii and straight sections, as experienced by a droplet moving with an upward or downward angle  $\alpha_v$  with respect to the horizontal plane. The plane of travel of the droplet shall remain perpendicular to the vanes themselves. The height  $H$  of the vane separator is assumed infinite.

<sup>33</sup> Courtesy of Siemens AG.

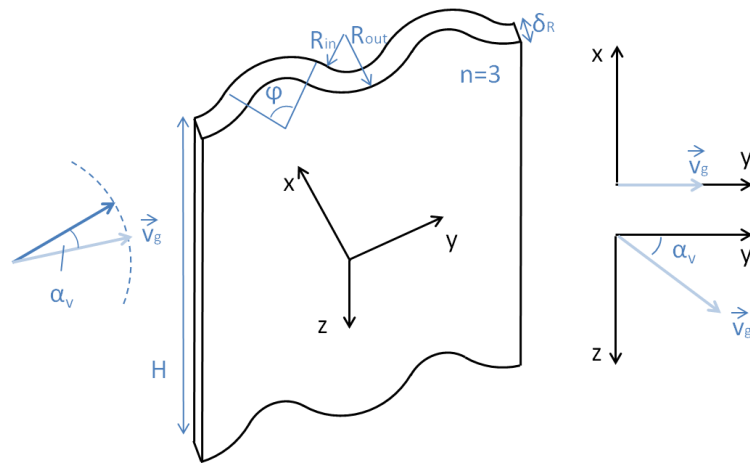


**Fig. 3.9 Schematic view of a non-orthogonal gas velocity vector, with top view (upper right) and side view (bottom right)**

The effective curvature of the skewed bend, in the plane of travel, is no longer circular, but represents an ellipsoidal cut of the vane (Fig. 3.10). The effective radius  $\widehat{R}$ , the effective angle  $\widehat{\alpha}_v$  of the gas velocity in the plane of travel and the effective traversed angle  $\theta$  are all affected by this rotational transformation. The analytical model should thus be written in terms of  $\widehat{R}$  and  $\theta$ .

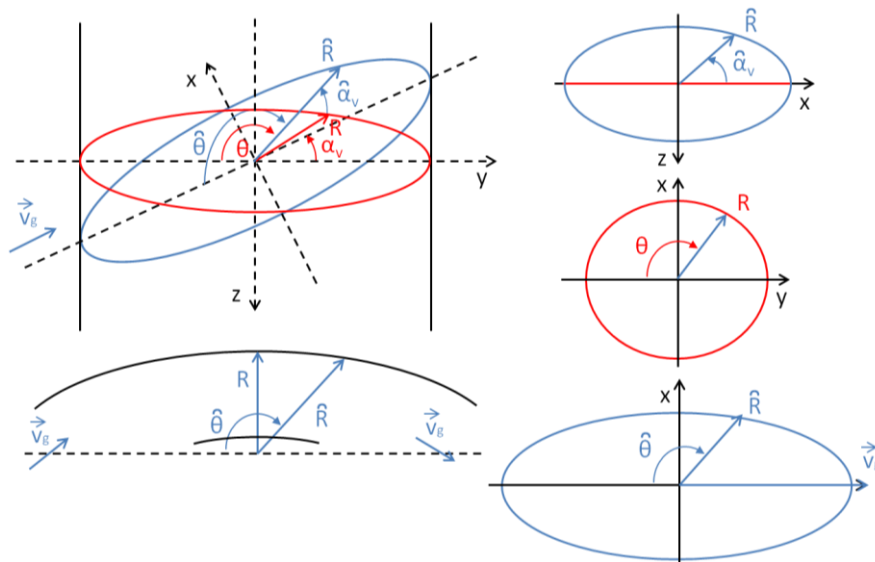


**Fig. 3.10 Ellipsoidal cut of a spherical vane (above left), side view along the plane of travel (top right), top view perpendicular to the vane (middle right) and perpendicular to the plane of travel (below left and right)**

The assumptions from section 1.3.2 (Stokes flow, no slip, etc.) shall remain valid. It is assumed that the product of *effective* tangential gas velocity  $v_g$  and *effective* channel width  $\widehat{\delta}_R$  is constant<sup>34</sup>:

$$v_g \widehat{\delta}_R \Big|_{\widehat{\theta}, L} = \text{constant} \quad (3.75)$$

<sup>34</sup> This assumption is equivalent to conservation of mass in the tilted system, for incompressible flow.

The ratio of deposited and entering mass flow for tilted flow equals

$$d \ln \dot{m}_d = -\frac{u_d \widehat{R}_{out}}{v_{g,0} \widehat{\delta}_{R,0}} d\theta \quad (3.76)$$

in which all parameters are functions of  $\theta$ . In analogy to equation (1.9), the radial droplet velocity at the wall is given by the following equation:

$$u_d(\theta) = \frac{\rho_d D_d^2}{18 \mu_g \widehat{R}_{out}} \left( \frac{v_{g,0} \widehat{\delta}_{R,0}}{\widehat{R}_{out} - \widehat{R}_{in}} \right)^2 \quad (3.77)$$

Inserting equation (3.77) into equation (3.76) leads to

$$d \ln \dot{m}_d = -\frac{\Delta \tau_{gd} v_{g,0} \widehat{\delta}_{R,0}}{(\widehat{R}_{out} - \widehat{R}_{in})^2} d\theta \quad (3.78)$$

Following the mathematical formulation of an ellipsoid, the effective radius can be written as

$$\frac{\widehat{R}^2 \cos^2 \theta}{(R^2 / \cos^2 \alpha_v)} + \frac{\widehat{R}^2 \sin^2 \theta}{R^2} = 1 \Rightarrow \widehat{R}^2 = \frac{R^2}{\sin^2 \theta + \cos^2 \theta \cos^2 \alpha_v} \quad (3.79)$$

which leads to

$$d \ln \dot{m}_d = -\frac{\Delta \tau_{gd} v_{g,0} \widehat{\delta}_{R,0}}{\delta_R^2} (\sin^2 \theta + \cos^2 \theta \cos^2 \alpha_v) d\theta \quad (3.80)$$

Carrying out the integration from  $\theta = \frac{\pi - \widehat{\varphi}}{2} \rightarrow \frac{\pi + \widehat{\varphi}}{2}$  and employing equation (3.75) leads to the separation efficiency of the bend, for non-orthogonal flow at an angle  $\alpha_v$ :

$$\begin{aligned} \eta_C &= 1 - \exp \left[ -\frac{\Delta \tau_{gd} v_g}{\delta_R} \left\{ \frac{\widehat{\varphi}}{2} (1 + \cos^2 \alpha_v) + \frac{\sin \widehat{\varphi}}{2} \sin^2 \alpha_v \right\} \right] \\ &\equiv 1 - \exp \left[ -\frac{\Delta \tau_{gd} v_g}{\delta_R} F(\alpha_v) \right] \end{aligned} \quad (3.81)$$

in which the effective total bend angle  $\widehat{\varphi}$  is defined by

$$\tan(\widehat{\varphi}/2) = \frac{\tan(\varphi/2)}{\cos \alpha_v} \quad (3.82)$$

The function  $F(\alpha_v)$  represents the influence of the effective channel width on the separation efficiency. In the limit  $\alpha_v \rightarrow 0$ , equation (3.81) reduces to equation (1.16) (for a single stage). The first part of  $F(\alpha_v)$  decreases with  $\alpha_v$ , and can be interpreted as the derogation of the separation efficiency, caused by the increasing effective channel width. The second part increases with  $\alpha_v$ , and can be interpreted as the improvement of the separation efficiency, due to the increasing integration length (in terms of the effective bend angle  $\hat{\varphi}$ ). In Fig. 3.11, the value of  $F(\alpha_v)/\varphi$  is plotted as a function of  $\alpha_v$ , allowing for a direct comparison with equation (1.16). Thus, if the gas velocity vector is tilted by an angle  $\alpha_v = 40^\circ$ , for a bend angle of  $\varphi < 50^\circ$  the tilting has effectively increased the bend angle with a factor 1.2. For  $\varphi < 109^\circ$ , the separation flow *initially increases* when the velocity plane is tilted, while the positive contribution from the increasing effective channel length is *larger* than the negative contribution from the increasing effective channel width. For  $\varphi < 109^\circ$  the opposite is true<sup>35</sup>. A second-order effect is present, related to the different signs of the derivatives with respect to  $\alpha_v$ , of the first and second term of  $F(\alpha_v)$ .

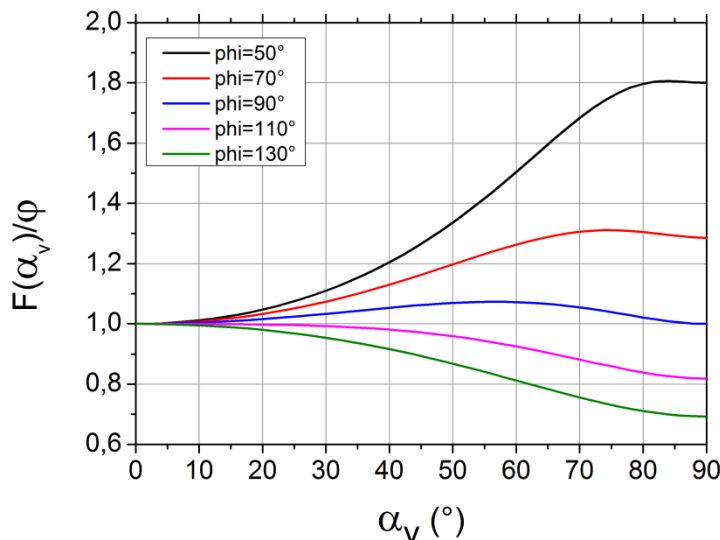


Fig. 3.11 Influence of non-orthogonal flow on droplet separation efficiency (for four stages)

### 3.3.2 Non-orthogonal flow in straight vane separator sections

The tilted velocity plane is not only at a vertical angle  $\alpha_v$  with the straight section, but also at a lateral angle  $\varphi/2$ . The lateral angle, however, does not affect the *effective* length of the straight section, which is given by

$$\hat{L} = L/\cos \alpha_v \tag{3.83}$$

<sup>35</sup> For  $90^\circ < \varphi < 109^\circ$ , the contribution to the separation efficiency is either positive or negative, depending on the value of  $\alpha_v$ .

Applying equation (3.82) to equation (3.79) with  $\theta = \widehat{\varphi}/2$ , the effective width  $\widehat{\delta}_R$  of the straight section can be written as

$$\widehat{\delta}_R = \delta_R \sqrt{1 + \tan^2 \alpha_v \sin^2 (\varphi/2)} \quad (3.84)$$

Analogous to equation (3.41), the radial droplet velocity in the straight part of the channel is given by

$$\begin{aligned} u_d(s) &= u_d \left( \frac{\pi + \widehat{\varphi}}{2} \right) \exp \left( -\frac{s}{\Delta \tau_{gd} v_g} \right) = \frac{\Delta \tau_{gd}}{\widehat{R}_{out}} \left( \frac{v_g \widehat{\delta}_R}{\widehat{R}_{out} - \widehat{R}_{in}} \right)^2 \exp \left( -\frac{s}{\Delta \tau_{gd} v_g} \right) \\ &= \frac{\Delta \tau_{gd} v_g^2}{R_{out}} \left( 1 + \tan^2 \alpha_v \sin^2 \left( \frac{\varphi}{2} \right) \right)^{-3/2} \exp \left( -\frac{s}{\Delta \tau_{gd} v_g} \sqrt{1 + \tan^2 \alpha_v \sin^2 \left( \frac{\varphi}{2} \right)} \right) \end{aligned} \quad (3.85)$$

Inserting into equation (3.80) and integrating over the length  $\widehat{L}$  of the straight section leads to the following equation for the separation efficiency  $\eta_S$  of the straight sections of the vane separator:

$$\eta_S = 1 - \exp \left( -\frac{(\Delta \tau_{gd} v_g)^2 \left( 1 - \exp \left( -\frac{L \sqrt{1 + \tan^2 \alpha_v \sin^2 (\varphi/2)}}{\Delta \tau_{gd} v_g \cos \alpha_v} \right) \right)}{R_{out} \widehat{\delta}_R \left( 1 + \tan^2 \alpha_v \sin^2 (\varphi/2) \right)^2} \right) \quad (3.86)$$

In the limit  $\alpha_v \rightarrow 0$ , equation (3.86) reduces to equation (3.46). The numerator in equation (3.86) increases with  $\alpha_v$  and can be interpreted as the improvement of the separation efficiency due to the combined effects of increasing integration length and increasing droplet relaxation length (due to a smaller effective gas velocity). The denominator in equation (3.86) also increases with  $\alpha_v$  and can be interpreted as the derogation of the separation efficiency due to the combined effects of decreasing terminal radial droplet velocity at the bend exit and increasing effective channel width. Fig. 3.12 depicts the normalized separation efficiency in the straight sections as a function of  $\alpha_v$ , showing the significant deterioration of the separation efficiency in the straight sections for non-orthogonal flow.

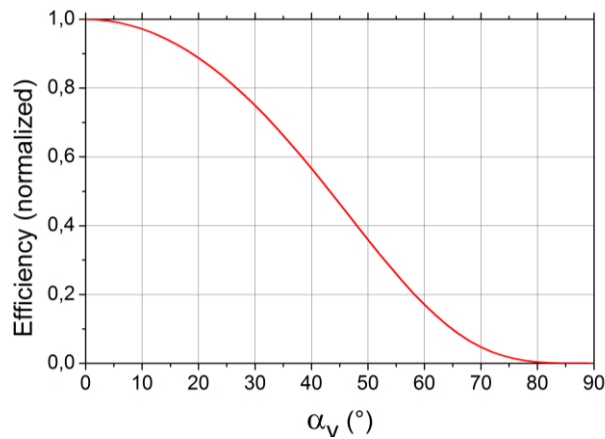


**Fig. 3.12 Influence of non-orthogonal flow on separation efficiency in straight vane separator sections**

The combined effect for bends and straight sections is depicted in Fig. 3.13. For this particular combination of input parameters<sup>36</sup>, the combined effect is *initially* positive for total bend angles of approximately  $\varphi < 85^\circ$ . For  $\varphi < 75^\circ$  it is positive for all  $\alpha_v$ . Without the influence of gravity, the results are symmetrical around  $\alpha_v = 0$ .

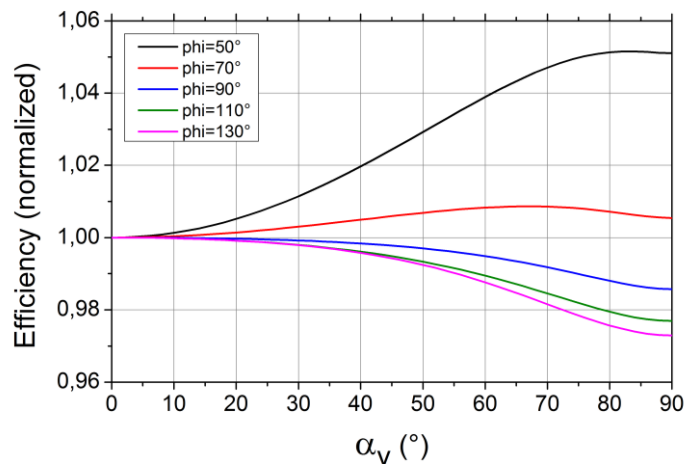


**Fig. 3.13 Influence of non-orthogonal flow on separation efficiency of an exemplary vane separator**

#### Quintessence

***An increasingly non-orthogonal flow angle, increases the effective path of the droplets, but also increases the effective channel width. The former has a positive and the latter has a negative effect on the separation efficiency. For decreasingly small bend angles, the net effect is increasingly positive, because for small bend angles the effective path increases more rapidly with increasing flow angle than the effective channel width. The maximum separation efficiency does not necessarily correspond with orthogonal flow conditions.***

<sup>36</sup> For both figures  $D_d = 20\mu m$ ,  $v_g = 5 m/s$ ,  $\mu_g = 20 mg/m \cdot s$ ,  $\delta_R = 1cm$ ,  $R_{out} = 2cm$ ,  $L = 6cm$  and  $n = 4$ .

### 3.3.3 Gravitational influence for non-orthogonal flow

#### 3.3.3.1 Curved sections

The influence of gravity for non-orthogonal flow is also investigated. The syntax for the angles of the gravitational vector, as defined by Fig. 3.7, remains valid, although the  $\hat{y}$ -axis shall lie in the tilted velocity plane (i.e. at an angle  $\alpha_v$ ), resulting in a  $z$ -axis perpendicular to this tilted plane. This rotational transformation of the velocity plane in a static geometry and gravitational field is depicted in Fig. 3.14<sup>37</sup>.

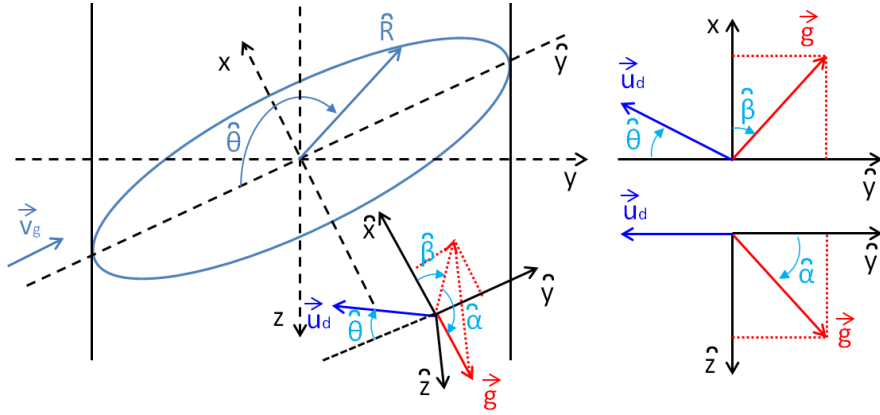


Fig. 3.14 Cartesian coordinate system including the gravity vector, for a rotated vane separator geometry, with top view of the tilted plane (upper right) and tilted side view (bottom right)

The droplet terminal radial velocity under the influence of gravity is

$$u_d(\theta) = \Delta\tau_{gd} \left( \frac{v_g^2 (\sin^2 \theta + \cos^2 \theta \cos^2 \alpha_v)^{3/2}}{R_{out}} + g \cos \hat{\alpha} \sin(\theta - \hat{\beta}) \right) \quad (3.87)$$

This leads to the following differential equation for the mass flow:

$$d \ln \dot{m}_d = -\frac{\Delta\tau_{gd}}{\delta_R} \left( v_g (\sin^2 \theta + \cos^2 \theta \cos^2 \alpha_v) + \frac{R_{out} g}{v_g} \frac{\cos \hat{\alpha} \sin(\theta - \hat{\beta})}{\sqrt{\sin^2 \theta + \cos^2 \theta \cos^2 \alpha_v}} \right) d\theta \quad (3.88)$$

Exploiting the symmetry of the integration around  $\theta = \theta = \pi/2$ , it can be shown that equation (3.88) reduces to

$$d \ln \dot{m}_d = -\frac{\Delta\tau_{gd} v_g}{\delta_R} \left[ (\sin^2 \theta + \cos^2 \theta \cos^2 \alpha_v) + \frac{R_{out} g}{v_g} \cos \hat{\alpha} \cos \hat{\beta} \frac{\sin \theta}{\cos \hat{\alpha}_v} \right] d\theta \quad (3.89)$$

<sup>37</sup> The angle  $\hat{\theta}$  is defined as in section 3.3.2, which is different from the analysis in Section 3.2.

For small angles of  $\alpha_v$ ,  $\cos \widehat{\alpha}_v$  is close to unity in the vicinity of  $\theta = \pi/2$ . Using this approximation<sup>38</sup> to carry out the integration from  $\theta = \frac{\pi - \widehat{\varphi}}{2} \rightarrow \frac{\pi + \widehat{\varphi}}{2}$  and employing  $\cos \widehat{\alpha} \cos \widehat{\beta} = \cos \alpha \cos \beta$ , results in the following equation for the separation efficiency:

$$\eta_C = 1 - \exp \left[ -\frac{\Delta \tau_{gd} v_g}{\delta_R} \left\{ \frac{\widehat{\varphi}}{2} (1 + \cos^2 \alpha_v) + \frac{\sin \widehat{\varphi}}{2} \sin^2 \alpha_v + \frac{2R_{out} g}{v_g^2} \cos \alpha \cos \beta \sin \left( \frac{\widehat{\varphi}}{2} \right) \right\} \right] \quad (3.90)$$

This equation is consistent with the fact that, according to equation (3.55), the influence of gravity is fully described by its component along the  $x$ -axis. In the limit  $\alpha_v \rightarrow 0$ , equation (3.90) reduces to equation (3.58). The first term inside the brackets in equation (3.90) is identical to the function  $F(\alpha_v)$  in equation (3.81).

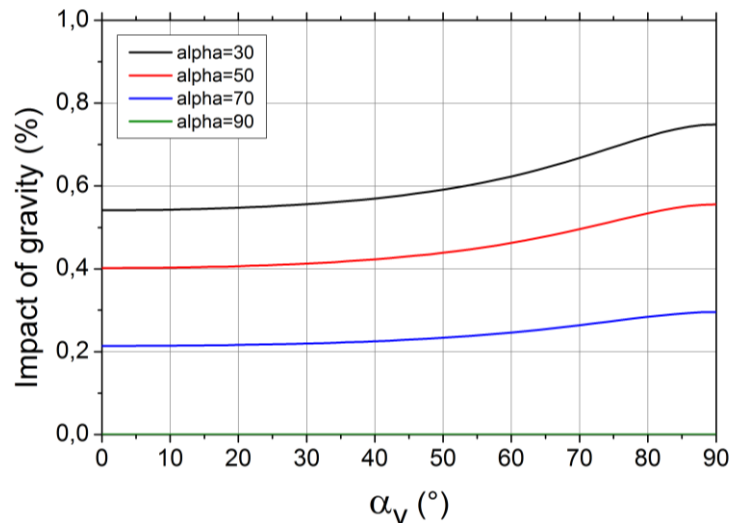


Fig. 3.15 Impact of gravity relative to  $F(\alpha_v)$

Fig. 3.15 shows the second term inside the brackets, *relative to* the first term, for different angles of  $\alpha$ <sup>39</sup>. For vertically oriented vane separators ( $\alpha = 90^\circ$ ), the impact of gravity is zero, independent of the flow angle. The influence of gravity is most pronounced for very large angles of  $\alpha_v$ , but in all cases smaller than  $F(\alpha_v)$ . The effect is not necessarily positive: for bends opposite the one depicted, the contribution is exactly negative.

<sup>38</sup> This will slightly underestimate the gravitational impact.

<sup>39</sup> The input parameters are the same as in section 3.3.2, with the addition of  $\beta = 30^\circ$ . The results are for a bend angle  $\varphi = 80^\circ$ .

### 3.3.3.2 Straight sections

Using the results from equations (3.66) and (3.86), the separation efficiency in straight vane separator sections, for non-orthogonal flow under the influence of gravity, is

$$\eta_S = 1 - \exp \left[ - \frac{(\Delta\tau_{gd}v_g)^2 \left( 1 - \exp \left( -L\sqrt{1 + \tan^2 \alpha_v \sin^2 (\varphi/2)} / \Delta\tau_{gd}v_g \cos \alpha_v \right) \right)}{R_{out}\delta_R \left( 1 + \tan^2 \alpha_v \sin^2 (\varphi/2) \right)^2} \mp \frac{\Delta\tau_{gd}Lg}{v_g\delta_R \cos \alpha_v} \cos \hat{\alpha} \cos \left( \hat{\beta} \mp \hat{\varphi}/2 \right) \right] \quad (3.91)$$

The effective angles of the bend and of the gravity vector are defined by the following equations:

$$\tan \left( \hat{\varphi}/2 \right) = \frac{\tan (\varphi/2)}{\cos \alpha_v} \quad (3.92)$$

$$\sin \hat{\alpha} = \cos \alpha_v \sin \alpha + \sin \alpha_v \cos \alpha \sin \beta \quad (3.93)$$

$$\cos \hat{\beta} = \frac{\cos \alpha \cos \beta}{\cos \hat{\alpha}} \quad (3.94)$$

In the limit  $\alpha_v \rightarrow 0$ , equation (3.91) reduces to equation (3.66).

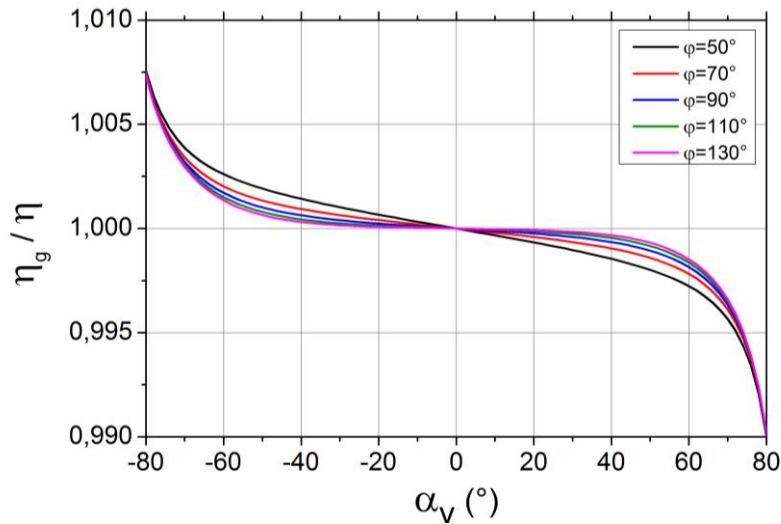


**Fig. 3.16 Gravitational influence on vane separator efficiency for non-orthogonal flow**

The ratio of the grade efficiencies, with<sup>40</sup> and without the influence of gravity (i.e. as compared to Fig. 3.13), is depicted in Fig. 3.16, for both negative and positive angles of  $\alpha_v$ . The depicted result is

<sup>40</sup> For input parameters see previous footnote. It is noted that the number of stages considered is four, thus eliminating the contradicting contributions of opposite bends and straight sections. The result for an uneven number of stages can be deduced from section 3.2.

for a gravitational angle of  $\alpha = 90^\circ$ , which represents a vertically oriented vane separator experiencing non-orthogonal gas flow at a certain angle  $\alpha_v$ . Consistent with the results from section 3.2, the influence of gravity is positive when the gravity and the gas velocity vector align (i.e. are in the same half-space). Therefore, the contribution of gravity is positive for negative angles of  $\alpha_v$  and negative for positive angles of  $\alpha_v$ <sup>41</sup>. It also increases with decreasing bend angles  $\varphi$ , which is also consistent with the results from section 3.2 (compare with A. Fig. 4 in appendix A.III). The results for  $\alpha = 90^\circ$  center around  $\alpha_v = 0$ . For other values of  $\alpha$  (i.e. for tilted vane separators), the influence of gravity is reduced and the graphs center around the value of  $\alpha_v$  that corresponds with  $\beta = 0$  (at which the gravity vector lies in the  $\hat{x} - \hat{z}$ -plane and aligns with the center of the ellipsoidal bend in the rotated coordinate system). An example is provided in Fig. 3.17, in which the dotted lines depict results for gravitational angles  $\alpha = 70^\circ$  and  $\beta = 30^\circ$ . The point of gravitational indifference is moved to  $\alpha_v \approx 12^\circ$ , which is exactly the value for which  $\beta = 0$ .

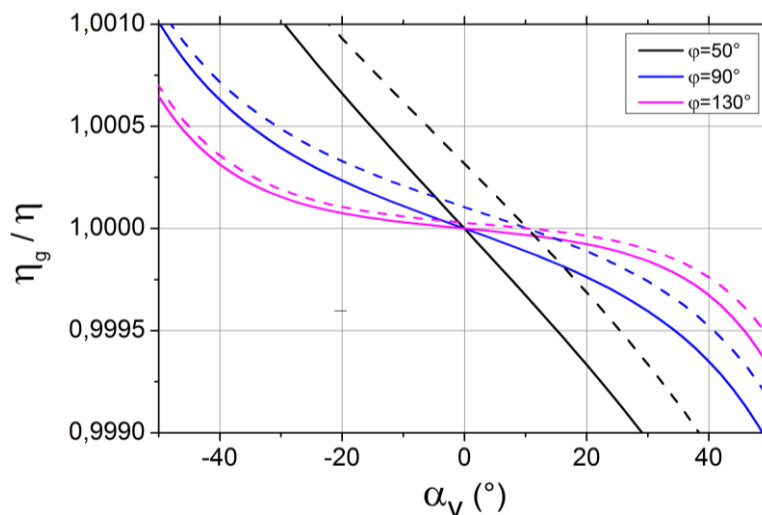


**Fig. 3.17 Gravitational influence on separation efficiency for different gravitational angles**

Fig. 3.18 depicts the normalized individual contributions<sup>42</sup> of each of the four vane separator sections: curved and straight sections on opposite sides (*left* and *right*). The influence of gravity on the curved sections is insignificant. The contributions from the straight sections are larger, but since the absolute separation efficiency in the straight sections is much smaller than in the curved sections, the overall effect is not as pronounced in Fig. 3.16. For very large angles of  $|\alpha_v|$ , the length of the straight sections tends towards infinity and their contributions (positive as well as negative) become excessively large. Such extreme angles of gas flow are not relevant to practical purposes.

<sup>41</sup> Positive angles of  $\alpha_v$  were defined to represent *upward* gas flow.

<sup>42</sup> The results are for a bend angle of  $\varphi = 50^\circ$  and are normalized with the equivalent sectional efficiency without gravity.

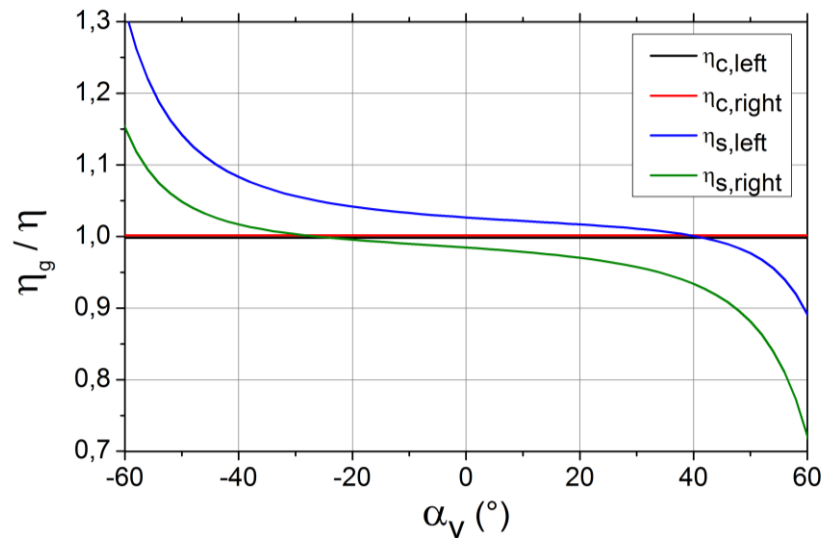


Fig. 3.18 Individual contributions of each section to the separation efficiency

#### Quintessence

*The impact of gravity on the separation efficiency is influenced by the orientation of the gas flow with respect to the vane separator, as well as by the spatial orientation of the vane separator itself. The optimum separation efficiency under non-orthogonal flow conditions thus depends on the spatial orientation of the vane separator with respect to gravity.*

## 3.4 Non-uniform velocity field

### 3.4.1 Velocity profiles

The gas velocity profile has been assumed flat and uniform throughout the vane separator channel, although it is zero at the channel wall and a steep velocity gradient is to be expected in the near-wall region. Velocity profiles inside a vane separator channel were measured by *Kall* [29], who found relatively small near-wall regions throughout the channel. Near the inlet the velocity profile was very flat, while halfway through a bend they were clearly skewed towards the inside of the bend, reaching almost a factor of 2 between inner and outer velocities [29, pp. 48-53]. *Gillandt et al.* [20] also recorded velocity profiles that were skewed towards the inner bend (Fig. 3.19 bottom left). Due to the influence of the previous bend, even the velocity profile *before* the bend is skewed toward the inner side. The normalized velocity profiles are independent of the Reynolds number. The computations by *Wang & James* [67] show that a large region exists at the outer wall of the bend for which near-zero velocities are computed (Fig. 3.19 bottom right). Depending on the specific model resolving the near-wall regions, even reverse flow is possible, reflecting large scale eddy behavior in the channel.

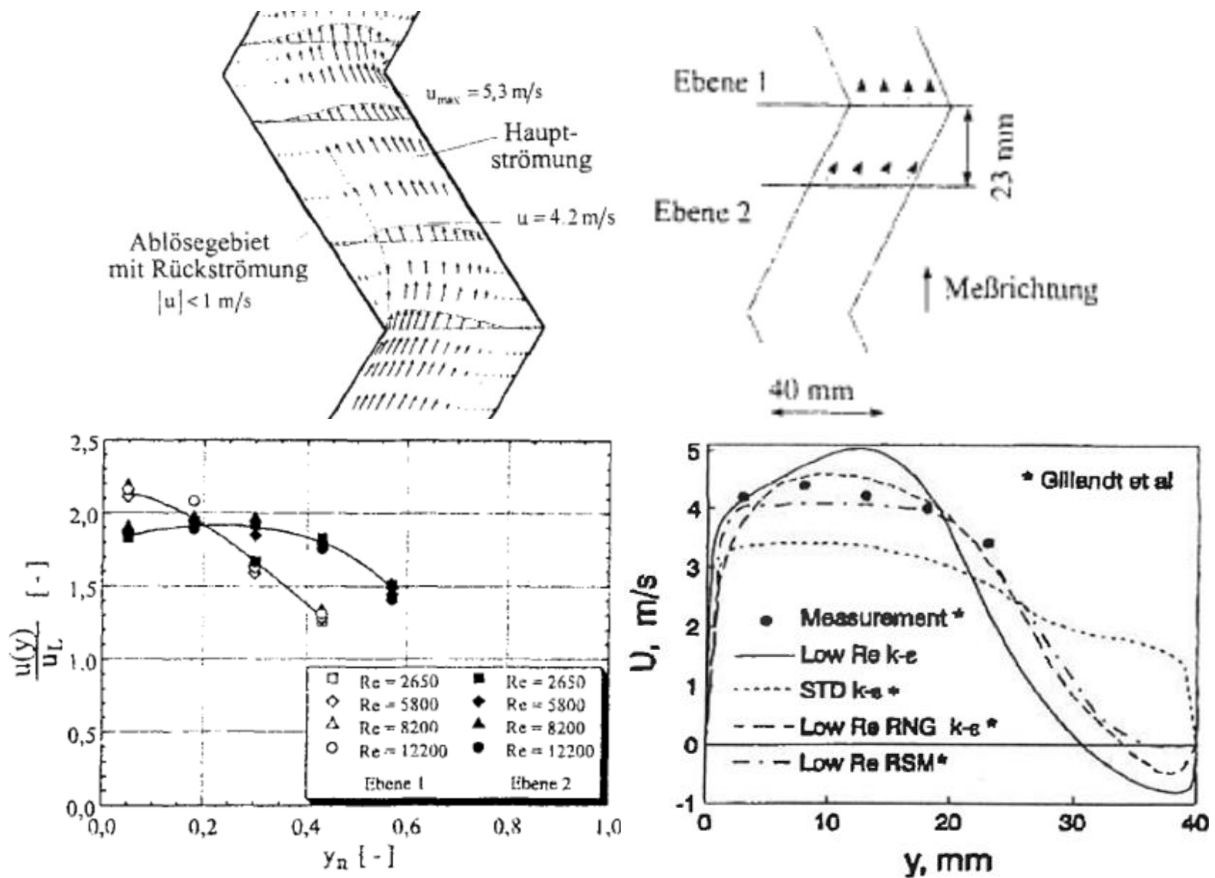


Fig. 3.19 Simulated velocity profile (above left) and measured velocity profiles (bottom left) at two cross-sections in a zig-zag vane separator channel (above right: "Ebene 1" and "Ebene 2")<sup>43</sup>. Computed velocity profiles at cross-section 2 (bottom right)<sup>44</sup>.

Jøsang [28, pp. 50-52] recorded velocity profiles at different axial positions in a vane separator channel with pick off hooks. Even at a relatively low inlet velocity of 2.4 m/s, negative velocities were recorded shortly behind each pick-off hook. A little further downstream the velocities were all positive, but still significantly skewed toward the outer wall of the bend (i.e. the inner wall of potential consecutive bends).

Droplet motion can be expected to be significantly influenced by such large disruptions of the velocity field, as discussed for the aforementioned examples. Specifically, the radial (outward) motion of droplets is affected by the tangential gas velocity profile across the width of the channel, which has a direct impact on droplet separation.

### 3.4.2 Significance to separation efficiency

Only the inertia of the droplets allows them to cross any near-wall regions with near-zero velocities and reach the channel wall. In order to estimate the impact of non-uniform velocity profiles on the droplet separation efficiency, a simplified version of the velocity profile depicted in Fig. 3.19 is assumed (Fig. 3.20). The homogeneous gas velocity is given by  $V_g$  and a boundary region with zero gas velocity is specified between  $y'$  and  $\delta_R$ . Assuming a constant mass flow through the channel

<sup>43</sup> Reprinted from [20, pp. 317-318], with kind permission from Springer Science and Business Media.

<sup>44</sup> Reprinted from [67, p. 981]. Copyright (1998), with permission from Elsevier.

leads to a maximum gas velocity outside the wall boundary region of  $v_g' = V_g \delta_R / y'$ . The depicted velocity profile is assumed valid throughout the bend (for all  $\theta$ ).

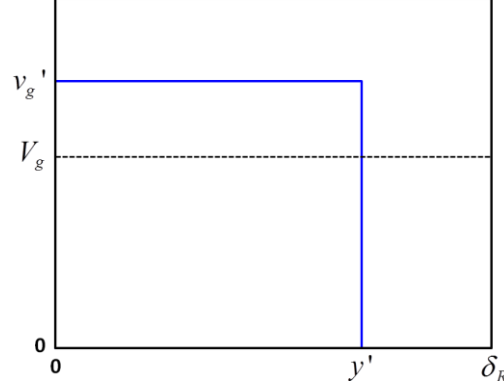


**Fig. 3.20** Simplified theoretical velocity profile through a channel cross-section

Assuming the droplets continue on a circular path inside the bend, the droplet radial and tangential velocity in the wall boundary region are given by (refer to equation (3.37))

$$u_d = u_{d,ini} \exp(-\Delta\tau / \Delta\tau_{gd}) \quad (3.95)$$

$$v_d = v_g' \exp(-\Delta\tau / \Delta\tau_{gd}) \quad (3.96)$$

The initial radial droplet velocity is defined as the terminal radial droplet velocity at the border of the wall boundary region, while assuming the maximum gas velocity  $v_g'$  (refer to equation (1.9)):

$$u_{d,ini} = \frac{\Delta\tau_{gd}}{(R_{in} + y')} \left( \frac{\delta_R V_g}{y'} \right)^2 \quad (3.97)$$

in which  $V_g$  is the homogeneous gas velocity. Integrating across the wall boundary region, it can be shown that, under these conditions, the time  $T_u$  it takes a droplet to cross the wall boundary region is given by

$$T_u = -\Delta\tau_{gd} \ln \left( 1 - \frac{\delta_R - y'}{\Delta\tau_{gd} u_{d,ini}} \right) \quad (3.98)$$

This directly implies that a limiting droplet size exists, defined by the limit  $T_u \rightarrow \infty$ , below which no droplet will ever reach the channel wall. Employing equations (1.17) and (3.97), this *droplet escape diameter* is given by

$$D_{esc}(\infty) = \left[ (\delta_R - y')(R_{in} + y') \left( \frac{18\mu_g y'}{\rho_d \delta_R V_g} \right)^2 \right]^{1/4} \quad (3.99)$$

The time to cross the wall boundary region is limited by the time  $T_v$  it takes the droplet to reach the end of the bend, which is given by

$$T_v = -\Delta\tau_{gd} \ln\left(1 - \frac{\varphi(R_{in} + y')}{\Delta\tau_{gd}v_g'}\right) \quad (3.100)$$

Equating equations (3.98) and (3.100) leads to a limiting droplet diameter  $D_{esc}(\varphi)$ , below which droplets cannot cross the wall boundary region before reaching the end of the bend:

$$D_{esc}(\varphi) = \sqrt{\frac{\delta_R - y'}{\varphi} \frac{18\mu_g y'}{\rho_d \delta_R V_g}} \quad (3.101)$$

Both droplet escape diameters tend to zero for vanishing wall boundary regions, as well as for wall boundary regions reaching channel width (Fig. 3.21 on the left). The latter limit can be explained by the maximum gas velocity  $v_g'$  tending to infinity for increasingly large wall boundary regions. In this specific example,  $D_{esc}(\infty)$  is larger than  $D_{esc}(\varphi)$ , meaning that all droplets large enough to cross the wall boundary region, require a path shorter than  $\varphi$  to do so (independent of the size of the wall boundary region). A comparison of equations (3.98) and (3.100) reveals that for decreasing values of  $R_{in}$  and  $\varphi$ ,  $D_{esc}(\varphi)$  may become larger than  $D_{esc}(\infty)$ , implying that the relevant droplet escape diameter for the particular bend would be given by  $D_{esc}(\varphi)$ . For the case at hand, the wall boundary region most difficult to cross equals approximately 30% of the channel width, which only droplets larger than  $18 \mu\text{m}$  would be able to cross.

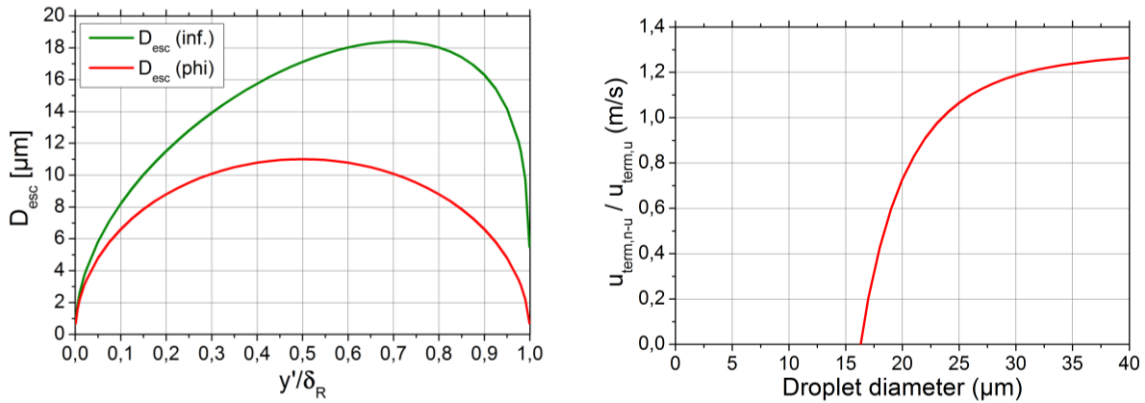


**Fig. 3.21** Escape diameters (left) and relative terminal radial droplet velocity (right) for an example for water droplets in air flow at atmospheric pressure, with a channel width of 1 cm, outer radius 2 cm, bend angle  $80^\circ$  and air velocity 5 m/s

In addition to a decrease in separation efficiency for small droplet diameters, due to the escape diameter, an increase in separation efficiency can be expected for larger droplet diameters, due to an increasing terminal radial droplet velocity, related to the larger velocity outside the wall boundary region. Accounting for this increased tangential velocity as well as its relaxation inside the wall boundary region, the terminal radial droplet velocity at the outer wall, is given by

$$u_{d,R_{out}} = u_{d,0} \exp\left(-\frac{T_u}{\Delta\tau_{gd}}\right) = \frac{\Delta\tau_{gd}}{R_{in} + y'} \left(\frac{\delta_R V_g}{y'}\right)^2 - \frac{\delta_R - y'}{\Delta\tau_{gd}} \quad (3.102)$$

For the given example (with  $y'/\delta_R = 0.9$ ), the terminal radial droplet velocity, relative to that for a uniform velocity profile, is given in Fig. 3.21 on the right. It is zero for droplet diameters below 16  $\mu\text{m}$ , corresponding to the escape diameter for  $y'/\delta_R = 0.9$  (Fig. 3.21 on the left). Beyond a diameter of 23  $\mu\text{m}$  the terminal radial droplet velocity for non-uniform velocity profiles exceeds that in a uniform velocity profile, increasing to a factor of 1.3 for droplets of 40  $\mu\text{m}$ . Accounting for the modified terminal radial droplet velocity, the separation efficiency of a single bend in a non-uniform velocity profile is

$$\eta_C = 1 - \exp\left(-\frac{R_{out}\phi}{v_g\delta_R} \left(\frac{\Delta\tau_{gd}}{R_{in} + y'} \left(\frac{\delta_R V_g}{y'}\right)^2 - \frac{\delta_R - y'}{\Delta\tau_{gd}}\right)\right) \quad (3.103)$$

Adjusting for the modified initial droplet radial velocity with which the droplets leave the bend (given by equation (3.97)<sup>45</sup>), leads to the following separation efficiency in the straight section:

$$\eta_S = 1 - \exp\left(-\frac{\delta_R}{(R_{in} + y')} \left(\frac{\Delta\tau_{gd} V_g}{y'}\right)^2 \left(1 - \exp\left(-\frac{L}{\Delta\tau_{gd} V_g}\right)\right)\right) \quad (3.104)$$

For  $y' = \delta_R$  these equations reduce to equations (1.16) and (3.46) respectively. The implications of a non-uniform velocity profile for the efficiency of a vane separator is visualized by Fig. 3.22, which depicts the separation efficiency of a single stage<sup>46</sup>. Below 16  $\mu\text{m}$  no droplets are separated, corresponding to the escape diameter for  $y'/\delta_R = 0.9$  in Fig. 3.21. Beyond 23  $\mu\text{m}$  the modified grade efficiency exceeds that of a uniform velocity profile.

<sup>45</sup> This implies that the droplets leave the bend *outside* of the wall boundary region. The relaxation of the terminal radial droplet velocity *inside* the wall boundary region is neglected.

<sup>46</sup> The single stage includes one bend and one straight section. Other parameters are as described in this section.

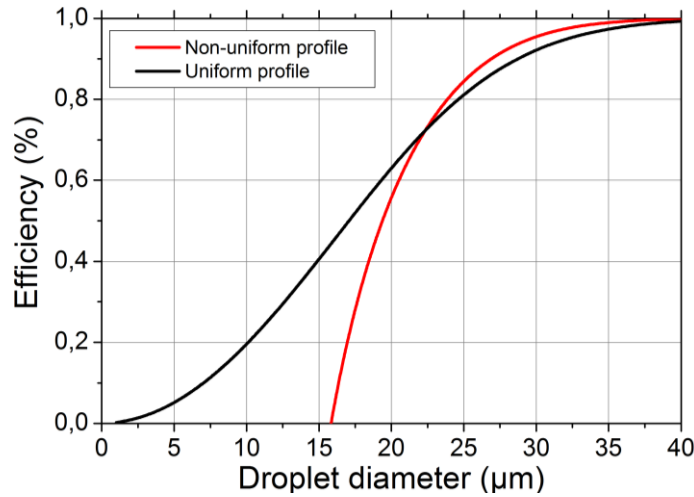


Fig. 3.22 Impact of the velocity profile on the droplet separation efficiency of a single stage

#### Quintessence

*An extreme simplification of non-uniform velocity profiles allows for an analysis of the droplet escape diameter, which defines the minimum droplet size required to cross the wall boundary region. It also allows for a modification of the terminal radial droplet velocity. In the presence of non-uniform velocity profiles, the droplet separation efficiency is expected to steeply drop to zero for droplet sizes below the droplet escape diameter. For droplet sizes a certain margin above the droplet escape diameter, it may be larger compared to uniform velocity profiles.*

### 3.5 Non-uniform droplet distribution and remixing

The initial radial position of each droplet as it enters a bend, depends on its radial migration distance(s) in the previous bend(s). If the terminal radial droplet velocity is no longer estimated to be at the outer wall ( $u_d = u_d(r)$ ), the radial migration distance  $\Delta r$  of a droplet through an entire stage (bend *and* straight section), starting at an initial radius  $r_0$ , can be approximated by

$$\begin{aligned} \Delta r &= \int_0^\varphi \frac{\Delta \tau_{gd} v_g^2}{r} \frac{rd\theta}{v_g} + \int_0^L \frac{\Delta \tau_{gd} v_g^2}{r_\varphi} \exp\left(\frac{-s}{\Delta \tau_{gd} v_g}\right) \frac{ds}{v_g} \\ &= \Delta \tau_{gd} v_g \varphi + \frac{(\Delta \tau_{gd} v_g)^2}{r_0 + \Delta \tau_{gd} v_g \varphi} \left[ 1 - \exp\left(\frac{-L}{\Delta \tau_{gd} v_g}\right) \right] \end{aligned} \quad (3.105)$$

This is a decreasing function in  $r_0$ , meaning the radial droplet migration is largest for  $r_0 \downarrow R_{in}$ , or equivalently  $y \downarrow 0$  for a distance  $y = r_0 - R_{in}$  from the channel wall. A droplet that is not separated, starting at a distance  $y$ , either reaches a position  $y' < y$  in the consecutive bend (solid line in Fig. 3.23) or a position  $y' > y$  (dashed line in Fig. 3.23). Because  $\Delta r$  decreases with  $r_0$ , the radial droplet migration distance in the *consecutive* bend, will in the first case be larger than before

(leading to  $y > y''$ ) and in the latter it is smaller (leading to  $y < y''$ ). This implies that droplet paths have a tendency toward the centerline of the channel and, if no remixing of the droplet distribution would occur and only uniform velocity profiles are considered, the droplet separation efficiency would theoretically drop to zero after the first bend. The droplet migration distance is therefore not a helpful tool when analyzing the impact of non-uniform droplet distributions on droplet separation efficiency.

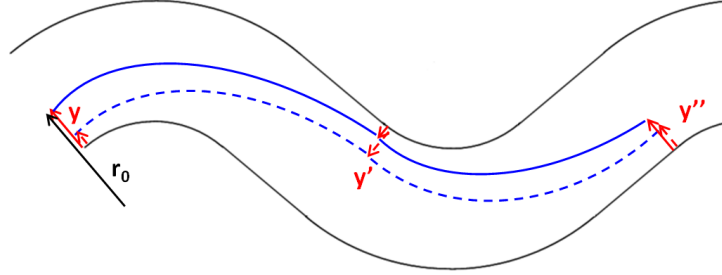


**Fig. 3.23 Droplet migration through consecutive bends**

Remixing can also be analyzed by correcting the droplet volume fraction at the outer wall for the non-uniform droplet distribution. An exponential growth of the droplet volume fraction  $\alpha_d(\theta)|_{R_{out}}$  along the outer wall, as a function of the bend angle  $\theta$ , tending toward its homogeneous value  $\alpha_d$ , can be described by the following mathematical relation proposed here:

$$\alpha_d(\theta)|_{R_{out}} = \left[ 1 - \lambda_1 \exp\left(-\lambda_2 \frac{\theta}{\varphi}\right) \right] \alpha_d \quad (3.106)$$

The parameter  $\lambda_1$  represents the relative reduction of the droplet volume fraction at the bend inlet, as a result of the centrifugal force in the previous bend, for which it is suggested to use *Wilkinson's* [70] remixing factor  $f_m$  (refer to chapter 2.1):

$$\lambda_1 = 1 - f_m = \exp\left(\frac{cC_{pb}}{cC_{pb} - 18St \delta_R/L}\right) \quad (3.107)$$

The parameter  $\lambda_2$  represents the rate with which the droplet volume fraction near the outer wall reaches its normal value, for which it is suggested to use an exponential function of the Reynolds number:

$$\lambda_2 = K Re^m \quad (3.108)$$

Employing equation (3.106) and integrating over the bend angle, the separation efficiency in each consecutive bend is given by

$$\eta = 1 - \exp\left(-\frac{\rho_d v_g D_d^2}{18\mu_g \delta_R} \varphi \left(1 + \frac{\lambda_1}{\lambda_2} [\exp(-\lambda_2) - 1]\right)\right) \quad (3.109)$$

This leads to a total grade efficiency for the vane separator (not including inlet and outlet sections) of

$$\eta = 1 - \exp\left(-\frac{\rho_d v_g D_d^2}{18\mu_g \delta_R} \varphi\left(n + (n-1)\frac{\lambda_1}{\lambda_2}[\exp(-\lambda_2) - 1]\right)\right) \quad (3.110)$$

The impact of a non-uniform droplet distribution, in the form of equation (3.110), is visualized in Fig. 3.24 for  $K = 0.1$  and  $m = 0.5$ . For small droplet diameters, the remixing factor is close to unity and the impact is small. For increasing droplet diameters, the remixing factor decreases rapidly towards zero, but the function defined by equation (3.106) limits the remixing effect to a small part of the bend, reducing the 'effective' bend angle by no more than 16%. The same figure also depicts the separation efficiency for uniform and non-uniform droplet distributions, as defined by *Wilkinson* [70] (equation (2.14)). Only data in the applicable range of Stokes numbers is depicted ( $0.1 < St < 0.66$ ). The curves for uniform distributions ( $f_m \equiv 1$ ) lie close together, but for non-uniform distributions they differ significantly, because the remixing factor by *Wilkinson* [70] is not limited by the exponent in equation (3.110).

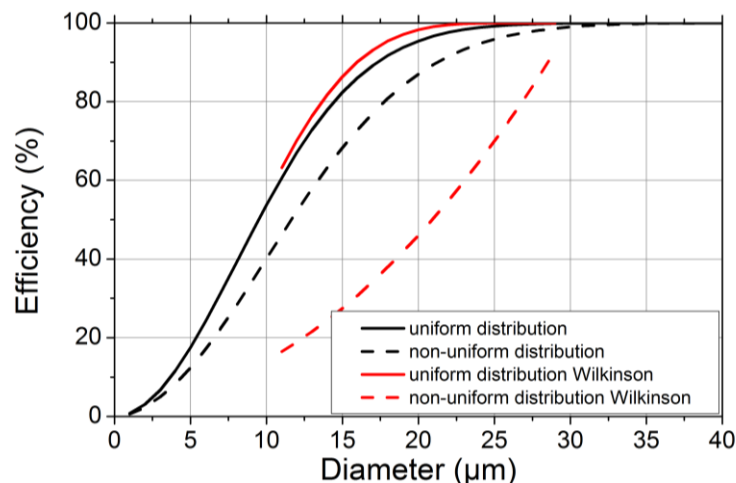


**Fig. 3.24** Impact of non-uniformity of droplet distribution on separation efficiency, for a vane separator with channel width 15 mm, outer radius 25 mm, bend angle  $80^\circ$ , straight section 20 mm and 7 stages, at a gas velocity of 4 m/s

#### Quintessence

*It is possible to represent the non-uniformity of the droplet distribution after the first bend by a compensation of the droplet volume fraction along the outer wall of the bend, accounting for the magnitude of non-uniformity and the rate of remixing. Mathematically, the effective bend angle is decreased by a factor dependent on *Wilkinson's* [70] remixing factor and the Reynolds number.*

## 3.6 Droplet size distributions and grade efficiency

### 3.6.1 Characterization of droplet size distributions

The grade efficiency is very dependent on the actual droplet size and therefore the total separation efficiency is very dependent on the actual droplet size distribution. In all practical cases the droplets entering the vane separator will be of different sizes, depending on the application. Droplet size spectra produced by commercially available nozzles are often denoted by the manufacturer with a certain mean diameter. Generally used are the arithmetic mean diameter  $d_{10}$ , the surface mean diameter  $d_{20}$  and the volumetric mean diameter  $d_{30}$ . These are defined as functions of the droplet diameter  $D_d$  and the droplet mass distribution function  $f(D_d)$  [4]:

$$d_{pq} = \left[ \frac{\int_0^{\infty} f(D_d) D_d^p dD_d}{\int_0^{\infty} f(D_d) D_d^q dD_d} \right]^{\frac{1}{p-q}} \quad (3.111)$$

For discrete spectra, this can also be written as

$$d_{pq} = \left[ \frac{\sum_{i=1}^{i_{\max}} \overline{D_{d,i}^p} f_{D,i}}{\sum_{i=1}^{i_{\max}} \overline{D_{d,i}^q} f_{D,i}} \right]^{\frac{1}{p-q}} \quad (3.112)$$

in which  $f_{D,i}$  is the mass fraction of the droplet size group  $i$  and  $i_{\max}$  is the amount of droplet size groups specified. In order to minimize discretization errors, the group average diameters  $\overline{D_{d,i}^y}$  should be computed according to their respective power  $p$  or  $q$  as follows:

$$\overline{D_{d,i}^y} = \sqrt[y]{\frac{1}{\Delta D_i} \int_{D_{\min,i}}^{D_{\max,i}} D_d^y dD_d} = \sqrt[y]{\frac{D_{\max,i}^{y+1} - D_{\min,i}^{y+1}}{(y+1)\Delta D_i}} \quad (3.113)$$

in which  $y = p, q$  and  $\Delta D_i = D_{\max,i} - D_{\min,i}$  is the width of the droplet size group  $i$  with lower boundary  $D_{\min,i}$  and upper boundary  $D_{\max,i}$ . The most commonly used form of equation (3.111) for efficiency studies is the Sauter mean diameter  $d_{32}$ . It represents the diameter of a sphere having the same volume-to-surface ratio as the particle of interest [58]. In the case of droplet spectra, it can be defined as the diameter of spherical mono-dispersed droplets having the same volume and area as the poly-dispersed droplet spectrum under investigation [4]. The use of the Sauter mean diameter for efficiency studies is very appropriate, because it captures both the cubic dependence of the centrifugal force on the diameter (assuming that all droplets have the same density) and the square dependence of the drag force.

### 3.6.2 Droplet size distributions in power plants

In most pressurized water reactors, either one or two separation stages are installed<sup>47</sup>. In the first case it concerns either a vane separator or some other type of demister, receiving a large range of droplet sizes, including many relatively large droplets (up to 200  $\mu\text{m}$ ). In the second case, the first separation stage will be a coarse separator in the form of a cyclone separator and the second separation stage is usually a vane separator, receiving a much smaller droplet size distribution. Few measurements of droplet spectra in (nuclear) power plants have been performed and they are therefore not well known<sup>48</sup>. The moisture mass content at different locations in the steam cycle is usually computed from energy balances after measurements of temperature, pressure and mass flows and rarely measured directly. The actual droplet spectra at crucial locations in the steam cycle can be estimated from the little available measurement data. One such dataset was produced by *KraftWerkUnion* (KWU), as reported by *Kolev* [34, p. 361], who extrapolates the measurement data using the following Boltzmann distribution model:

$$\frac{\sum_{D_d < D_{d,i}} \dot{m}_{d,i}}{\dot{m}_d} = \frac{a_1 - a_2}{1 + \exp((D_{d,i} - D_{d,0})/\Delta D)} + a_2 \quad (3.114)$$

where  $a_1 = -70.408$ ,  $a_2 = 92.947$ ,  $D_{d,0} = 10.987\mu\text{m}$ ,  $\Delta D = 32.661\mu\text{m}$  and  $\frac{1}{\dot{m}_d} \sum_{D_d < D_{d,i}} \dot{m}_{d,i}$  is

the cumulative mass fraction of all droplets below a diameter  $D_{d,i}$ . A more commonly used relation for droplet size distributions is the Rosin-Rammler distribution [54] defined by<sup>49</sup>

$$1 - \nu = \exp\left(-\left(D/\bar{D}\right)^\delta\right) \quad (3.115)$$

in which  $\nu$  is the cumulative mass fraction of all droplets below a diameter  $D$  and  $\bar{D}$  and  $\delta$  are a size and a distribution parameter respectively. The experimental data, the Boltzmann model and the Rosin-Rammler model ( $\bar{D} = 60\mu\text{m}$  and  $\delta = 1.2$ ) are depicted in Fig. 3.25. Both models represent the data well, although the Rosin-Rammler model crosses the origin and displays a more natural approach towards unity.

<sup>47</sup> This applies to the steam generator as well as to the Moisture Separator & Reheater (MSR).

<sup>48</sup> Certain methods for moisture measurement exist, e.g. with the use of radio-active or chemical tracers from which the amount of moisture can be deduced, but measurement data is not abundant. Although, the reliability of these methods is limited, their application appears to become more frequent.

<sup>49</sup> As cited by *Mugele & Evans* [48, p. 1319].

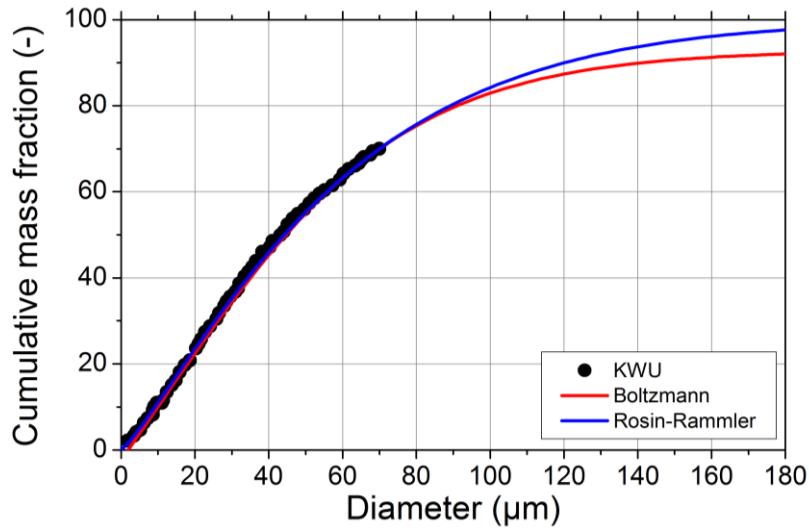


**Fig. 3.25 Droplet size distribution at the exit of an HP turbine; KWU experiments (black) and as modeled using a Boltzmann (red) [34, p. 361] or a Rosin-Rammler distribution (blue)**

Using equation (3.115) to describe the droplet mass distribution and employing equation (3.113) to derive the group average diameters, twenty droplet size groups are defined, with which a representative discrete droplet size distribution is constructed (Table 2).

**Table 2 Representative droplet distribution for PWRs, based on KWU measurements reported by Kolev [34, p. 361]**

Group	Average diameter	Mass fraction	Cum. mass fraction
µm	µm	%	%
0-4	2.52	3.80	3.80
4-6	5.07	2.31	6.11
6-8	7.05	2.41	8.53
8-10	9.04	2.47	10.99
10-15	12.66	5.01	16.00
15-20	17.62	7.47	23.48
20-25	22.59	4.85	28.32
25-30	27.58	6.97	35.29
30-35	32.56	4.41	39.70
35-40	37.56	6.22	45.92
40-45	42.55	3.88	49.80
45-50	47.54	5.42	55.22
50-60	55.15	7.99	63.21
60-70	65.13	6.76	69.98
70-80	75.11	5.67	75.64
80-90	85.10	4.70	80.34
90-100	95.09	3.87	84.21
100-150	126.64	10.82	95.04
150-200	176.18	2.58	97.62
>200	250	2.38	100.00

### 3.6.3 Evaluation of total separation efficiency from grade efficiencies

The efficiency of demisters can be given in terms of the critical (cut-off) diameter. It represents the theoretical smallest droplet diameter that can still be separated by the demister. The separation efficiency of all larger droplets is assumed unity; below this diameter it is assumed to be zero. Because this assumption does not fit theoretical models with non-zero separation efficiency for all droplet sizes, and is too simplistic to fit the experimental evidence, cut-size diameters are also reported. These represent the bounding diameter for a certain separation efficiency, e.g.  $d_{50}$  is the cut-size diameter above which 50% of the droplet mass is separated<sup>50</sup>. For example, in his description of cyclone theory, *Bürkholz* [10, p. 78] describes an imaginary cylinder of a certain radius  $r_i$ , inside a conventional cyclone separator with tangential inlet. This imaginary cylinder separates the purely rotational flow on the inside of this cylinder (for which  $v_d/r \approx \text{constant}$ ), from the flow governed by the conservation of angular momentum on the outside (for which  $v_d r \approx \text{constant}$ ). He consequently concludes that the radial droplet velocity is largest at the radius  $r_i$ . After equating centrifugal and frictional forces at the radius  $r_i$ , with  $u(r_i)$  for the inward radial velocity of the gas and  $v(r_i)$  for the tangential velocity, he arrives at a limiting droplet diameter of

$$d_{50} = \sqrt{\frac{18\mu_g u(r_i) r_i}{\rho_d v(r_i)^2}} \quad (3.116)$$

This definition of the limiting droplet diameter is in fact equal to equation (1.9). In this case, equation (3.116) implies is that droplets with a smaller diameter than  $d_{50}$  will not make it across this imaginary border at  $r_i$  and will not be separated.

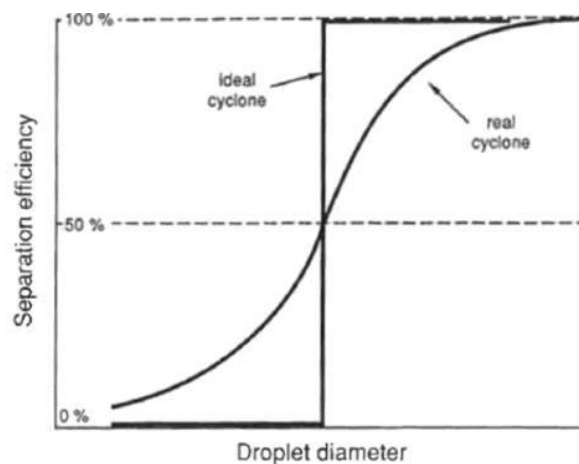


Fig. 3.26 Cyclone separation efficiency for an ideal and a real cyclone separator<sup>51</sup>

<sup>50</sup> The syntax of the cut-size diameter is the same as for the mean droplet diameter described before. The same syntax is also used to describe a droplet size distribution for which 50% of the droplet volume is below and 50% is above the diameter  $d_{50}$  (e.g. [64, p. 62]), which can lead to confusion.

<sup>51</sup> Reprinted from [10, p. 79]. Copyright Wiley-VCH Verlag GmbH&Co. KGaA. Reproduced with permission.

*Bürkholz* [10] visualizes the interpretation of the limiting droplet diameter in Fig. 3.26, which incorporates both the notion of a cut-off diameter (for the ideal cyclone separator) as well as the notion of a cut-size diameter  $d_{50}$  (for the real cyclone separator). This approach is only applicable to cyclone separators with inward rotating gas flows<sup>52</sup> and even for those its value is limited. Additional difficulties for the determination of the actual separation efficiency are; knowing where  $r_i$  is located; knowing the actual radial droplet velocity  $u(r_i)$ ; and knowing how much to 'tilt' the graph displayed in Fig. 3.26 to represent a 'real' cyclone separator. Instead of a critical or a cut-size diameter, sometimes the Sauter mean diameter is used, not only to describe the droplet distribution, but to evaluate the overall separation efficiency as well.

Mean or cut-size diameters will not be used in this paper to evaluate the overall separation efficiency; it will be computed directly from the grade efficiencies. This is only possible if the grade efficiencies are not correlated to the actual droplet size distribution. The correlation of droplet size distribution and grade efficiency was investigated for cyclone separators by *Ontko* [50], by performing an experimental regression analysis on two batches of test particles with different particle size distributions. According to *Hoekstra* [22, p. 17] no relation was found between grade efficiency and particle size distribution, but in fact, the data was inconclusive and circumstantial evidence suggests the contrary [50, p. 100]. Cyclone separators can be designed to withstand large droplet mass fractions while maintaining reasonable separation efficiencies for droplets that are not too small. Vane separators are designed for smaller droplet spectra and for large liquid mass fractions the overall separation efficiency is seriously diminished. This is mainly caused by the instability of the growing liquid film on the vane walls, which greatly increases liquid re-entrainment, enhanced by the inability to drain the separated liquid flow from the flow channel<sup>53</sup>. In the regime of small liquid mass fractions and low Reynolds numbers, droplet coalescence and droplet break up are insignificant with relevance to the initial droplet size distribution<sup>54</sup>. This strengthens the assumption that droplet size distribution and grade efficiency are uncorrelated in vane separators. The overall separation efficiency  $\eta$ , given a certain droplet mass distribution  $f(D_d)$ , is then defined as

$$\eta = \int_0^{\infty} \eta_D(D_d) f(D_d) dD_d \approx \sum_{i=1}^{i_{\max}} \overline{\eta_{D_{d,i}^3}} f_{D,i} \quad (3.117)$$

in which  $\overline{\eta_{D_{d,i}^3}}$  is the grade efficiency computed for the group volume averaged diameter  $\overline{D_{d,i}^3}$  (defined by equation (3.113)) with mass fraction  $f_{D,i}$ . The sum is over all specified droplet size groups. The total separation efficiency shall mean in a theoretical context the weighted sum of all grade efficiencies, as prescribed by equation (3.117). In an experimental context, the total separation efficiency is determined directly by the ratio of measured separated and inlet mass flows.

<sup>52</sup> *Bürkholz* [10] defines  $u(r_i)$  as the volumetric flow rate divided by the outer area  $r_i h_i$  of the imaginary cylinder. For vane separators, the radial gas velocity  $u_g$  was fully neglected in section 1.3.2.

<sup>53</sup> More on this topic will be discussed in chapter 4.1.

<sup>54</sup> Refer to chapter 4.1.4.1.

### 3.6.4 Total grade efficiency

The total efficiency of the vane separator can be calculated from the separate stage efficiencies in the following way ([52], [10]):

$$\eta_D = 1 - \prod_{s=1}^n (1 - \eta_s) \quad (3.118)$$

in which  $\eta_s$  is the separation efficiency for each stage and  $\eta_D$  is the separation efficiency of the entire vane separator, for a given droplet diameter  $D$  (grade efficiency). This equation is slightly altered to account for the contributions of both bends and straight sections:

$$\eta_D = 1 - (1 - \eta_C)^n (1 - \eta_S)^{n-1} \quad (3.119)$$

#### 3.6.4.1 Inlet and outlet sections

It is noted that equation (3.119) assumes each vane separator to start and end with full and identical bends, in between which straight sections of equal length are located. For practical reasons, vane separators usually start and end with one half of a full bend. From equation (1.16) it is clear that the separation efficiency  $\eta_{1/2}$  of one half of a full bend is given by

$$\eta_{1/2} = 1 - \sqrt{1 - \eta_C} \quad (3.120)$$

This result was already noted by *Ushiki* [63, p. 293]. Not counting the inlet and outlet sections as stages, and assuming they are directly connected to a full bend (i.e. there are no additional straight sections to be accounted for), leads to the following modification of the original equation (3.119):

$$\eta_D = 1 - (1 - \eta_C)^n (1 - \eta_L)^{n-1} (1 - \eta_{1/2})^2 = 1 - (1 - \eta_C)^{n+1} (1 - \eta_S)^{n-1} \quad (3.121)$$

This modification is noteworthy when carrying out comparisons with empirical data. In many sources in literature, the inlet and outlet sections are not counted as stages, but they definitely contribute to the separation efficiency of the vane separator. This convention will be followed in this paper as well, but it should be noted that whenever the number of stages  $n$  is mentioned, the inlet and outlet sections account for the contribution of an additional full bend, leading to an *effective* number of curved sections of  $n + 1$ . If the inlet and outlet sections resemble straight sections rather than half bends, equation (3.121) reads

$$\eta_D = 1 - (1 - \eta_C)^n (1 - \eta_S)^n \quad (3.122)$$

## 4 Film flow, re-entrainment and pressure drop

Not all phenomena relevant to droplet paths and the separation efficiency of vane separators in general, are captured by the analytical model described in the previous chapter. Because the impact of certain phenomena on the performance of vane separators can be significant, their elaboration is imperative for a decent analysis of experimental results. The most relevant phenomena are related to liquid film flow, re-entrainment and pressure drop.

### 4.1 Film separation, carry-over and re-entrainment

In the analytical model described in the previous chapter, all droplets hitting the vane separator wall are considered separated from the flow. Droplets that were previously separated from the flow can, however, get re-entrained into the gas flow. Several mechanisms can be responsible for re-entrainment:

- At sufficiently high gas velocity and liquid film thickness, the waves forming on the liquid film surface become unstable and droplets are separated from the wave crests into the gas flow. This is often referred to as the *over-entrained regime*.
- At high liquid loading factors, the amount of droplets deposited on the wall may cause the liquid film to exceed a certain limiting equilibrium thickness and become unstable. This is often referred to as the *under-entrained regime*.
- At sharp convex corners in the vane separator geometry, centrifugal forces can surmount the surface tension, causing the liquid film to separate from the wall entirely. This is referred to as *liquid film detachment*.
- At high gas velocities in relatively high vertically oriented vane separators, the gravitational down-flow of the liquid film may not suffice to drain the film before it reaches the next or even the ultimate separation stage. Re-entrainment then occurs *after* the vane separator, as the liquid film literally flows into thin air. The transportation of liquid film into the next stage is referred to as *carry-over*.
- In general, insufficient drainage of the liquid film can cause a rising water level at the bottom of the vane separator. At high liquid loading in relatively narrow channels, the liquid film can reach across the channel and block the gas flow. This is often referred to as *flooding*.

Liquid film flow and re-entrainment effects are relevant for the functionality and efficiency of the vane separator design. Its analysis is helpful for selecting the correct design and the amount of vane separators<sup>55</sup> for the physical conditions at hand.

#### 4.1.1 Liquid film formation

A good vane separator is designed to avoid, or at least minimize re-entrainment effects caused by the mechanisms listed in the previous section. In order to estimate such effects, the formation of the

---

<sup>55</sup> Assuming a certain optimum channel width for each vane separator, the total frontal area for the flow is defined by the total amount of vane separators installed. For a given mass flow, the amount of vane separators defines the gas velocity through each of the channels.

liquid film on the walls is investigated. *Azzopardi & Sanaullah* [3] studied liquid film wave formation as well as film separation in a vane separator. They performed measurements of liquid film thicknesses upon a vertical plate, under the influence of a transverse gas flow. Comparing their results with a Nusselt flow profile without transverse gas flow<sup>56</sup>, it appeared that the liquid film thickness increases with liquid flow rate, but is almost insensitive to the gas flow rate [3, p. 3559]. This led to the assumption that the horizontal shear force and the gravitational body force are uncorrelated [3, p. 3561]. Using this result, *James et al.* [27] provide an analysis of a falling liquid film under transverse gas flow. They consider a simple vertically oriented plate along which a liquid film propagates in two directions (see Fig. 4.1). The flow in the  $z$ -direction it is driven by gravity only and in the  $x$ -direction it is driven by the superficial force from the gas flow only.

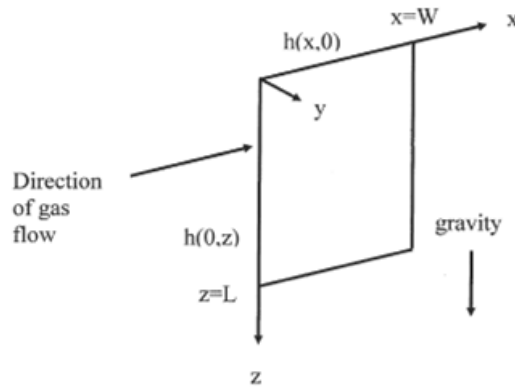


Fig. 4.1 Schematic diagram of a flat surface with local coordinates<sup>57</sup>

The two-dimensional mass conservation of the liquid film is given by

$$\frac{\partial}{\partial x} \{ h_f(x,z) \bar{u}(x,z) \} + \frac{\partial}{\partial z} \{ h_f(x,z) \bar{w}(x,z) \} = \frac{G_d(x)}{\rho_f} \quad (4.1)$$

in which  $h_f$  is the film thickness (height),  $G_d$  the droplet deposition flux (independent of  $z$ ),  $\rho_f$  the density of the liquid film and  $\bar{u}$  and  $\bar{w}$  denote the height-averaged velocities in  $x$ - and  $z$ -direction. *James et al.* [27] assumed a linear velocity profile for  $u(x,z)$  and a Nusselt profile for  $w(x,z)$ <sup>58</sup>, arriving at the following governing equations for the liquid film motion:

$$\bar{u}(x,z) = \frac{\tau_{yx}(x) h_f(x,z)}{2\mu_f} \quad (4.2)$$

$$\bar{w}(x,z) = \frac{\rho_f g h_f^2(x,z)}{3\mu_f} \quad (4.3)$$

<sup>56</sup> Details of the Nusselt flow profile will follow later in this section.

<sup>57</sup> Reprinted from [27, p. 473]. Copyright (2005), with permission from Elsevier.

<sup>58</sup> The Nusselt profile describes the flow along a vertical wall of a viscous condensing fluid, driven by gravity only. In this case, the film growth is not driven by thermal (condensation), but by mechanical mass transfer (droplet separation).

in which  $\mu_f$  is the dynamic viscosity and  $\tau_{yx}$  is the interfacial shear stress on the liquid film surface in the  $x$ -direction. Inserting this into equation (4.1) leads to

$$\frac{\partial}{\partial x} \left\{ \frac{\tau_{yx}(x) h_f^2(x, z)}{2\mu_f} \right\} + \frac{\partial}{\partial z} \left\{ \frac{\rho_f g h_f^3(x, z)}{3\mu_f} \right\} = \frac{G_d(x)}{\rho_f} \quad (4.4)$$

Neglecting gravity, the authors reach the following solution for the thickness  $h_{ng}$  at the end of a wall section with length  $W$  :

$$h_{ng}(W) = \sqrt{\frac{2\mu_f W \overline{G_d}}{\tau_{yx}(W) \rho_f}} \quad (4.5)$$

where  $\overline{G_d}$  is the average droplet flux over the wall length  $W$ . The actual film thickness at the upper right hand corner of the plate will, under the influence of gravity, be less than equation (4.5) prescribes, due to the downward motion of the liquid film. *James et al.* [27] continue to show that, for sufficiently large  $z$ , the film thickness will reach a limiting value equal to  $h_{ng}(W)^{59}$ . This limiting value exists, because it represents the equilibrium value at which the gravitational force is balanced by the interfacial shear stress. The distance at which this equilibrium height is reached, decreasing with increasing gas velocity.

*James et al.* [27] compute the results from equation (4.5) with the use of CFD. By evaluating the interfacial shear stress analytically, the limiting liquid film height can be given an analytical interpretation. The interfacial shear stress is given by

$$\tau_{yx}(x) = \frac{1}{2} c_{gf}^d \rho_g (u_g - u_{f, surface})^2 = \frac{1}{2} c_{gf}^d \rho_g (u_g - 2\bar{u}(x, z))^2 \quad (4.6)$$

Inserting equation (4.2) and solving for  $\tau_{yx}(x)$  leads to<sup>60</sup>

$$\frac{h_f(x, z)}{\mu_f} \tau_{yx}(x) = u_c + \frac{\mu_f}{c_{gf}^d \rho_g h_f(x, z)} \left\{ 1 - \sqrt{1 + \frac{2c_{gf}^d \rho_g u_g h_f(x, z)}{\mu_f}} \right\} = 2\bar{u}(x, z) \quad (4.7)$$

Defining the variable  $q = \mu_f / (c_{gf}^d \rho_g h_f u_g)$ , equation (4.7) can be written as

$$\frac{2\bar{u}(x, z)}{u_g} = 1 + q \left( 1 - \sqrt{1 + \frac{2}{q}} \right) = F(q) \quad (4.8)$$

<sup>59</sup> The section under investigation had a width of 23mm and a height of 130mm. From their model, the liquid film height at the end of the section ( $x = W$ ) appears to have reached its maximum at the bottom ( $z = L$ ), for gas velocities at or above 8 m/s [27].

<sup>60</sup> The quadratic formula is applied. The negative square root is chosen to ensure the physical limit  $\lim_{u_g \rightarrow 0} 2\bar{u} = 0$ .

$F(q)$  is a decreasing function of  $q$ , for which  $\lim_{q \downarrow 0} F(q) = 1$  and  $\lim_{q \rightarrow \infty} F(q) = 0$ . The first limit involves large liquid film velocities and liquid film heights, representing an increasingly linear liquid film velocity profile, for which  $\bar{u}(x, z) \uparrow u_g/2$ . The second limit involves increasingly small liquid film velocities and liquid film heights, for which  $\bar{u}(x, z) \downarrow 0$ . For large  $q$ ,  $F(q)$  varies only slowly with  $q$  (Fig. 4.2).

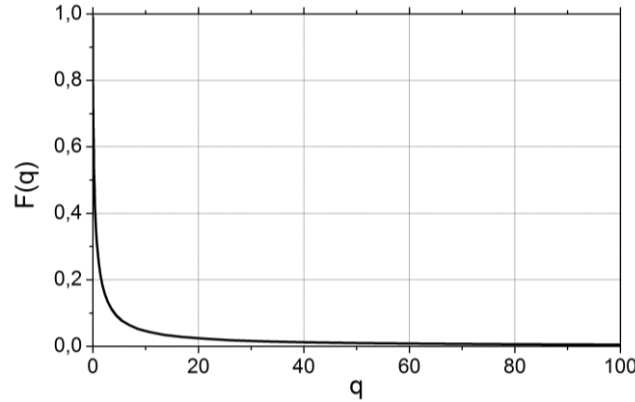


**Fig. 4.2** The function  $F(q)$  that defines the ratio of gas and film velocities

Fig. 4.2 implies that for small liquid film heights ( $q \gg 1$ )<sup>61</sup>,  $u_g - u_f \approx u_g$  and equation (4.6) reduces to

$$\tau_{yx}(x) = \frac{1}{2} c_{gf}^d \rho_g (u_g - 2\bar{u}(x, z))^2 \approx \frac{1}{2} c_{gf}^d \rho_g u_g^2 \quad (4.9)$$

Equation (4.9) is a common equation for the interfacial shear stress, following the assumption  $\bar{u} \ll u_g$  for all gas velocities. The function  $F(q)$  relates the validity of this assumption to the physical conditions of the system expressed by the parameter  $q$ .

*Verlaan* [64, p. 69] used the interfacial Fanning friction coefficient  $f_i$  given by *Wallis* [65]<sup>62</sup>, with twice the channel width minus the film thickness ( $D_h = 2(\delta_R - h_f)$ ) for the hydraulic diameter:

$$c_{gf}^d = f_i = 0.005 \left( 1 + 300 \frac{h_f}{D_h} \right) \quad (4.10)$$

<sup>61</sup> For example: in a water film of 1 mm thickness in air flow of 5 m/s at atmospheric conditions ( $q \approx 9.4$ ), the film surface velocity is below 5% of the air velocity.

<sup>62</sup> It is noted that *Wallis* [65] was investigating stratified and annular flow in a pipe and not film flow on plates. The interfacial Fanning friction factor was defined as a function of the film thickness relative to the pipe diameter:  $h_f/D$ . The supposed equivalence of the pipe diameter and the hydraulic diameter of non-cylindrical geometries in this formula has, to the knowledge of this author, not explicitly been established. However, for relatively thin liquid films at low and mid-range Reynolds numbers, the interfacial friction factor does not deviate much from the gas-wall friction factor and equation (4.10) is a good approximation (refer also to *Fore et al.* [16]).

Assuming a no slip condition, the average droplet flux  $\overline{G}_d$  can be written in terms of the separation efficiency  $\eta_s$  of the stage  $s$  in question:

$$\overline{G}_d = \frac{\dot{m}_d \eta_s}{HW} = \frac{\rho_d u_g \delta_R \alpha_{d,s} \eta_s}{W} \quad (4.11)$$

in which  $H$  represents the total height of the vane separator and  $\alpha_{d,s}$  represents the droplet volume fraction at the inlet of stage  $s$ . Considering film flow along a straight section of a vane separator (where most deposition occurs), the analysis for a flat plate described above is valid. Equations (4.9) and (4.11) are inserted into equation (4.5), leading to an alternative formulation of the limiting liquid film height at the end of the stage, in terms of vane separator specific parameters:

$$\frac{150}{\delta_R - h_{f,W}} h_{f,W}^3 + h_{f,W}^2 = \frac{800 \mu_f \delta_R \alpha_{d,s} \eta_s}{\rho_g u_g} \quad (4.12)$$

It is noted that equation (4.12) implicitly accounts for the stage width  $W$ , through the integration length included in the stage separation efficiency  $\eta_s$ . The liquid film height decreases with increasing gas velocities, due to the influence of the shear stress. This contradicts the statement made by *Azzopardi & Sanaullah* [3] that the liquid film height appeared insensitive to the gas velocity, but it concurs with *James et al.* [27, p. 475] who note the same (Table 3).

**Table 3 Limiting liquid film height (by numerical simulation) at various gas velocities for droplet distributions A and B with average droplet diameters of 25  $\mu\text{m}$  and 40  $\mu\text{m}$  respectively**

Bulk gas speed (m/s)	Liquid film height for inlet droplet size distribution ( $\mu\text{m}$ )	
	Distribution A	Distribution B
2.96	246	352
4.14	248	307
8.00	194	230

Fig. 4.3 depicts liquid film heights computed with the model from *James et al.* [27]<sup>63</sup>, with the application of the interfacial Fanning friction coefficient (resulting in equation (4.12)). The result is compared to the data reported by *Azzopardi & Sanaullah* [3, p. 3560]. The blue line depicts the result for the Nusselt model without shear gas flow, i.e. for the following solution of equation (4.4):

$$h_f(H) = \left( 3 \mu_f H G_d / \rho_f^2 g \right)^{\frac{1}{3}} \quad (4.13)$$

<sup>63</sup> For the applied parameters refer to *Azzopardi & Sanaullah* [3]. The gas velocity is 13.3 m/s.

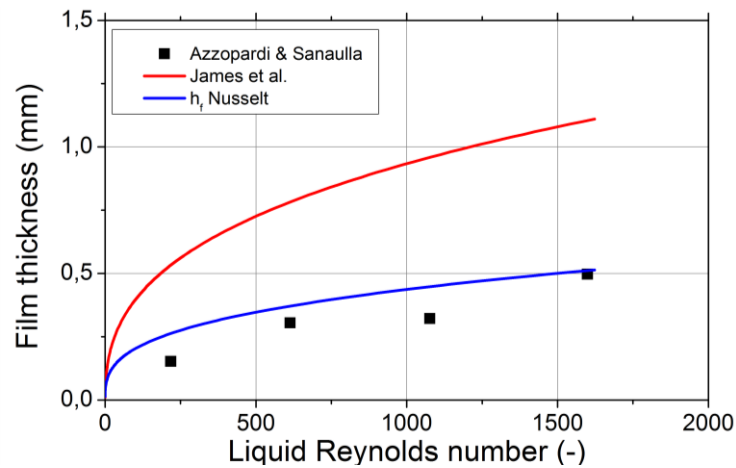


**Fig. 4.3** Liquid film thickness as a function of liquid Reynolds number

The liquid film height predicted by equation (4.12) is twice as high as the measured value and as the shearless Nusselt model. The model by *James et al.* [27] suggests that the vertical plate used by *Azzopardi & Sanaullah* [3] is high enough for the liquid film to reach its limiting value. Furthermore, Fig. 4.4 shows that a possible underestimation of the average film thickness by *Azzopardi & Sanaullah* [3], due to a still growing liquid film along the width of the plate, is highly unlikely.

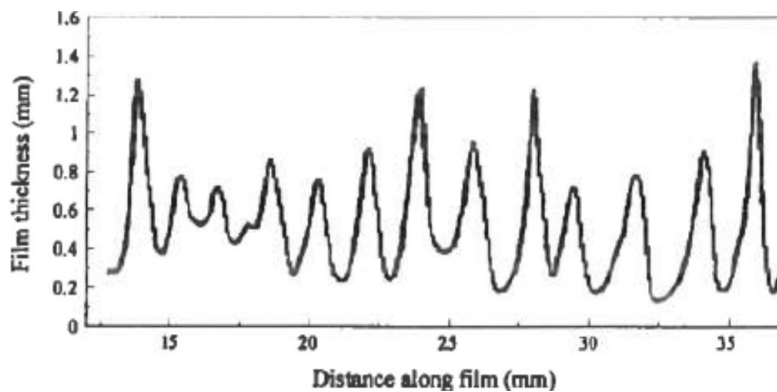


**Fig. 4.4** Liquid film thickness measured along the width of a vertical plate for  $Re_g = 39500$  and  $Re_l = 1600$ <sup>64</sup>

This implies that the liquid film height computed from equation (4.5) should correspond more closely to the experimental results reported by *Azzopardi & Sanaullah* [3]. One possible reason for the discrepancy could be an under-estimation of the interfacial shear stress. Fig. 4.4 shows that the film surface was quite rough and *Verlaan* [64, p. 70] reported that waves on the liquid film caused a higher gas/liquid interaction (as opposed to smooth film flow). *Kowalski* [37] suggests two different relations for the interfacial shear stress:

$$f_i = 0.96 Re_G^{-0.52} \quad (4.14)$$

$$f_i = 7.5 \cdot 10^{-5} (1 - \alpha_g)^{-0.25} Re_g^{-0.3} Re_l^{0.83} \quad (4.15)$$

<sup>64</sup> Reprinted from [3, p. 3560]. Copyright (2005), with permission from Elsevier.

These equations are valid for smooth and wavy stratified flow, respectively<sup>65</sup>. Although the transition regime defined by the same author suggests smooth film flow for the conditions of the experiment in Fig. 4.3, in view of the film roughness displayed by Fig. 4.4, it is relevant that equation (4.15) gives higher interfacial friction factors than equation (4.14). However, to reach the film thickness predicted by the Nusselt profile would require an interfacial friction factor of approximately 5 times the interfacial Fanning friction factor, which is unlikely to be the case.

The Nusselt profile defined by equation (4.13) apparently gives decent approximations of liquid film heights under transverse gas flows, corresponding to the recommendation by *Kolev* [32, p. 363]. This equation will therefore be applied for the purpose of estimating liquid film height at vane separator walls. The interfacial Fanning friction factor, as defined by equation (4.10), is applied for the computation of interfacial shear stress and liquid film velocity.

#### 4.1.2 Liquid film carry-over

Vane separators depend on some form of gravitational drainage of the liquid film. In vertically oriented vane separators, the liquid film that is formed on the vane walls will flow downward at a certain angle, until it reaches some type of collector at the bottom of the stage. The flow angle with which the liquid film moves along the vane walls is relevant for the drainage characteristics of the vane separator. Pick-off hooks of some type are a safe way to ensure drainage of the separated liquid within the same stage, but they increase pressure drop and perform poorly at higher flow velocities (refer to chapter 4.2.2). Perforations are also used to provide means to transport the liquid film into parallel drainage channels, that are separated from the main flow. These measures do not prevent carry-over of the liquid film into subsequent stages. The physical limits of carry-over under different conditions are investigated in the following sections.

##### 4.1.2.1 Limiting drainage

The ratio of the height-averaged velocities  $\bar{u}(x, z)$  and  $\bar{w}(x, z)$  defines the film flow angle  $\vartheta(x, z)$  with the horizontal axis, of the two-dimensional path along the wall, which a control volume in the liquid film will follow, under the influence of gravity<sup>66</sup>:

$$\frac{\bar{w}(x, z)}{\bar{u}(x, z)} = \tan \vartheta(x, z) = \frac{2\rho_f g h_f(x, z)}{3\tau_{yx}(x)} \quad (4.16)$$

Assuming the width of the wall is sufficient for the liquid film to be approximated by the Nusselt profile, equation (4.13) is inserted into equation (4.16), leading to an expression for the film flow angle in terms of the height  $z$  of the vane wall (as measured from the top):

<sup>65</sup> The latter equation is valid for  $22600 \leq Re_g \leq 430600$  and  $8800 \leq Re_l \leq 47800$ .

<sup>66</sup> The control volume describes the path a separated droplet would take, while submerged in the liquid film. It represents the angle with which the bulk of the liquid is expected to flow and does not necessarily correspond to the film flow angle, visible when observing the superficial flow of the liquid film (refer to [3, p. 3559]).

$$\tan \vartheta(z) = \frac{\frac{800}{\rho_g u_g^2} \left( \frac{\mu_f \rho_f g^2 z G_d}{9} \right)^{\frac{1}{3}}}{1 + 150 \left[ \delta_R \left( \rho_f^2 g / 3 \mu_f z G_d \right)^{\frac{1}{3}} - 1 \right]^{-1}} \quad (4.17)$$

Equation (4.17) is a decreasing function of  $z$ , corresponding to the fact that the liquid film height increases with  $z$  and the film flow angle increases with the liquid film height, due to the increasing influence of gravity. For a vane wall with height  $H$ , the maximum flow angle  $\vartheta_H$  thus exists at the bottom of the vane. Since  $\tan \vartheta(x, z)$  scales with  $h_f(x, z)$ , the liquid film will start on a horizontal path and gradually move downward (Fig. 4.5).

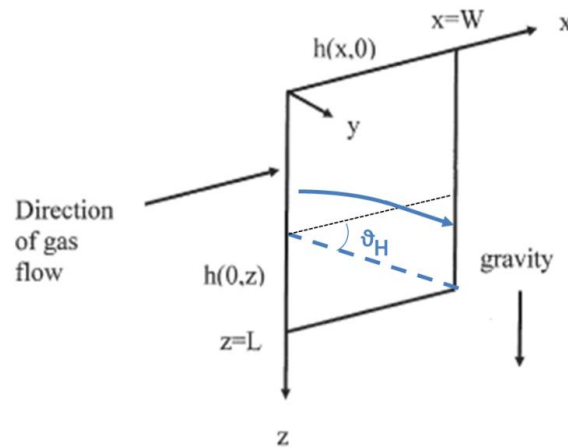


Fig. 4.5 Limiting angle for downward liquid film flow<sup>67</sup>

When an imaginary line is drawn from the bottom right corner of the plate upward with angle  $\vartheta_H$ , it represents a virtual border which can only be crossed by the liquid film from the left, but never from above. This implies that a limiting vertical distance  $Z$  exists, which no droplet, after being immersed into the liquid film, will travel beyond before reaching the edge of the plate at  $W$ . This vertical limit is given by

$$Z = W \tan \vartheta_H = \frac{\frac{800W}{\rho_g u_g^2} \left( \frac{\mu_f \rho_f g^2 z G_d}{9} \right)^{\frac{1}{3}}}{1 + 150 \left[ \delta_R \left( \rho_f^2 g / 3 \mu_f z G_d \right)^{\frac{1}{3}} - 1 \right]^{-1}} \quad (4.18)$$

For small values of  $\vartheta_H$ , the height is greater than this vertical limit ( $H > Z$ ) and the largest part of the separated droplets will not reach the bottom of the stage before they have reached its end<sup>68</sup>.

<sup>67</sup> Reproduced from [27, p. 473]. Copyright (2005), with permission from Elsevier.

<sup>68</sup> Because the film has an initial downward velocity of zero, part of the liquid film *below* this limit will also reach the right end of the stage. This fraction of droplets is neglected.

Making the approximation that the droplet deposition rate is uniformly constant, at maximum a portion  $Z/2H$  of the droplets can be drained down the bottom of the vane, within the same stage as they were separated. The result is that part of the liquid film will be carried over to the next separation stage. The lower limit of deposited mass flow, that cannot be gravitationally drained down the bottom of the stage, is in this case described by  $1 - Z/2H$ . For larger values of  $\mathcal{G}_H$ , for which  $H < Z$ , this limit is described by

$$\begin{aligned} 1 - Z/2H, & \quad Z < H \\ 1 - \left( Z - (Z - H)^2/Z \right) / 2H, & \quad Z > H \end{aligned} \quad (4.19)$$

#### 4.1.2.2 Limiting carry-over mass flow

The existence of a limiting liquid film height implies a limiting horizontal liquid film mass flow. According to equation (4.7), the liquid film velocity  $\bar{u}_{f,W}(z)$  at the edge of the wall is given by

$$\bar{u}_{f,W}(z) = u_g \left( \frac{1}{2} + \frac{1 - \sqrt{1 + C}}{C} \right) \quad (4.20)$$

in which the dimensionless parameter  $C$  is given by

$$C = \frac{u_g \rho_g h_{f,W}(z)}{\mu_f} \left( 0.01 + \frac{1.5}{\delta_R / h_{f,W}(z) - 1} \right) \quad (4.21)$$

The dimensionless parameter  $C$  is related to the ability of the gas flow to induce a certain velocity in the film and will be referred to as the *liquid film susceptibility coefficient*. If the Nusselt liquid film height is employed, equation (4.20) is a slowly increasing function of  $z$ . A conservative approximation of the maximum (height-averaged) liquid film velocity along the edge of the wall is thus given by  $\bar{u}_{f,W}(z) \approx \bar{u}_{f,W}(H)$ . The maximum liquid film mass flow that can propagate to the next stage, is then given by

$$\dot{m}_{f,W} = h_{f,W} H \rho_f \bar{u}_{f,W} = h_{f,W} H \rho_f u_g \left( \frac{1}{2} + \frac{1 - \sqrt{1 + C}}{C} \right) \quad (4.22)$$

Employing equation (4.11), the ratio of propagating liquid film mass flow over deposited mass flow is given by

$$\frac{\dot{m}_{f,W}}{\overline{G}_d H W} = \frac{h_{f,W}}{\delta_R \alpha_{d,s} \eta_s} \left( \frac{1}{2} + \frac{1 - \sqrt{1 + C}}{C} \right) \quad (4.23)$$

Equation (4.23) represents the upper limit of deposited mass flow that can be carried over to the subsequent stage.

### 4.1.2.3 Expected carry-over

The drainage and carry-over limits, defined by equations (4.19) and (4.23) respectively, are depicted as a function of the gas velocity in Fig. 4.6<sup>69</sup>. This figure also shows the film flow angle  $\vartheta_H$  (blue), prescribed by equation (4.17). At very low gas velocities, the liquid film flows straight downward and the transverse liquid film velocity is zero, leading to limits of 0% (0% of the separated liquid can be carried over to the next stage and 0% can *not* be gravitationally drained). At increasing gas velocity, the transverse liquid film velocity increases at constant liquid film height (the applied shearless Nusselt liquid film height is independent of gas velocity). At just below 5 m/s the transverse liquid film velocity has reached a value at which all deposited liquid can potentially be carried over to the next stage. As the film flow angle decreases with the gas velocity, the amount of deposited film that will not reach the bottom significantly increases. At 10 m/s about 90% of the deposited droplets can no longer be drained gravitationally and will be carried over to the next stage. This large value is a direct consequence of the relatively high and narrow plate (height x width = 130 x 23 mm). With no droplet re-entrainment considered, the actual amount of liquid being carried over to the next stage is expected to lie within these limits. With droplet re-entrainment considered, the effective amount of liquid building the film is reduced and its height will be smaller. This leads to a significant decrease of the carry-over limit (red line), to a reduction of the film flow angle (blue line) and thus to a slight increase of the drainage limit (green line). Droplet entrainment thus reduces the range in which the actual carry-over is expected to lie.

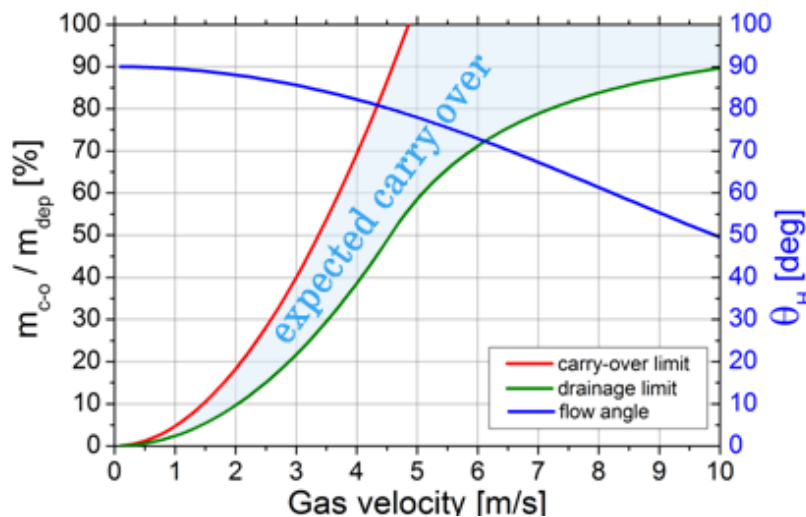


Fig. 4.6 Carry-over (red) and drainage limits (green) and film flow angle (blue) as a function of gas velocity

At around 4.5 m/s the film flow angle is such that the limiting vertical distance equals the height of the vane separator wall:  $Z = H$ . This point is schematically illustrated in Fig. 4.7. Beyond this film flow angle, the amount of liquid film that can no longer be gravitationally drained (the area of the wall above the dotted line in Fig. 4.7) increases much slower than below this film flow angle, leading to the decreasing growth rate of the drainage limit in Fig. 4.6.

<sup>69</sup> Physical and geometrical parameters are taken from *James et al.* [27]: water droplets in air at atmospheric pressure, an effective channel width of 10 mm, a channel height of 130 mm, a wall length of 23 mm and a constant liquid mass flow (for all gas velocities) of 0.01 kg/s. The same parameters are applied in the following sections as well.

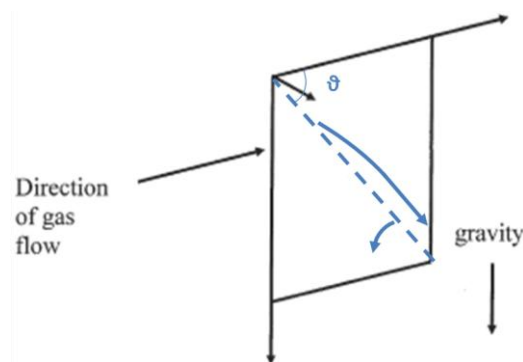


Fig. 4.7 Transition from  $Z < H$  to  $Z > H$ <sup>70</sup>

If the liquid film height is no longer given by the shearless Nusselt profile (equation (4.13)), it can be used to equate the carry-over and drainage limits (as given by equations (4.19) and (4.23)). The resulting liquid film height can be interpreted as the average liquid film height at the end of the wall section, needed to carry over the liquid that cannot be drained gravitationally. The result is depicted in Fig. 4.8. The film flow angle and the drainage limit are affected only slightly; the carry-over limit coincides with the drainage limit. The resulting liquid film height<sup>71</sup> is depicted in Fig. 4.8 on the right, along with the constant liquid film height from the shearless Nusselt profile. The variable liquid film height lies about 100  $\mu\text{m}$  below the shearless Nusselt value. Below 4.5 m/s (for which  $Z = H$ ), the liquid film is relatively constant, because here both limits are nearly linear in  $h_f$  (compare equations (4.16), (4.18) and (4.23)). Beyond this gas velocity, the liquid film height decreases, because here the drainage limit increases more slowly, thus reducing the necessity for a sustaining liquid film height.

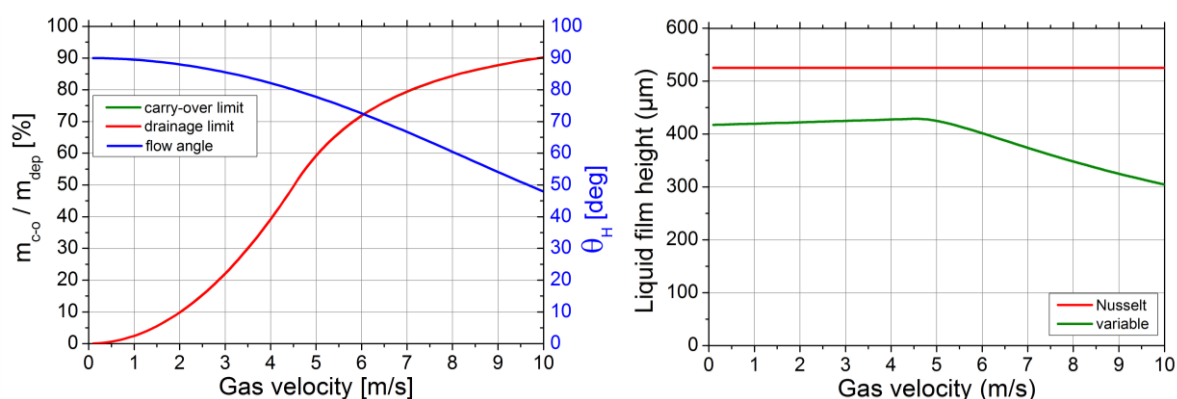


Fig. 4.8 Equalized carry-over and drainage limits and consequent flow angle (left) and corresponding liquid film height (right)

Adding all carried-over liquid from the previous stage to the droplet deposition in the next stage (not considering the height or the flow angle at which it enters), the amount of liquid film present in each stage can be deduced as well as the part of it that is drained. The result is depicted in Fig. 4.9, for a gas velocity of 5 m/s and a separation efficiency of 90%. As in Fig. 4.8, carry-over and drainage limits have been set equal to arrive at the depicted liquid film height. In the first stage, 90% of the droplets

<sup>70</sup> Reproduced from [27, p. 473]. Copyright (2005), with permission from Elsevier.

<sup>71</sup> Because there is no straightforward solution for the liquid film height from the equation of carry-over and drainage limits, the result has been reached numerically.

are deposited, but only 37% (of the inlet droplet mass) is being gravitationally drained. After the fourth stage, the droplet mass no longer contributes to the liquid mass deposition, but the liquid film being carried over from the last stages is with 23% still significant. Not accounting for carry-over, the total droplet separation efficiency after the fourth stage would be 99.99%. Even after seven stages, 3.9% of the initial liquid mass is being carried over and can be expected to become entrained in the air flow, corresponding to an effective separation efficiency of 96.1%. The liquid film height decreases from 410  $\mu\text{m}$  in the first to 157  $\mu\text{m}$  in the last stage. This result is conservative, because the liquid film carried over from the previous stages has been treated equivalent to a droplet deposition uniformly distributed over the stage wall area. In reality, most of the liquid film mass will have flowed down a significant distance as it enters the next stage, leading to a larger part of the carried over liquid film to be drained gravitationally in the subsequent stage(s) than is accounted for.

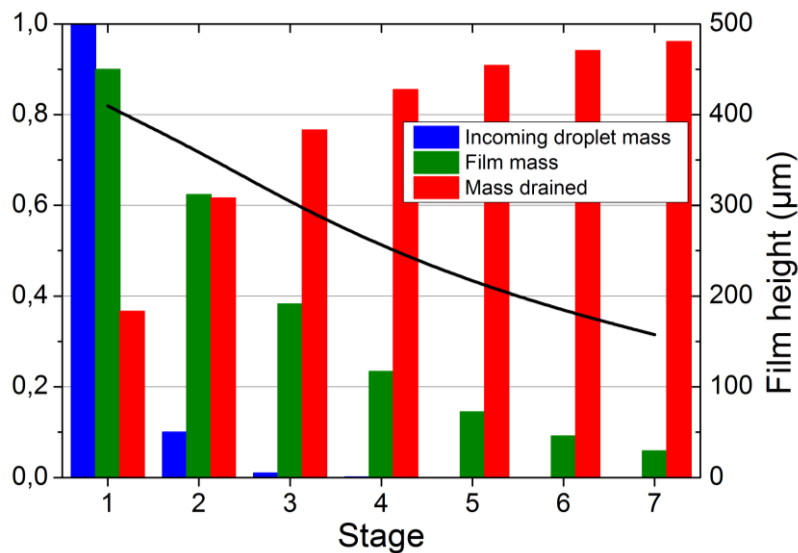


Fig. 4.9 Carry-over and drainage (green and red columns) and liquid film height (black line) through several stages of a vane separator for a gas velocity of 5 m/s

#### **Quintessence**

*Considering the limiting liquid film height, transverse velocity and flow angle, upper limits can be defined for the percentages of liquid film that can be gravitationally drained and that can potentially be carried over by the liquid film. Not regarding droplet re-entrainment, the actual amount of carry-over is expected to lie within these limits. By equating these limits, a liquid film height can be deduced, that lies below the shearless Nusselt film height and represents the average liquid film height for carry-over of the liquid film. This allows for an analysis of the liquid film mass being carried over through the consecutive stages of a vane separator.*

#### **4.1.2.4 Perforated wave plates**

Vane separators can be equipped with perforated walls in order to enhance the liquid drainage by separating the film from the air flow into separate drainage channels. *Kolev* [34, p. 369] assumes re-entrainment from the liquid film to occur at non-perforated wall sections only and decreases the

entrainment accordingly. One can also consider a reduction of the liquid film height by the amount of liquid drained from the flow channel by the perforations. Adjusting the droplet deposition rate by introducing the dimensionless film growth rate  $G_f = 1 - G_{perf}/G_d$ , which accounts for the perforation drainage, leads to the following shearless Nusselt profile for the liquid film height:

$$h_f(H) = \left( \frac{3\mu_f H G_f G_d}{\rho_f^2 g} \right)^{\frac{1}{3}} \quad (4.24)$$

Accounting for drainage through the perforations, of the part of the film which cannot be drained gravitationally (down the bottom of the wall), leads to the following adjustment of the drainage limits:

$$\begin{aligned} G_f (1 - Z/2H), & \quad Z < H \\ G_f \left( 1 - \left( Z - (Z - H)^2 / Z \right) / 2H \right), & \quad Z > H \end{aligned} \quad (4.25)$$

Assuming half of the deposited droplet mass to be drained through perforations ( $G_f = 50\%$ ), leads to an adjustment of the expected carry-over according to Fig. 4.10 (compare with Fig. 4.6).

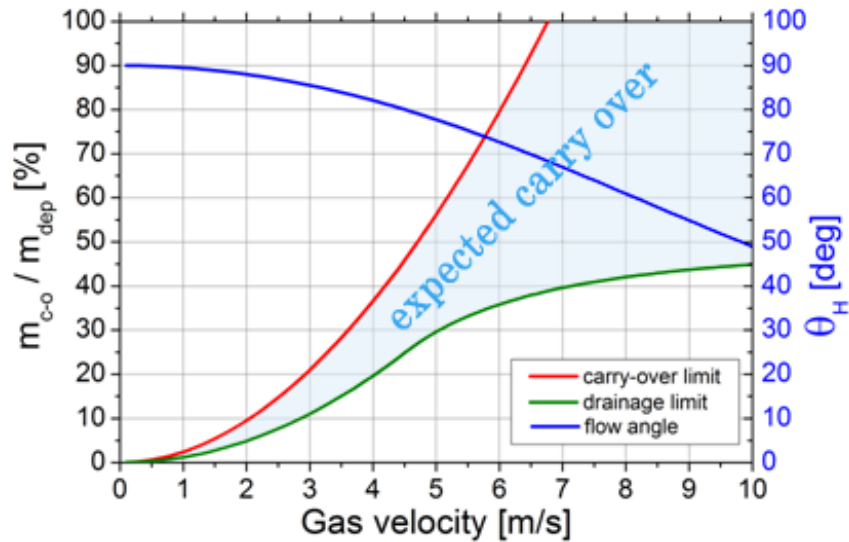


**Fig. 4.10** Carry-over (red) and drainage limits (green), and film flow angle (blue), accounting for 50% perforation drainage

The impact of perforated plates on the liquid carry-over through the consecutive stages ( $G_f = 50\%$ ) is depicted in Fig. 4.11. Contrary to Fig. 4.9, the total drainage is close to 100% after the fifth stage and the liquid film height is reduced to 43  $\mu\text{m}$  in the last stage.

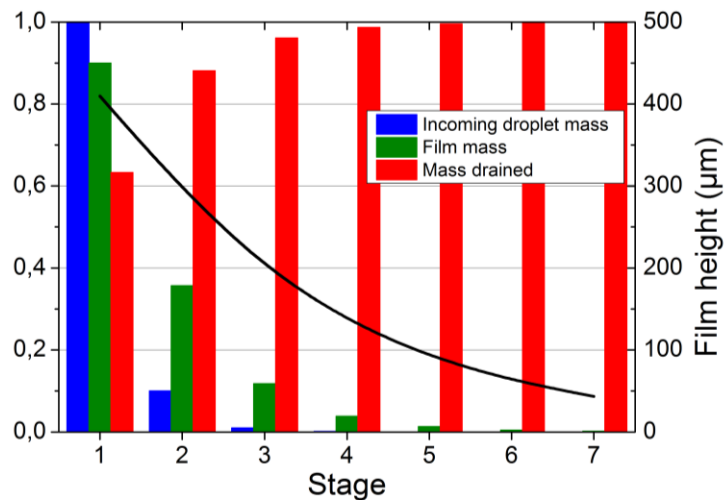


Fig. 4.11 Carry-over and drainage through several stages of a vane separator with 50% perforated plates

**Quintessence**

*Additional drainage channels, separated from the main air flow, but connected to the liquid film through perforations in the channel walls, can lead to a significant reduction of liquid film carry-over, as compared to non-perforated channels walls.*

**4.1.3 Film detachment**

Film detachment from convex corners is an important mechanism for entrainment in vane separators, leading to potentially large amounts of re-entrained liquid. Because most of the deposition occurs shortly before each convex bend, the potential for wave crest formation before the bend is small, while the liquid film height reaches its maximum as it flows around the corner. Fig. 4.12 depicts the deposition rate reported by *James et al.* [27, p. 473], showing the droplet deposition rate as a function of the position  $x$  along the width of the specific vane. In this geometry, no deposition at all occurs in the first one third of the vane width and most of it occurs on the very edge.

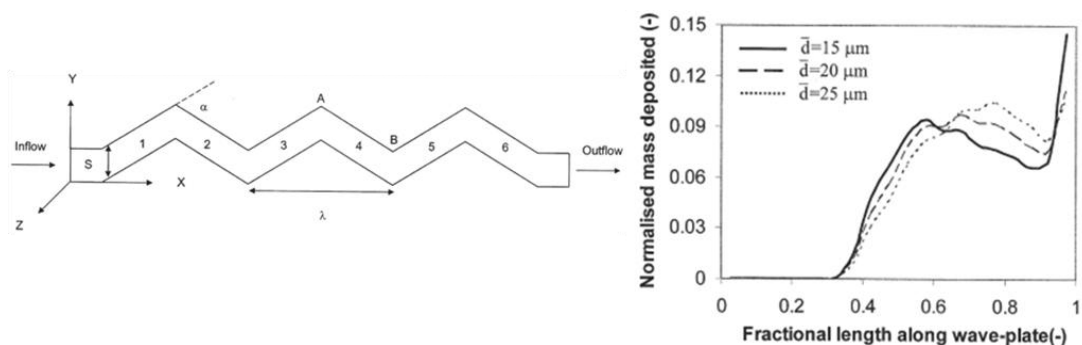


Fig. 4.12 Investigated separator geometry (left) and droplet deposition along the width of the straight wall sections of the wave-plate (right)<sup>72</sup>

<sup>72</sup> Reprinted from [27, p. 473]. Copyright (2005), with permission from Elsevier.

Azzopardi & Sanaullah [3] model re-entrainment by modifying the model by Owen & Ryley [51] for thin film flow around sharp corners, by decoupling gravity and interfacial shear. Balancing centrifugal and surface tension forces, they arrive at the following relation for which the compression force becomes negative, defining film separation from the inner wall [3, p. 3562]<sup>73</sup>:

$$\frac{\rho_f \tau_{yx}^2 h_f^3}{3\mu_f^2 R} = \frac{\sigma}{R + h_f} \quad (4.26)$$

in which  $\sigma$  is the surface tension,  $R$  is the inner radius of the bend and  $h_f$  is the film thickness. According to James *et al.* [27, p. 475], this model over-predicts the critical film thickness found in experiments and the discrepancy increases with bend radius  $R$ . A different model for the critical film thickness by Llory *et al.* [43], based on the displacement of the film surface as it flows around a corner, leads to a better agreement with the experimental values (Fig. 4.13) [27, p. 476]. The analysis by Llory *et al.* [43] does not lead to a simple equation for the critical film thickness, which is a direct advantage of the model by Azzopardi & Sanaullah [3].

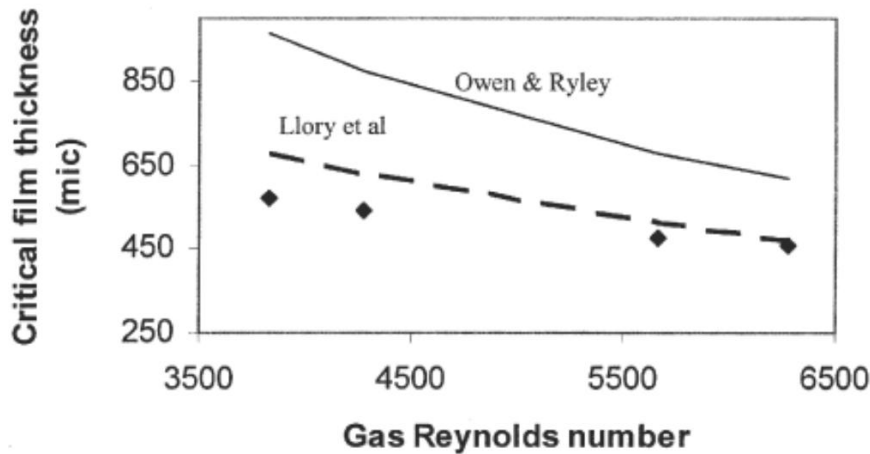


Fig. 4.13 Critical film thicknesses predicted by different authors as compared to experimental values<sup>74</sup>

Equation (4.26) can also be interpreted in terms of the critical gas velocity at which a liquid film will separate as it flows around a convex corner. Employing equations (4.9) and (4.10), the following relation for the critical gas velocity  $u_c$  can be obtained:

$$u_c = \frac{26.32}{h_f} \left[ \frac{\rho_f \rho_g^2}{\mu_f^2 R \sigma} \left( 1 + \frac{R}{h_f} + 300 \frac{R + h_f}{\delta_R - h_f} \left( 1 + \frac{75h_f}{\delta_R - h_f} \right) \right) \right]^{-4} \quad (4.27)$$

Applying the shearless Nusselt profile for the liquid film height and an inner bend radius of 1 cm, this leads to a critical gas velocity for liquid film separation of 6.7 m/s<sup>75</sup>, although the local gas velocity

<sup>73</sup> Azzopardi & Sanaullah [3] missed a power of 2 on their mean transverse velocity. This error has been corrected here.

<sup>74</sup> Reprinted from [27, p. 476]. Copyright (2005), with permission from Elsevier.

<sup>75</sup> For the physical and geometrical parameters refer to James *et al.* [27] (see also footnote 69).

across a sharp convex corner can significantly exceed the average gas velocity. This is visualized nicely by *James et al.* [27] (Fig. 4.14), who summarize that a high speed jet detaches from each convex corner, creating a region of very slow moving medium immediately behind it. In addition to promoting film detachment from the convex corners, extreme sharpness can cause recirculation zones behind each bend.

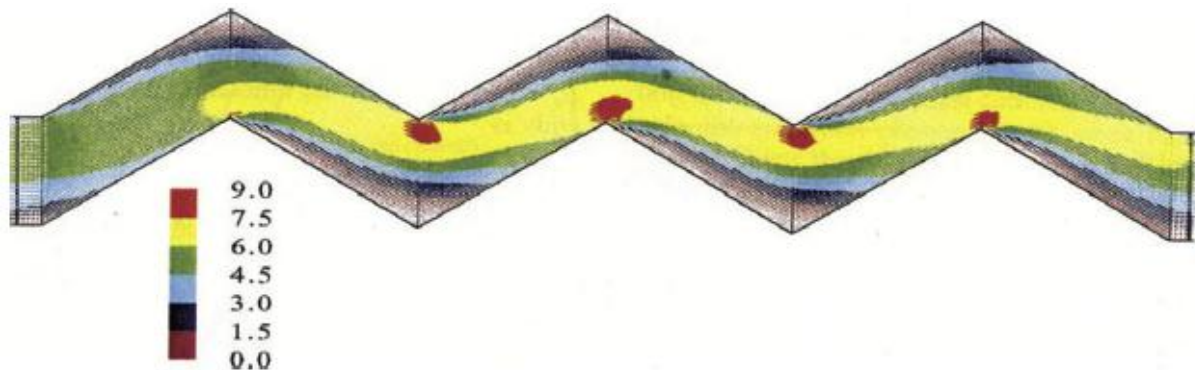


Fig. 4.14 Velocity field (in m/s) through a vane separator channel<sup>76</sup>

#### 4.1.4 Droplet re-entrainment

##### 4.1.4.1 Droplet generation mechanisms

Droplet generation mechanisms can be divided in four distinct classes: droplet-droplet interaction, droplet break-up, splashing of impinging droplets and re-entrainment of droplets from a liquid film<sup>77</sup>. Droplet-droplet interaction can cause both coalescence and fragmentation of droplets in the channel, but requires a certain minimum liquid volume fraction for the droplets to interact. For fine droplet separators, even for those operating in high pressure steam systems, droplet volume fractions seldom exceed 0.1%, from which it is safe to conclude that droplet-droplet interaction does not play a significant role in vane separators [28, p. 97]. Due to the small size of the droplets and the relatively low velocities in the vane separator channel, the same can be said for droplet break-up [28, p. 99]. Because the threshold for splashing of impinging droplets predicted by most models is too high for normal vane separator flow conditions, this mechanism also cannot account for the generation of new droplets inside the channel [28, pp. 105-106]. Re-entrainment from the liquid film thus appears to be the main mechanism for droplet generation.

##### 4.1.4.2 Film stability

Droplet re-entrainment, as occurring from wavy liquid film flow on flat surfaces, can be instigated in several ways. Different mechanisms for droplet re-entrainment are handsomely illustrated by *Ishii & Grolmes* [25, p. 312] (Fig. 4.15). If and when the different mechanisms occur, depends on factors mainly related to the turbulence of the liquid film and the consequent roughness of its surface. In Fig. 4.15 on the right, the authors show that below a certain liquid film Reynolds number, no re-entrainment is expected to occur, independent of gas velocity. For very large liquid film Reynolds numbers, the critical gas velocity is expected to be constant.

<sup>76</sup> Reprinted from [27, p. 470]. Copyright (2005), with permission from Elsevier.

<sup>77</sup> A nice visualization of droplet generation mechanisms is provided by *Josang* [28, p. 97].

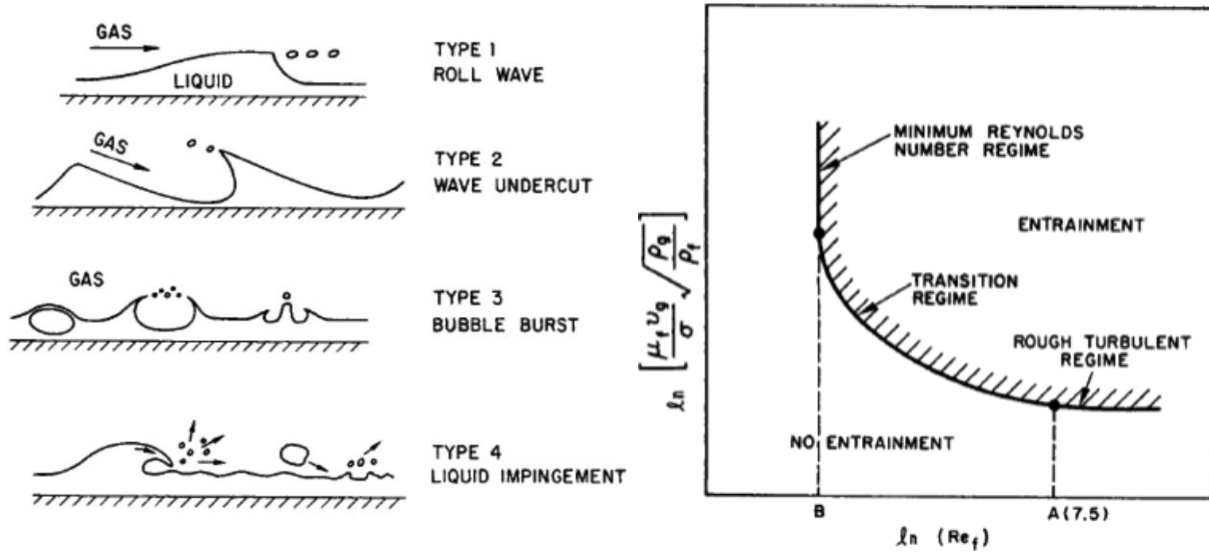


Fig. 4.15 Mechanisms for droplet re-entrainment (left) and logarithmic relationship between critical gas velocity and liquid film Reynolds number (right)<sup>78</sup>

Miles [47, p. 606] concludes that in order for a film, bounded below by a fixed wall and above by a free surface, having a linear velocity profile, to be stable (i.e. not to have enough energy to produce wave crests), it is sufficient that either a certain film Reynolds number or a certain film Weber number is not exceeded:

$$Re_f = \frac{\rho_f u_f h_f}{\mu_f} < 203 \quad (4.28)$$

$$We_f = \frac{\rho_f u_f^2 h_f}{\sigma} < 3 \quad (4.29)$$

where  $u_f$  is the liquid film velocity at the film surface and  $\sigma$  the surface tension. These limits are interpreted as the inception of re-entrainment in the over-entrained regime.

Nakao *et al.* [49, p. 428] apply a modified version of the Weber number and report a limiting value of 1.5 for the stability of a falling film:

$$We_f = \frac{\rho_g (u_g - u_f)^2 h_f}{\sigma} < 1.5 \quad (4.30)$$

According to Swanborn [61, p. 73] roll waves (type 1) are associated with thick liquid films and occur at  $Re_f = 4\rho_f \bar{u}_f h_f / \mu_f > 200$ , in which the liquid film velocity  $\bar{u}_f$  is defined as the superficial liquid film velocity. Wave undercutting (type 2) is associated with high gas velocities and thin films and, independent of the direction of the gravity vector, occurs at  $Re_f < 200$ .

<sup>78</sup> Reprinted from [25, p. 312]. Copyright (1975) M. Ishii and M.A. Grolmes. Permission granted.

*Ishii & Grolmes* [25, p. 315] report that for  $Re_f = 4\rho_f \bar{u}_f h_f / \mu_f < 160$  (horizontal or vertical upflow) or  $Re_f < 2$  (downflow), the critical Weber number for the inception of roll wave re-entrainment is 17, provided the gas velocity is sufficiently high. Below these limits, assuming a similarity with the process for break-up of falling droplets, these authors report the following inception point for re-entrainment by wave undercutting:

$$\frac{\bar{u}_g \mu_f}{\sigma} \sqrt{\frac{\rho_g}{\rho_f}} \geq \frac{1.5}{\sqrt{Re_f}} \Leftrightarrow \bar{u}_g \geq \frac{0.75\sigma}{\sqrt{\mu_f \rho_g \bar{u}_f h_f}} \quad (4.31)$$

*Ishii & Grolmes* [25, p. 316] also report a minimum film Reynolds number, below which no re-entrainment can occur, because the wall boundary layer is larger than the liquid film thickness:

$$Re_{f\min} = \frac{4\rho_f \bar{u}_f h_f}{\mu_f} = \left(\frac{10}{0.347}\right)^{\frac{3}{2}} \left(\frac{\rho_f}{\rho_g}\right)^{\frac{3}{4}} \left(\frac{\mu_g}{\mu_f}\right)^{\frac{3}{2}} \quad (4.32)$$

From this equation it follows that for air-water systems at atmospheric pressure the minimum liquid film Reynolds number is 56. Therefore, according to these authors wave undercutting is not a phenomenon to be expected for vertical down flow of air-water systems at atmospheric pressure. The same is valid for water-steam systems at any pressure.

*Wallis* [65, p. 317] claims that, as long as viscous forces can be ignored, which corresponds to a certain minimum liquid film height, the critical gas velocity is given by the equation

$$\frac{\bar{u}_g \mu_g}{\sigma} \sqrt{\frac{\rho_g}{\rho_f}} > 2.5 \cdot 10^{-4} \Leftrightarrow \bar{u}_g > 2.5 \cdot 10^{-4} \frac{\sigma}{\mu_g} \sqrt{\frac{\rho_f}{\rho_g}} \quad (4.33)$$

*Verlaan* [64, p. 72] reports a gas velocity for the transition from stable to unstable waves that is dependent on gravity and is valid for horizontal flow:

$$u_g = \sqrt{\frac{2\sqrt{\rho_f \sigma g}}{\rho_g}} \quad (4.34)$$

He also reports a minimum Reynolds number below which no entrainment is possible, irrespective of the gas velocity:

$$Re_{\min} = 38.7 \left(\frac{\rho_f}{\rho_g}\right)^{3/4} \left(\frac{\mu_g}{\mu_f}\right)^{3/2} \quad (4.35)$$

which for an air-water system leads to a minimum Reynolds number of 14.7 [64, p. 72].

The relation between the inception of re-entrainment and its rate of increase is illustrated by *Ishii & Grolmes* [25, p. 309] (Fig. 4.16). The rate of increase of entrainment is slow when the gas velocity for the inception of entrainment is only slightly exceeded, but there exists a certain gas velocity at which the rate of increase of re-entrainment suddenly increases and becomes linear with the gas velocity.

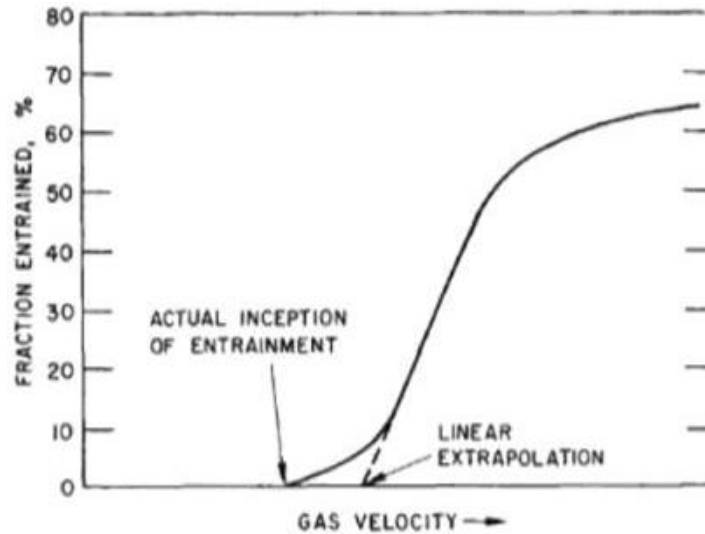


Fig. 4.16 The onset of entrainment<sup>79</sup>

From the equations listed above, critical superficial velocities can be deduced, at which the inception of re-entrainment is expected to occur (Table 4)<sup>80</sup>. These limits suggest that beyond these gas velocities, wave crests will form and a certain amount of droplets may be re-entrained. Considering that the listed liquid film heights correspond to the *maximum* film thickness under the given conditions, the table contains conservative values.

Table 4 Critical superficial film and gas velocities for water-air systems according to relations by different authors

Author(s)	Flow direction	Relation	Critical superficial velocity (m/s)	
			film	gas
Miles [47]	horizontal	$Re_f > 203$	0.20	
	horizontal	$We_f > 3$	0.34	
Nakao et al. [49]	down	$We_f > 1.5$		13.62 <sup>81</sup>
Swanborn [61]	all	$Re_f > 200$	0.10	
Ishii & Grolmes [25]	down	$Re_{f\min}$	0.0279	
Wallis [65]	horizontal	$u_g$		30.61
Verlaan [64]	horizontal	$u_g$		6.72

<sup>79</sup> Reprinted from [25, p. 309]. Copyright (1975) M. Ishii and M.A. Grolmes. Permission granted.

<sup>80</sup> For the physical and geometrical parameters refer to *James et al.* [27] (see also footnote 69).

<sup>81</sup> The film velocity has been neglected.

### 4.1.5 Experimental critical gas velocities

In the context of experimental data, the critical gas velocity is usually a more general limit for the onset of re-entrainment, comprising all mechanisms of re-entrainment. The velocity beyond which re-entrainment becomes significant, is an important aspect for the application of vane separators. The influence of the critical gas velocity on the separation efficiency of vane separators is schematically depicted by Verlaan [64, p. 30] (Fig. 4.17).

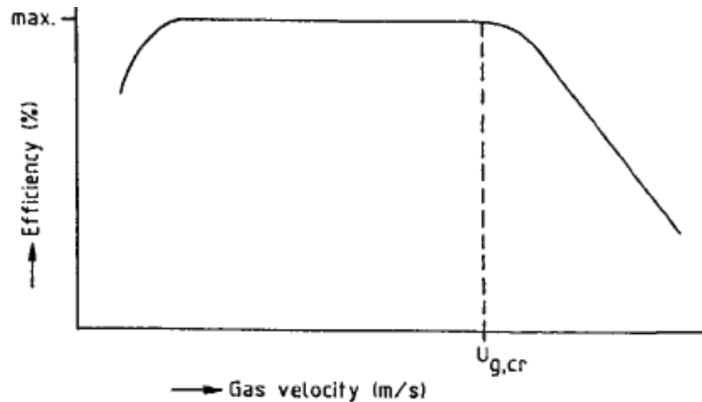


Fig. 4.17 Schematic representation of critical gas velocity<sup>82</sup>

Verlaan [64, pp. 62-63] reports experimental separation efficiencies for different homogeneous gas velocities and ascertains that the increase in separation efficiency becomes ever smaller with increasing gas velocity (Fig. 4.18). He concludes that for the investigated vane separator, at about 6 m/s a maximum separation efficiency is reached which cannot be increased further.

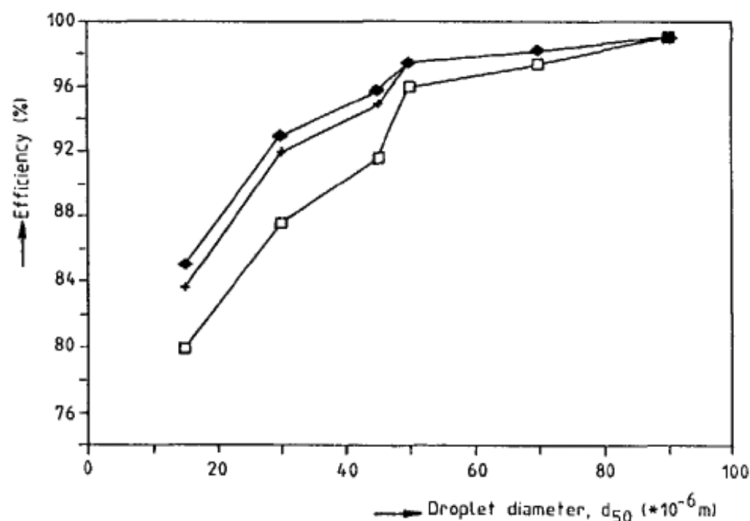


Fig. 4.18 Separation efficiency as a function of droplet size for homogeneous gas velocities of 4 m/s (squares), 6 m/s (stars) and 8 m/s (diamonds)<sup>83</sup>

<sup>82</sup> Reprinted from [64, p. 30]. Copyright (1991) C.C.J. Verlaan. Permission granted.

<sup>83</sup> Reprinted from [64, p. 63]. Copyright (1991) C.C.J. Verlaan. Permission granted.

The data in Fig. 4.18 is taken from vane separator type *a* in Fig. 4.19. Fig. 4.19 also depicts two other vane separator types, which show a sharp *decrease* in separation efficiency beyond gas velocities of 10 m/s and 8 m/s respectively. Decreasing channel widths and increasing bend angles appear to have a strong negative effect on the critical gas velocity.

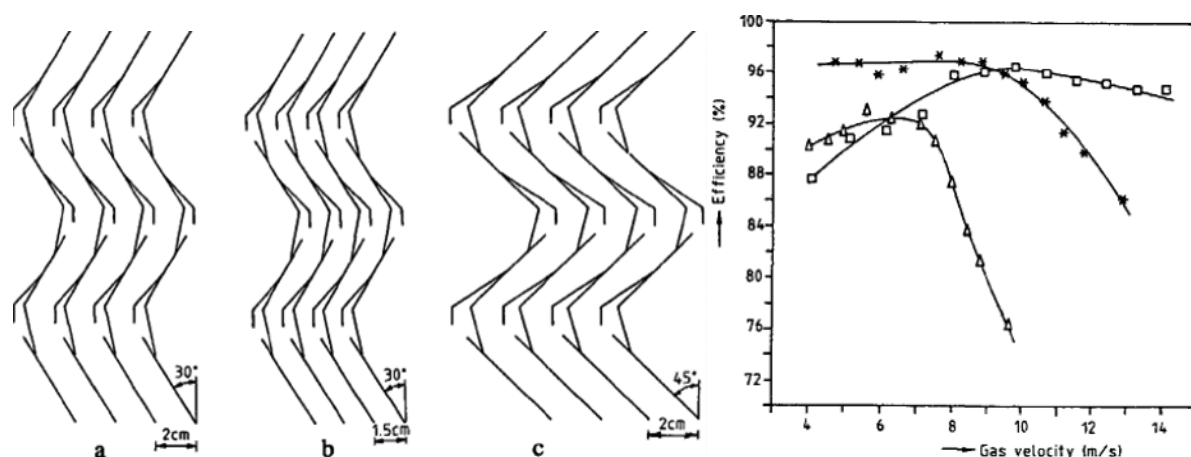


Fig. 4.19 Separation efficiency as a function of gas velocity for vane separator type a (squares), type b (stars) and type c (triangles)<sup>84</sup>

Swanborn [61, pp. 120-121] lists minimum homogeneous gas velocities (Table 5) at which film instabilities could be observed, for flow through a vane separator geometry of the type *Burgess Manning 625*<sup>85</sup>. He also records values of 8 m/s, although at increased liquid loading the instabilities occur at much lower homogeneous gas velocities.

Table 5 Film instabilities according to experiments by Swanborn [61, p. 121]

Liquid loading ( $\cdot 10^{-5}$ vol%)	Homogeneous gas velocity (m/s) for which first film instabilities occurred
2	8
5	8
10	4 - 4,5

Swanborn [61, p. 127+191] also discusses re-entrainment effects for three other vane separator geometries<sup>86</sup>, for which he plotted the experimental separation efficiency as a function of the superficial gas velocity. Although the interpolations between the measurement points appear to be a little arbitrary, a sharp decrease in measured separation efficiency was observed above a certain critical gas velocity. The critical gas velocity decreased with increasing liquid volume fraction<sup>87</sup>.

Kall [29, pp. 80-81] reports separation efficiencies at different liquid loadings and air velocities, from which it can be deduced that at high liquid mass flows the separation efficiency *decreases* with air velocity. For instance, at a liquid mass flow of 25 kg/m<sup>2</sup>s the reported separation efficiency is close to unity at an air velocity of 7.5 m/s, but is down by 12% at 12.5 m/s. The data from Kall [29, pp. 80-81]

<sup>84</sup> Reprinted from [64, p. 80]. Copyright (1991) C.C.J. Verlaan. Permission granted.

<sup>85</sup> A depiction of the specific vane separator model can be found in Swanborn [61, p. 125].

<sup>86</sup> The specific geometries are depicted in Swanborn [61, p. 125+191] and are referred to as *Burgess Manning 627*, *Euroform T271* and *Prototype*.

<sup>87</sup> Refer to figures 6.31 and 8.12 in Swanborn [61, p. 127+191].

suggests an inception of entrainment (for sufficiently high liquid mass flows) at a critical gas velocity of about 7 m/s. A similar result is reported by Sorokin et al. [60, p. 782]: for increasing liquid mass fractions the critical gas velocity decreases (Fig. 4.20). At an initial liquid loading of 10% the critical gas velocity is approximately 9 m/s.

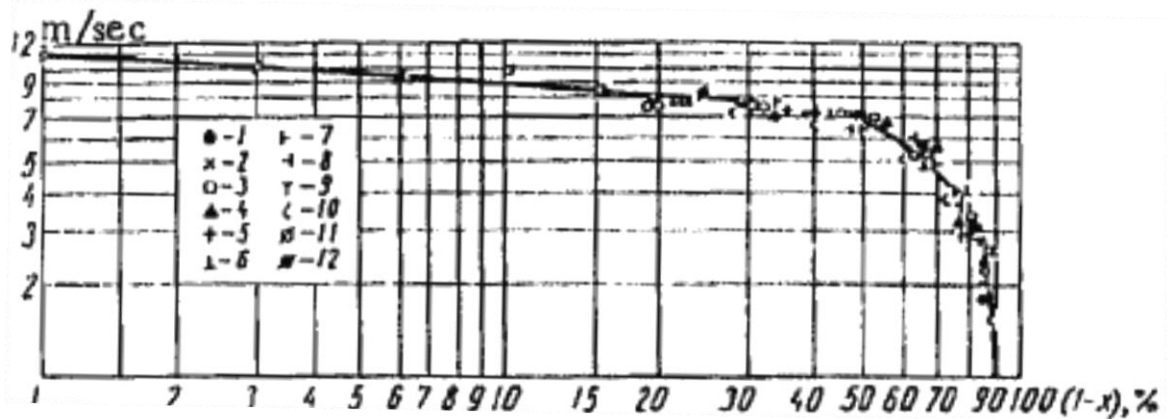


Fig. 4.20 Critical gas velocity as a function of liquid mass flow for 12 different vane separator types<sup>88</sup>

The critical gas velocity found by Calvert et al. [11, p. 973] is between 6 m/s and 7 m/s (Fig. 4.21). These authors also report values recorded by Houghton & Radford [23] and Bell & Strauss [5]. From the first set of data a similar critical gas velocity could be approximated. From the latter data set a smaller value of approximately 4 m/s can be deduced for the critical gas velocity, although according to Bell & Strauss the separation efficiency was 76% at the maximum experimental velocity of 16 ft/s (ca. 4,9 m/s) and the entrainment velocity was at this point not yet reached [5, p. 968].

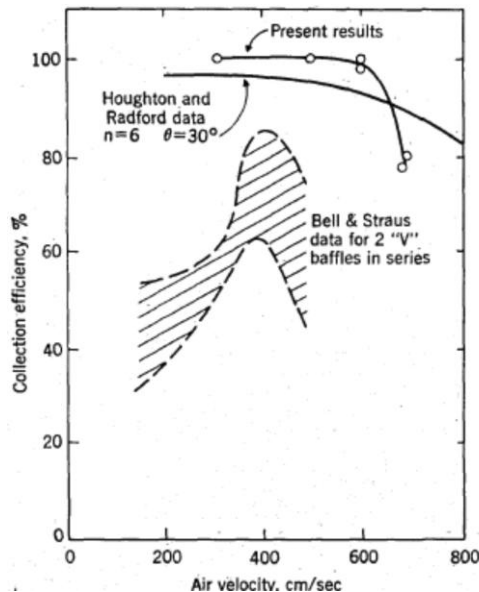


Fig. 4.21 Separation efficiency as a function of air velocity<sup>89</sup>

<sup>88</sup> Reprinted from [60, p. 782], with kind permission from Springer Science and Business Media.

<sup>89</sup> Reprinted from [11, p. 973]. Copyright (1974) Taylor & Francis. Permission granted.

*Leber* [40, p. 122] defines the inception of re-entrainment by a flooding point, which contains the flow energy and the density and surface tension of the liquid:

$$K_{FL} = \frac{\rho_g}{\rho_f \sigma_f} v^2 \quad (4.36)$$

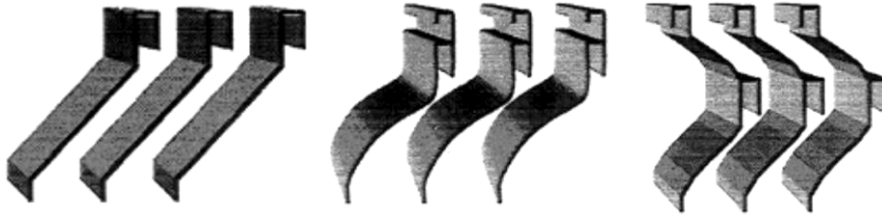


Fig. 4.22 Vane separator types Lam01, Le02 and KL01, as tested by *Leber* [40]<sup>90</sup>

The constant  $K_{FL}$  is representative for the influence of the particular vane separator geometry. For the vane separator geometries depicted in Fig. 4.22, *Leber* [40, p. 122] finds the experimental values for the flooding point constant and gas velocity listed in Table 6. The liquid volume fraction in the air-water experiments was varied between  $2 \cdot 10^{-6}$  and  $2 \cdot 10^{-5}$ , for which a dependence of the flooding point on the liquid volume fraction was not observed. This corresponds with the experiments by *Swanborn* [61], who only found an influence for volume fractions higher than  $2 \cdot 10^{-5}$  (refer to Table 5). The results in Table 6 are not discussed by *Leber* [40], but they imply that the critical gas velocity decreases with increasing channel width (disagreeing with *Verlaan* [64]; refer to Fig. 4.19) and that smoothly curved channel walls have a positive effect on the critical gas velocity, as opposed to segmented walls.

Table 6 Experimental values of flooding point constants and corresponding flooding velocities [40, p. 122]

Geometry	$K_{FL}$	Gas velocity [m/s]
Lam01 ( $\delta_R = 14$ mm)	0.40	5.0
Lam01 ( $\delta_R = 21$ mm)	0.35	4.5
Le02 ( $\delta_R = 15$ mm)	0.80	7.0
KL01 ( $\delta_R = 15$ mm)	0.60	6.0

*Azzopardi & Sanaulla* [3, p. 3560] investigated the disruption of a falling liquid film falling along a zigzag wave plate and recorded the conditions at which the disruption first occurred (Table 7). A clear trend between increasing liquid loading and decreasing critical gas velocity can again be discerned.

<sup>90</sup> Reprinted from [40, p. 120]. Permission granted.

Table 7 Conditions at inception of re-entrainment according to *Azzopardi & Sanoulla* [3, p. 3560]

Liquid mass flow rate [kg/s]	Film thickness [mm]	Gas velocity [m/s]	Weber number
0.014	0.57	5.0	4.7
0.012	0.54	5.6	5.9
0.008	0.47	7.4	10.4
0.0072	0.46	8.2	12.3

The same authors provide a stability-map for the stripping of droplets from the internal surfaces of a horizontal vane separator, in terms of liquid and gas Reynolds numbers (Fig. 4.23). Increasing liquid and/or gas Reynolds number can thus precipitate re-entrainment.

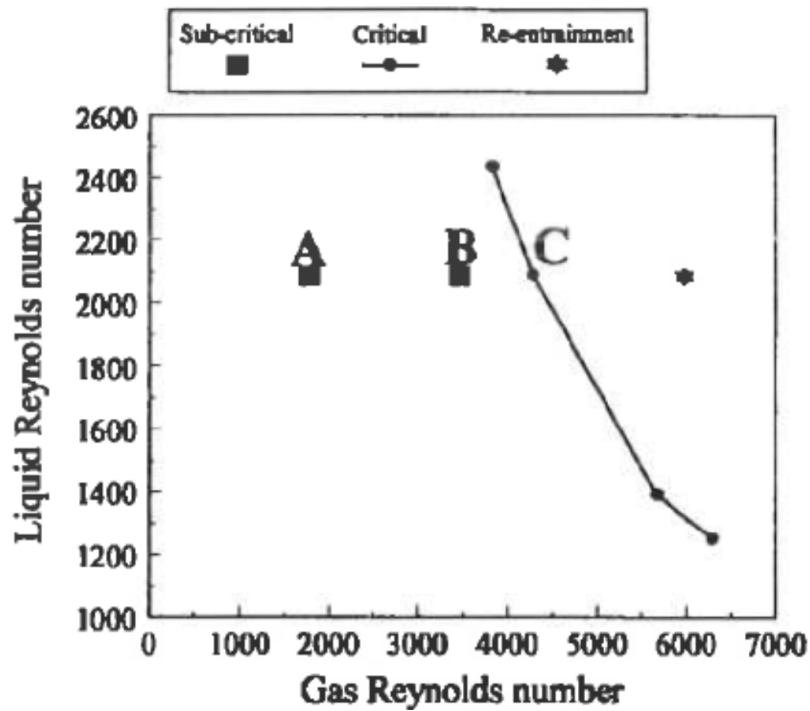


Fig. 4.23 Re-entrainment boundary for a horizontal vane separator<sup>91</sup>

#### Quintessence

*Values of 5-8 m/s are regularly reported for critical air velocities in vane separator channel flow, beyond which the separation efficiency significantly drops. Reported critical air velocities decrease with increased liquid loading.*

<sup>91</sup> Reprinted from [3, p. 3560]. Copyright (2002), with permission from Elsevier.

## 4.2 Pressure drop, pick-off hooks and drainage channels

### 4.2.1 Pressure drop

Pressure drop is an important aspect of vane separator performance, because it can affect the necessary pumping power to advance the flow or the thermal efficiency of power plants, thereby increasing electrical power demand or decreasing electrical power output. It is a relevant part of the vane separator design process, since most efficiency increasing measures have a negative impact on pressure drop.

The total coefficient of friction  $\zeta$  of a vane separator comprises the sum of the contributions of the straight sections of the channel (including in- and outlet), the curved sections and the half-angle curved sections at in- and outlet [34, p. 382]:

$$\zeta = \frac{2\Delta p}{\rho_g v_g^2} = \lambda_{fr} ((n+1)L + L_{in} + L_{out})/D_h + n(\zeta_b + \zeta_{b,loc}) + 2(\zeta_b/2 + \zeta_{in,loc}) \quad (4.37)$$

The Darcy friction factor  $\lambda_{fr}$  is given by

$$\lambda_{fr} = \begin{cases} 64/\text{Re}_m, & \text{Re}_m < 2300 \\ 0.03, & \text{Re}_m > 2300 \end{cases} \quad (4.38)$$

where  $\text{Re}_m \approx \rho_m v_1 D_h / \eta_1$  is the Reynolds number for the steam-droplet mixture. The contributions of the curved sections to the total friction consist of a regular part  $\zeta_b = \lambda_{fr} 2\varphi \bar{R} / D_h$ , which equals the friction of an equivalent straight section, and an additional local part  $\zeta_{loc}$ , which is given by the following formula<sup>92</sup>:

$$\zeta_{loc} = (k_f + 1)\zeta_{sim,loc} + A/\text{Re}_m \quad (4.39)$$

The similarity friction factor  $\zeta_{sim,loc}$  is equivalent to the friction factor  $\zeta_b$ , but with  $\lambda_{fr}$  computed for  $\text{Re}_m = 2 \cdot 10^5$ . The coefficients  $k_f$  and  $A$  depend on the angle of the curved section. The parameter  $k_f$  can be taken from tables provided by *Idelchik* [24], or, performing an exponential fit of the data, it can be calculated as

$$k_f = 18.66488 \exp(-2\varphi/23.38706) + 0.83656 \quad (4.40)$$

The parameter  $A$  is given as

$$A = 1600\varphi/\pi \quad (4.41)$$

<sup>92</sup> Valid for  $\text{Re} < 2000$ .

*Nakao et al.* [49] investigated the influence of the bend angle on the pressure drop of a vane separator. The authors tested three two-stage vane separator geometries, of 60° (geometry *b*), 90° (geometry *c*) and 120° bend angle (geometry *d*), and compared them to a standard four-stage vane separator of 60° bend angle (geometry *a*)<sup>93</sup>. The geometry and the experimental results are given in Fig. 4.24. The reduction from four to two stages has only a minor effect on the pressure drop; only the pressure drop for geometry *d* differs significantly from the standard four-stage vane separator. Because the inlet channel width and the wavelength were kept constant, the effective channel width reduces with increasing bend angle (see footnote 93). This contributes to the increased pressure loss, although this contribution is less pronounced in the presence of flow constrictions [10, p. 110]. The separation efficiency at 2 m/s was reported to increase with bend angle, being approximately equal for geometries *a* and *c* and lowest for geometry *b*.

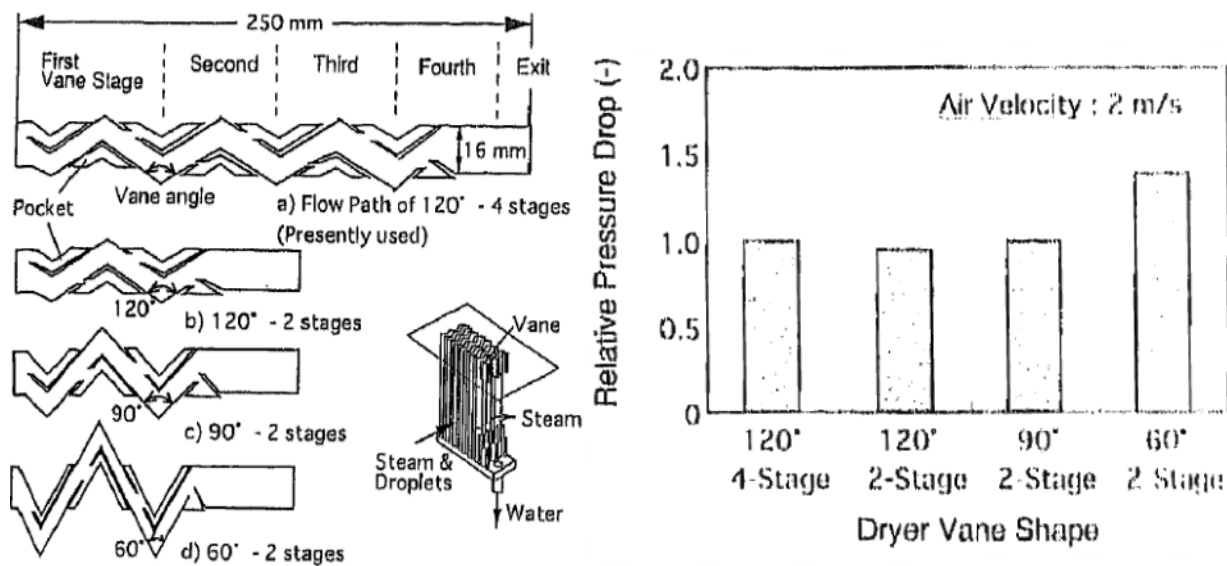


Fig. 4.24 Vane separator types investigated by *Nakao et al.* and their relative pressure drops<sup>94</sup>

*Galetti et al.* [17] used the *SST turbulence* model to predict pressure drops of two different geometries: a single channel narrow vane separator *a* and a broader three channel vane separator *b* (Fig. 4.25). Both are equipped with pick-off hooks. A comparison of the results for geometry *b* with experiments provides confidence in the CFD model. The results for geometry *a* are several times higher than those for geometry *b*, reflecting both the influence of the narrower channel and of the size of the pick-off hooks, relative to the channel width. Experimental data from *Ghetti* [19]<sup>95</sup> confirms that geometry *a* has a better separation efficiency in all cases, for velocities between 2 m/s and 5 m/s. The influence of the number of channels, if any, cannot be determined from this analysis.

<sup>93</sup> *Nakao et al.* [49] use a definition of the bend angle contrary to the one applied in this and many other papers (see Fig. 4.24). The reference here and any other references to bend angles are in accordance with the definition in chapter 3.

<sup>94</sup> Reprinted from [49, p. 430]. Copyright (1999) Taylor & Francis. Permission granted.

<sup>95</sup> As cited by *Galetti et al.* [17].

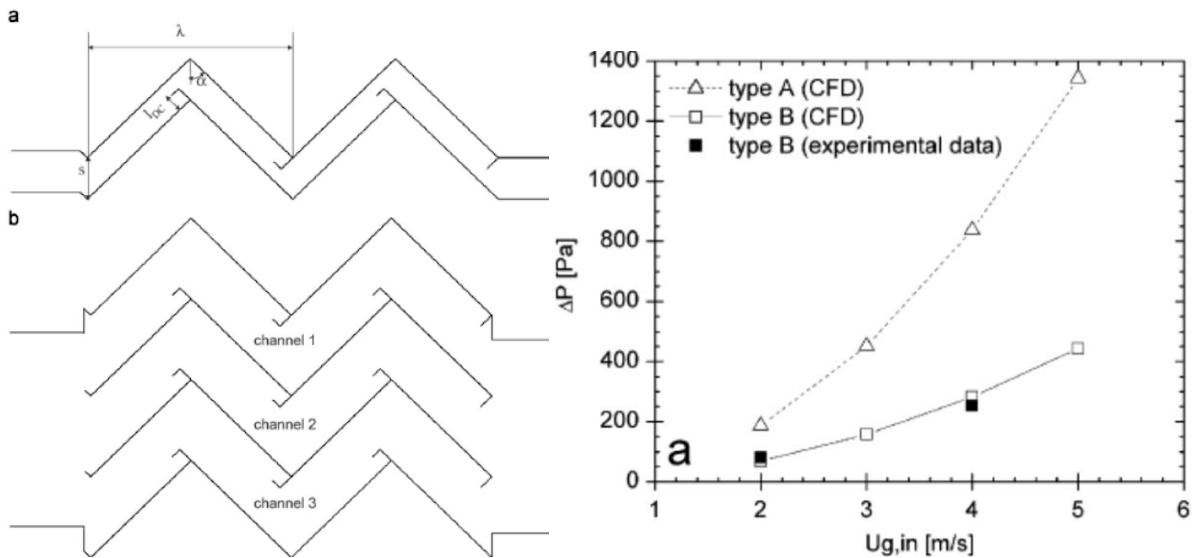


Fig. 4.25 Vane separator geometries *a* and *b* (left) and their pressure drops as a function of gas velocity (right)<sup>96</sup>

The CFD model applied by *Zamora & Kaiser* [72] showed quite remarkable results for the pressure loss coefficients as a function of Reynolds numbers, for different width-to-length ratios of different types of vane separator geometries (Fig. 4.26). The results for geometries *a* and *b* are more or less as expected, with higher coefficients for smaller width-to-length ratios. The results for geometries *c* and *d* can be called extraordinary, because, for high Reynolds numbers, the broader channels cause an increase of the pressure loss coefficient. The authors contributed this effect to the different flow patterns occurring in the channels. In general, for equal Reynolds numbers the pressure drop for the different geometries increased in the order *a-b-c-d*. The separation efficiency increased in the same order of geometries.

<sup>96</sup> Reprinted from [17, p. 5651]. Copyright (2008), with permission from Elsevier.

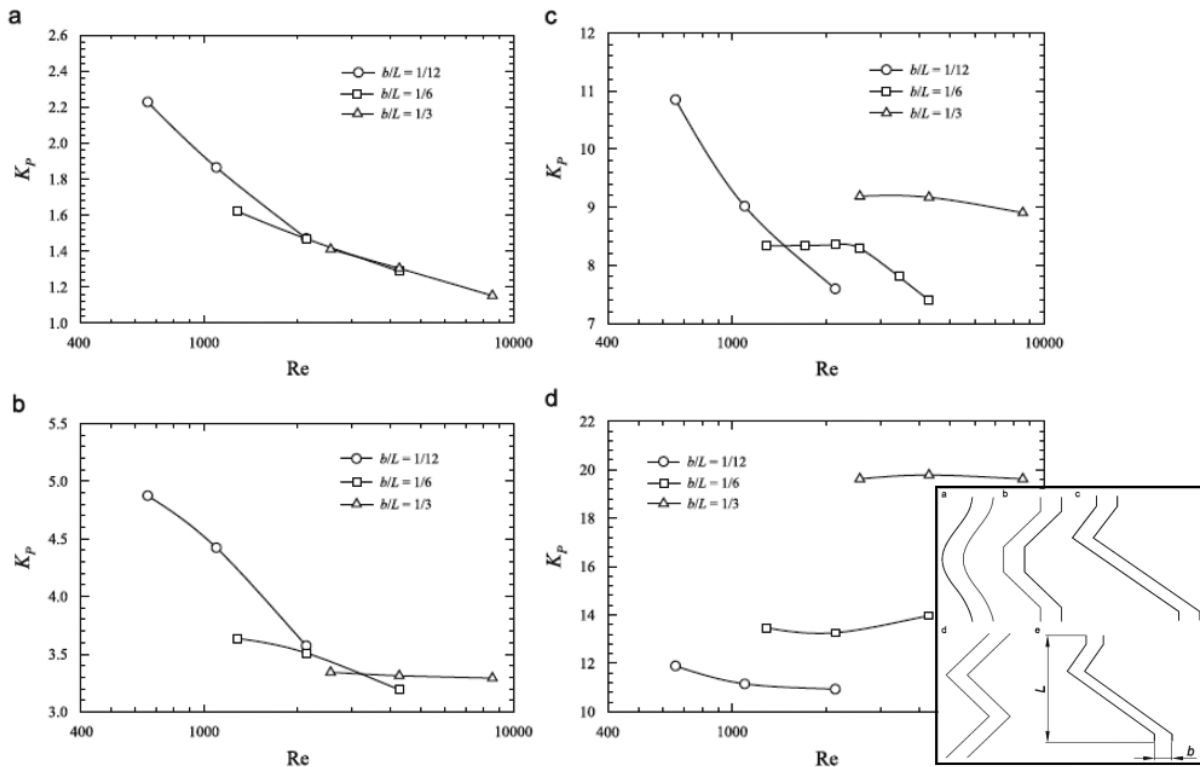


Fig. 4.26 Pressure loss coefficients as a function of the Reynolds number for different width-to-length ratios of vane separator types *a-d* (inlay)<sup>97</sup>

Verlaan [64, p. 145] experimentally determined pressure loss coefficients for vane separator geometries with channel widths of 2 cm (*c*) and 1.5 cm (*d*) (Fig. 4.27). He reported pressure loss coefficients for geometry *c* and *d* of 3.5 and 6.1 respectively. In contrast to the results by Zamora & Kaiser [72], these numbers clearly reflect a significant negative impact of narrowing channel width on pressure drop.

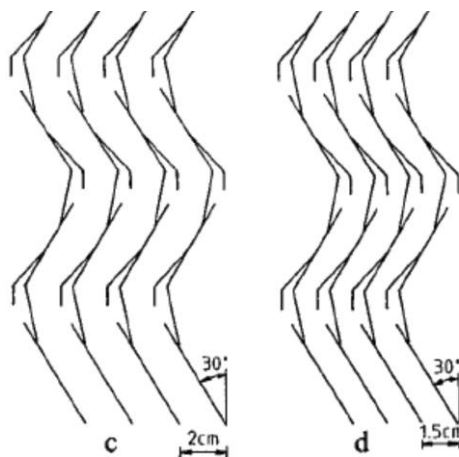


Fig. 4.27 Vane separator geometries of different channel width, as investigated by Verlaan [64]<sup>98</sup>

<sup>97</sup> Reprinted from [72, pp. 1234, 1240]. Copyright (2011), with permission from Elsevier.

<sup>98</sup> Reprinted from [64, p. 145]. Copyright (1991) C.C.J. Verlaan. Permission granted.

*Ushiki et al.* [63] investigated the relationship between pressure loss and the number of stages and the bend angle. They confirmed a proportional relationship between pressure loss and the number of stages  $n - 0.5$ , which accounts for the half bend of the inlet. The pressure loss coefficient was reported to increase by a factor of 2.3 for an increasing bend angle from  $30^\circ$  to  $45^\circ$ .

*Bürkholz* [10, p. 111] showed that wall roughness increases pressure drop, but can have a positive impact on separation efficiency, especially for relatively small droplets. He associated this effect with turbulent eddies destroying the potentially thick wall boundary layer that would otherwise block (small) droplets from reaching the wall. Depending on the droplet size distribution and the required separation efficiency, ultra-smooth channel walls are therefore not always the optimum choice.

*Wilkinson* [70] performed a series of pressure loss experiments on straight type vane separators. Anticipating  $n$  full bends of angle  $\varphi$ , inlet and outlet sections equaling half a bend each, and  $n + 1$  straight sections, he suggests the following pressure loss coefficient for the vane separator:

$$c_p = \frac{2\Delta p}{\rho_g v_g^2} = 2c_{pb}(\varphi/2) + nc_{pb}(\varphi) + (n+1)c_{ps} \quad (4.42)$$

The partial pressure loss coefficients  $c_{pb}$  and  $c_{ps}$ , for bends and straight sections respectively, that best represented experimental results, were given by

$$c_{pb} = \begin{cases} \left(0.0649 + \frac{22.3}{\sqrt{\text{Re}_w}}\right)\varphi, & \text{Re}_w < 7760 \\ 0.318\varphi, & \text{Re}_w > 7760 \end{cases}$$

$$c_{ps} = \frac{0.008325}{\left[\log(10.7/\text{Re}_w^{0.9})\right]^2} \frac{L}{\delta_R} \quad (4.43)$$

$$\text{Re}_w = \frac{\rho v \delta_R}{\mu}$$

These expressions are valid for  $30^\circ < \varphi < 120^\circ$ ,  $1200 < \text{Re}_w < 10^5$ ,  $0.088 < L/\delta_R < 0.6$  and  $5 < n < 9$ . According to these expressions, the partial pressure drop coefficients for bends and straight sections can be expected to increase linearly with bend angle and wall section length, respectively. Notwithstanding the Reynolds number, the latter coefficient is also inversely proportional to the channel width. For  $\text{Re}_w > 7760$ , the pressure loss contributions from the bends appear to be independent of anything but the bend angle. From equation (4.42), not accounting for straight sections, the total pressure loss coefficient is proportional to  $n - 0.5$ , corresponding to the results reported by *Ushiki et al.* [63].

#### 4.2.2 Pick-off hooks and drainage channels

Several authors (e.g. [42]) have reported on the positive influence of pick-off hooks on the separation efficiency. These pick-off hooks increase efficiency at lower gas velocities and reduce re-entrainment at higher liquid loading. However, they increase pressure drop and increase complexity and costs of

manufacturing. Also, they can be counterproductive at higher velocities, when stagnation pressure builds up in the drainage channels. Pick-off hooks drain the separated liquid film from the wall and to prevent carry-over to the next stage. If this is their sole purpose, the pick-off hooks will be designed to be least invasive in order to minimize additional pressure loss. An extreme example is the vane separator depicted in Fig. 4.28 on the left, in which the drainage channels are practically without pick-off hooks. If, in addition, the pick-off hooks are meant to actively increase the primary separation efficiency, they can be designed to be more invasive, as is the case in Fig. 4.28 on the right. The more invasive pick-off hooks will have a dominant impact on the total pressure loss.

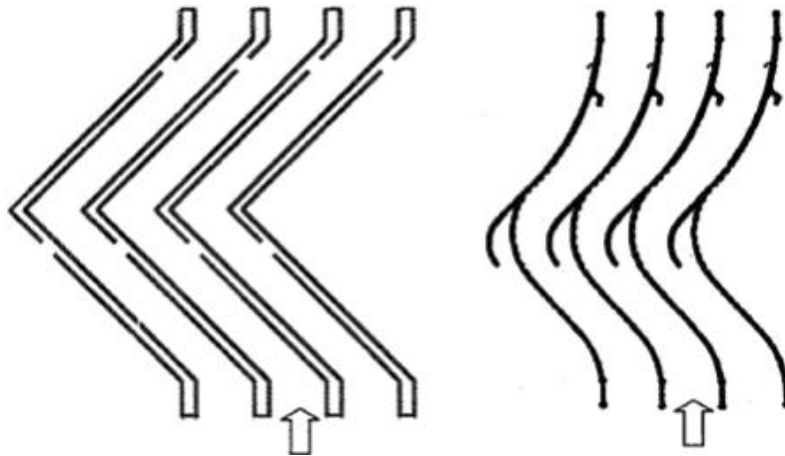


**Fig. 4.28** Vane separator channels with less invasive (Burgess Manning, left) and more invasive (Euroform, right) pick off hooks<sup>99</sup>

Examples of more and less invasive drainage channels are also given by *Kall* [29, pp. 70-74]. The open hooks situated in the channel not only drain the liquid film, but capture a certain amount of droplets out of the gas stream, thus contributing to the primary separation efficiency. The velocity increase through the narrower channel created by the pick-off hook also contributes to the separation efficiency (see also *Li et al.* [42, p. 497]). As the gas velocity increases, stagnation pressure builds up inside the pick off hook, forcing the flow around it. In the more extreme example discussed by *Kall* [29, pp. 70-71], the turbulent eddy inside the pick-off hook is strong enough to sweep the incoming liquid film back into the gas flow. In a less invasive drainage design the pick-off hook does not penetrate the flow channel, but the upstream inner wall bends inward into the drainage volume, creating a small opening for the liquid film to escape through. Nonetheless, as the drainage channel fills with liquid, the turbulent eddy inside the drainage channel can still cause part of the separated liquid to be swept back into the flow<sup>100</sup>. *Kall* [29, pp. 72-73] also reports that these less invasive drainage channels are only effective in the presence of a certain minimum liquid film thickness. In the latter stages of the vane separator, where the liquid mass content is much smaller, the adhesive forces in the much thinner discontinuous liquid film tend to block the openings into the drainage channels, obscuring them for the remaining separated liquid.

*Li et al.* [42] investigate the influence of pick-off hooks with two otherwise identical vane separators (Fig. 4.29). The pick-off hooks have a tremendous effect on the total pressure drop, being almost an order of magnitude higher than for the geometry *a*. Beyond 6 m/s the pressure drop starts to

<sup>99</sup> Reprinted from [40, p. 73]. Permission granted.

<sup>100</sup> Refer to *Kall* [29, pp. 71-72]. The specific geometry is depicted in 'Bild 25' [29, p. 72].

increase for the hookless geometry  $a$  as well. The pick-off hooks increase separation efficiency, although the contribution clearly decreases above approximately 4.5 m/s, at which point the separation efficiency itself even decreases for geometry  $b$ . The decrease of separation efficiency, also seen at 7.5 m/s for geometry  $a$ , is by the authors contributed to re-entrainment effects.

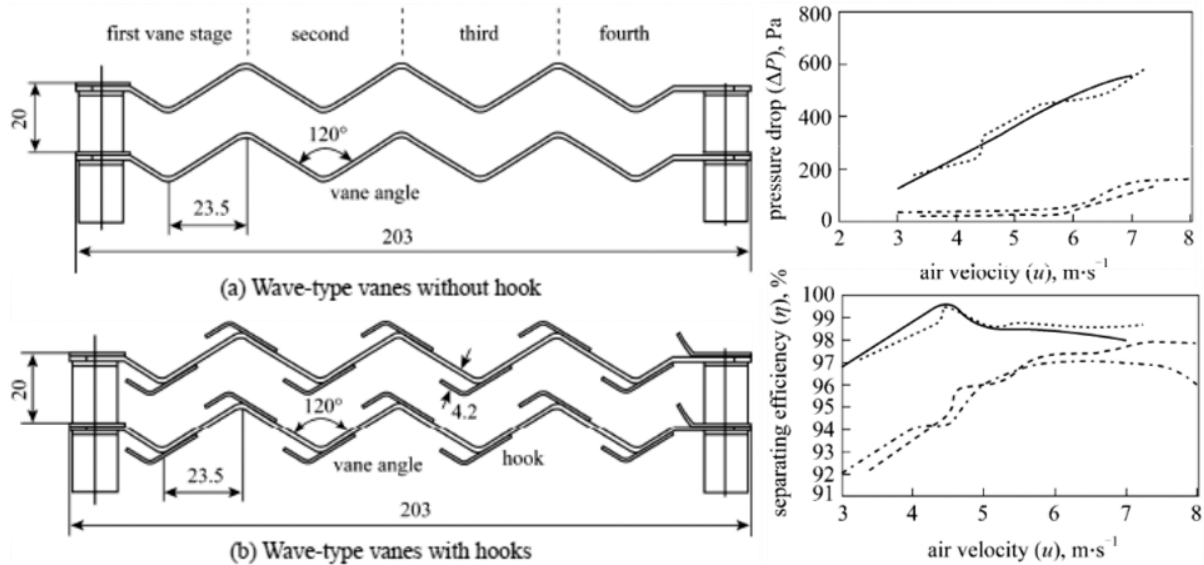


**Fig. 4.29 Vane separators with and without hooks and pressure drop and separation efficiency for computations with hooks (solid), experiments with hooks (dotted), computations without hooks (dots and stripes) and experiments without hooks (stripes)<sup>101</sup>**

The increasing ineffectiveness of the pick-off hooks is visualized by the CFD results of the velocity vector field for geometry  $b$ , recorded at 5 m/s (Fig. 4.30). The pockets almost completely block the incoming flow, possibly forcing part of the liquid separated in the previous bend back into the flow, as reported by *Kall* [29] and discussed in chapter 4.1.5.

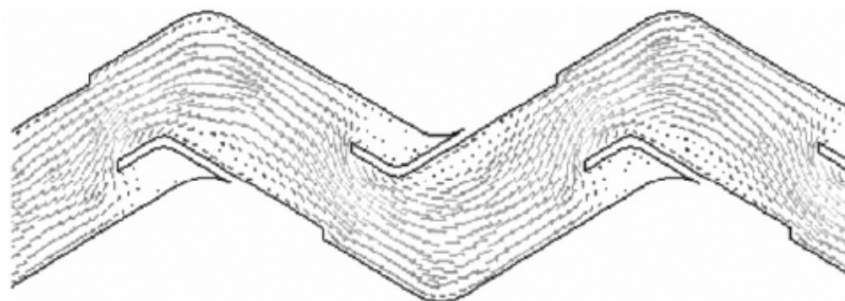


**Fig. 4.30 CFD results of velocity vector field recorded at 5 m/s<sup>102</sup>**

The examples discussed here, as well as the vane separator types displayed in chapter 1, typify that pick-off hooks and drainage channels come in many different shapes and forms. Their impact on the velocity profiles inside the channel differs largely, as does their impact on the total pressure drop,

<sup>101</sup> Reprinted from [42, p. 492]. Copyright (2007), with permission from Elsevier.

<sup>102</sup> Reprinted from [42, p. 496]. Copyright (2007), with permission from Elsevier.

both of which are dependent on Reynolds numbers. The same can be claimed for the effectiveness of the drainage and different possible re-entrainment phenomena related to the pick-off hooks and drainage channels. For these reasons, it is hard to quantify their impact on separation efficiency and pressure loss with the use of analytical or empirical formulas. From the discussion in this section and the work of *Nakao et al.* [49], *Galetti et al.* [17] and *Zamora & Kaiser* [72] in the previous section, one may in general assume the following:

1. At small gas velocities, the more invasive the pick-off hooks, the more they contribute both to separation efficiency and pressure drop. The larger the contribution to the separation efficiency at small gas velocities, the larger the pressure loss.
2. The contribution of pick-off hooks to the separation efficiency of smaller droplets decreases with increasing gas velocity, but their contribution to the pressure loss remains.

#### **Quintessence**

***Pick-off hooks increase both the pressure drop of the vane separator and the separation efficiency of smaller droplets. At small gas velocities these effects are roughly proportionate; both increase with increasing invasiveness of the hooks. With increasing gas velocity the contribution to the separation efficiency vanishes, but the contribution to the pressure drop remains.***

## 5 Model validation

### 5.1 Experiments from literature

#### 5.1.1 Single stage vane separators

##### 5.1.1.1 Bends

*Bürkholz* [10] performed experiments with droplets in air, for several types of vane separators. Among the tested vane separators are *B4* and *B6*, which serve well for a comparison with a single bend vane separator (Fig. 5.1). The radius of the bend central axis is in both cases 120 mm and the plates are spaced 5 mm respectively 10 mm apart.

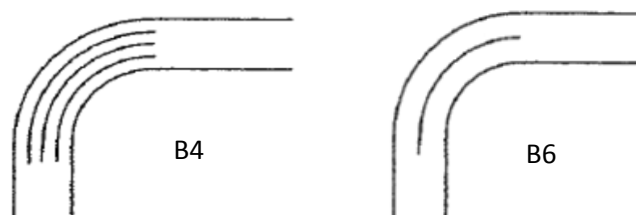
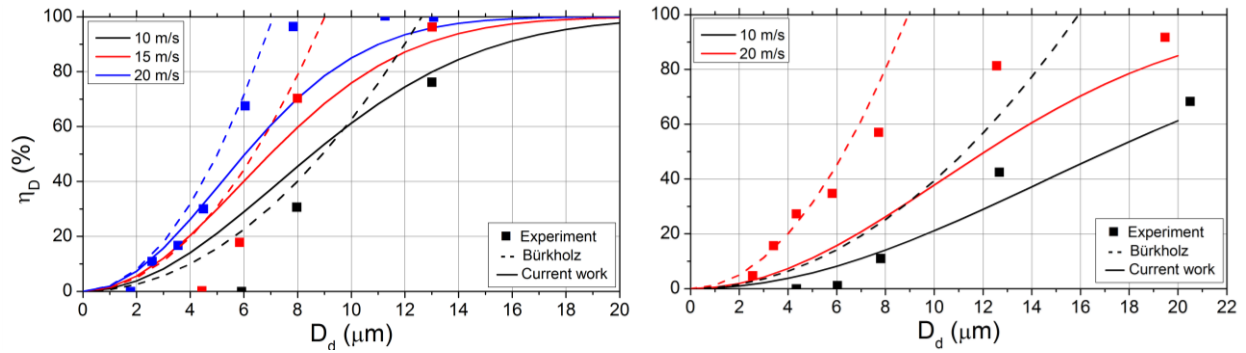


Fig. 5.1 Singular bend separators B4 and B6<sup>103</sup>

The measured separation efficiencies for these vane separators are depicted in Fig. 5.2, in which also the results predicted by *Bürkholz* [10] (equation (2.11)) and the results as predicted by the model discussed in this paper are depicted<sup>104</sup>. Both theoretical models predict higher-than-zero separation efficiencies for droplet diameters below 5  $\mu\text{m}$  at lower gas velocities, although in the experiments it takes a gas velocity of 20 m/s to separate them. In general, the separation efficiency appears to be more dependent on the gas velocity than predicted by the model, leading to an under-prediction of the separation efficiency at high gas velocities. It is unclear how the irrigation of the separated water was performed during the experiments, but entrainment effects and a corresponding decrease of the separation efficiency above a certain gas velocity, appear to be absent. The current model shows an improvement as compared to the model by *Bürkholz* [10]. It does not grow beyond unity above a certain droplet diameter and gives reasonable to good results in the upper efficiency region.

<sup>103</sup> Reprinted from [10, p. 105]. Copyright Wiley-VCH Verlag GmbH&Co. KGaA. Reproduced with permission.

<sup>104</sup> *Bürkholz* [10] recorded results for gas velocities up to 60 m/s. These extremely high gas velocities are omitted, because they are far beyond the range of application of the vane separators discussed in this paper.



**Fig. 5.2** Experimental and analytical separation efficiencies for different gas velocities in vane separator types *B4* (left) and *B6* (right), as tested by Bürkholz [10]

### 5.1.1.2 Straight sections

Leber [40, p. 119] investigated several single stage vane separators, one of which is of specific interest to the analytical work on the straight parts of vane separators (Fig. 5.3). The effective channel width is 8.5 mm and the effective length of the straight section is 70 mm<sup>105</sup>.

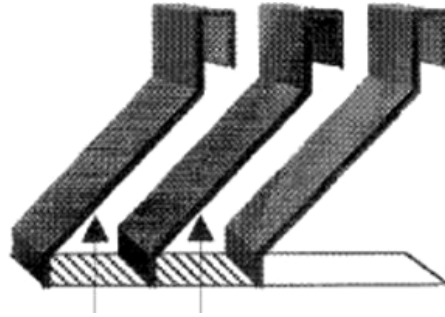


**Fig. 5.3** Single stage straight vane separator<sup>106</sup>

For a correct representation of the depicted geometry, equation (3.46) needs to be adjusted to account for the fact that the initial droplet velocity into the straight section is not defined by the centrifugal and drag forces in the bend, but by the inlet gas velocity vector. Assuming that the gas velocity inside the channel is uniform and defined by the continuity of mass under incompressible conditions, the radial droplet velocity is given by  $u_d(s) = v_{g,in} \sin \varphi \exp(-s \cos \varphi / \Delta \tau_{cd} v_{g,in})$ . This leads to the following separation efficiency for this geometry:

$$\eta_S = 1 - \frac{\dot{m}_{d,out}}{\dot{m}_{d,in}} \approx 1 - \exp\left(-\frac{\Delta \tau_{cd} v_{g,in} \tan(\varphi_{in})}{\delta_R} \left(1 - \exp\left(-\frac{L}{\Delta \tau_{cd} v_{g,in} / \cos(\varphi_{in})}\right)\right)\right) \quad (6.1)$$

The experimental separation efficiencies, measured by Leber [40] from 6 different gas velocities ranging from 0.5 - 5 m/s, are depicted in Fig. 5.4. The results from the analytical model are shown in the same figure. At low gas velocities the experimental data is under-predicted by the model. At velocities of 2 - 5 m/s the analytical model agrees well with the experimental data.

<sup>105</sup> To account for the plates in the specified plate spacing, a plate thickness of 2 mm was assumed.

<sup>106</sup> Reprinted from [40, p. 120]. Permission granted.

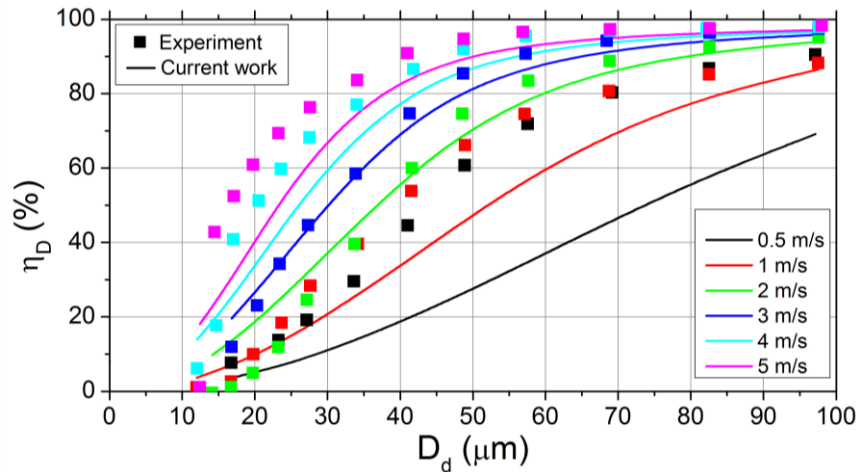


Fig. 5.4 Experimental and analytical separation efficiencies for a single stage straight vane separator tested by *Leber* [40]

## 5.1.2 Multiple stage vane separators

### 5.1.2.1 Bends

*Phillips & Deakin* [52] performed experiments on a wavy vane separator described as *Pack A*, consisting of eight stages<sup>107</sup> with a channel width of 8 mm. The total bend angle is 66.2° and each bend is equipped with pick-off hooks. The experimental results by *Phillips & Deakin* [52] and the model predictions are depicted in Fig. 5.5. The separation efficiencies are partly under-predicted by the model, which is to be expected, because the pick-off hooks are not accounted for by the model. The pick-off hooks separate part of the droplets by acting as an inertial wall. This effect is most significant at low gas velocities (refer to chapter 4.2.2). As a result, the model prediction of the experimental values improves with increasing gas velocities.

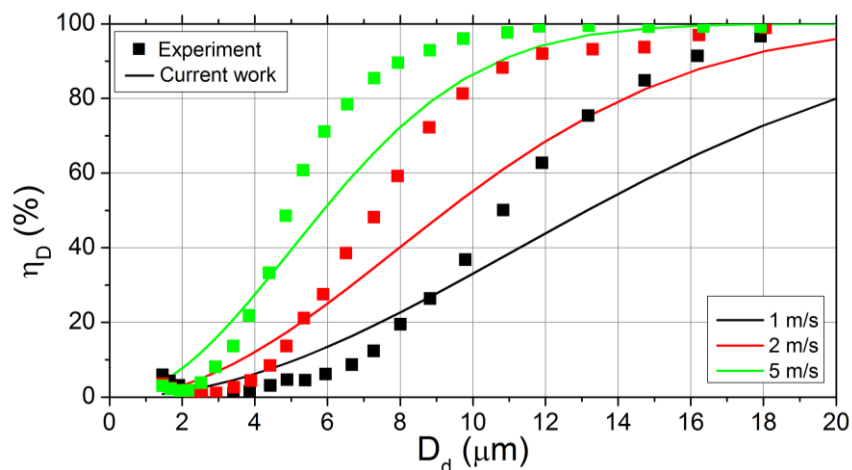


Fig. 5.5 Experimental and analytical separation efficiencies of the wavy vane separator *Pack A* tested by *Phillips & Deakin* [52]

<sup>107</sup> Only part of the geometry of *Pack A* is depicted by *Phillips & Deakin* [52]. The number of stages, according to the definition in chapter 3.6.4, is deduced from the depicted and reported number of stages of vane separator *pack B* [52] (refer to the following section).

### 5.1.2.2 Straight sections

Droplet separation efficiency in straight type vane separators is also well represented by the current model. The definition of each sharp corner as a bend with vanishing inner radius (Fig. 5.6 on the left), allows for a valid description of the relevant physics.

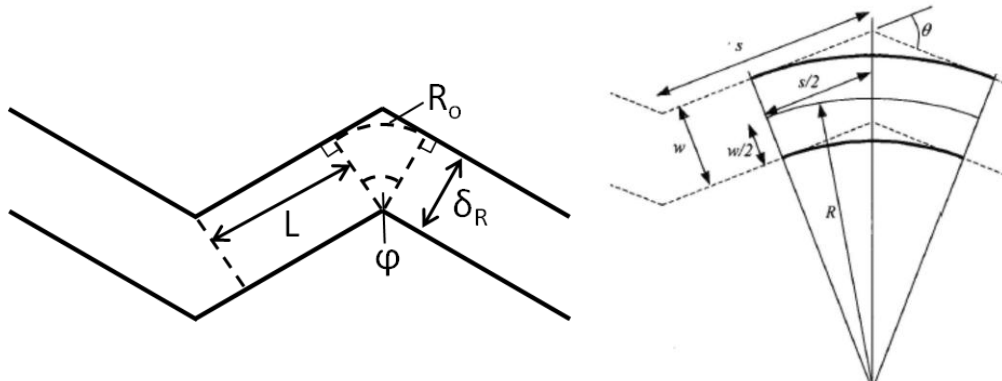


Fig. 5.6 Schematic representation of a straight type vane separator according to the current model (left) and according to Wilkinson [70] (right)<sup>108</sup>

Several authors, including Gillandt *et al.* [20], James *et al.* [27], Galletti *et al.* [17] and Verlaan [64], have reported recirculation zones with near zero flow velocities in the outer channel regions near these sharp corners (Fig. 5.7). Fine droplets passing by these regions are either captured and held or migrate on to be deposited on the nearby straight wall section. This appears to justify this geometrically simplified representation proposed here. Wilkinson [70] applied a very similar simplification, but instead of treating them separately, he integrated the straight sections into each bend by using a non-zero inner radius (Fig. 5.6 on the right).

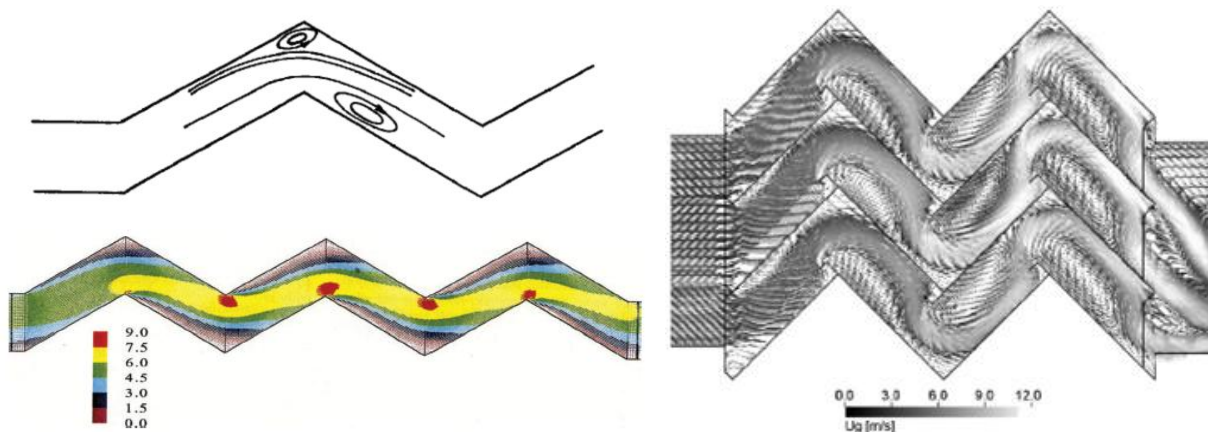


Fig. 5.7 Representation of circulation zones from visual inspections using smoke tracers (above left)<sup>109</sup> and velocity vectors from numerical simulations (below left)<sup>110</sup> and (right)<sup>111</sup>

<sup>108</sup> Reprinted from [70, p. 267].

<sup>109</sup> Reprinted from [64, p. 48]. Copyright (1991) C.C.J. Verlaan. Permission granted.

<sup>110</sup> Reprinted from [27, p. 470]. Copyright (2005), with permission from Elsevier.

<sup>111</sup> Reprinted from [17, p. 5644]. Copyright (2008), with permission from Elsevier.

*Bürkholz* [10] performed experiments with zigzag vane separators of the type depicted in Fig. 5.8, which are of the simplest form for straight type vane separators and consist of 3, 5, 9 or 13 stages (according to the definition in chapter 3.6.4). The channel width is 28 mm in all four geometries.

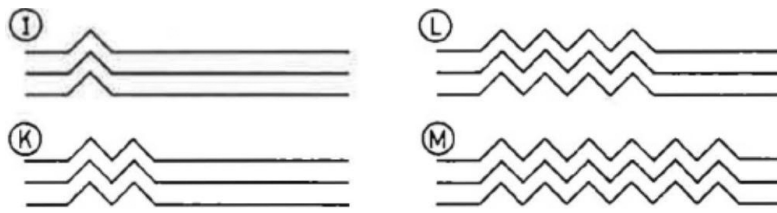


Fig. 5.8 Straight type vane separators<sup>112</sup>

*Bürkholz* [10, p. 113] describes the separation efficiency  $\eta$  of a vane separator with  $n$  stages as a function of the single stage separation efficiency  $\eta_s$  (as discussed in chapter 3.6.4):

$$\eta = 1 - (1 - \eta_s)^n \quad (6.2)$$

By fitting the single stage results and extrapolating with the use of equation (6.2), *Bürkholz* [10] achieves a very good agreement with experiments for larger numbers of stages. A decisive disadvantage of this procedure is that an initial set of data is needed to perform the extrapolation.

The experiments for the straight type vane separators were performed at a gas velocity of 10.3 m/s. The experimental separation efficiencies and the current model results are depicted in Fig. 5.9. The results as predicted by *Bürkholz* [10] (by inserting equation (2.11) into equation (6.2)) are also shown. Due to the increased number of stages, droplets below a diameter of 5  $\mu\text{m}$  can be separated. Each additional stage adds a smaller contribution to the separation efficiency. The separation efficiencies are in all cases under-predicted by the model. The results from the model by *Bürkholz* [10] are a little higher (refer also to Fig. 5.2), but, due to the even number of stages, the multiple stage results curve down after the single stage separation efficiency reaches values above unity.

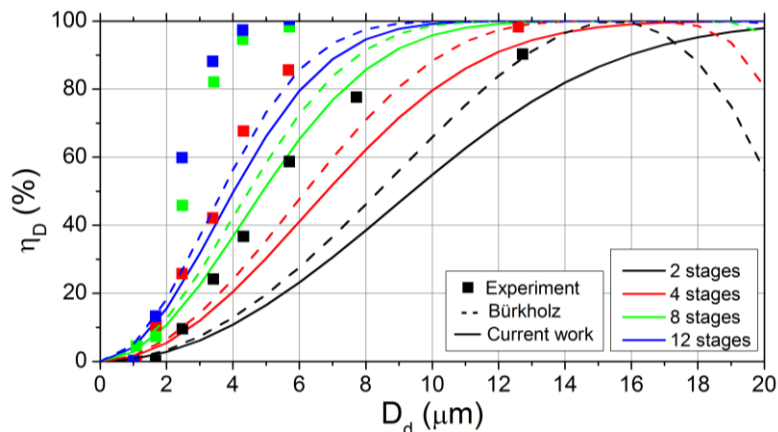
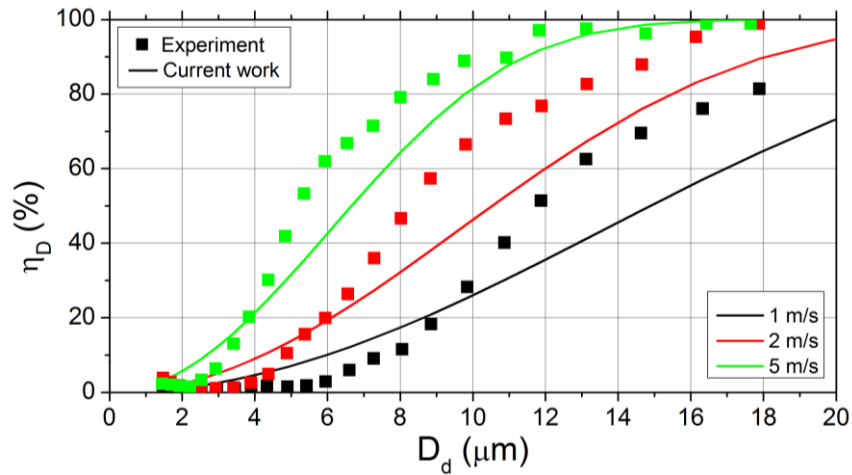


Fig. 5.9 Experimental and analytical separation efficiencies of straight type vane separators tested by *Bürkholz* [10]

<sup>112</sup> Reprinted from [10, p. 105]. Copyright Wiley-VCH Verlag GmbH & Co. KGaA. Reproduced with permission.

*Phillips & Deakin* [52] performed experiments on a straight type vane separator described as *Pack B*, consisting of seven stages with a channel width of 9 mm. The total bend angle is  $65^\circ$  and each bend is equipped with a pick-off hook. The experimental results and the model results are depicted in Fig. 5.10. The predicted values are in better agreement with the measurements, as compared with Fig. 5.5, although a similar impact of pick-off hooks can be discerned. As in Fig. 5.5, the predictions improve with increasing gas velocity.



**Fig. 5.10** Experimental and analytical separation efficiencies of the straight type vane separator *Pack B* tested by *Phillips & Deakin* [52]

The experimental data provided by *Verlaan* [64] was measured from a vane separator with a geometry resulting from cutting the corners of a pure zigzag vane separator (Fig. 5.11). The space that has thus become available is used to provide for drainage channels. The effective channel width is 17.3 mm, the number of channels does not affect the separation efficiency.

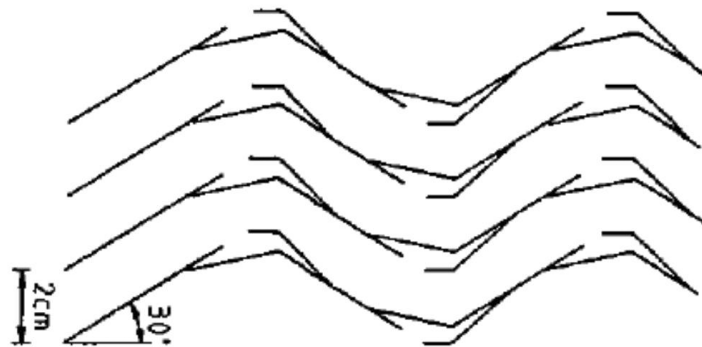


**Fig. 5.11** Straight type vane separator tested by *Verlaan* [64]<sup>113</sup>

The experimental results reported by *Verlaan* [64] and the prediction by the model are given in Fig. 5.12. Results for droplet diameters below  $15 \mu\text{m}$  are not provided, thus only a small part of the entire separation curve is captured. Contrary to most previous results, the experimental data shows less dependence on the droplet diameter than the model predicts, although it is possible that the experimental separation efficiency would also show a steep decline for droplets below  $15 \mu\text{m}$ .

<sup>113</sup> Reprinted from [64, p. 62]. Copyright (1991) C.C.J. Verlaan. Permission granted.

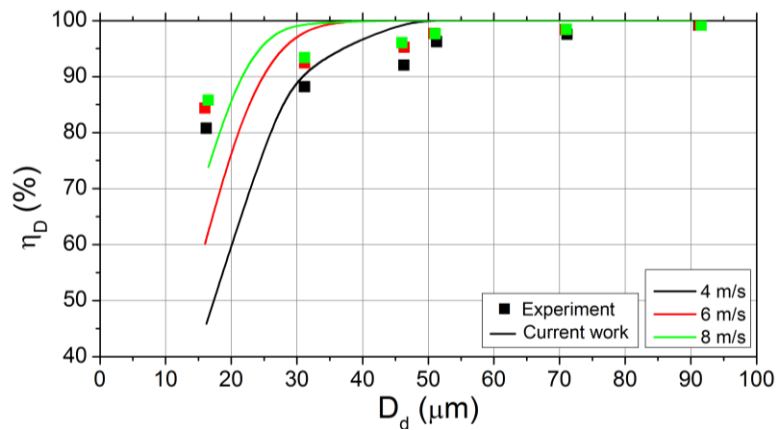


**Fig. 5.12** Experimental and analytical separation efficiencies of a straight type vane separator tested by *Verlaan* [64]

### 5.1.3 Discussion

From the experiments presented before, some common points can be observed. Although the number of cases investigated is too small to make a strong statement, the assumption that straight type geometries without bends are represented well by the model, appears to be valid. In nearly all cases, the analytical model showed the best results for gas velocities at around 5 m/s, while under-predicting separation efficiencies for lower gas velocities. This is expected to be related to the more significant impact of pick-off hooks for lower gas velocities. Due mainly to these pick-off hooks, many vane separator geometries are more complex than can be represented in the analytical model. The uncertainty incurred from such a simplification of the geometry is very difficult to quantify.

The separation efficiency appears to be more strongly dependent on the droplet size than predicted by the model, which can partly be explained by assuming non-uniform velocity profiles. Referring to the discussion in chapter 3.4.2, the separation efficiency is expected to decrease more strongly below a certain *escape diameter*. Fig. 3.21 showed that even for very small wall boundary regions, the escape diameter can be significant. Looking at the results from *Bürkholz* [10] for the *B4* and *B6* geometries, assuming a wall boundary region of 10  $\mu\text{m}$  would in both cases lead to escape diameters of 6  $\mu\text{m}$  and 4  $\mu\text{m}$  for gas velocities of 10 m/s and 20 m/s, respectively (Fig. 5.13). This assumption leads to a better representation of the separation efficiency for small droplets, at least for gas velocities below 20 m/s.

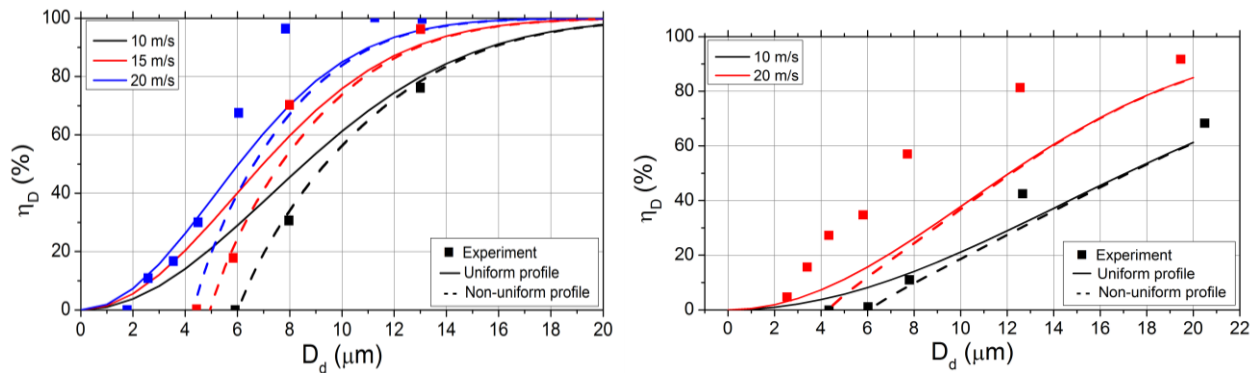


**Fig. 5.13** Experimental (squares, *Bürkholz* [10]) and analytical separation efficiencies for different velocities assuming uniform (solid) and non-uniform flow (dashed) in vane separator types *B4* (left) and *B6* (right)

## 5.2 Comparison with CFD results

The numerical work performed by *Wang & James* ([67], [68]) was discussed in chapter 2.2; the governing flow equations for the droplet path are equivalent to the equations presented in chapter 3.1.2.2. In both articles the experimental work reported by *Phillips & Deakin* [52] concerning the *Pack A* vane separator was used for comparison with the numerical models. *Zamora & Kaiser* [72] use the basic turbulence functions available in the applied CFD package, which constitutes a Constant EIM approach. They analyze the impact of the eddy lifetime on the separation efficiency, for the  $k-\varepsilon$  turbulence model (turbulent kinetic energy dissipation) as well as for the  $k-\omega$  turbulence model (characteristic frequency of turbulence). The eddy lifetime is manipulated by changing the value for the empirical constant  $C_\tau$  in equation (3.29). A commonly used value is  $C_\tau = 0.201$  [27, p. 471]; *Zamora & Kaiser* [72] compare the results for  $C_\tau = 0.10, 0.15$  and  $0.20$ . They also include a comparison with the results from *Wang & James* ([67], [68]). Fig. 5.14 displays the results from all three articles, as well as the experimental results from *Phillips & Deakin* [52], the results predicted by *Bürkholz* [10] (as presented by *Wang & James* [67]) and the analytical model presented here. The experimental data reported by *Phillips & Deakin* [52] has already been discussed in comparison with the analytical model in this chapter, where it was noted that the pick-off hooks resulted in higher separation efficiencies than to be expected from a hookless geometry. The numerical data presented in Fig. 5.14 reveals that the numerical models without turbulence, as well as the STD and Low  $Re$   $k-\varepsilon$  models, severely under-predict the experimental data, for almost all droplet sizes up to a separation efficiency close to unity. These models are very sensitive to the droplet size, perceivable from the steep gradients of the corresponding curves. The Constant EIM results show very high separation efficiencies for all droplet sizes, presumably due to the long living eddies that sooner or later transport all small droplets to a wall. The Varied EIM results lie in between, due to the less effective transport of droplets by the eddies, because they are broken up each time a control volume boundary is traversed. The difference between the Const EIM and the  $k-\varepsilon$  model with  $C_\tau = 0.20$  is noteworthy, because apart from this parameter, the models are basically equal [72, p. 1236]. *Zamora & Kaiser* [72] reach the best results for  $C_\tau = 0.15$ .

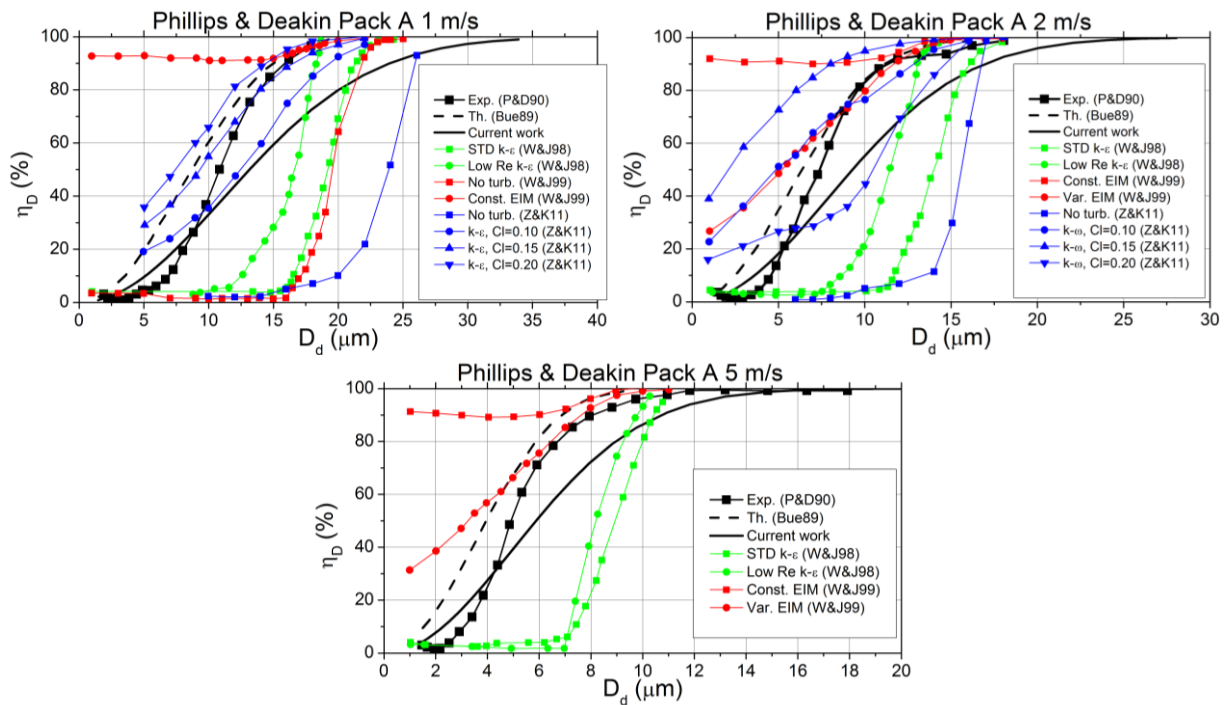


**Fig. 5.14** Experimental data from *Phillips & Deakin* [52] for vane separator *Pack A* (black squares), in comparison with analytical models from *Bürkholz* [10] and current work (black) and with numerical results from *Wang & James* ([67], [68]) (green and red) and from *Zamora & Kaiser* [72] (blue)

In conclusion, the impact of turbulence on separation efficiency appears over-predicted by these numerical models. The turbulent kinetic energy vanishes at the wall [72, p. 1236] and consequently the turbulent eddies die out near the wall regions. If the droplets are deposited on the wall, depends on the governing equations for the boundary layer, the applied droplet deposition and separation model and possibly on the resolution near the wall. Possible causes for the discrepancy with the experimental data is that the numerical models neither account for the minimum inertia required for the droplets to cross the laminar boundary layer, nor for re-entrainment effects through splashing from the wall or liquid film (rebounding).

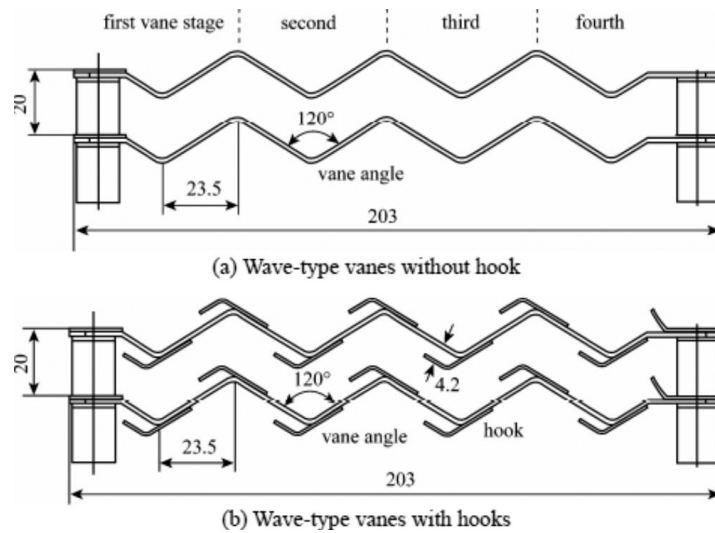


Fig. 5.15 Straight type vane separators, as investigated by *Li et al.* [42]<sup>114</sup>

*Li et al.* [42] investigated two types of very similar straight type vane separators: one with and one without pick-off hooks, both comprising eight stages<sup>115</sup> (Fig. 5.15). Accounting for the plate thickness, the effective channel width is 16.5 mm.

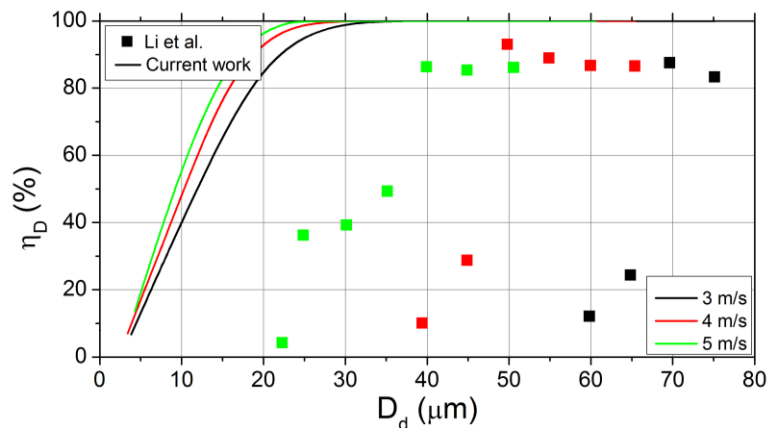


Fig. 5.16 Numerical and analytical separation efficiencies of the hookless vane separator tested by *Li et al.* [42]

The numerical results by *Li et al.* [42] for the hookless geometry and those predicted by the model are depicted in Fig. 5.16. Due to the large number of stages, the model predicts separation efficiencies of unity above 30  $\mu\text{m}$ ; the curves from the numerical model are at surprisingly high droplet diameters. This discrepancy is partly attributed to droplet impingement effects on the vane separator walls, included by *Li et al.* [42] in their model, according to which larger droplets can break up into smaller droplets after a collision with the wall. This introduces a larger number of smaller droplets, which are more difficult to separate. The authors mention that break-up of liquid droplets by impingement on the liquid film is the most important mechanism for entrainment, as compared to break-up of droplets due to shear stress in the continuous phase and break-up of the liquid film due to interfacial shear stress.

<sup>114</sup> Reprinted from [42, p. 492]. Copyright (2007), with permission from Elsevier.

<sup>115</sup> According to the definition in chapter 3.6.4.



Fig. 5.17 Droplet paths through a straight type hookless vane separator as computed by *Li et al.* [42]<sup>116</sup>

In addition, the experimental separation efficiencies appear to be much more dependent on the gas velocity than predicted by the model, for which the curves all coincide with the origin. The measured values appear to depict a cut-off droplet size, below which the separation efficiency sharply drops to zero. This phenomenon can be explained by the broad channel width, in relation to the rather blunt bend angles. It is good engineering practice to design vane separators in such a way that the bend angles and the stage lengths are large enough to ensure that no straight path through the vane separator is possible, in order to prevent large droplets to *strike through* the channel; something *Kall* [29, p. 44] already pointed out. Judging from Fig. 5.15, a straight path appears to be available to the droplets in the hookless vane separator, also clearly visible in the droplet paths computed by *Li et al.* [42] (Fig. 5.17). Droplets starting out in the middle of the entrance pass through almost without altering their direction<sup>117</sup>, a phenomenon that is not captured by the analytical model, in which an increasing number of stages will always lead to increasing separation efficiencies. Contrary to the analytical model, the efficiency in the first two stages is in Fig. 5.17 significantly higher than in subsequent stages, which contribute very little to droplet separation. The smaller the gas velocity is, the larger the droplets are that will *strike through* the vane separator. For comparison, even if only one effective stage is accounted for in the model and a wall boundary region of 10% of the channel width is assumed, the resulting efficiencies are still larger than the numerical results from *Li et al.* [42] (Fig. 5.18).

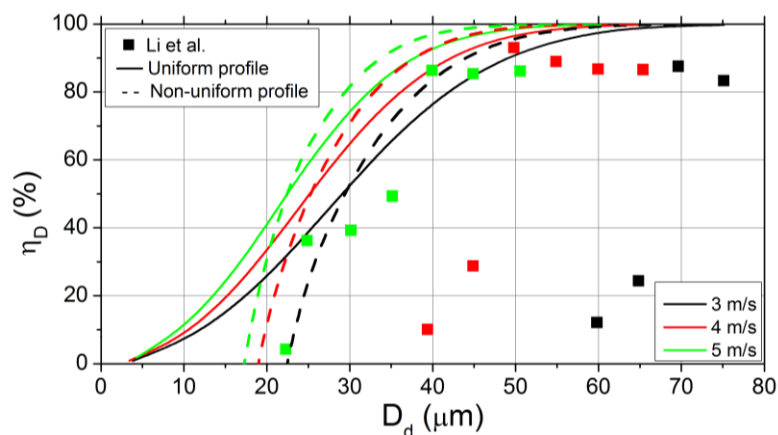


Fig. 5.18 Experimental results (squares) for the hookless vane separator tested by *Li et al.* [42] and analytical results assuming a single stage with uniform (solid) and non-uniform flow (dashed)

<sup>116</sup> Reprinted from [42, p. 495]. Copyright (2007), with permission from Elsevier.

<sup>117</sup> The depicted result is for droplets of 30  $\mu\text{m}$  at 5 m/s. The experimental separation efficiency for this diameter is approximately 40%, which does not appear to correspond well with the depicted droplet paths. The 'secondary' and 'tertiary' droplet paths are also visible, especially in stage two and three. These paths result from the applied model, which allows droplets to stick, rebound, splash or spread upon impact [42, p. 494]. Rebounding and splashing lead to subsequent droplet paths, the first of which is said to occur at low impingement energy, causing a reduction of the separation efficiency mainly at low gas velocities.

The results for the vane separator with pick-off hooks are depicted in Fig. 5.19. The numerical separation efficiencies are much higher than before, which can be attributed to a direct capture of droplets by the pick-off hooks, increased gas velocities around the pick-off hooks through the narrowed channels and additional capture of secondary droplets produced by splashing of large droplets in the vicinity of the pick-off hooks [42, p. 497]. The results produced by the analytical model are in much closer correspondence to this geometry, as compared to the hookless vane separator.

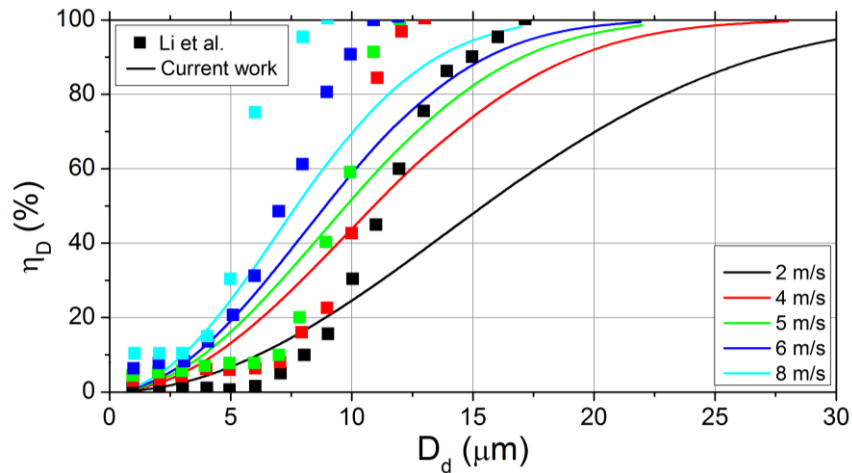


Fig. 5.19 Numerical and analytical separation efficiencies of the vane separator with pick-off hooks tested by *Li et al.* [42]

## 5.3 Experiments on a wavy vane separator

### 5.3.1 Research goals

The analytical approach to droplet separation in vane separators presents some boundaries as to the application of the relevant physical and geometrical parameters in the theory. Because they are expected to be very small, changes in the physical properties of the gas and/or the droplets along the channel, for instance due to pressure or temperature gradients, are not accounted for. Major changes in the equation of state can be expected only when phase changes occur, which is not relevant for air-water systems, but for saturated steam systems mass transfer between the phases cannot be ruled out. For isothermal flows of saturated steam experiencing a small negative pressure gradient, a small amount of droplet evaporation would take place, having a positive effect on the separation efficiency in terms of liquid mass, but also a negative impact on droplet separation due to the shifting of the droplet size spectrum towards smaller droplets. Such evaporation effects do not have a significant impact on the separation efficiency<sup>118</sup>.

In addition, limits exist for the geometrical complexity of the vane separator that can be accounted for in the analytical model. Asymmetries of the vane geometry cannot be represented realistically and neither can additional structures, such as pick-off hooks. The unavoidable simplification of vane separator geometries introduces an unquantified impact on the results, making the comparison with

<sup>118</sup> Assuming instantaneous mass transfer and complete thermal equilibrium, the liquid enthalpy drop associated with a negative pressure gradient of 1 kPa at an absolute pressure of 10 bar, would evaporate about 0.1% of the droplet mass.

experiments more difficult. Experimental results using a vane separator geometry that is arbitrarily close to the assumed geometry of the analytical model are thus invaluable. The simplified test geometry provided for the experiments carried for the current research has a bend angle of  $80^\circ$ , an inner radius is 10 mm, a constant channel width of 11.45 mm, straight sections with a length of 17.6 mm<sup>119</sup> and is manufactured from 3 mm Makrolon® (Fig. 5.20).

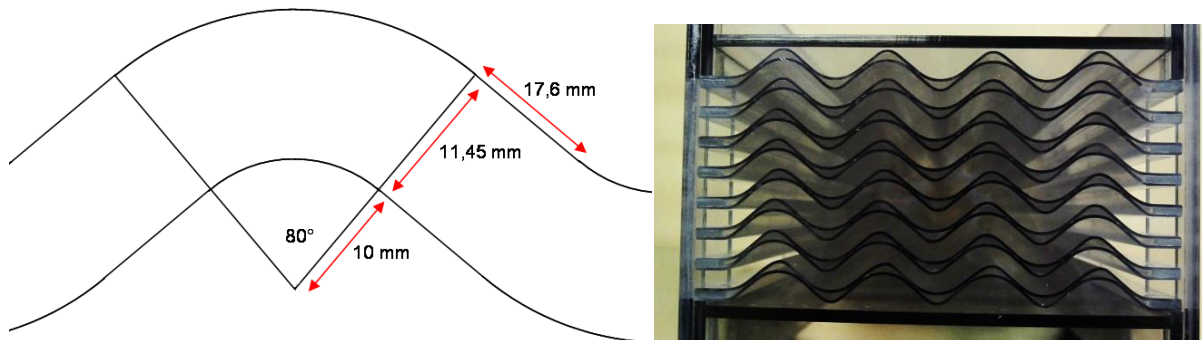


**Fig. 5.20** Simplified vane separator test geometry

In order to validate the results from the analytical model, the experimental results shall convey the influence of the homogeneous gas velocity on the separation efficiency. In addition, the influence of moisture content on the separation efficiency and the pressure drop at various flow rates are investigated. The experiments were performed by members of the Institute of Fluid Mechanics (LSTM) of the Friedrich-Alexander University in Erlangen, where a test facility was set up for this purpose. The following description of the test facility is based on information supplied by LSTM (with courtesy of Siemens AG), as partly published by *Kolev et al.* [35] and *Koopman et al.* [36].

## 5.3.2 Experimental setup

### 5.3.2.1 Overview

The test facility comprised an open-loop wind tunnel, with air as the flowing medium in which droplets of water were entrained (Fig. 5.21). The experiments were performed at ambient pressure, using a 15 kW radial fan to suction the necessary air flow, equipped with a frequency transformer to adjust its rotational speed. The air velocity was measured with a Prandtl tube in the 150 mm x 500 mm inlet section of the spray chamber. Arrays of nozzles were installed to spray the droplets into the spray chamber, supplied with water from a 15 kW high pressure pump, for which the pressure was limited to 100 bar. After leaving the spray chamber, the air-droplet mixture entered a flow channel which provided optical access on both sides for the droplet size measurement instrumentation, consisting of a PDA system. At the end of the flow channel a vane separator module was installed, consisting of seven stages with a height of 500 mm. Behind the vane separator module a second set of windows provided optical access for droplet size measurements. The exiting flow was exhausted into the atmosphere.

<sup>119</sup> Efforts were made to reduce machining tolerances to a minimum.

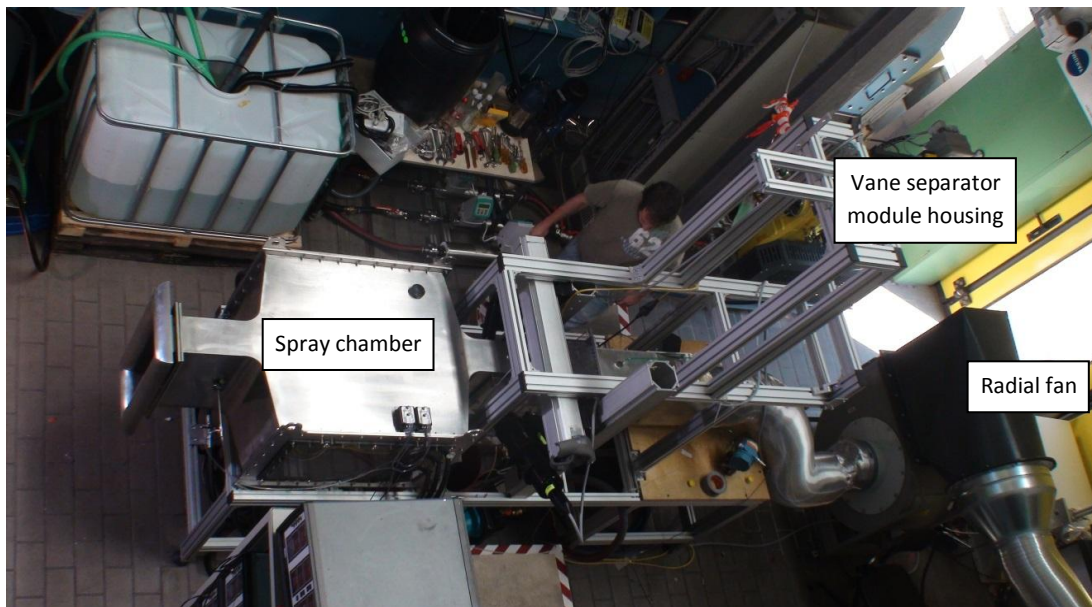


**Fig. 5.21** Experimental test facility at the Institute of Fluid Mechanics (LSTM) of the Friedrich-Alexander University in Erlangen<sup>120</sup>

### 5.3.2.2 Flow channel and spray system

A schematic view of the spray system, as an integrated part of the 2.5 m long stainless steel flow channel, is given in Fig. 5.22. Because not all droplets were carried off by the air flow and many droplets were deposited along the channel before entering the vane separator module, in addition to the collector at the bottom of the vane separator module (Fig. 5.22 on the right), water was also collected at a point slightly upstream of the vane separator module. In order not to distort the pressure measurements, the channel sections upstream and downstream of the vane separator module had the same cross-section.

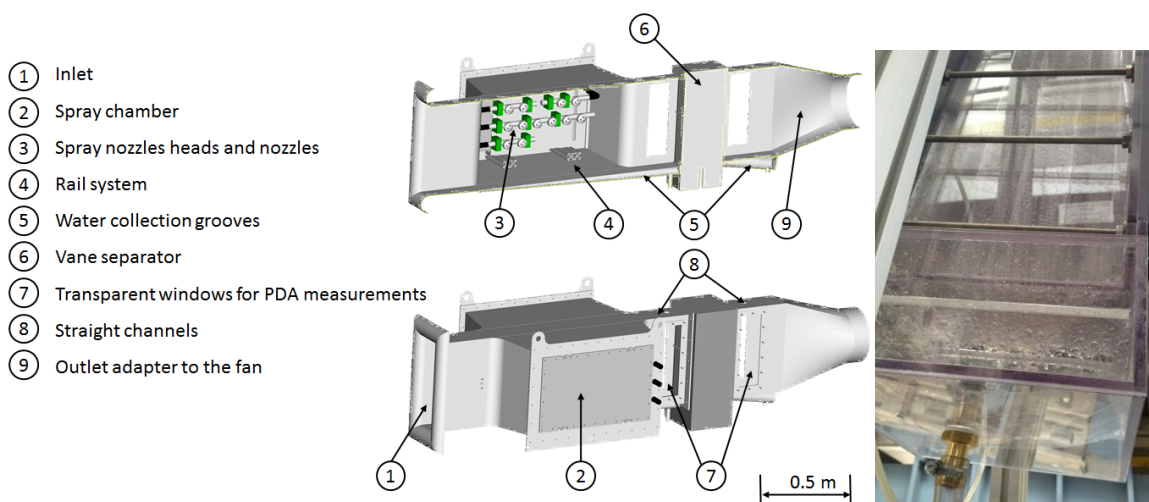


**Fig. 5.22** Flow channel with integrated spray system (left)<sup>121</sup> and collection of separated liquid mass from the vane separator module (right)

<sup>120</sup> Courtesy of Siemens AG.

<sup>121</sup> Courtesy of Siemens AG.

The spray chamber contained hollow cone spray nozzles installed on nozzle heads, which were mounted on several different pipes, each of which was connected to a shut-off valve. This allowed for serial switching of sets of nozzles. The distribution of nozzles is provided in Fig. 5.23, as well as an inside view of the spray chamber. The nozzle distribution was chosen in such a way that the desired droplet mass flows could approximately be attained by different combinations of valve settings.

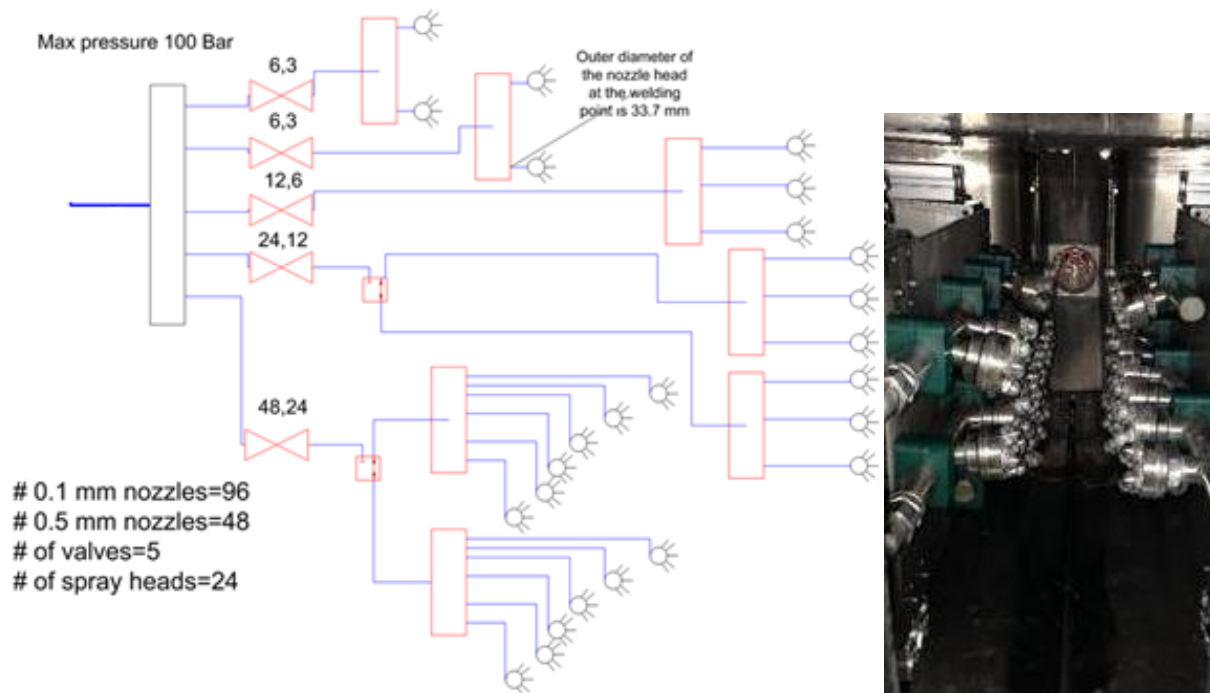


Fig. 5.23 Schematic view of spray nozzle distribution (left) and inside view of spray chamber (right)<sup>122</sup>

Two types of nozzles were used: 96 nozzles with an opening diameter 0.5 mm and 48 nozzles with an opening diameter of 0.1 mm. The droplet size distributions for the measurement could be adjusted by installing the different nozzle types and by adjusting the water pressure. The desired liquid mass fraction was approximated by different settings of the shut-off valves. The distance of the nozzle heads from the center-line of the channel could also be adjusted, thereby altering the separation characteristics of the spray chamber itself and allowing for an optimum in terms of the amount of droplets being carried off by the air flow.

### 5.3.2.3 Measurements and instrumentation

The liquid mass balance during the measurements comprised the mass flow  $\dot{m}_{pump}$  supplied to the high pressure pump, the mass flow  $\dot{m}_{coll}$  collected from the bypass line and upstream of the vane separator, the mass flow  $\dot{m}_{VS}$  collected from the vane separator, and the liquid mass flow  $\dot{m}_{exhaust}$  exhausted into the atmosphere. The liquid mass flow to the pump and from the combined bypass and upstream collection line were measured using coriolis meters. The liquid mass flow separated by the vane separator was not continuously measured, but collected in a basin and extracted by a pump after reaching a certain level. The experimental separation efficiency is defined as the cumulated

<sup>122</sup> Courtesy of Siemens AG.

liquid mass flow separated by the vane separator during the measurement, divided by the cumulated liquid mass flow of the pump, after subtraction of the cumulated collected liquid mass flow:

$$\eta = \frac{\int \dot{m}_{VS} dt}{\int \dot{m}_{pump} dt - \int \dot{m}_{coll} dt} \quad (6.3)$$

The droplet mass fraction  $\chi_d$  entering the vane separator is defined as the ratio of liquid and total mass flows reaching the vane separator:

$$\chi_d = \frac{\dot{m}_{pump} - \dot{m}_{coll}}{\dot{m}_{pump} - \dot{m}_{coll} + \dot{m}_{air}} \quad (6.4)$$

An overview of the relevant liquid mass flows is provided in Fig. 5.24, which also shows a typical liquid mass balance, as measured during the experiments. From the pie chart it is clear that only one fifth of the droplets in the spray chamber made it to the vane separator.

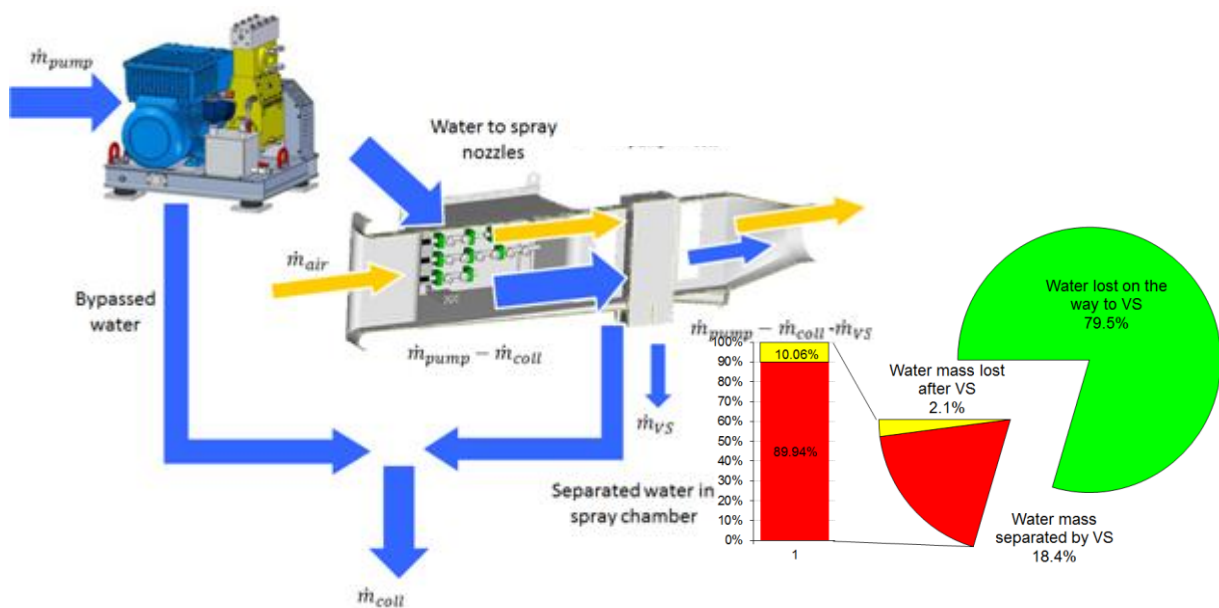


Fig. 5.24 Schematic representation of the liquid mass balance and its typical experimental values<sup>123</sup>

The air velocity was measured in dry air with the use of a Prandtl tube installed at the center of the inlet section to the spray chamber. Pressure was recorded near the entrance and the exit of the vane separator module by two pressure transducers and temperature was recorded upstream of the vane separator module. A plate heat exchanger was installed in the feedline of the high pressure pump to cool the water to below 40°C. The droplet sizes and velocities were measured with the use of a Phase-Doppler Anemometer (Fig. 5.25). Each measurement duration corresponded to a registration by the PDA system of 200,000 single droplets.

<sup>123</sup> Courtesy of Siemens AG.

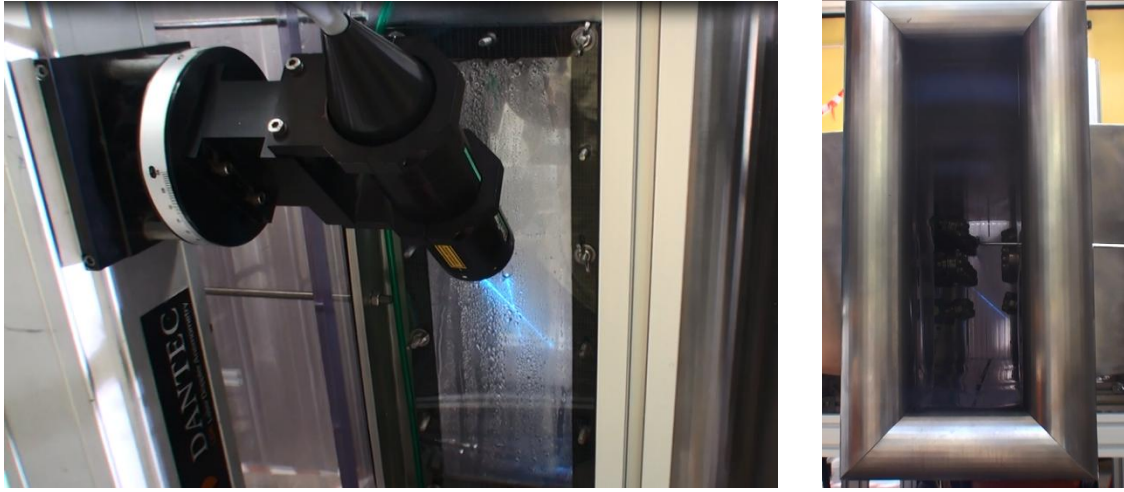


Fig. 5.25 The PDA system

#### 5.3.2.4 Uncertainty analysis

The relative uncertainty in the measurement of the separation efficiency is driven by the relative uncertainty  $\delta\dot{m}/\dot{m} = 0.1\%$  of the coriolis meters. Due to some ambiguity in the deactivating point of the drainage pump, there is an additional uncertainty in the collected and separated integrated mass flows of  $\delta\left(\int \dot{m}_{coll} dt\right) \approx 1\text{kg}$  and  $\delta\left(\int \dot{m}_{VS} dt\right) \approx 0.2\text{kg}$  respectively [35]. The relative uncertainty  $\delta\eta/\eta$  of the experimental separation efficiency is thus given by

$$\frac{\delta\eta}{\eta} = \sqrt{\left[\frac{\delta\left(\int \dot{m}_{VS} dt\right)}{\int \dot{m}_{VS} dt}\right]^2 + \left[\frac{\delta\left(\int \dot{m}_{pump} dt - \int \dot{m}_{coll} dt\right)}{\int \dot{m}_{pump} dt - \int \dot{m}_{coll} dt}\right]^2} \quad (6.5)$$

with

$$\begin{aligned} \delta\left(\int \dot{m}_{VS} dt\right) &= \sqrt{\left[\frac{\delta\dot{m}}{\dot{m}} \cdot \int \dot{m}_{VS} dt\right]^2 + \left[\delta\left(\int \dot{m}_{VS} dt\right)\right]^2} \\ \delta\left(\int \dot{m}_{pump} dt - \int \dot{m}_{coll} dt\right) &= \sqrt{\left[\frac{\delta\dot{m}}{\dot{m}} \cdot \int \dot{m}_{pump} dt\right]^2 + \left[\frac{\delta\dot{m}}{\dot{m}} \cdot \int \dot{m}_{coll} dt\right]^2 + \left[\delta\left(\int \dot{m}_{coll} dt\right)\right]^2} \end{aligned} \quad (6.6)$$

The use of two parallel pressure transducers with an uncertainty of  $\delta p/p = 0.25\%$ , connected to the Prandtl tube, and an additional pressure transducer with an uncertainty of  $\delta p = \pm 22.5\text{Pa}$  for the air density measurement, resulted in uncertainties in the air velocity and integrated air mass flow measurements according to Fig. 5.26. The jump in the data at 7 m/s is due to the switching from a 25 Pa pressure transducer to a 250 Pa pressure transducer.

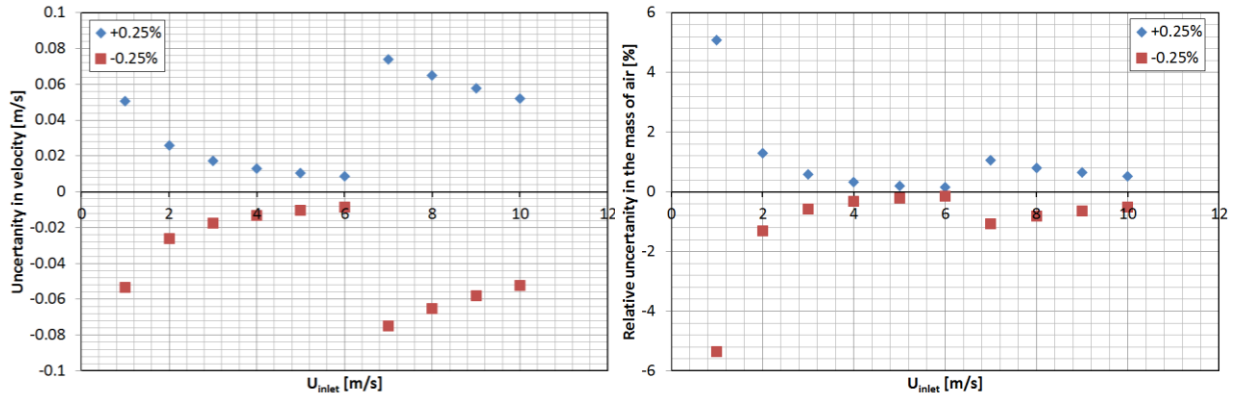


**Fig. 5.26** Absolute measurement uncertainty in air velocity (left) and relative measurement uncertainty in integrated air mass flow (right) as a function of air velocity (at the spray chamber inlet)<sup>124</sup>

The relative uncertainty in the measurement of the liquid mass fraction is

$$\frac{\delta\chi_d}{\chi_d} = \sqrt{\left[ \frac{\delta\left(\int \dot{m}_{air} dt\right)}{\int \dot{m}_{air} dt} \right]^2 + \left[ \frac{\delta\left(\int \dot{m}_{pump} dt - \int \dot{m}_{coll} dt\right)}{\int \dot{m}_{pump} dt - \int \dot{m}_{coll} dt} \right]^2} \quad (6.7)$$

The reported absolute uncertainty in the measurement of the droplet diameter is  $\delta D = \pm 1 \mu\text{m}$ . Consequently, the relative uncertainty in the Sauter mean diameter is estimated as follows:

$$\frac{\delta d_{32}}{d_{32}} = \sqrt{\left[ \frac{\delta\left(\sum_{i=1}^{i_{max}} \overline{D_{d,i}^3} f_{D,i}\right)}{\sum_{i=1}^{i_{max}} \overline{D_{d,i}^3} f_{D,i}} \right]^2 + \left[ \frac{\delta\left(\sum_{i=1}^{i_{max}} \overline{D_{d,i}^2} f_{D,i}\right)}{\sum_{i=1}^{i_{max}} \overline{D_{d,i}^2} f_{D,i}} \right]^2} \quad (6.8)$$

with

$$\delta\left(\sum_{i=1}^{i_{max}} \overline{D_{d,i}^y} f_{D,i}\right) = \sqrt{\sum_{i=1}^{i_{max}} \left[ \delta\left(\overline{D_{d,i}^y} f_{D,i}\right) \right]^2} = \sqrt{\sum_{i=1}^{i_{max}} \left[ \overline{D_{d,i}^y} f_{D,i} \sqrt{y \frac{\delta D}{D_{d,i}}} \right]^2} \quad (6.9)$$

### 5.3.3 Results

One set of experiments was performed with a constant liquid mass flow of around 5% at varying air velocity and one set with varying initial liquid mass flow at a constant air velocity of about 9.5 m/s. For each of the 18 combinations of air velocity and nozzle distribution, the droplet size distribution was measured once through the optical window before the vane separator and once after (not simultaneously). The measurement points are listed in Table 8. The effective air velocities are corrected for the blockage factor of the vanes and are thus representative for the velocity inside the flow channel of the vane separators. The achieved initial liquid mass fractions deviate slightly from the desired values, due to the discrete settings of the liquid mass flow nozzle valves.

<sup>124</sup> As reported by the Institute of Fluid Mechanics (LSTM) at the F.-A. University. Courtesy of Siemens AG.

**Table 8** Measurement points achieved during the experiments

Spray chamber air velocity [m/s]	Effective air velocity [m/s]	Liquid mass fraction [%]
1.0	1.9	3.73
		3.93
2.0	3.8	4.65
3.0	5.7	4.78
4.0	7.6	5.7
5.0	9.5	5.66
		2.05
		3.37
		4.63
		4.87
		6.52
		8.75
9.15		
6.0	11.4	5.3
7.0	13.3	5.42
8.0	15.2	4.5
9.0	17.1	5.05
10.0	19.0	5.53

### 5.3.3.1 Experimental separation efficiencies

The measured droplet separation efficiencies are depicted in Fig. 5.27 for both datasets<sup>125</sup>. The graphs also show the Sauter mean diameters of the inlet droplet size distribution, which was not only affected by the nozzle opening diameter, the water pressure and the air velocity, but was also significantly dependent on the droplet separation characteristics of the spray chamber. The latter was influenced by the asymmetry of the nozzle distributions (with respect to the vertical center-plane of the chamber) and the distance of the nozzles from the center-plane. For the measurements with varying air velocity the nozzle distributions were symmetric, but particularly the measurements with liquid mass fractions of 2.1% and 4.9% were performed with asymmetric nozzle distributions. The smaller Sauter mean diameters for these measurements are due to smaller amounts of large droplets (>100  $\mu\text{m}$ ) in the measured inlet droplet size distributions. It is very likely that an asymmetry of the nozzle distribution leads to uneven distributions of droplets into the air channel, causing it to be skewed towards one side of the channel as it reaches the PDA measurement volume. This would result in smaller inlet Sauter mean diameters measured at the channel center line, although the actual droplet size distribution into the vane separator and thus the separation efficiency remain unaffected<sup>126</sup>.

<sup>125</sup>The uncertainty in the air velocity is based on the uncertainty in the air velocity measurement at the spray chamber inlet. It does not account for the possible spread of air velocities through the different channels of the vane separator, e.g. due to turbulent effects upstream of the vane separator module.

<sup>126</sup>The liquid mass fraction of 4.6% was produced with a symmetric nozzle distribution, but also had a comparatively small amount of large droplets in the inlet droplet size distribution. It remains unclear what could have caused this discrepancy.

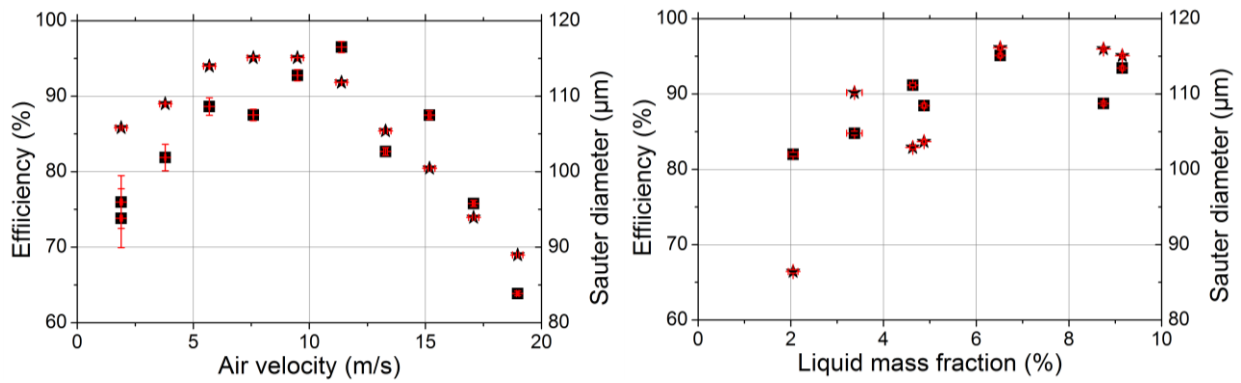


**Fig. 5.27 Measured droplet separation efficiencies (squares) and inlet Sauter mean diameters (stars) as a function of effective air velocity (left) and of liquid mass fraction (right)**

The experimentally observed values conflict with analytical predictions for the droplet separation efficiency, which, based on the inlet droplet size distributions, are in all cases very close to unity. This can be attributed to re-entrainment effects, supported by the observation in Fig. 5.27 that the separation efficiency reveals an increasing trend with effective air velocity, up to a value of about 11 m/s, after which a sharp decrease can be discerned. The re-entrainment boundary reported by *Azzopardi & Sanaullah* [3] (Fig. 4.23), lies, for a liquid Reynolds number that is about 1150 for the current liquid mass fraction and geometrical parameters, at a gas Reynolds number of approximately 6500. This corresponds to a gas velocity of about 9 m/s, which is roughly in agreement with Fig. 5.27.

However, the correlation with the inlet Sauter mean diameter suggests that the inlet droplet size spectrum is the most significant parameter for the separation efficiency. The droplet separation efficiency as a function of liquid mass fraction in Fig. 5.27 reveals a similar correlation with the inlet Sauter mean diameter. If re-entrainment causes the deteriorated separation efficiency, it must be correlated to the inlet Sauter mean diameter as well. This correlation can be explained by the fact that larger droplets are separated earlier and create a thicker film on the vane walls, thus enlarging the migration distance to the end of the vane separator as well as increasing the downward velocity of the liquid film. This causes a larger portion of the separated liquid to be drained gravitationally, as compared to droplet size distributions with smaller Sauter mean diameters.

### 5.3.3.2 Adjustment for re-entrainment effects

The outlet droplet size distributions contained droplets typically below 40  $\mu\text{m}$ , although many contained a very small number of droplets in the 40-60  $\mu\text{m}$  range, or in the 80-100  $\mu\text{m}$  range, without recording any droplets in between. Based on visual inspections, it appears that these droplet recordings are associated with liquid film breaking off from the last stage of the vane separator, releasing fractional droplets back into the air flow. In particular, streams of separated droplets were carried over from one stage to the next and reached the end of the last stage before being gravitationally drained down the bottom of the vane separator. The larger the air velocity, the higher the average point of release of such droplet streams, incidentally leading to a recording of a relatively large number of entrained droplets where the main point of release coincided with the measurement volume of the PDA system. In general only a small number of droplets are concerned, having no significant impact on the droplet size number distributions. But being very large droplets, the droplet size mass distributions are significantly affected, as exemplified by Fig. 5.28.

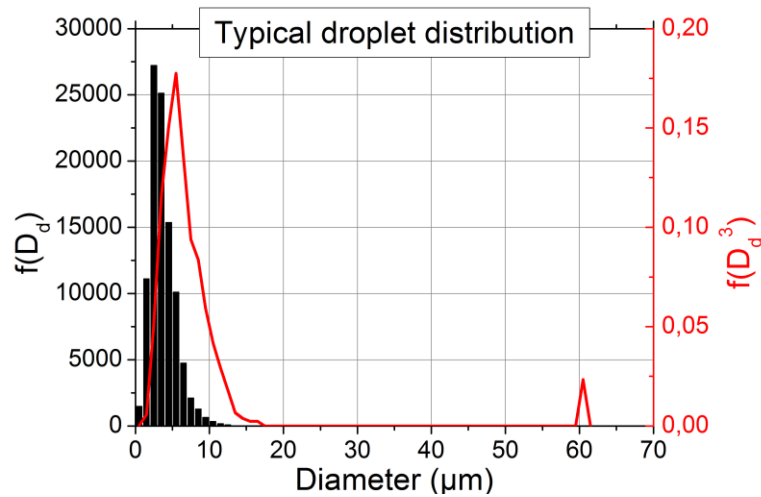


Fig. 5.28 Typical droplet number (black) and mass (red) distributions

In order to enable a comparison of the grade efficiencies without re-entrainment effects, a cut-off filter was applied to the measurement data, eliminating droplet size recordings above 40  $\mu\text{m}$ . The following results consider the application of this cut-off filter. The Sauter mean diameters as well as the typical size ranges of the inlet and outlet droplet size distributions after application of the cut-off filter are listed in Table 9.

Table 9 Sauter mean diameter and range of inlet and outlet droplet size distributions computed from the PDA measurements

	Inlet		Outlet	
	$D_{\text{Sauter}} (\mu\text{m})$	Range ( $\mu\text{m}$ )	$D_{\text{Sauter}} (\mu\text{m})$	Range ( $\mu\text{m}$ )
var. $v_g$	50 - 78	0 - 150	4.9 - 14.4	0 - 40
var. $\chi_d$	50 - 84	0 - 150	5.0 - 6.7	0 - 18
var. $v_g$	43 - 69	0 - 150	3.2 - 7.5	0 - 25
var. $\chi_d$	51 - 78	0 - 150	3.7 - 4.5	0 - 15

### 5.3.3.3 Varying liquid mass fraction

Fig. 5.29 depicts the droplet size distribution before and after the vane separator, for the experiment with 2% liquid mass fraction. The black line depicts the droplet size distribution as predicted from the model presented in this paper (equations (1.16), (3.46) and (3.121)). The relevant physical parameters are provided appendix A.IV. The measured and predicted droplet size distributions are enlarged in the inset. Above a droplet size of about 12  $\mu\text{m}$ , virtually all droplets are separated, as predicted by the model. Between droplet sizes of approximately 2 and 8  $\mu\text{m}$ , the cumulative droplet mass fraction is slightly under-predicted, apparently caused by a slight under-prediction of the separation efficiency at small droplet diameters<sup>127</sup>.

<sup>127</sup> It must be noted that, since cumulative droplet mass fractions are compared, instead of separation efficiencies, the comparison is valid only under the assumption that the measured droplet size distribution by the PDA system corresponds to the actual inlet droplet size distribution entering the vane separator: discrepancies would cause differences in cumulative droplet mass fractions, even if the separation efficiencies are equal, as will become clear in the following discussion.

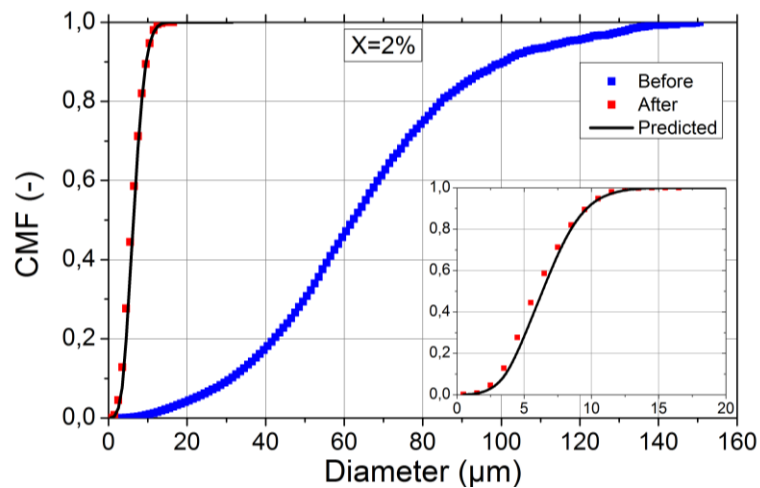


**Fig. 5.29** Cumulative droplet mass fraction before (blue) and after (red) the vane separator as compared to the model (black) for a liquid mass fraction of 2%

The droplet size distributions from the remaining experiments for different liquid mass fractions are given in appendix A.V-a. These results show much similarity to Fig. 5.29: in all cases experiment and model agree very well, although, in general, the predicted cumulative mass fractions are slightly steeper, implying a slightly stronger dependence on droplet diameter than reflected in the measurements<sup>128</sup>.

#### 5.3.3.4 Varying air velocity

The model predictions for the experiments with varying gas velocity do not agree as well with the measurements as those with varying liquid mass fraction, as exemplified by Fig. 5.30. It would appear that the separation efficiency is under-predicted at small droplet sizes, but it is more likely that the fraction of small droplets present in the inlet droplet size distribution is larger than measured by the PDA system, causing a visibly similar effect. This will be explained in more detail in the next section.

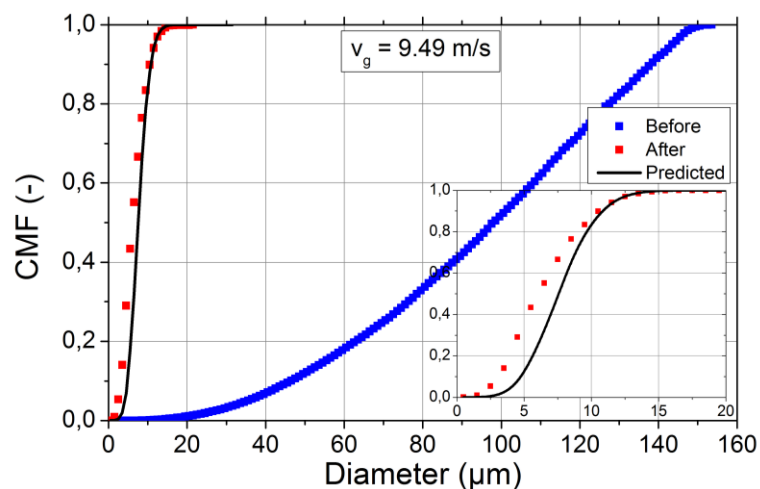


**Fig. 5.30** Cumulative droplet mass fraction before (blue) and after (red) the vane separator module as compared to the model (black) for an air velocity of 9.5 m/s

<sup>128</sup> See previous footnote.

The smallest droplet diameter beyond which all droplets are separated ( $d_{100}$ ) is predicted accurately. The measured and predicted cumulated mass fractions for the experiments with varying gas velocity are presented in appendix A.V-b. All of these graphs display a similar trend as depicted in Fig. 5.30; an apparent under-prediction of the cumulative droplet mass fraction at small droplet sizes, but an accurate representation of  $d_{100}$ .

### 5.3.4 Discussion

Applying the theoretical grade efficiencies to the inlet droplet size distribution and renormalizing the results, theoretical outlet droplet mass fractions can be computed, from which theoretical Sauter mean diameters can be deduced. The model predictions for both sets of experiments are compared to the experimental Sauter mean diameters in Fig. 5.31.

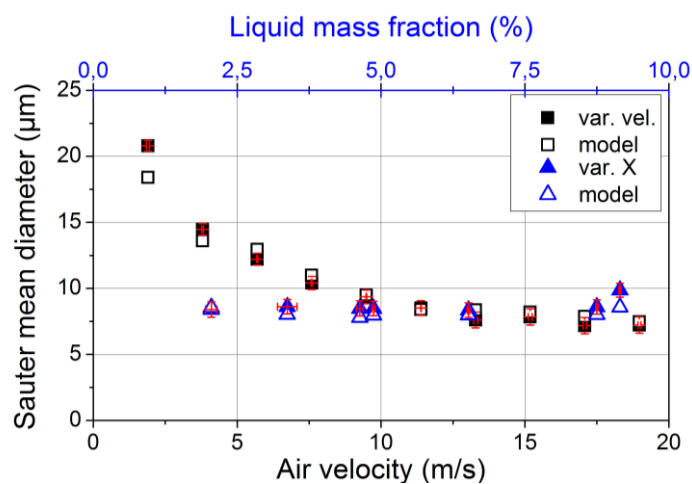


**Fig. 5.31** Experimental Sauter mean diameters at the outlet for varying effective air velocities (solid squares) and varying liquid mass fraction (solid triangles) as compared to the model predictions (open symbols)

The model corresponds well with the experimental values. As compared to the classical model without straight sections, the extended model predicts slightly higher separation efficiencies and thus slightly lower Sauter mean diameters at the vane separator outlet, in the order of magnitude of  $0.35 \mu\text{m}$  (not depicted). As expected, the experimental Sauter mean diameters for variable gas velocity and variable liquid mass fraction cross at  $9.5 \text{ m/s}$  and  $5\%$ . The model predictions for the experiments with variable gas velocity do not agree as well with the measurements as those for varying liquid mass fraction; the Sauter mean diameters are somewhat over-predicted. This is due to higher contents of very small droplets in the measured outlet droplet size distributions, as compared to the model predictions. The inlet droplet size distributions for both sets of measurements are depicted in Fig. 5.32, which shows a clear difference in the measured content of small droplets, as a result of the different nozzle distributions and nozzle types applied in the experiments. The model assumes no correlation between grade efficiencies and droplet size distributions, which is supported by the agreement of the experimental results at a gas velocity of  $9.5 \text{ m/s}$  and  $5\%$  liquid mass fraction, and also in literature is considered unlikely [22], however inconclusive [50] (refer to the discussion in chapter 3.6.3).

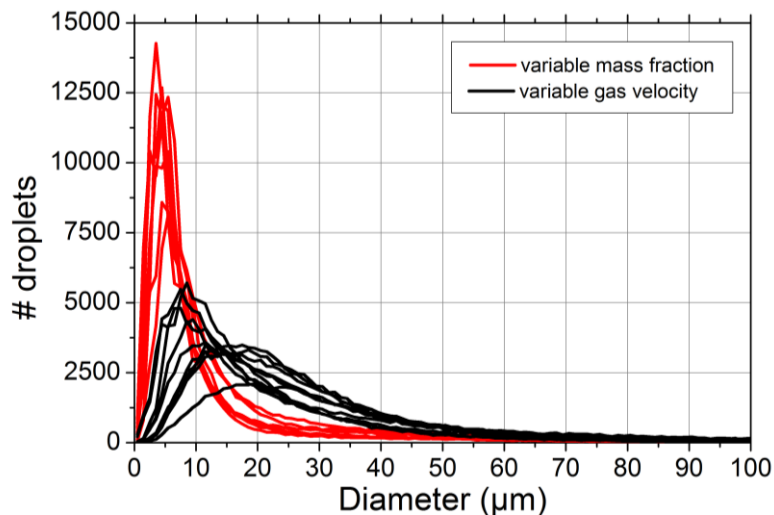


**Fig. 5.32** Inlet droplet size distributions for measurements with variable mass fraction (red) and gas velocity (black)

The good agreement between the cumulative outlet droplet mass fractions from measurement and model for the variable liquid mass fraction experiment, and the similarity of these with the data from the variable gas velocity experiment (Fig. 5.33), suggests the model discrepancy could be caused by non-uniform droplet distributions at the PDA measurement point for the variable gas velocity data set. An increased concentration of large droplets near the center of the channel would cause a shift of the perceived (measured) inlet droplet size distribution towards larger diameters. This could be related to droplet coalescence produced by the impinging sprays being centered more at the middle of the spray chamber, as compared to the asymmetrical nozzle distribution during the variable liquid mass fraction experiment (refer to section 5.3.3.1). The under-representation of small droplet fractions in the PDA measurements of the *inlet* droplet mass fractions is directly reflected in the predicted cumulative *outlet* droplet mass fractions in Fig. 5.30 and appendix A.V-b: based on the measured *inlet* values, lower mass fractions of small droplets are predicted at the *outlet*, as compared to the *measured* values at the outlet.

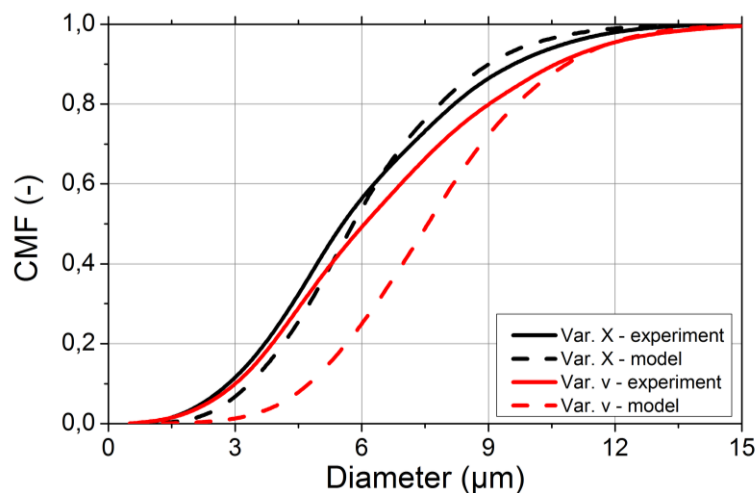


**Fig. 5.33** Measured (solid lines) and predicted (dashed lines) cumulative outlet droplet mass fractions for the measurements with 9.5 m/s and 5% liquid mass fraction, during the variable liquid mass fraction (black) and variable gas velocity (red) experiments

The contributions of the straight wall sections, according to the proposed extension of the analytical model, were for the geometries under investigation too small to isolate for a valid comparison of the *overall* droplet separation efficiency with experiments. The reason is that the vane separator geometry under investigation is quite efficient. According to the model, the contribution of the straight wall sections decreases rapidly with decreasing droplet diameter, thus for the relatively small outlet droplet distributions it was not very significant. These contributions become relevant when vane separators are of a less efficient design, e.g. when they are optimized for costs and/or space restrictions (comprising fewer number of stages and/or smaller bend angles). They are also relevant when specific grade efficiencies are concerned; for certain ranges of droplet diameters the difference in efficiency can be significant. In particular, the sensitivity of the droplet separation efficiency with respect to the droplet diameter is increased by the presence of straight wall sections.

#### Quintessence

*The droplet separation experiments were influenced by re-entrainment from the last vane separator stage. After adjustment of the experimental data for re-entrainment effects the analytical model gives quite accurate predictions for the cumulative outlet droplet mass fractions. Non-uniform droplet distributions at the PDA measurement point seem to offset the model predictions in comparison with the measurements. For the tested geometries the contribution of the straight sections to the total separation efficiency is very small.*

## 5.4 Pressure drop

Experimental values for the pressure drop as a function of effective air velocity are depicted in Fig. 5.34. The formula given by *Wilkinson* [70] (equation (4.42)) has been employed to produce theoretical pressure drop values.

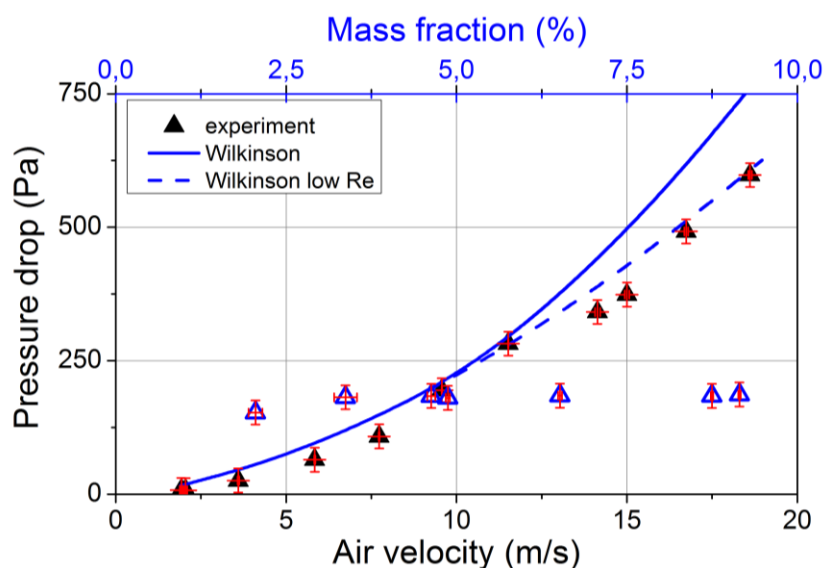


**Fig. 5.34** Pressure drop as a function of effective air velocity (closed symbols) and as a function of mass fraction (open symbols). Solid and dashed lines represent predictions by the Wilkinson model.

The pressure drop is very reasonably estimated by the formula for gas velocities up to 12 m/s. *Wilkinson* [70] reported a change in the pressure loss coefficient for the bends at a Reynolds number of 7760; from a decreasing function of the Reynolds number, to a Reynolds number independent function<sup>129</sup>. In this case, this regime change occurs at a gas velocity of approximately 10 m/s. It is interesting to note, that the *low Reynolds number* pressure drop formula gives better results for the experimental pressure drop beyond Reynolds numbers of 7760 (dashed line in Fig. 5.34). This suggests, that the dependence of the pressure drop coefficient on the Reynolds number is valid for higher Reynolds numbers than reported by *Wilkinson* [70]. Fig. 5.34 also depicts the pressure drop as a function of liquid mass fraction. No specific dependence of the pressure drop on the liquid mass fraction can be discerned.

---

<sup>129</sup> Refer to chapter 4.2.1.

## 6 Optimizing vane separator design

### 6.1 Introduction

Several authors have investigated and discussed design criteria for vane separators. For instance, *Kall* [29, pp. 43-47] discusses design criteria for a particular vane separator geometry, including an inner bend radius equal to the (constant) channel width to prevent film detachment, a minimum overlap of consecutive bends to prevent *strike through* of large droplets<sup>130</sup>, and a minimum vane profile thickness  $t_v$ , to incorporate drainage. This resulted in specific values for the relative vane pitch  $w_v/\delta_R$ , the relative wavelength  $\lambda_v/\delta_R$ , the relative length of the straight section  $L/\delta_R$  and the bend angle  $\varphi$  (Fig. 6.1). Fixing these parameters, the author concluded that smaller channel widths create larger drainage volumes and thus increase effective gas velocity, decrease film thickness (because the liquid is divided over more channels), decrease total vane separator length (at a prescribed number of 7 stages), but increase manufacturing costs. Obeying a minimal sheet thickness of 1 mm, *Kall* [29, pp. 43-47] arrives at a channel width of 8 mm.

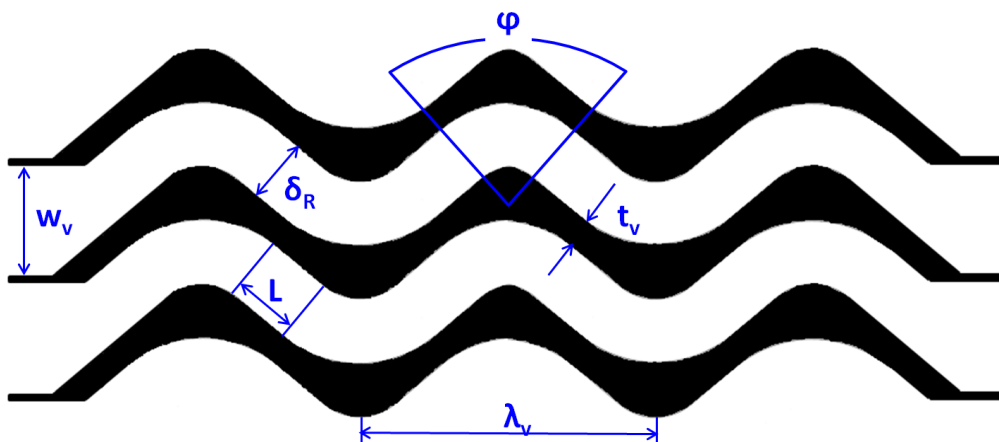


Fig. 6.1 Geometric parameters with relevance to vane separator design, according to *Kall* [29]

*Wilkinson* [70] investigated optimal vane separator designs with which a minimum of 50% separation efficiency could be achieved with minimum pressure drop. Target droplet sizes between 1-20  $\mu\text{m}$  and vane separators with 3, 5, 7 and 9 stages were investigated and channel width, length of straight section, bend angle and gas velocity were varied. The relevant geometrical parameters are given in Fig. 6.2. Using one empirical equation for pressure drop and one for separation efficiency, optimization was performed by the generalized reduced gradient method [39]. Assuming constant bend angles, the optimal bend angle was in all cases approximately 66°. Channel width decreased and gas velocity increased with decreasing target droplet size, reaching impractically narrow channels for target droplet sizes below 5  $\mu\text{m}$ . The vane pitch  $b$  varied from 4.3 - 8.6 mm for different numbers of stages at a target droplet size of 5  $\mu\text{m}$ , and increased to 34.5 mm for a target droplet size of 20  $\mu\text{m}$  and 9 stages. The gas velocity varied between 2.1 - 4.2 m/s and decreased to 0.5 m/s, respectively. The variation in pressure loss between different numbers of stages was very small.

<sup>130</sup> Refer to chapter 1.2.

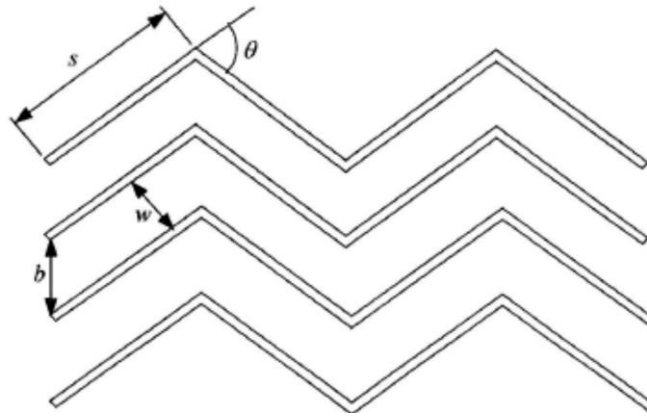


Fig. 6.2 Geometric parameters relevant to vane separator design, according to Wilkinson [70]<sup>131</sup>

Both authors quoted above both considered a particular basic geometry for which they tried to achieve the optimal geometrical parameters, given certain boundary conditions. Before optimal geometrical parameters are discussed, the next section summarizes from the previous chapters general aspects of vane separators that are expected to improve their performance. Taking these into consideration, as well as the applicable boundary conditions, a specific novel vane separator design will be introduced and tested experimentally, the results of which are discussed at the end of this chapter.

## 6.2 Optimizing vane separator geometry

### 6.2.1 General considerations

The following factors all have a positive influence on the droplet separation efficiency, but a negative influence on the pressure drop: increasing the gas velocity, reducing the channel width, increasing the bend angle, increasing the length of the straight sections, increasing the number of stages and introducing pick-off hooks (for low gas velocities). Keeping this in mind, the following points are observed while optimizing the design:

- Because high gas velocities promote high efficiencies, while enabling small cross-sectional areas and thus reducing costs, the general goal set forward is to achieve the prescribed separation efficiency at high gas velocities, without exceeding the prescribed pressure drop and/or the critical gas velocity.
- Based on the discussion on pick-off hooks in chapter 4.2.2, their incorporation in the design will be avoided.
- Some type of separated drainage, in addition to pure gravitational drainage, possibly through perforated plates, will be advantageous (as discussed in chapter 4.1.2.4).
- Following the discussion in chapter 4.1.3, convex corners should be of a smooth shape, reducing re-entrainment by film detachment, and avoiding increased pressure drop due to additional turbulent effects (recirculation zones).

<sup>131</sup> Reprinted from [70, p. 266].

- The straight sections should be just long enough for the droplet distribution to remix, without unnecessarily increasing total separator length and pressure drop.
- The combination of bend angle and length of straight section should prevent large droplets from *striking through*.

### 6.2.2 Optimizing the flow channel

It was ascertained in chapters 3.1.3 and 3.4.1 that the droplets entering each consecutive bend, tend to concentrate along its inner wall. In order to shift the entire flow towards the outer wall and thus suppress the outer low velocity regions, an offset is created between outer and inner walls of the bend, leading to a variable channel width that becomes narrower when approaching each bend (Fig. 6.3).



Fig. 6.3 Variable channel width of novel vane separator geometry

The offset between inner and outer walls naturally creates intermittent spaces between the corrugated plates, which can be utilized for drainage purposes, if a pathway for the liquid film to penetrate the wall and enter these volumes is provided. A straightforward manner to achieve this, is to apply perforations in the wall sections shortly downstream of each bend; where most of the inert droplets are separated. This is depicted in Fig. 6.4, in which the drainage channels are marked with *T* and the perforations with *Q*.

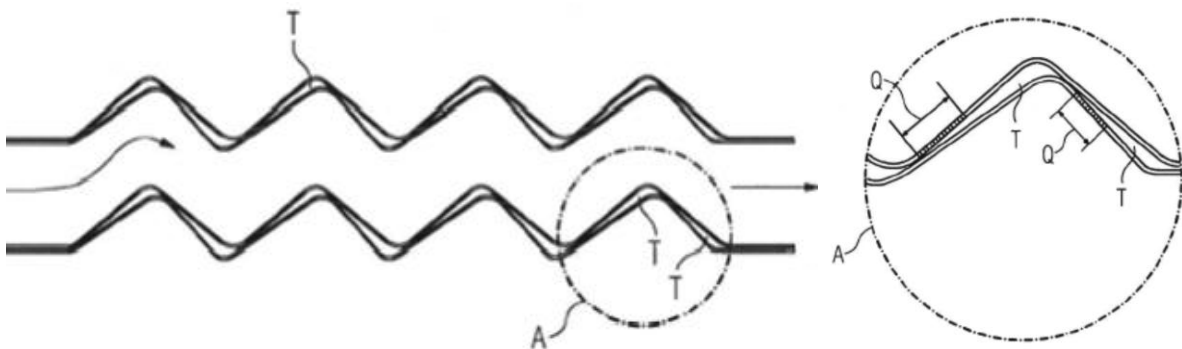


Fig. 6.4 Drainage channels and perforated walls of novel vane separator design<sup>132</sup>

The general design has thus been established. The specific geometrical parameters have not yet been quantified, because they vary with the specific application and boundary conditions.

<sup>132</sup> Reprinted from [46]. Courtesy of Siemens AG.

### 6.2.3 Boundary conditions

Before discussing an optimal vane separator geometry, the design goals must be defined and prioritized, as well as the boundary conditions under which these must be achieved. For instance: total cross-sectional area and mass flow could be fixed, and separation efficiency would be maximized while not exceeding a certain maximum pressure drop. As a practical example, the application of vane separators in a Moisture Separator & Reheater<sup>133</sup> shall be worked out, for which a vertical orientation in horizontal orthogonal flow is assumed, thus excluding non-orthogonal flow and gravitational effects. The following conditions shall be valid:

1. Inlet steam mass flow, moisture content and pressure are prescribed.
2. The total vane separator cross-section and thus the effective gas velocity can be manipulated within the limits allowed by the dimensions of the reheater tube bundles and the general design of the pressure vessel. Smaller cross-sections reduce costs, especially when they enable a reduction of the pressure vessel diameter and length.
3. A certain maximum droplet mass fraction at the vane separator outlet, as well as a certain maximum pressure drop shall not be exceeded. Staying within these limits, costs and secondly separation efficiency are optimized.
4. The vane separator inlet droplet size distribution can be manipulated by choosing a particular design of the coarse (cyclone) separator.
5. A certain conservative margin is observed, mainly due to uncertainties in actual physical parameters. These include uncertainties in actual droplet size distributions, partial load and transient conditions, but also a macroscopically uneven velocity field (due to the large dimensions of the vessel), producing regions of higher and lower effective gas velocities. The amount of re-entrainment is also a factor of uncertainty.

The following boundary conditions at the MSR inlet are defined for the subsequent design optimization:

- the steam is saturated at a pressure of 12 bar
- the inlet steam mass flow is 1300 kg/s
- the initial liquid mass fraction is 8%
- the droplet size distribution is given by Table 2 in chapter 3.6.2

Furthermore, the outlet liquid mass fraction shall not exceed 0.5% and the pressure drop shall not exceed 500 Pa.

### 6.2.4 Design optimization

The formula provided by *Kolev* [34, p. 366] for the separation efficiency of cyclone separators can be used to estimate the inlet droplet size distribution for downstream vane separators. The relevant geometrical parameters of the cyclone separator are its length, its inner and outer diameters and its blade angle. A representative cyclone separator for the current application could be 4 m in length, with an inner diameter of 0.5 m, an outer diameter of 1 m and a blade angle of 45°. This cyclone

---

<sup>133</sup>MSRs were introduced in chapter 3.3.

separator would be capable of separating nearly all droplets above 40  $\mu\text{m}$ , leading, for the prescribed inlet droplet distribution, to a separation efficiency of 83.3%. The resulting downstream droplet mass distribution for the prescribed inlet droplet mass distribution is depicted in Fig. 6.5. The liquid mass fraction has at this point been reduced to 1.4%. In order to further reduce the liquid mass fraction to 0.5%, the vane separator must perform well for droplets of 5 - 40  $\mu\text{m}$  in diameter.

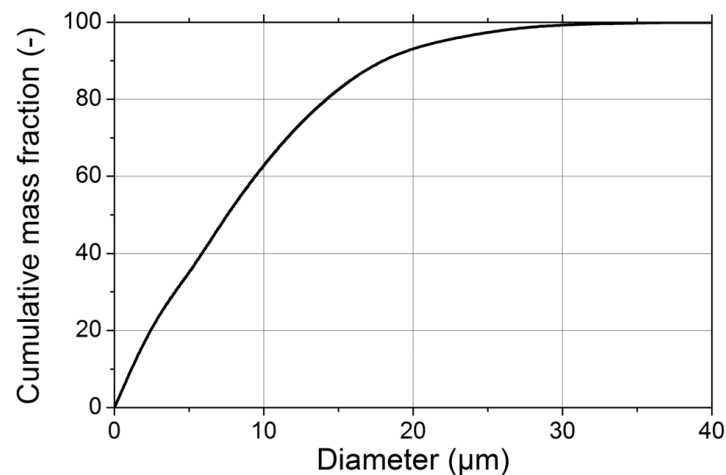


**Fig. 6.5** Theoretical droplet mass distribution downstream of a representative cyclone separator, based on the inlet distribution given in Table 2

Given the geometry introduced in chapter 6.2.1, it remains to specify the geometrical parameters for this example. The relevant points discussed throughout this paper, that should be kept in mind when deciding on a final geometry, are summarized in Table 10.

**Table 10** Consequences of sub-optimal design of vane separator geometry

	<b>Too small</b>	<b>Too large</b>
<b>Channel width</b>	- pressure drop increases - number of channels (manufacturing costs) increases	- insufficient efficiency for small droplet sizes - liquid film thickness (re-entrainment) increases
<b>Inner bend radius</b>	- liquid film detachment - recirculation zones - large pressure drop	- total vane separator length increases
<b>Bend angle</b>	- total vane separator length increases - possibility of <i>strike through</i> of large droplets	- pressure drop increases - channel pitch increases (parallel channels may require more space)
<b>Length of straight parts</b>	- possibility of <i>strike through</i> of large droplets - no remixing of droplet distribution	- pressure drop increases - total vane separator length increases
<b>Number of stages</b>	- conservative margin is not observed	- pressure drop increases

Considering the narrow passages in the channel, the inlet width is chosen not too small at 11.5 mm. Following Kall [29], the inner radius of 10 mm is of similar dimension as the channel width. From chapter 4.1.5, the critical air velocity for re-entrainment is expected to lie at 5 - 8 m/s. Although not

tested for steam, according to equation (4.36), the critical velocity is higher for steam than for air, but decreases with pressure (while the gas-to-liquid density ratio decreases). Choosing a gas velocity of 6 m/s as the design basis is justifiable only when re-entrainment is countered by re-separation of re-entrained droplets through a sufficient number of stages. The absence of pick-off hooks allows for a conservative number of 7 stages, representing an adequate margin for re-entrainment, without an unreasonable increase in pressure drop. To ensure the required separation efficiency, the bend angle is chosen at  $80^\circ$  and a straight channel section of 17.6 mm should allow proper remixing of droplets, while preventing *strike through* of large droplets. The resulting geometry is listed in Table 11.

**Table 11 Geometrical parameters of novel design**

inner bend radius	<i>m</i>	0.01
channel width	<i>m</i>	0.0115
total vane angle	<i>deg</i>	80
length of straight parts between bends	<i>m</i>	0.0176
number of stages	-	7

Given the cyclone separator introduced before, the theoretical separation efficiency of this vane separator for the resulting droplet mass distribution is 65.1%, leading to a combined efficiency of 94.2% and a resulting steam quality of 99.5%. The inlet, intermediate and outlet droplet mass fractions in this example are shown in Fig. 6.6, which also depicts both separation efficiencies. The figure typifies the cyclone as the *heavy duty* separator, necessary to separate the bulk of the liquid, while the vane separator is imperative to reach the prescribed steam quality in the presence of small droplets.

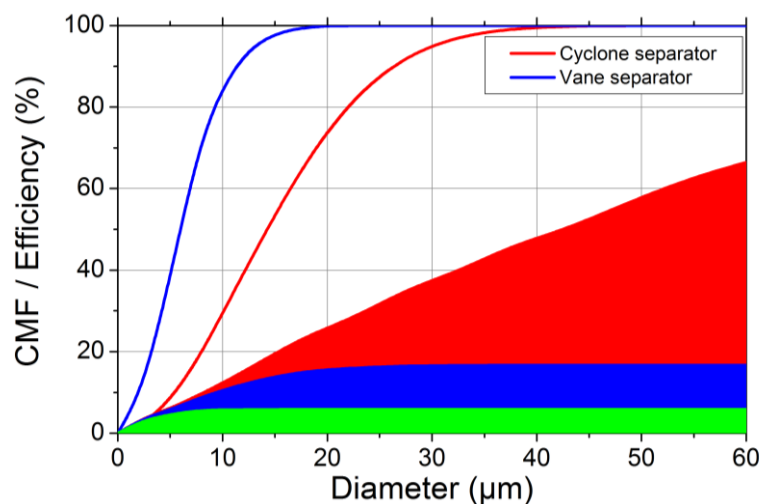


**Fig. 6.6** Cumulative droplet mass fractions at cyclone inlet (red), vane separator inlet (blue) and outlet (green) with cyclone separation efficiency (red line) and vane separator efficiency (blue line)

## 6.3 CFD results of the novel design

### 6.3.1 Comparison with the analytical model

The novel geometry was tested through numeric computation by Siemens AG Corporate Research & Technology in Moscow, using ANSYS CFX software. The numerical model included fully coupled flow and a Shear Stress Transport model for turbulence, with a low Re number approach near the walls. Water droplets of 10, 20, 30, 40, 50, 100, 200, 300, 400 and 500  $\mu\text{m}$  were considered, each group representing 10% of the total droplet mass, which was never more than 1% of the total mass flow. To simulate the physical conditions inside an MSR, the flow medium was saturated steam at a pressure of 12 bar. No phase changes were allowed. Homogeneous steam velocities of 1 - 10 m/s were investigated. The result for 6 m/s is depicted in Fig. 6.7, which also lists the separation efficiency after each of the uneven stages. More than 90% of the droplet mass is separated in the first stage, after which the subsequent double stages separate an additional 4%, 2% and 1.4% respectively. Noting that re-entrainment is not considered in the model, this testifies to the conservative nature of adding the last couple of stages to the design.

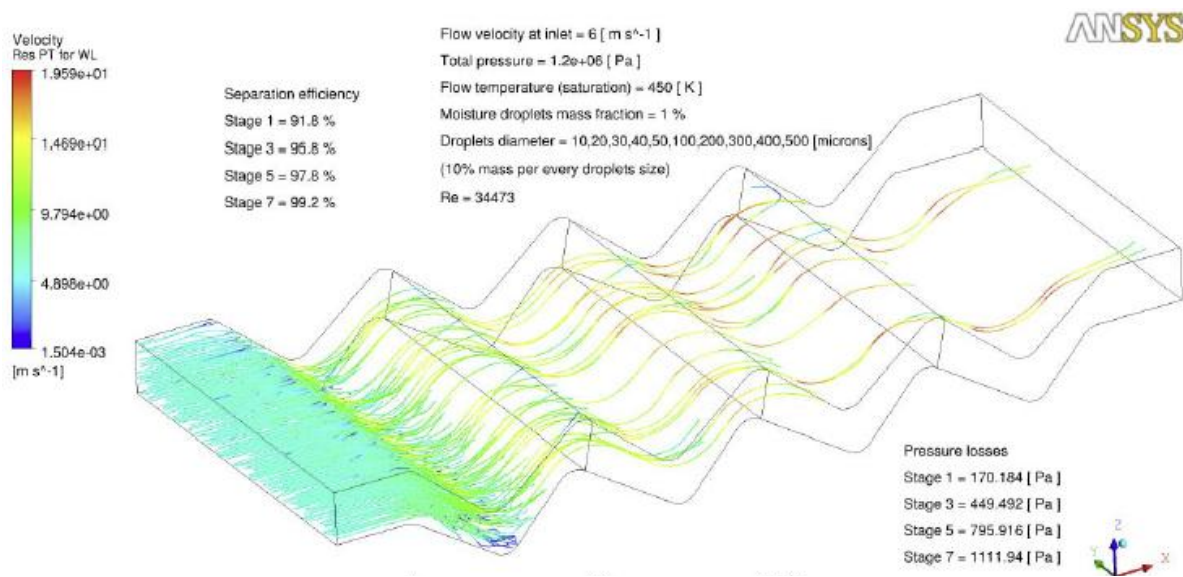


**Fig. 6.7 Particle tracking in the novel geometry, at a homogeneous steam velocity of 6 m/s and a pressure of 12 bar<sup>134</sup>**

The numerical results for the separation efficiency for the investigated steam velocities are depicted in Fig. 6.8, which also shows the results obtained from the analytical model (equation (3.122)). Especially at lower velocities, the analytical model predicts lower efficiencies than the numerical model. It is likely that the variable channel width, causing increased effective gas velocity around the bends that are not accounted for in the analytical model, has a positive effect on separation efficiency, especially at low velocities. A further explanation could be that turbulent effects play a positive role in separating small droplets at lower velocities. At homogeneous velocities beyond 5 m/s the results are in good agreement. Since the relevant input parameters for the analytical model do not differ for the novel design and the simplified geometry introduced in chapter 5.3.1; given the results of chapter 5.3, the analytical results can be considered representative for the simplified

<sup>134</sup>Courtesy of Siemens AG.

geometry. The direct comparison with the numerical model thus suggests an improved separation efficiency for the novel design features introduced in this chapter.

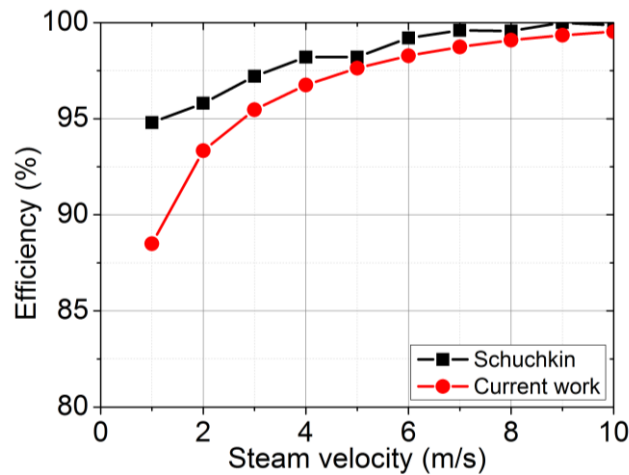


**Fig. 6.8** Numerical results with ANSYS CFX (black) as compared to the current analytical work (red) for the novel geometry with saturated steam at 12 bar

### 6.3.2 Comparison with a commercial geometry

Steinmüller GmbH also investigated the novel design *VS-2*, using ANSYS CFX software, and compared the results to numerical computations on a *Burgess Manning* design, under the same physical conditions as those described above (Fig. 6.9). At low gas velocities, the pick-off hooks in the *Burgess Manning* design increase the separation efficiency in comparison to the smooth geometry of *VS-2*. As the velocity increases, the separation efficiency of *VS-2* clearly increases, whereas that of the *Burgess Manning* geometry remains at around 95% for all depicted velocities. Since re-entrainment is not accounted for in the models, this is solely due to pressure stagnation in the pockets and turbulent eddies blocking their entrance.

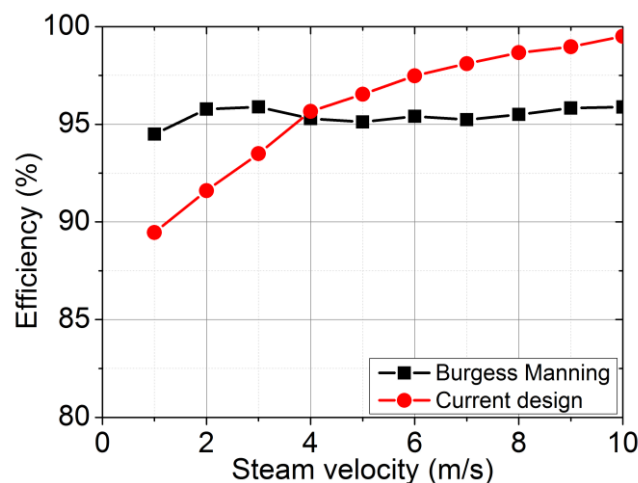


**Fig. 6.9** Burges Mining vane separator design (above) and numerical results (below) for this geometry (black) as compared to the current novel design *VS-2* (red)

From these results, the conclusion is drawn that *VS-2* is most effective beyond gas velocities of ca. 4 m/s. The main advantage of the novel design thus lies in its increased efficiency at higher gas velocities, which allows for a decreased number of vane separators to be installed. Recalling the difference in pressure drops between geometries with and without pick-off hooks (Fig. 4.29), the pressure drop of *VS-2* at this higher operational velocity is expected to remain below that of geometries with pick-off hooks operating at lower gas velocities.

## 6.4 Experimental results of the novel design

### 6.4.1 Research goals and experimental setup

For the novel design introduced in this chapter the same experiments were carried out as laid out in chapter 5.3. The goal of this investigation is to determine if the novel design is represented well by the analytical model described in this paper, as well as to ascertain if the performance has increased in direct comparison to its simplified counterpart, which was introduced in chapter 5.3<sup>135</sup>. The simplified model shall be referred to as *VS-1* and the novel design as *VS-2*. The experimental setup is identical to the description in chapter 5.3.2 and the test geometry consists of 9 parallel channels of 500 mm in height, manufactured from 3 mm Makrolon® (Fig. 6.10). Measurements were carried out with the same spray chamber velocities and the same approximate liquid mass fractions as for *VS-1*. The measurements points, including the effective air velocity through the channel and the achieved liquid mass fractions for *VS-2*, are listed in Table 12. The effective air velocities are smaller, because the blockage factor for *VS-2* is smaller, providing space for 9 parallel channels instead of 7 for *VS-1*.



Fig. 6.10 Schematic view of the optimized vane separator design (left)<sup>136</sup> and the test module (right)

<sup>135</sup> Because the values in Table 11, although in a sense averaged, equal the geometrical parameters for the simplified geometry provided in Fig. 5.20, the comparison is valid.

<sup>136</sup> Courtesy of Siemens AG.

Table 12 Measurement points for the experiments with the novel design (*VS-2*)

Spray chamber air velocity [m/s]	Effective air velocity [m/s]	Liquid mass fraction [%]
1.0	1.5	5.25
		4.88
		5.07
		5.57
2.0	2.9	5.19
3.0	4.4	5.80
4.0	5.8	5.56
5.0	7.3	5.25
		2.09
		3.63
		4.68
		5.32
		6.71
		8.40
8.75		
6.0	8.8	5.58
7.0	10.2	5.36
8.0	11.7	5.10
9.0	13.1	5.09
10.0	14.6	5.12

### 6.4.2 Results

The measured separation efficiencies for both geometries are depicted in Fig. 6.11. No significant differences can be discerned between the two geometries, although the decrease in separation efficiency for large effective air velocities (above ca. 12 m/s) appears to be less pronounced for *VS-2*.

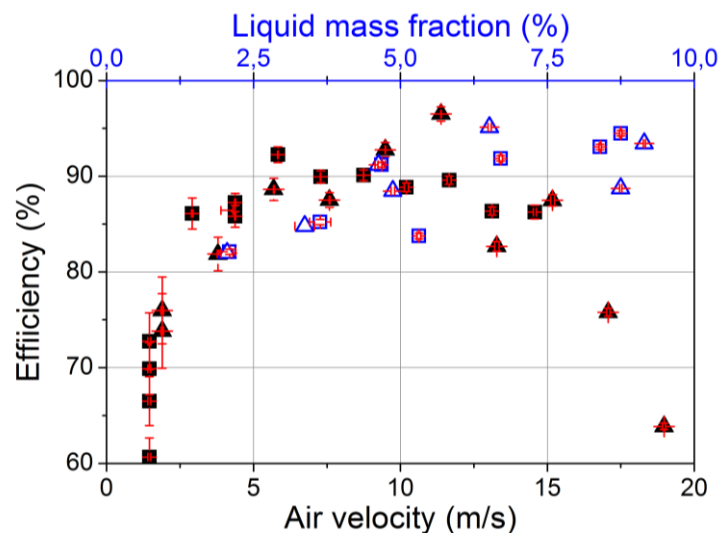
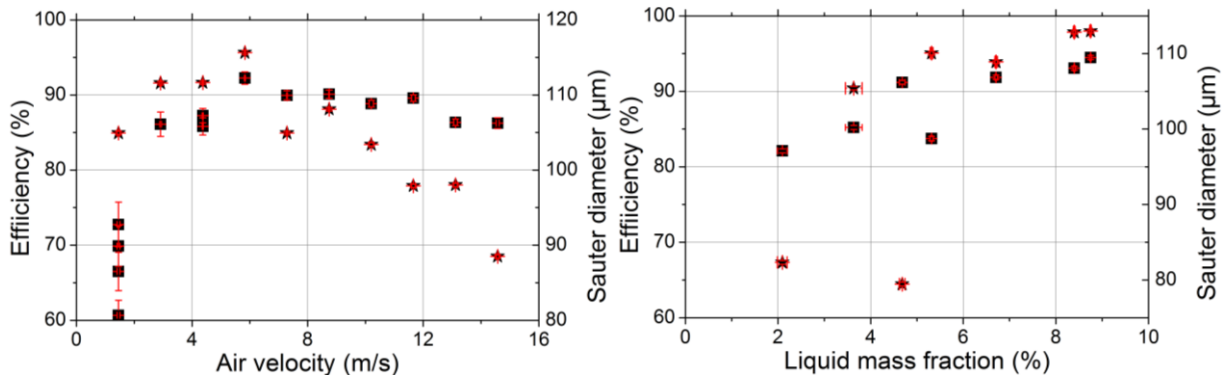


Fig. 6.11 Experimental efficiencies for *VS-1* (triangles) and *VS-2* (squares) for varying effective air velocity (closed symbols) and varying liquid mass fraction (open symbols)

This supposition is substantiated by Fig. 6.12, which depicts the correlation with the inlet Sauter mean diameter for VS-2. Compared to Fig. 5.27, the separation efficiency appears less affected by the decreasing inlet Sauter mean diameters at higher air velocities. The separation efficiency of VS-2 displays a more constant trend as that of VS-1 and remains between 82% and 95% for all recorded air velocities above 1.5 m/s, including the measurements with varying liquid mass fractions. In chapter 5.3.3.1 the correlation was attributed to the thicker liquid films that are associated with larger inlet Sauter mean diameters, and the resulting better gravitational drainage thereof. This implies that the drainage of the liquid film in VS-2 at high air velocities is less impaired by decreasing inlet Sauter mean diameters than in VS-1.



**Fig. 6.12** Measured droplet separation efficiencies (squares) and inlet Sauter mean diameters (stars) as a function of effective air velocity (left) and of liquid mass fraction (right)

The re-entrainment from the last stage, as discussed in chapter 5.3.3.2, was also observed for VS-2. The following results thus concern values obtained after application of the same cut-off filter at 40  $\mu\text{m}$ . The measured inlet and outlet droplet distributions and the predicted outlet droplet distributions are depicted in Fig. 6.13, exemplary for the measurements at 2% liquid mass fraction and at an effective air velocity of 5.8 m/s.

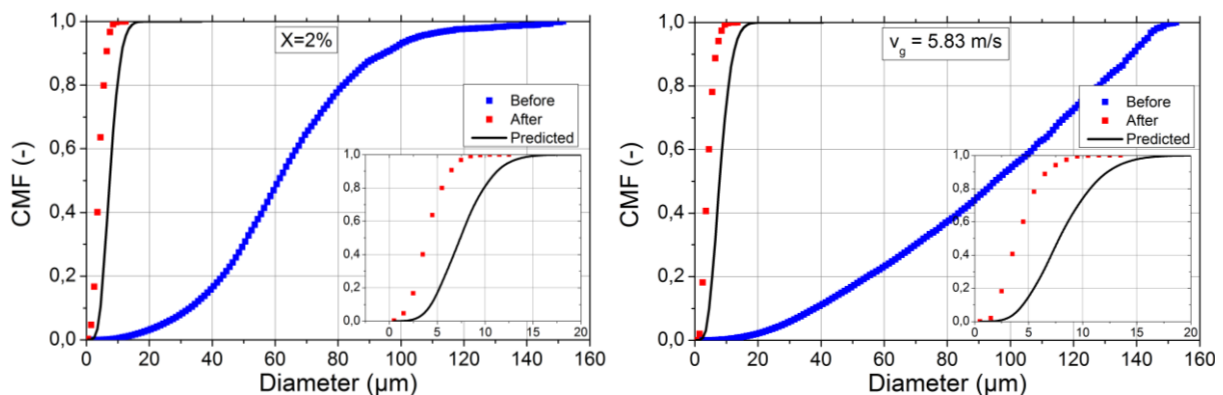


**Fig. 6.13** Cumulative droplet mass fraction before (blue) and after (red) the vane separator as compared to the model (black), for the measurements at 2% liquid mass fraction (left) and at an effective air velocity of 5.83 m/s (right)

The model results for *VS-1* were in good agreement with the measurements<sup>137</sup>, which implies that the model results in Fig. 6.13 can be considered representative for the performance of *VS-1* under the same conditions. It follows from these figures that the experimental separation efficiency of *VS-2* exceeds that of *VS-1*. The same conclusion can be drawn from the corresponding figures for the other measurements of *VS-2*, which are provided in appendix A.VI.

The outlet Sauter mean diameters for all recorded effective air velocities are depicted in Fig. 6.14. In accordance with Fig. 6.13, *VS-2* appears to be capable of separating smaller droplets at equal (effective) air velocities: with increasing air velocity, the outlet Sauter mean diameters settle at about 5  $\mu\text{m}$  and 3  $\mu\text{m}$  for *VS-1* and *VS-2* respectively. The outlet Sauter mean diameters for the recorded liquid mass fractions are depicted in the same figure on the right. No clear trend is discernible. The values for *VS-2* are again lower than those for *VS-1*, even though they are recorded at lower effective air velocities.

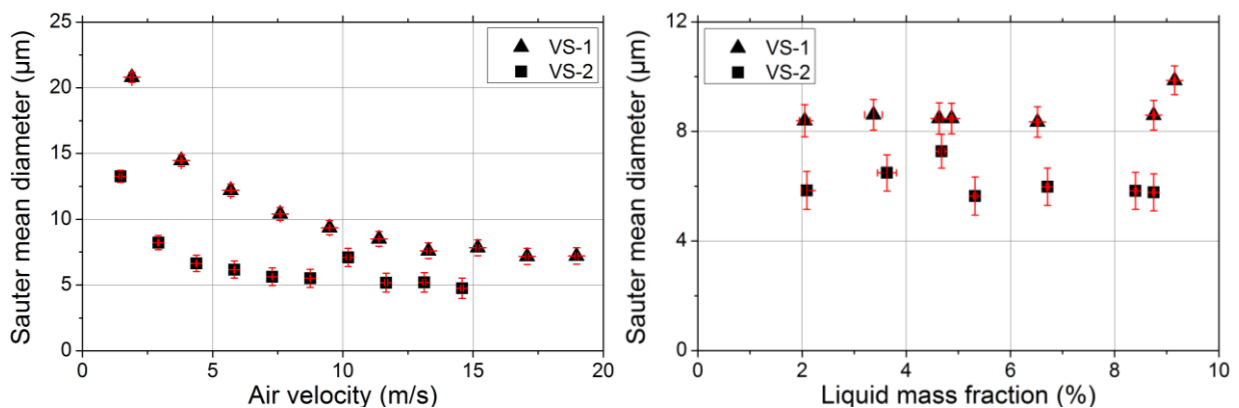


**Fig. 6.14** Experimental Sauter mean diameters at the outlet of *VS-1* (triangles) and *VS-2* (squares) for varying effective air velocities (left) and varying liquid mass fractions (right)

### 6.4.3 Discussion

Based on the Sauter mean diameter of the filtered outlet droplet size spectra, vane separator *VS-2* consistently outperforms *VS-1* throughout all measurements. The experimental separation efficiencies based on the measured liquid mass balances do not show a superior performance of *VS-2* and are in some cases even lower for *VS-2* than for *VS-1*, as can be deduced from Fig. 6.11. If this phenomenon is to be attributed to re-entrainment, the drainage in *VS-2* is apparently less effective than in *VS-1*, even though *VS-2* is equipped with perforated wall sections. It is plausible that this is partly caused by the slightly sharper corners of *VS-2*, because the contribution to *internal* re-entrainment, i.e. film detachment from the inner bend (as opposed to re-entrainment from the edge of the last stage), is expected to be larger for corners of smaller radii (compare *Owen & Ryley* [51] and the discussion in chapter 4.1.3). In addition, *VS-2* has a higher separation efficiency than *VS-1* only in the range of very small droplets. These will generally be separated in later stages and therefore have a shorter migration distance along the wall until the end of the last stage, where they are likely to be re-entrained. Nonetheless, these points would be less relevant if the perforations were very effective, which does not appear to be the case. The size and shape of the perforations are

<sup>137</sup> Refer to appendix A.V.

expected to play a role, as well as the wall thickness. Vertically elongated perforations likely help prevent the migration of liquid film across the perforated wall sections and thinner vane separator walls (e.g. 1 mm steel instead of 3 mm Makrolon®) might reduce capillary effects inside the borehole.

#### Quintessence

***The better performance of the novel vane separator design is clouded by re-entrainment effects. Adjusting for these effects the separation efficiency of the novel design is clearly higher at smaller droplet diameters, leading to smaller outlet Sauter mean diameters for all applied measurement conditions. Optimizing the wall perforations of the novel design is expected to reduce re-entrainment through more effective drainage. No correlation between separation efficiency and inlet liquid mass fraction can be discerned.***

#### 6.4.4 Pressure drop

Experimental values for the pressure drop as a function of effective air velocity are depicted in Fig. 6.15, for both geometries. As expected, VS-2 displays a higher pressure drop, caused by the variable channel width in contrast with the constant channel width of VS-1. In addition, the slightly sharper corners and the macroscopic roughness of the straight wall sections of VS-2, due to the perforations, can be expected to contribute to the pressure drop. The pressure drop ratio between VS-2 and VS-1 increases with air velocity, signifying a more than linear dependence.

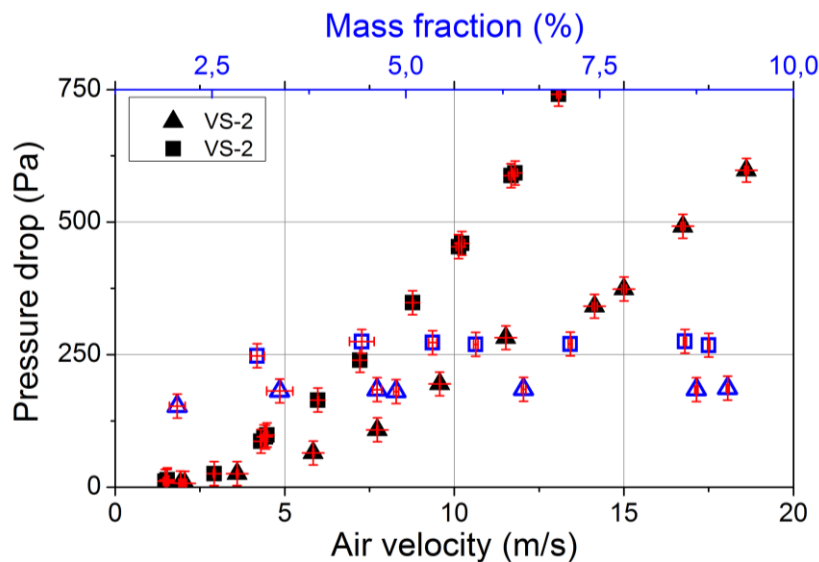


**Fig. 6.15** Pressure drop as a function of effective air velocity (closed symbols) and as a function of liquid mass fraction (open symbols) for VS-1 (triangles) and VS-2 (squares)

Fig. 6.15 also depicts pressure drops for both geometries as a function of liquid mass fraction. Again, the values for VS-2 are higher than those for VS-1. No specific dependence of the pressure drop on the liquid mass fraction can be discerned. This was also reported by *Galletti et al.* [17] and is consistent with most equations for the pressure loss coefficient (including those from *Wilkinson* [70]), as long as the mixture density of the continuum is not significantly affected. Pressure drops in

the range of a few 100 Pa at air velocities below 10 m/s are typical for vane separators (e.g. [64], [17]), with significantly higher pressure drops for vane separators with pick-off hooks (e.g. [42]). For effective air velocities up to 8 m/s, both geometries cause pressure drops below 300 Pa. Compared to the commonly accepted industrial standard of 400 Pa at nominal velocities, which is anywhere between 1 and 5 m/s depending on the type and amount of vane separators, both vane separator geometries perform well.

## 7 Conclusion

The comparison of the analytical model introduced in this paper with experiments, showed that, although not perfect, it is a very useful tool in predicting droplet separation efficiencies of vane separators of many shapes and sizes. Furthermore, numerical results gained from CFD, often with additional algorithms to convey some particular physical mechanism (e.g. entrainment effects, wall boundary conditions or turbulent effects), do not appear to perform much better than the analytical model, but cost much more effort and time. In addition, the discussed numerical models were often fine-tuned to fit the experimental data (e.g. by setting turbulence parameters). The absence of empirical parameters is a strong advantage of the analytical model<sup>138</sup>. Numerical models, however, can handle the complexity of many geometries that are not accounted for in the analytical model, the presence of pick-off hooks being the most prominent example. The analytical model appears to achieve decent predictions for many geometries, which led to the conclusion that straight type geometries are represented well by the model, but the quantitative impact of the simplification of complex geometries in the analytical model remains unknown. The representation of non-uniform velocity profiles proved helpful in explaining the vanishing separation efficiency at very small droplet diameters, but determining the actual width of the profile without comparative data is arbitrary and the impact of a more *skewed* profile has not been investigated. The same can be said for the representation of remixing of non-uniform droplet distributions.

The experiments provided several important insights. First of all, in the presence of re-entrainment it proves hard to achieve separation efficiencies close to unity. Specifically the carry-over of liquid film through the subsequent stages and the consequent re-entrainment from the edge of the last stage had a major impact, which is apparently correlated to the inlet droplet size distribution; the actual stage in which droplets are separated (i.e. the distance from the vane separator exit) playing an important role. The analysis of the cumulative droplet mass fractions, after application of a cut-off filter, allowed for a detailed investigation of the experimental results, with very satisfactory results. The symmetry of the nozzle distribution and the separation characteristics of the spray chamber proved relevant for the measurement of the inlet droplet size distribution. In the case of *asymmetric* nozzle distributions, larger droplets are thought to shoot past the PDA measuring point towards the opposite wall, causing a comparatively low number of them to be measured, which results in an *under-estimation* of the inlet Sauter mean diameter. In the case of *symmetric* nozzle distributions, larger droplets are thought to concentrate in the center of the channel, possibly also coalescing, causing a comparatively high number of them to be measured, which results in an *over-estimation* of the inlet Sauter mean diameter. Specifically for the experiment with varying gas velocity, the accumulation of larger droplets near the channel center caused an under-representation of smaller droplets in the PDA measurement data, leading to under-predicted cumulative droplet mass fractions in the range of very small droplets. It is noted that this automatically leads to a steeper profile for the cumulative mass fractions, as is visible in the data (appendix A.V-b), which means that the predicted separation efficiency does *not* necessarily have a stronger dependence on the droplet diameter than the experimental data suggests.

---

<sup>138</sup> With the exception of the width of the non-uniform velocity profile and the remixing of non-uniform droplet distributions.

The (predicted) contribution from the straight channel sections to the separation efficiency was not large enough for an isolated investigation. The reason is that the vane separator geometry under investigation already reached high efficiencies at low Stokes numbers, for which the relative contribution from the straight sections is very small (refer to Fig. 3.5). This effect is enhanced by the fact that a large number of stages are present, reducing the *relative* contribution from the straight sections to the *total* separation efficiency with each additional stage. Referring to Fig. 3.5, the straight channel sections become relevant in vane separators operating at higher Stokes numbers, e.g. when they are optimized for costs and/or space restrictions (comprising fewer number of stages and/or smaller bend angles).

The pressure drop measurements revealed that, even at higher Reynolds numbers, the low-Reynolds number formulation by *Wilkinson* [70] was in better agreement with experiment than his predictions following the high-Reynolds number regime change. *Wilkinson* [70] performed experiments on straight type geometries: it is likely that the round bends of the simplified model caused the turbulent effects underlying the regime change proposed by *Wilkinson* [70] to occur at higher Reynolds numbers. A dependence of the pressure drop on the liquid mass fraction can clearly be denied for liquid mass fractions below 10%.

The optimization of the vane separator design carried out in chapter 6, led to better separation characteristics in the range of very small droplets. Clouded by re-entrainment effects (caused by liquid film carry-over), this improvement was made evident through the analysis of the cumulative droplet mass fractions, for both sets of experiments, and most clearly visualized by the comparison of the outlet Sauter mean diameters. For the simplified design *VS-1* there was no improvement in separation efficiency beyond gas velocities of 12 m/s; for the novel design *VS-2* beyond gas velocities of 10 m/s, the difference being due to the earlier inducement of turbulent effects caused by the variable channel width of *VS-2*, in combination with its sharper corners and its perforations, which increased wall roughness. These channel characteristics were also the cause of the increased pressure drop of *VS-2*, in comparison with *VS-1*. A correlation between separation efficiency and liquid mass fraction was not evident.

It was shown that many physical phenomena of two-phase flow through vane separator channels find a representation in an analytical model of the droplet separation efficiency. The predictive power of the analytical model is satisfactory for the use as algorithm in larger numerical models, as well as in engineering methods for design, and is in many cases not inferior to numerical modeling. Its fast and simple application allows significant cost savings when determining the optimum geometrical parameters of the vane separator as a system component (e.g. the application in an MSR), for a given set of boundary conditions.

## 8 Summary

The industrial use of vane separators in steam power plants and their importance with regard to drying the steam is explained, through several examples of material erosion and a reference to thermo-dynamic efficiency. A short overview is provided of different vane separator types and their most relevant geometrical features. The intention of this paper is to extend the analytical description of droplet separation efficiency and improve its predictive power, allowing for a more effective and cheaper design process, as well as maintaining the possibility of its direct application in numerical simulations of the water-steam cycle. A number of papers on droplet separation in vane separators has been reviewed, in which most authors focus on experimental results and/or numerical simulations, presenting analytic results only in the form of a simple balance of forces, incorporating the basic physical mechanisms of inertia and drag along a circular path. Occasionally some form of remixing and/or turbulence is accounted for. Some authors fit experimental results using different empirical relations that are not always founded on a strong physical background. The relatively simple formulas for separation efficiency that were established before the widespread use of CFD tools, often achieve decent results in comparison with experiments. The exponential form of the separation efficiency, based on an analysis of droplet concentration along the vane separator bend, is chosen as the analytical foundation for the extending investigations introduced in this paper.

Different forces acting on droplets migrating in a gas velocity field are summarized and discussed, after which a simple numerical model is introduced for Lagrangian tracking of the droplet paths through a vane separator channel, resulting in an explicit representation of the contribution of the straight channel sections to the overall separation efficiency. Apart from centrifugal and drag forces, only the gravitational force is incorporated in the model and investigated in relation with the droplet separation efficiency. It can be concluded that its effect is significant only in combination with low Stokes numbers and correspondingly small centrifugal forces; for example for small droplets in slow-moving media through separators comprising only a few stages. The possibility of different spatial orientations of the vane separators, or the flow field itself, is accounted for in the model by allowing a rotation of the gas velocity vector. Such a rotation induces two counter-acting effects: it elongates the channel, increasing the effective length of both bends and straight sections, but it also widens the channel, increasing the effective channel width. Which of these is predominant, depends mainly on the bend angle of the channel and the angle of rotation, meaning that the maximum separation efficiency does not necessarily correspond to orthogonal flow conditions. In combination with gravitational effects, it turns out that this optimum is influenced by the gravity vector as well.

Measured and computed velocity profile inside the channel, reported by different authors, convey distortions of the flow field, consisting of low-velocity regions near the outside wall of the bends. The absence of the driving centrifugal force inside these wall boundary regions prevents smaller droplets with too little inertia from reaching the outer wall. The corresponding adjustment of the terminal radial droplet velocity results in a modified separation efficiency that vanishes at droplet diameters below the *escape diameter*, which is defined as the minimum droplet diameter required to cross the wall boundary region, possibly limited by the total bend angle. Above a certain droplet diameter, the modified separation efficiency is larger, due to the increased gas velocities outside the wall boundary region, as compared to uniform velocity profiles.

The phenomenon of a non-uniform droplet distribution after passage through the first bend, and its consequent remixing, is represented by a modified droplet volume fraction that accounts for the *magnitude* of the deformity of the droplet distribution at the entrance of the bend and the *rate* of remixing. The resulting modification of the separation efficiency is equivalent to a reduction of the total bend angle, due to the diminished droplet volume fraction in the first part of the bend. After the analysis of the different relevant parameters and physical phenomena, and their impact on single stage grade efficiency, the combination of single stage grade efficiencies into a total vane separator efficiency, for a given droplet distribution, is discussed.

An investigation of vane separator efficiency is not complete without discussing re-entrainment. Different mechanisms for re-entrainment exist; film detachment and droplet separation from liquid film flow being the most relevant for vane separators. Carry-over of liquid film through subsequent stages is also relevant, because, reaching the end of the last stage, the liquid film can detach and become re-entrained in the gas flow. In order to estimate liquid film carry-over, liquid film flow and liquid film thickness are analyzed, leading to a formulation of the maximum gravitational drainage, given the film flow angle and the geometry of the plate, and of the maximum carry-over mass flow, bound by the liquid film velocity, the film flow angle and the film thickness. These two limits identify the boundaries between which actual carry-over is expected to lie. If these limits are equalized, an alternative method emerges for the computation of liquid film thickness, varying with gas velocity and differing from the constant shearless Nusselt film thickness. This result is used to visualize the incoming droplet mass, the liquid film mass on the wall and the amount of liquid drained, in subsequent stages of a vane separator. It is shown that the separation characteristics of a vane separator can be significantly improved when carry-over of liquid film is diminished by providing additional drainage through perforations in the walls.

By analyzing the conditions for stability of the liquid film, several authors have arrived at different definitions for critical film flow and the onset of re-entrainment of droplets from the film, resulting in a wide range of critical film and gas velocities from literature. Comparing different sources investigating critical gas velocities through experiments, it is concluded that values between 5 - 8 m/s are most commonly reported. A comparison of sources reporting experimental and computed pressure drops for different types of vane separators, conveyed a general trend that the contribution of pick-off hooks to the separation efficiency decreases with increasing gas velocities, but their corresponding contribution to the pressure drop does not.

Several experiments reported in literature are compared with predictions from the analytical model introduced in this paper, which in most cases is in good agreement. It is concluded that straight type geometries, i.e. without rounded bends, are represented well by the model, and that the assumption of non-uniform velocity profiles can improve the agreement with experiment, although many of the vane separators under investigation feature relatively complex geometries (e.g. with pick-off hooks), the simplification of which in the analytical model is difficult to evaluate, let alone quantify. The experiments performed on a simplified vane separator geometry provide additional insight. The measured separation efficiency, and implicitly also re-entrainment, appears to be correlated to the Sauter mean diameter of the inlet droplet distribution. This is explained by the earlier separation of larger droplets, increasing the average migration distance toward the end of the separator as well as downward film flow velocity, thus limiting carry-over and improving gravitational drainage. After

compensating for liquid film carry-over and consequent re-entrainment at the edge of the last stage, the cumulative droplet mass fractions at the separator outlet, from experiment and model, are in very good agreement, especially so for the experiment with varying liquid mass fractions. The liquid mass fraction has no impact on droplet separation efficiency in the recorded range of 2 - 9%. The slight discrepancy in the predictions for the experiment with varying gas velocity is thought to be related to non-uniform droplet distributions at the PDA recording point shortly downstream of the spray chamber. The conditions of the experiments did not allow an isolated investigation of the contributions from the straight channel sections to the overall separation efficiency, and these are, for the given physical conditions and vane separator geometry, too small for a quantitative discussion. The pressure drop as a function of gas velocity is represented well by the model from *Wilkinson* [70], although his proposed regime change for higher Reynolds numbers leads to disagreement with the experiment. The liquid mass fraction appears to have no effect on pressure drop in the recorded range.

Based on the investigations presented in this paper, a novel vane separator design is proposed, incorporating the major findings in earlier chapters. Exemplary boundary conditions are defined for the particular industrial application inside an MSR, according to which the remaining physical and geometrical parameters are determined that are expected to lead to an optimum geometry. The example is worked out using a simple analytical formulation of a cyclone separator and the analytical vane separator model introduced in this paper. Numerical computations on the resulting geometry display higher separation efficiencies, as compared to the model predictions, especially at low gas velocities, which is thought to be due to increased gas velocities around the narrowed bends, which are not accounted for in the analytical model. A numerical comparison with a commercial geometry featuring pick-off hooks, showed that for saturated steam at 12 bar, the novel design has a higher separation efficiency than the commercial design for gas velocities above 4 m/s. From the liquid mass flow balances measured during the experiments performed on the novel design, no clear advantage can be discerned in comparison with the measurements on the simplified design, apart from a more consistent separation efficiency at high gas velocities, visible also from the comparison with the inlet Sauter mean diameters. Both the analysis of the cumulative droplet mass fractions and the comparison of the outlet Sauter mean diameters, clearly convey the increased separation characteristics of the novel design. While the increased separation efficiency is at very small droplet diameters, which are separated later in the channel and thus have a large probability for re-entrainment from the last stage, the increased performance does not show, without the isolation of re-entrainment effects. The pressure drop of the novel design is about twice as high as that of the simplified design, but, with a value of 300 Pa at a velocity of 8 m/s, remains very acceptable.

It is concluded that the analytical model presented in this paper represents a useful tool in predicting droplet separation efficiencies of vane separators of different shapes and sizes, and that its predictive power is satisfactory for the intended applications.

## 8.1 Summary of scientific results

Although the 'classical' equation for the separation efficiency that forms the basis of the analytical work in this paper, was formulated several decades ago, few efforts to extend this analysis, on a physical rather than an empirical basis, such as to allow a broader investigation into the dependence

of the separation efficiency on its input parameters, as has been provided in this paper, have been reported in literature.

The additional droplet separation due to droplet relaxation in straight channel parts had not been explicitly reported and its impact on separation efficiency has firstly been defined.

Droplet migration across low-velocity wall-boundary regions has been investigated mainly through the application of CFD. The analytical relations for the limiting droplet escape diameters reported in this paper are new, and the decrease in separation efficiency due to impaired droplet migration across low-velocity wall-boundary regions, had thus far not been expressed in analytical terms.

The interdependence of the impacts of gravity and non-orthogonal gas flow through the vane separator channels and its quantification along a continuous spectrum of geometrical and physical parameters is a novelty.

This paper provides a connection between film flow angle, film thickness and carry-over of liquid film for arbitrary vane separator geometries, and a quantification of the related re-entrainment in terms of deteriorated total separation efficiency. The use of this result to provide an approximation for the average liquid film height for the given conditions also embodies a new approach to this topic.

### **8.2 Proposal for future work**

Several physical phenomena have been discussed in this paper, for which experimental data for a proper validation are lacking. An experimental validation of the presented investigation into the impact of the spatial orientation of vane separators, both with respect to gravity as with respect to the gas flow field, would be very interesting, especially because such conditions are quite common in industrial applications.

Measurements of the terminal radial droplet velocity across low-velocity wall boundary regions, and in general through non-uniform velocity profiles, would help to quantify their impact on separation efficiency (as well as validate numerical models for droplet motion). These experiments could include measurements in straight wall sections of vane separator channels and would then also provide insight into the redistribution of droplets in these sections, allowing for a validation of remixing models and a testing of the suggested formula for non-uniform droplet distributions. Such measurements could be performed with PDA systems, although high-speed camera recordings would also provide very interesting data.

Liquid film flow and film flow angles have been investigated and experimental data on these subjects is available. Nonetheless, the relationship between shear gas velocity, liquid mass fraction, liquid film thickness and film flow angle, in combination with perforated walls, would certainly provide valuable data for further investigation of this subject. Carry-over of liquid film had a major impact on the presented results. Investigating the effectiveness of gravitational drainage in this context, as well as the effectiveness of different perforation types (e.g. holes or slits), would certainly be invaluable to the potential reduction of carry-over and possibly of droplet re-entrainment from liquid films in general.

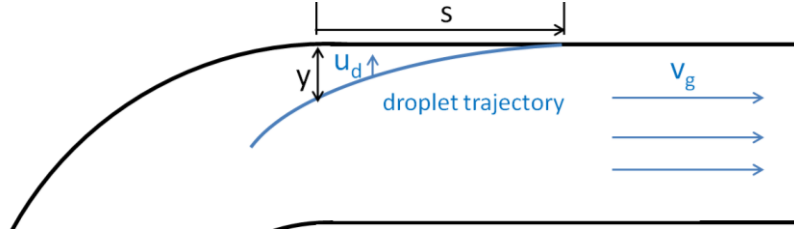
# Appendices

- A.I Determination of droplet radial velocity in straight sections
- A.II Gravitational influence on efficiency in inlet and outlet sections
- A.III Quantitative analysis of gravitational influence on efficiency
- A.IV Physical parameters of an air-water system
- A.V Experimental results for a wavy vane separator
- A.VI Experimental results for the novel vane separator design



## A.I Determination of droplet radial velocity in straight sections

The trajectory of a droplet exiting the bend and entering the straight section is schematically shown in A. Fig. 1.



A. Fig. 1 Droplet trajectory in straight section

The time  $\Delta\tau$  it takes for a droplet, after leaving the previous bend, to reach a given location  $s$  on the wall of the straight section, equals

$$\Delta\tau = s/v_g \quad (1.1)$$

The terminal radial velocity with which it leaves the bend is given by

$$u_{d,term} = \frac{\Delta\tau_{gd}v_g^2}{r} = \frac{\Delta\tau_{gd}v_g^2}{R_{out} - y} \quad (1.2)$$

in which  $r$  is the radial position of the droplet and  $y$  is the distance from the outer wall. The radial velocity of the droplet in the straight section, at a given time  $\tau$  after exiting the bend, was determined by equation (3.37), resulting in

$$u_d(\tau) = u_{d,term} \exp\left(\frac{-\tau}{\Delta\tau_{gd}}\right) = \frac{\Delta\tau_{gd}v_g^2}{R_{out} - y} \exp\left(\frac{-\tau}{\Delta\tau_{gd}}\right) \quad (1.3)$$

The radial distance  $y$  (i.e. the distance perpendicular to the plane of the wall) that has been traversed by the droplet as it hits the wall at position  $s$  at time  $\Delta\tau$ , is then given by

$$y = \int_0^{\Delta\tau} u_d(\tau) d\tau = \int_0^{\Delta\tau} \frac{\Delta\tau_{gd}v_g^2}{R_{out} - y} \exp\left(\frac{-\tau}{\Delta\tau_{gd}}\right) d\tau = \frac{(\Delta\tau_{gd}v_g)^2}{R_{out} - y} \left\{ 1 - \exp\left(\frac{-\tau}{\Delta\tau_{gd}}\right) \right\} \quad (1.4)$$

Combining equations (1.1) and (1.4) and solving for  $y$  with use of the quadratic formula, leads to

$$y = \frac{R_{out}}{2} \pm \sqrt{\left(\frac{R_{out}}{2}\right)^2 - (\Delta\tau_{gd}v_g)^2 \left\{ 1 - \exp(-s/\Delta\tau_{gd}v_g) \right\}} \quad (1.5)$$

Rejecting the plus sign in front of the square root and making use of the approximation  $\sqrt{a^2 - \varepsilon} \approx a - \varepsilon/(2a)$ , valid for  $\varepsilon \ll a$ , leads to

$$y \approx \frac{(\Delta\tau_{gd}v_g)^2}{R_{out}} \left\{ 1 - \exp\left(\frac{-s}{\Delta\tau_{gd}v_g}\right) \right\} \quad (1.6)$$

The terminal radial velocity at the bend exit, of a droplet hitting the wall in the straight section at the location  $s$ , is thus given by

$$u_{d,term} = \frac{\Delta\tau_{gd}v_g^2}{R_{out} - \frac{(\Delta\tau_{gd}v_g)^2}{R_{out}} \left\{ 1 - \exp\left(\frac{-s}{\Delta\tau_{gd}v_g}\right) \right\}} = \frac{\Delta\tau_{gd}}{\frac{R_{out}}{v_g^2} - \frac{\Delta\tau_{gd}^2}{R_{out}} \left\{ 1 - \exp\left(\frac{-s}{\Delta\tau_{gd}v_g}\right) \right\}} \quad (1.7)$$

The droplet radial velocity in the straight section, for a droplet being separated at position  $s$ , equals

$$u_d(s) = \frac{\Delta\tau_{gd} \exp\left(\frac{-s}{\Delta\tau_{gd}v_g}\right)}{\frac{R_{out}}{v_g^2} - \frac{\Delta\tau_{gd}^2}{R_{out}} \left\{ 1 - \exp\left(\frac{-s}{\Delta\tau_{gd}v_g}\right) \right\}} = \frac{\tilde{u}_d(s)}{1 - \left(\frac{\Delta\tau_{gd}v_g}{R_{out}}\right)^2 \left\{ 1 - \exp\left(\frac{-s}{\Delta\tau_{gd}v_g}\right) \right\}} \quad (1.8)$$

in which  $\tilde{u}_d(s)$  is the approximated radial droplet velocity defined by equation (3.43) in chapter 3.1.4. For small droplets, in the regime  $\Delta\tau_{gd} \ll 1$ , the approximation  $u_d(s) \approx \tilde{u}_d(s)$  is valid.

## A.II Gravitational influence on efficiency in inlet and outlet sections

The ratio of separated and inlet mass flows for curved vane separator sections under the influence of gravity was given by equation (3.52):

$$d \ln \dot{m}_d = -\frac{u_d}{v_d} \frac{R_{out}}{\delta_R} d\theta = -\frac{\Delta \tau_{gd}}{\delta_R} \left( v_g + \frac{R_{out}}{v_g} g \cos \alpha \cos(\beta - \theta) \right) d\theta \quad (2.1)$$

For inlet sections at positive  $x$ -coordinates, this equation is integrated between the limits  $\theta = 0 \rightarrow \varphi/2$ , resulting in

$$[\ln \dot{m}_d]_0^{\varphi/2} + C = -\frac{\Delta \tau_{gd}}{\delta_R} \left[ v_g \varphi/2 - \frac{R_{out}}{v_g} g \cos \alpha \{ \sin(\beta - \varphi/2) - \sin \beta \} \right] \quad (2.2)$$

For inlet sections at negative  $x$ -coordinates, this equation is integrated between the limits  $\theta = \pi - \varphi/2 \rightarrow \pi$ , resulting in

$$\begin{aligned} [\ln \dot{m}_d]_{\pi-\varphi/2}^{\pi} + C &= -\frac{\Delta \tau_{gd}}{\delta_R} \left[ v_g \varphi/2 - \frac{R_{out}}{v_g} g \cos \alpha \{ \sin(\beta - \pi) - \sin(\beta - \pi + \varphi/2) \} \right] \\ &= -\frac{\Delta \tau_{gd}}{\delta_R} \left[ v_g \varphi/2 - \frac{R_{out}}{v_g} g \cos \alpha \{ \sin(\beta + \varphi/2) - \sin \beta \} \right] \end{aligned} \quad (2.3)$$

For outlet sections at positive  $x$ -coordinates, this equation is integrated between the limits  $\theta = -\varphi/2 \rightarrow 0$ , resulting in

$$[\ln \dot{m}_d]_{-\varphi/2}^0 + C = -\frac{\Delta \tau_{gd}}{\delta_R} \left[ v_c \varphi/2 - \frac{R_{out}}{v_c} g \cos \alpha \{ \sin \beta - \sin(\beta + \varphi/2) \} \right] \quad (2.4)$$

For outlet sections at negative  $x$ -coordinates, this equation is integrated between the limits  $\theta = \pi \rightarrow \pi + \varphi/2$ , resulting in

$$\begin{aligned} [\ln \dot{m}_d]_{\pi}^{\pi+\varphi/2} + C &= -\frac{\Delta \tau_{gd}}{\delta_R} \left[ v_g \varphi/2 - \frac{R_{out}}{v_g} g \cos \alpha \{ \sin(\beta - \pi - \varphi/2) - \sin(\beta - \pi) \} \right] \\ &= -\frac{\Delta \tau_{gd}}{\delta_R} \left[ v_g \varphi/2 + \frac{R_{out}}{v_g} g \cos \alpha \{ \sin(\beta - \varphi/2) - \sin \beta \} \right] \end{aligned} \quad (2.5)$$

It is now easy to see that the addition of equations (2.2) and (2.5), as well as the addition of equations (2.3) and (2.4), both of which imply an *even* number of stages, lead to the *cancellation* of

the contributions of gravity in these equations. Thus, for a single stage ( $n = 1$ ) the resulting efficiency is:

$$\eta = 1 - \exp\left(-\frac{\Delta\tau_{gd}v_c\varphi}{\delta_R}\right) \quad (2.6)$$

The addition of equations (2.2) and (2.4), and the addition of equations (2.3) and (2.5), which both imply an *uneven* number of separation stages, lead to an *addition* of the contributions of gravity to that of a full bend, thus ultimately resulting in equation (3.58):

$$\eta_C = 1 - \exp\left[-\frac{\varphi\Delta\tau_{gd}v_c}{\delta_R} \mp \frac{2\Delta\tau_{gd}R_{out}}{\delta_R v_c} g \cos\alpha \cos\beta \sin(\varphi/2)\right] \quad (2.7)$$

## A.III Quantitative analysis of gravitational influence on efficiency

The default input parameters for the ceteris paribus calculations are given in A. Table 1 below. The number of stages is either 4 or 5; for even or uneven numbers of stages. In all cases, inlet and outlet sections are included, leading to an effective number of curved sections of  $n + 1$ . Configurations are abbreviated with  $U$ ,  $Ep$  and  $En$  for uneven number of stages and even number of stages with inlet oriented towards positive and negative  $x$ , respectively.

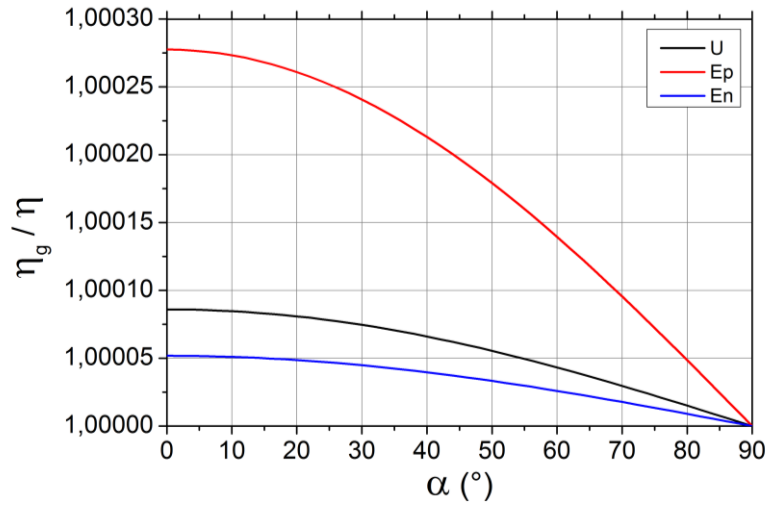
A. Table 1 Default input parameters

$D_d$	20	$\mu m$
$v_g$	5	$m s^{-1}$
$\mu_g$	20	$mg m^{-1} s^{-1}$
$\varphi$	80	$deg$
$n$	4 / 5	-
$\delta_R$	1	$cm$
$R_{out}$	2	$cm$
$L$	6	$cm$
$\alpha$	0	$deg$
$\beta$	30	$deg$

### A.III-a Geometrical and gravitational variations

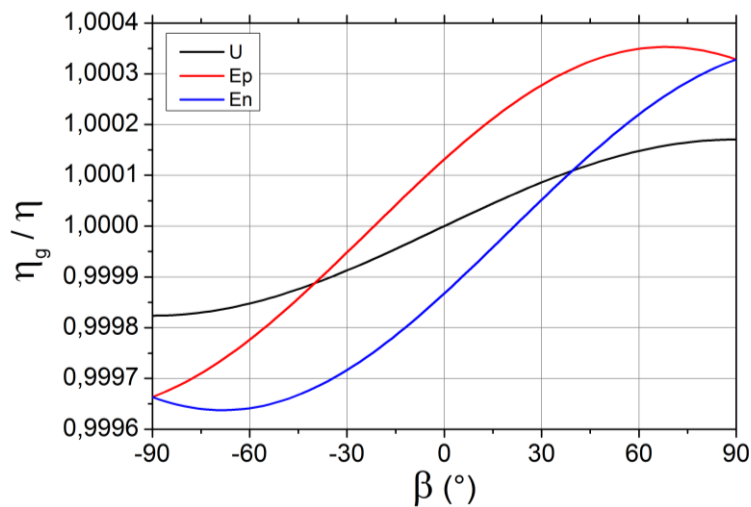
A. Fig. 2 depicts the separation efficiency as a function of the gravitational angle  $\alpha$ , normalized with the equivalent separation efficiency without the influence of gravity<sup>139</sup>. The influence of gravity for  $\alpha = 90^\circ$  is zero and grows as  $\alpha \downarrow 0^\circ$ . All contributions are positive, because the velocity and the gravity vector are in the same half-plane. The largest impact is recorded for an even number of stages with an inlet towards positive  $x$ .

<sup>139</sup>The results for even and uneven number of stages are normalized using different separation efficiencies with the corresponding numbers of stages.



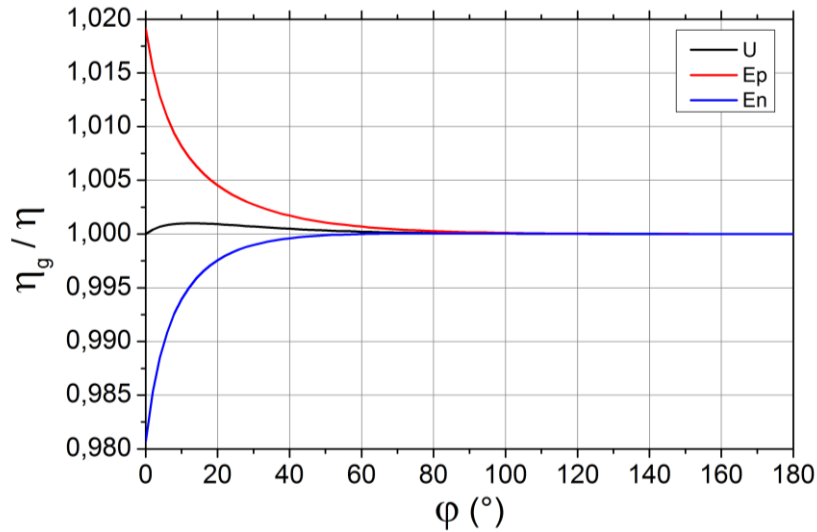
A. Fig. 2 Normalized separation efficiency as a function of the gravitational angle  $\alpha$

A. Fig. 3 depicts the separation efficiency as a function of the gravitational angle  $\beta$ . The influence of gravity for an uneven number of stages is zero at  $\beta = 0^\circ$ , because the contributions in the curved sections, including inlet and outlet, in this case cancel. The contribution of gravity tends to increase for increasing  $\beta$ , representing an increasing alignment with the gas velocity vector. It is noteworthy that the maximum and minimum separation efficiencies are not at  $\beta = \pm 90^\circ$ , but lie at  $\beta \approx \pm 69^\circ$ . This is explained by the fact that, for the asymmetrical configurations, there is an optimum orientation at which the gravity vector does not fully align with the velocity vector, but is slightly slanted towards the side with the greatest number of bends. This optimum is at  $\beta = 0^\circ$  in the limit  $\varphi \downarrow 0^\circ$  and approaches  $\beta = 90^\circ$  for  $\varphi \rightarrow 180^\circ$ . It further approaches  $\beta = 90^\circ$  for an increasing number of stages  $n \rightarrow \infty$ .



A. Fig. 3 Normalized separation efficiency as a function of the gravitational angle  $\beta$

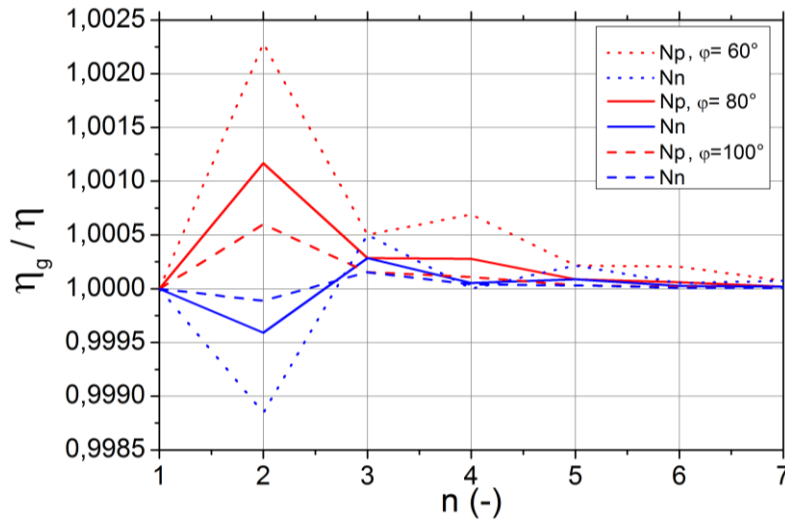
The gravitational influence as a function of the vane angle  $\varphi$  is plotted in A. Fig. 4. As  $\varphi$  increases, the increasing separation efficiency in the curved sections increasingly dominates the contribution of gravity in the straight sections, resulting in a general tendency toward unity. The maximum contribution of gravity thus lies at very small angles of  $\varphi$  and further increases for  $\beta \rightarrow 0^\circ$ . The contribution of gravity for configurations with an uneven number of stages is much smaller, being positive (negative) for positive (negative) angles  $\beta$ .



A. Fig. 4 Normalized separation efficiency as a function of total bend angle  $\varphi$

A. Fig. 5 depicts the normalized separation efficiency as a function of the number of stages  $n$ .  $Np$  and  $Nn$  refer to the orientation of the inlet toward positive or negative  $x$ , respectively. For  $n = 1$ , the contribution of gravity from the single stages is cancelled by the contributions from the inlet and outlet section<sup>140</sup>. For configurations with an uneven number of stages, their orientation ( $Np$  or  $Nn$ ) has no effect on the outcome (refer to equation (3.74)). For  $\beta = 0^\circ$ , the contribution of gravity would be zero for all uneven number of stages. For an increasing number of stages, the separation efficiency tends towards unity and the relative contribution due to gravity decreases. Consistent with A. Fig. 4, the contribution *increases* with *decreasing*  $\varphi$ . Consistent with A. Fig. 3, the difference between the two configurations with an even number of stages ( $Np$  and  $Nn$ ) decreases as  $\beta \rightarrow 90^\circ$  (not depicted). In all figures, due to the particular *physical* default parameters, the contribution from gravity is very small.

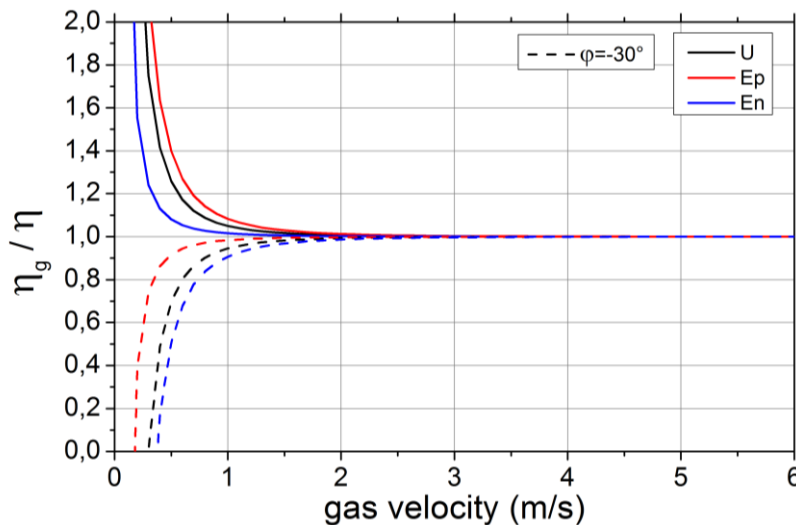
<sup>140</sup>It is noted that this result for  $n = 1$  does not signify that gravity has no contribution to the separation efficiency of a single bend. If inlet and outlet sections are not present, this contribution does not cancel and has a non-zero value.



A. Fig. 5 Normalized separation efficiency as a function of the number of stages

### A.III-b Variation of physical parameters

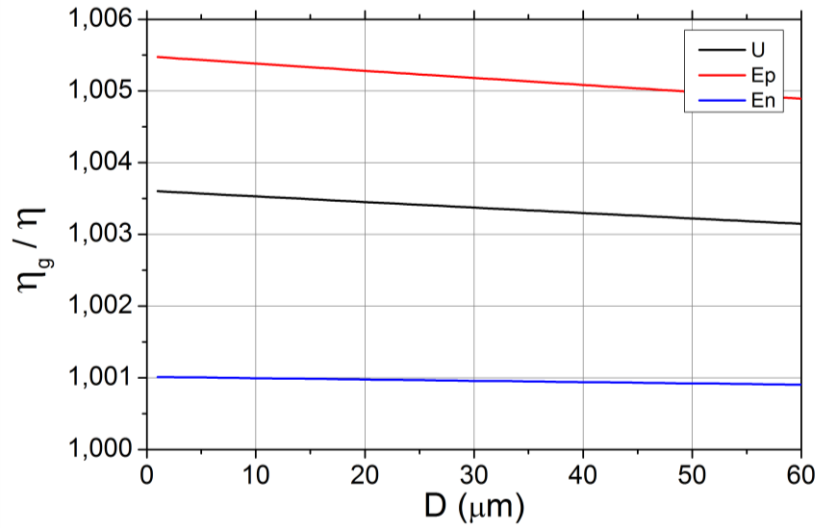
Regarding the influence of gravity, the two most significant physical parameters are the gas velocity and the droplet diameter. A. Fig. 6 depicts the impact of the gas velocity on the contribution from gravity to the separation efficiency. With increasing gas velocity, the separation efficiency tends to unity and the relative contribution from gravity decreases. For  $v_g \downarrow 0$  m/s, the contribution from gravity tends towards positive (negative) infinity for positive (negative) angle  $\beta$ , because in this limit, the gravitationally incited terminal radial droplet velocity drives more droplets towards the wall, than can be replenished by the incoming gas flow. The equations tend to break down for  $v_g^2 / R_{out} < g$ .



A. Fig. 6 Normalized separation efficiency as a function of gas velocity

A. Fig. 7 depicts the gravitational influence for different droplet diameters. Contrary to the intuitive expectation that the contribution from gravity would *increase* with increasing droplet diameter,

relative to the separation efficiency without gravity, it *decreases*. The reason is that the exponential powers for the curved sections and for the contribution of gravity from the straight sections ( $C$  and  $H_{\pm}$  in equations (3.68) and (3.72), respectively) are linear in  $D_d$ , but the general contribution from the straight sections ( $S$  in equation (3.71)) is quadratic in  $D_d$ . Thus, for increasing droplet diameter, the *non-gravitational* contribution to the separation efficiency increases faster than the *gravitational* contribution.



A. Fig. 7 Normalized separation efficiency as a function of droplet diameter



## A.IV Physical parameters of an air-water system

The relevant physical parameters of the air-water system at which the experiments at the Institute of Fluid Mechanics (LSTM) of the Friedrich-Alexander University in Erlangen-Nuremberg were performed, are listed in the table below.

**A. Table 2 Physical parameters of the applied air-water system**

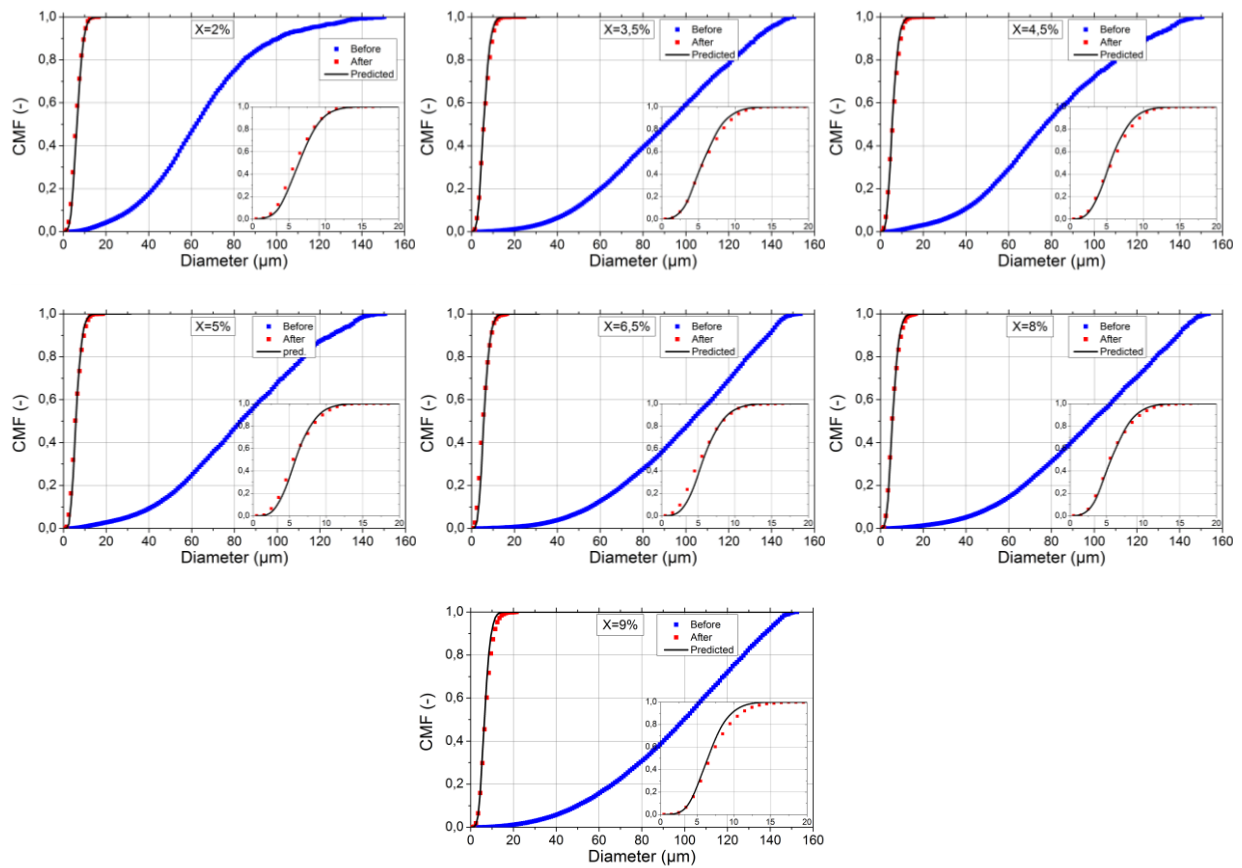
$g$	gravitational acceleration	9.8	$m s^{-2}$
$p$	pressure	$1 \cdot 10^5$	$Pa$
$T$	temperature	20	$^{\circ}C$
$\mu_f, \mu_l$	dynamic viscosity of water	$1.0 \cdot 10^{-3}$	$kg m^{-1} s^{-1}$
$\mu_g$	dynamic viscosity of air	$1.8 \cdot 10^{-5}$	$kg m^{-1} s^{-1}$
$\rho_f, \rho_l$	density of water	958	$kg m^{-3}$
$\rho_g$	density of air	1.2	$kg m^{-3}$
$\sigma$	surface tension water-air	0.078	$kg s^{-2}$



# A.V Experimental results for a wavy vane separator

## A.V-a Varying liquid mass fraction

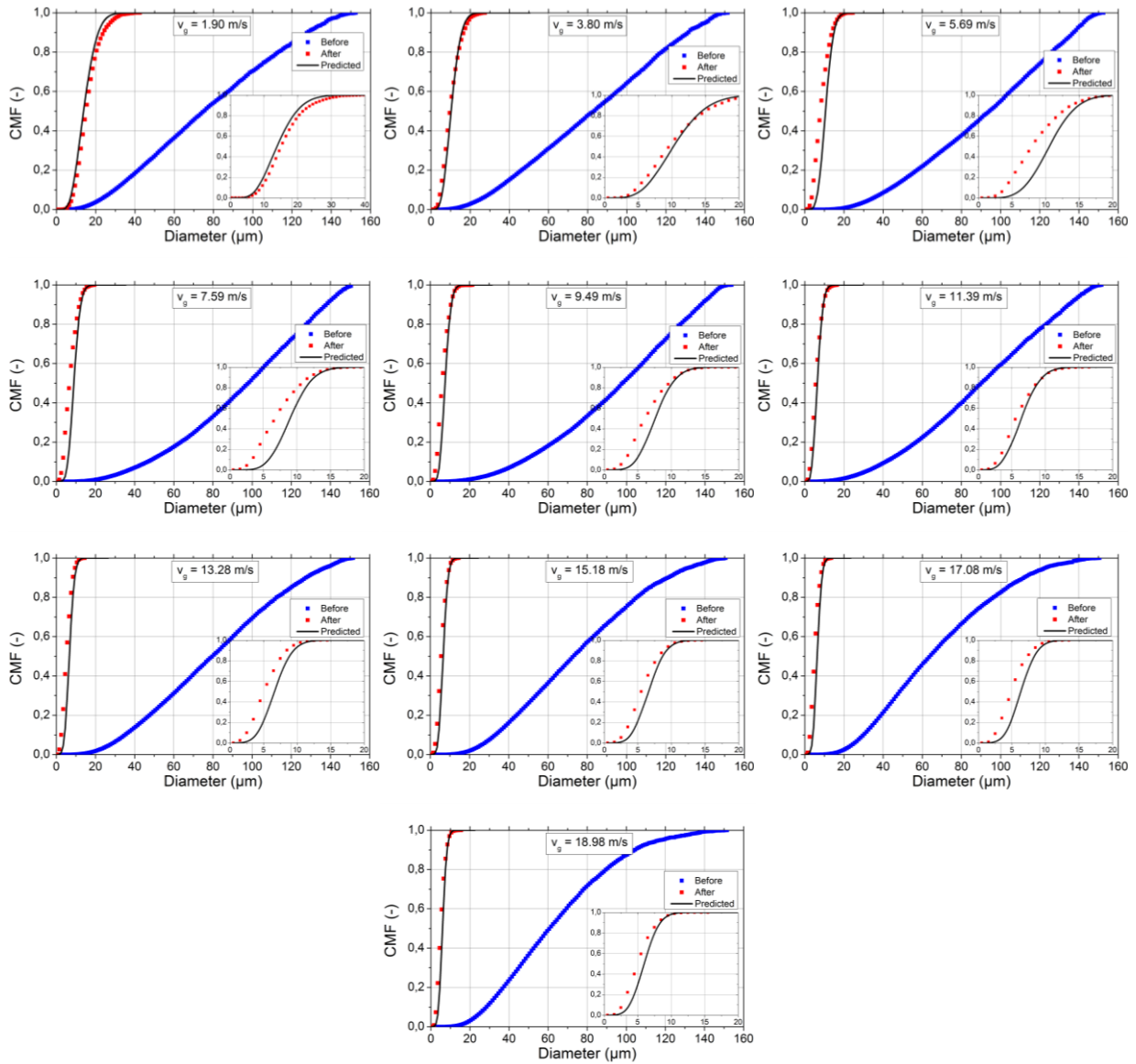
The following graphs display the cumulated mass fraction of the measured inlet droplet distribution (blue), of the measured outlet droplet distribution after application of the cut-off filter (red) and of the computed outlet droplet distribution (black), corresponding to the experiments with varying liquid mass fraction. The inset provides a magnification of the latter two graphs.



A. Fig. 8 Cumulative droplet mass fractions for the measurements with varying liquid mass fraction

### A.V-b Varying gas velocity

The following graphs display the cumulated mass fraction of the measured inlet droplet distribution (blue), of the measured outlet droplet distribution after application of the cut-off filter (red) and of the computed outlet droplet distribution (black), corresponding to the experiments with varying gas velocity. The inset provides a magnification of the latter two graphs.

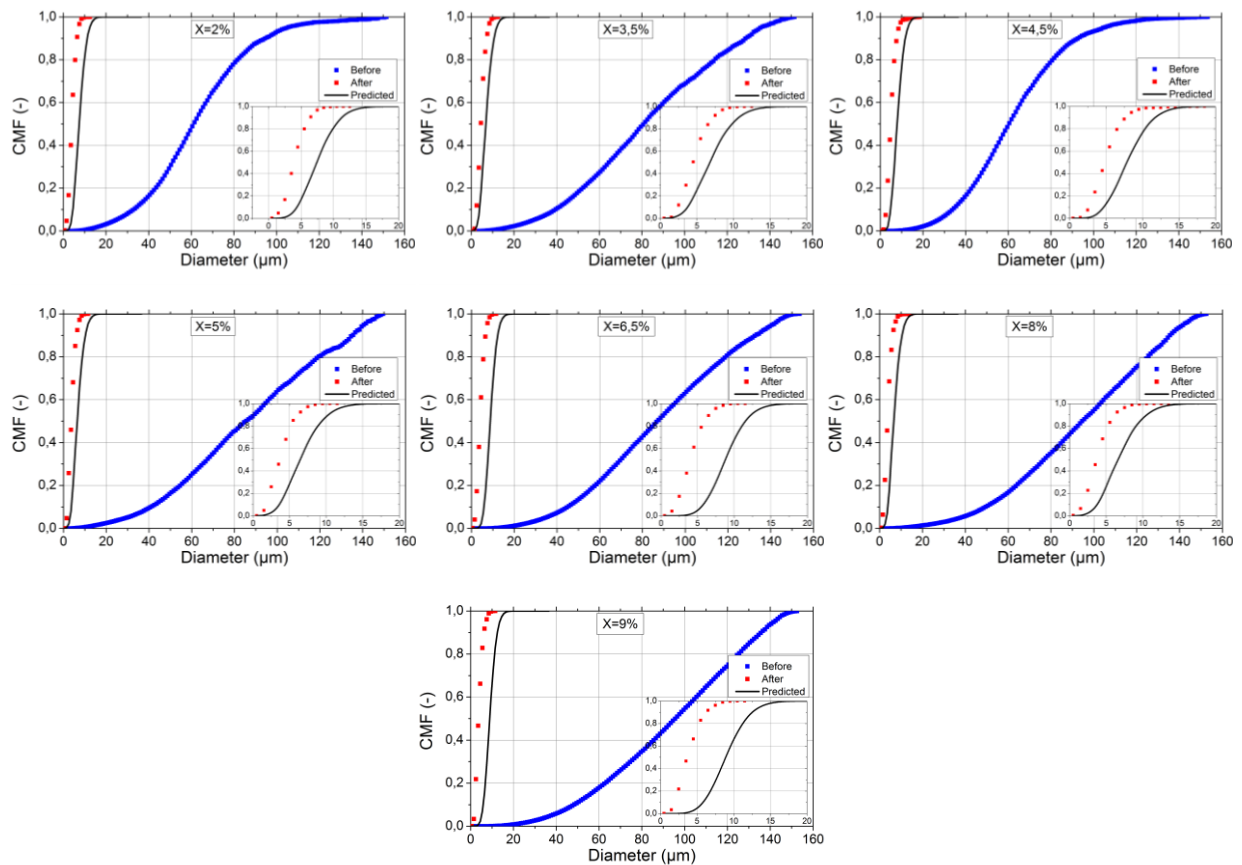


A. Fig. 9 Cumulative droplet mass fractions for the measurements with varying air velocity

# A.VI Experimental results for the novel vane separator design

## A.VI-a Varying liquid mass fraction

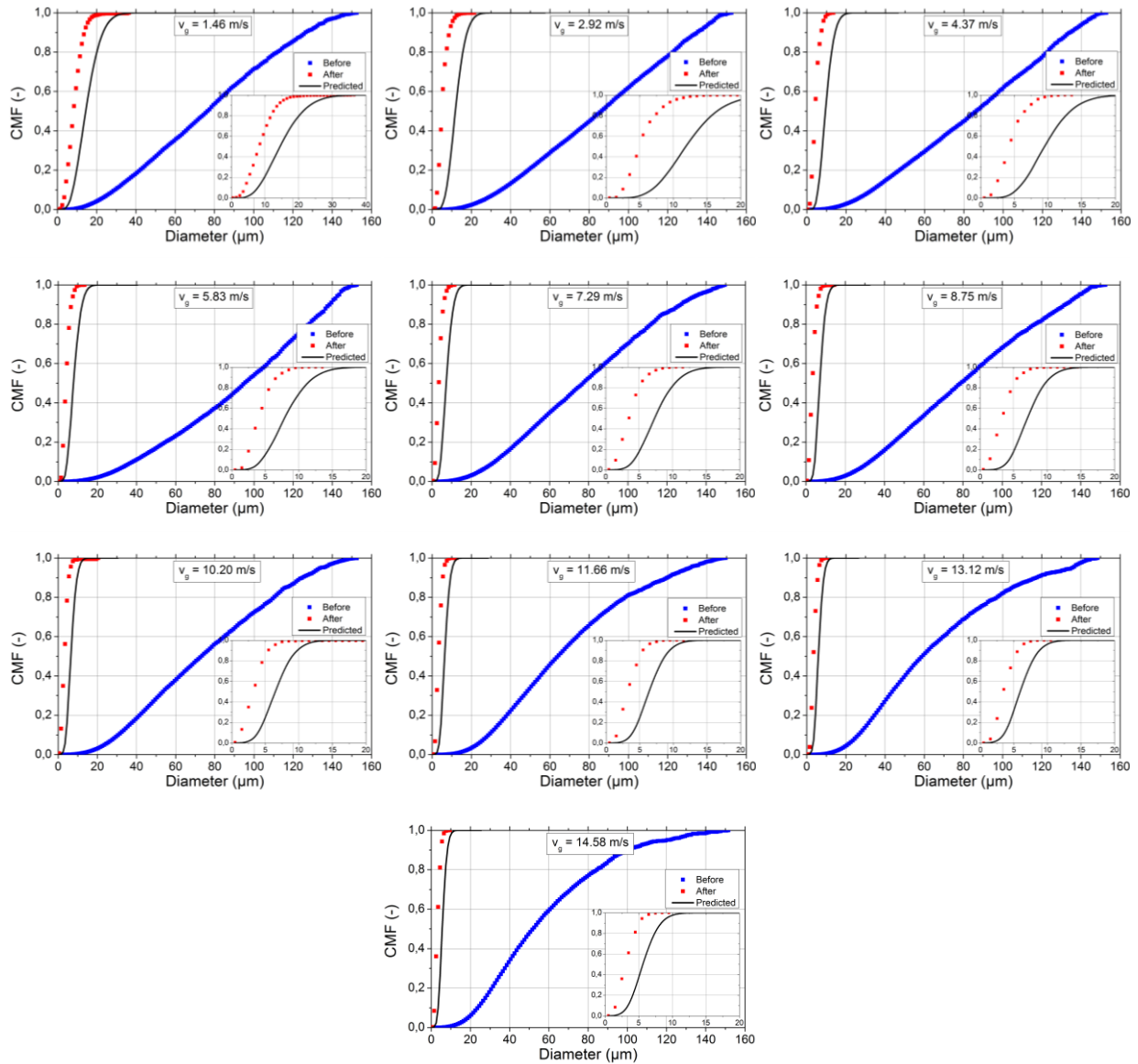
The following graphs display the cumulated mass fraction of the measured inlet droplet distribution (blue), of the measured outlet droplet distribution after application of the cut-off filter (red) and of the computed outlet droplet distribution (black), corresponding to the experiments with varying liquid mass fraction. The inset provides a magnification of the latter two graphs.



A. Fig. 10 Cumulative droplet mass fractions for the measurements with varying liquid mass fraction

### A.VI-b Varying gas velocity

The following graphs display the cumulated mass fraction of the measured inlet droplet distribution (blue), of the measured outlet droplet distribution after application of the cut-off filter (red) and of the computed outlet droplet distribution (black), corresponding to the experiments with varying gas velocity. The inset provides a magnification of the latter two graphs.



A. Fig. 11 Cumulative droplet mass fractions for the measurements with varying air velocity

# Nomenclature

## Symbols

### Latin

$A$	$m^2$	area
$c^d$	-	drag coefficient
$c_p$	-	pressure loss coefficient
$c^{vm}$	-	virtual mass coefficient
$D$	$m$	diameter
$D_{esc}$	$m$	droplet escape diameter
$D_h$	$m$	hydraulic diameter
$\delta_R$	$m$	channel width
$f$	-	probability density function
$f_m$	-	mixing factor
$G$	$kg\ m^{-2}\ s^{-1}$	flux
$g$	$m\ s^{-2}$	gravitational acceleration
$H$	$m$	height
$h_f$	$m$	film thickness
$k$	$m^2\ s^{-2}$	specific turbulent kinetic energy
$L$	$m$	length of straight wall section
$\ell_e$	$m$	turbulent eddy length
$M$	$kg$	mass
$\dot{m}$	$kg\ s^{-1}$	mass flow
$p$	$Pa$	pressure
$R$	$m$	radius
$r$	$m$	radial coordinate
$s$	$m$	(lateral) spacing
$T$	$^{\circ}C$	temperature
$t$	$s$	time (continuous)
$t_v$	$m$	vane profile thickness
$u$	$m\ s^{-1}$	radial velocity
$V$	$m\ s^{-1}$	homogeneous velocity
$v$	$m\ s^{-1}$	circumferential velocity
$w$	$m\ s^{-1}$	axial velocity
$w_v$	$m$	vane pitch
$y$	$m$	transverse droplet migration distance

**Greek**

$\alpha$	-	volume fraction
$\alpha$	<i>rad</i>	polar angle of gravity vector
$\alpha_v$	<i>rad</i>	inlet flow angle
$\beta$	<i>rad</i>	azimuthal angle of gravity vector
$\delta$	-	uncertainty
$\varepsilon$	$m^2 s^{-3}$	dissipation of turbulent kinetic energy
$\varphi$	<i>rad</i>	bend angle
$\chi$	-	mass fraction
$\eta$	-	efficiency
$\Lambda$	-	removal geometric parameter
$\lambda$	<i>m</i>	micro-scale turbulent eddy length
$\lambda_{fr}$	-	friction factor
$\lambda_v$	<i>m</i>	vane wavelength
$\mu$	$kg m^{-1} s^{-1}$	dynamic viscosity
$\nu$	$m^2 s^{-1}$	kinematic viscosity
$\theta$	<i>rad</i>	azimuthal angle of droplet position
$\vartheta$	-	liquid film flow angle
$\rho$	$kg m^{-3}$	density
$\sigma$	$kg s^{-2}$	surface tension
$\tau_{ij}$	$kg m^{-1} s^{-2}$	interfacial shear stress
$\Delta\tau$	<i>s</i>	timestep (discrete)
$\Delta\tau_{gd}$	<i>s</i>	droplet relaxation time constant
$\omega$	$s^{-1}$	turbulent frequency

**Superscripts**

*t* turbulent

**Subscripts**

0	initial
10	arithmetic mean
20	surface mean
30	volumetric mean
32	Sauter mean
<i>b</i>	bend
<i>coll</i>	collected
<i>C</i>	curved section
<i>c</i>	critical
<i>d</i>	droplet
<i>e</i>	eddy
<i>f</i>	liquid film
<i>g</i>	gas
<i>in</i>	inner (radius)
<i>l</i>	liquid
<i>ng</i>	no gravity
<i>out</i>	outer (radius)
<i>pump</i>	pump
<i>S</i>	straight section
<i>s</i>	stage
<i>term</i>	terminal
<i>VS</i>	vane separator
<i>w</i>	wetted

**Operators**

~	Laplace transformation
^	effective
-	average
∪	OR



# Abbreviations

BWR	Boiling Water Reactor
CFD	Computational Fluid Dynamics
EIM	Eddy Interaction Model
HP	High Pressure
HRSG	Heat Recovery Steam Generator
KWU	KraftWerkUnion
LP	Low Pressure
LSTM	Institute of Fluid Mechanics at the F.-A. University in Erlangen-Nuremberg
MSR	Moisture Separator & Reheater
PDA	Phase-Doppler Anemometer
PWR	Pressurized Water Reactor
RPV	Reactor Pressure Vessel



# List of figures

Fig. 1.1	Schematic views of different types of vane separators .....	4
Fig. 1.2	Schematic model of a cyclone separator .....	6
Fig. 1.3	Schematic view of a vane separator channel.....	8
Fig. 2.1	Droplet path through a bend with inner radius $R_{in}$ , outer radius $R_{out}$ and initial droplet starting radius $R_{d,0}$ .....	11
Fig. 2.2	Packed bed separator as parametrized by <i>Calvert et al.</i> [11] .....	12
Fig. 3.1	Transition functions (red) for $\psi$ .....	24
Fig. 3.2	Lift force acting on a droplet .....	25
Fig. 3.3	Schematic view of a straight-type vane separator.....	30
Fig. 3.4	Droplet paths through a straight-type vane separator channel with rounded bends .....	31
Fig. 3.5	The separation efficiency in a straight section, relative to that in a curved sections, as a function of the Stokes number .....	33
Fig. 3.6	Schematic view of a horizontal pressure vessel with a reheater tube bundle and a non-vertical arrangement of vane separators .....	34
Fig. 3.7	Cartesian coordinate system depicted with arbitrary gravity vector, with top view (upper right) and side view (bottom right) .....	35
Fig. 3.8	Schematic view of steam flow through a MSR (left) and gas velocity vectors through a MSR (right) .....	41
Fig. 3.9	Schematic view of a non-orthogonal gas velocity vector, with top view (upper right) and side view (bottom right) .....	42
Fig. 3.10	Ellipsoidal cut of a spherical vane (above left), side view along the plane of travel (top right), top view perpendicular to the vane (middle right) and perpendicular to the plane of travel (below left and right).....	42
Fig. 3.11	Influence of non-orthogonal flow on droplet separation efficiency (for four stages) .....	44
Fig. 3.12	Influence of non-orthogonal flow on separation efficiency in straight vane separator sections .....	46
Fig. 3.13	Influence of non-orthogonal flow on separation efficiency of an exemplary vane separator .....	46
Fig. 3.14	Cartesian coordinate system including the gravity vector, for a rotated vane separator geometry, with top view of the tilted plane (upper right) and tilted side view (bottom right).....	47
Fig. 3.15	Impact of gravity relative to $F(\alpha_v)$ .....	48
Fig. 3.16	Gravitational influence on vane separator efficiency for non-orthogonal flow.....	49
Fig. 3.17	Gravitational influence on separation efficiency for different gravitational angles.....	50
Fig. 3.18	Individual contributions of each section to the separation efficiency .....	51
Fig. 3.19	Simulated velocity profile (above left) and measured velocity profiles (bottom left) at two cross-sections in a zig-zag vane separator channel (above right: "Ebene 1" and "Ebene 2"). Computed velocity profiles at cross-section 2 (bottom right). .....	52
Fig. 3.20	Simplified theoretical velocity profile through a channel cross-section .....	53

Fig. 3.21	Escape diameters (left) and relative terminal radial droplet velocity (right) for an example for water droplets in air flow at atmospheric pressure, with a channel width of 1 cm, outer radius 2 cm, bend angle $80^\circ$ and air velocity 5 m/s.....	54
Fig. 3.22	Impact of the velocity profile on the droplet separation efficiency of a single stage .....	56
Fig. 3.23	Droplet migration through consecutive bends .....	57
Fig. 3.24	Impact of non-uniformity of droplet distribution on separation efficiency, for a vane separator with channel width 15 mm, outer radius 25 mm, bend angle $80^\circ$ , straight section 20 mm and 7 stages, at a gas velocity of 4 m/s .....	58
Fig. 3.25	Droplet size distribution at the exit of an HP turbine; KWU experiments (black) and as modeled using a Boltzmann (red) [34, p. 361] or a Rosin-Rammler distribution (blue) .....	61
Fig. 3.26	Cyclone separation efficiency for an ideal and a real cyclone separator .....	62
Fig. 4.1	Schematic diagram of a flat surface with local coordinates .....	66
Fig. 4.2	The function $F(q)$ that defines the ratio of gas and film velocities .....	68
Fig. 4.3	Liquid film thickness as a function of liquid Reynolds number .....	70
Fig. 4.4	Liquid film thickness measured along the width of a vertical plate for $Re_g = 39500$ and $Re_l = 1600$ .....	70
Fig. 4.5	Limiting angle for downward liquid film flow .....	72
Fig. 4.6	Carry-over (red) and drainage limits (green) and film flow angle (blue) as a function of gas velocity .....	74
Fig. 4.7	Transition from $Z < H$ to $Z > H$ .....	75
Fig. 4.8	Equalized carry-over and drainage limits and consequent flow angle (left) and corresponding liquid film height (right) .....	75
Fig. 4.9	Carry-over and drainage (green and red columns) and liquid film height (black line) through several stages of a vane separator for a gas velocity of 5 m/s .....	76
Fig. 4.10	Carry-over (red) and drainage limits (green), and film flow angle (blue), accounting for 50% perforation drainage .....	77
Fig. 4.11	Carry-over and drainage through several stages of a vane separator with 50% perforated plates .....	78
Fig. 4.12	Investigated separator geometry (left) and droplet deposition along the width of the straight wall sections of the wave-plate (right) .....	78
Fig. 4.13	Critical film thicknesses predicted by different authors as compared to experimental values .....	79
Fig. 4.14	Velocity field (in m/s) through a vane separator channel .....	80
Fig. 4.15	Mechanisms for droplet re-entrainment (left) and logarithmic relationship between critical gas velocity and liquid film Reynolds number (right) .....	81
Fig. 4.16	The onset of entrainment .....	83
Fig. 4.17	Schematic representation of critical gas velocity .....	84
Fig. 4.18	Separation efficiency as a function of droplet size for homogeneous gas velocities of 4 m/s (squares), 6 m/s (stars) and 8 m/s (diamonds) .....	84
Fig. 4.19	Separation efficiency as a function of gas velocity for vane separator type a (squares), type b (stars) and type c (triangles) .....	85
Fig. 4.20	Critical gas velocity as a function of liquid mass flow for 12 different vane separator types .....	86
Fig. 4.21	Separation efficiency as a function of air velocity .....	86

Fig. 4.22	Vane separator types Lam01, Le02 and KL01, as tested by <i>Leber</i> [40] .....	87
Fig. 4.23	Re-entrainment boundary for a horizontal vane separator .....	88
Fig. 4.24	Vane separator types investigated by <i>Nakao et al.</i> and their relative pressure drops .....	90
Fig. 4.25	Vane separator geometries <i>a</i> and <i>b</i> (left) and their pressure drops as a function of gas velocity (right) .....	91
Fig. 4.26	Pressure loss coefficients as a function of the Reynolds number for different width-to-length ratios of vane separator types <i>a-d</i> (inlay) .....	92
Fig. 4.27	Vane separator geometries of different channel width, as investigated by <i>Verlaan</i> [64]...92	
Fig. 4.28	Vane separator channels with less invasive (Burgess Manning, left) and more invasive (Euroform, right) pick off hooks.....	94
Fig. 4.29	Vane separators with and without hooks and pressure drop and separation efficiency for computations with hooks (solid), experiments with hooks (dotted), computations without hooks (dots and stripes) and experiments without hooks (stripes) .....	95
Fig. 4.30	CFD results of velocity vector field recorded at 5 m/s .....	95
Fig. 5.1	Singular bend separators B4 and B6 .....	97
Fig. 5.2	Experimental and analytical separation efficiencies for different gas velocities in vane separator types <i>B4</i> (left) and <i>B6</i> (right), as tested by <i>Bürkholz</i> [10] .....	98
Fig. 5.3	Single stage straight vane separator.....	98
Fig. 5.4	Experimental and analytical separation efficiencies for a single stage straight vane separator tested by <i>Leber</i> [40] .....	99
Fig. 5.5	Experimental and analytical separation efficiencies of the wavy vane separator <i>Pack A</i> tested by <i>Phillips &amp; Deakin</i> [52] .....	99
Fig. 5.6	Schematic representation of a straight type vane separator according to the current model (left) and according to <i>Wilkinson</i> [70] (right).....	100
Fig. 5.7	Representation of circulation zones from visual inspections using smoke tracers (above left) and velocity vectors from numerical simulations (below left) and (right) .....	100
Fig. 5.8	Straight type vane separators.....	101
Fig. 5.9	Experimental and analytical separation efficiencies of straight type vane separators tested by <i>Bürkholz</i> [10].....	101
Fig. 5.10	Experimental and analytical separation efficiencies of the straight type vane separator <i>Pack B</i> tested by <i>Phillips &amp; Deakin</i> [52] .....	102
Fig. 5.11	Straight type vane separator tested by <i>Verlaan</i> [64].....	102
Fig. 5.12	Experimental and analytical separation efficiencies of a straight type vane separator tested by <i>Verlaan</i> [64] .....	103
Fig. 5.13	Experimental (squares, <i>Bürkholz</i> [10]) and analytical separation efficiencies for different velocities assuming uniform (solid) and non-uniform flow (dashed) in vane separator types <i>B4</i> (left) and <i>B6</i> (right) .....	104
Fig. 5.14	Experimental data from <i>Phillips &amp; Deakin</i> [52] for vane separator <i>Pack A</i> (black squares), in comparison with analytical models from <i>Bürkholz</i> [10] and current work (black) and with numerical results from <i>Wang &amp; James</i> ([67], [68]) (green and red) and from <i>Zamora &amp; Kaiser</i> [72] (blue) .....	105
Fig. 5.15	Straight type vane separators, as investigated by <i>Li et al.</i> [42].....	106
Fig. 5.16	Numerical and analytical separation efficiencies of the hookless vane separator tested by <i>Li et al.</i> [42] .....	106

## LIST OF FIGURES

---

Fig. 5.17	Droplet paths through a straight type hookless vane separator as computed by <i>Li et al.</i> [42] .....	107
Fig. 5.18	Experimental results (squares) for the hookless vane separator tested by <i>Li et al.</i> [42] and analytical results assuming a single stage with uniform (solid) and non-uniform flow (dashed).....	107
Fig. 5.19	Numerical and analytical separation efficiencies of the vane separator with pick-off hooks tested by <i>Li et al.</i> [42].....	108
Fig. 5.20	Simplified vane separator test geometry .....	109
Fig. 5.21	Experimental test facility at the Institute of Fluid Mechanics (LSTM) of the Friedrich-Alexander University in Erlangen.....	110
Fig. 5.22	Flow channel with integrated spray system (left) and collection of separated liquid mass from the vane separator module (right).....	110
Fig. 5.23	Schematic view of spray nozzle distribution (left) and inside view of spray chamber (right).....	111
Fig. 5.24	Schematic representation of the liquid mass balance and its typical experimental values .....	112
Fig. 5.25	The PDA system .....	113
Fig. 5.26	Absolute measurement uncertainty in air velocity (left) and relative measurement uncertainty in integrated air mass flow (right) as a function of air velocity (at the spray chamber inlet).....	114
Fig. 5.27	Measured droplet separation efficiencies (squares) and inlet Sauter mean diameters (stars) as a function of effective air velocity (left) and of liquid mass fraction (right) .....	116
Fig. 5.28	Typical droplet number (black) and mass (red) distributions .....	117
Fig. 5.29	Cumulative droplet mass fraction before (blue) and after (red) the vane separator as compared to the model (black) for a liquid mass fraction of 2% .....	118
Fig. 5.30	Cumulative droplet mass fraction before (blue) and after (red) the vane separator module as compared to the model (black) for an air velocity of 9.5 m/s .....	118
Fig. 5.31	Experimental Sauter mean diameters at the outlet for varying effective air velocities (solid squares) and varying liquid mass fraction (solid triangles) as compared to the model predictions (open symbols) .....	119
Fig. 5.32	Inlet droplet size distributions for measurements with variable mass fraction (red) and gas velocity (black).....	120
Fig. 5.33	Measured (solid lines) and predicted (dashed lines) cumulative outlet droplet mass fractions for the measurements with 9.5 m/s and 5% liquid mass fraction, during the variable liquid mass fraction (black) and variable gas velocity (red) experiments.....	120
Fig. 5.34	Pressure drop as a function of effective air velocity (closed symbols) and as a function of mass fraction (open symbols). Solid and dashed lines represent predictions by the Wilkinson model.....	121
Fig. 6.1	Geometric parameters with relevance to vane separator design, according to <i>Kall</i> [29].	123
Fig. 6.2	Geometric parameters relevant to vane separator design, according to <i>Wilkinson</i> [70].	124
Fig. 6.3	Variable channel width of novel vane separator geometry.....	125
Fig. 6.4	Drainage channels and perforated walls of novel vane separator design .....	125
Fig. 6.5	Theoretical droplet mass distribution downstream of a representative cyclone separator, based on the inlet distribution given in Table 2 .....	127

Fig. 6.6	Cumulative droplet mass fractions at cyclone inlet (red), vane separator inlet (blue) and outlet (green) with cyclone separation efficiency (red line) and vane separator efficiency (blue line) .....	128
Fig. 6.7	Particle tracking in the novel geometry, at a homogeneous steam velocity of 6 m/s and a pressure of 12 bar .....	129
Fig. 6.8	Numerical results with ANSYS CFX (black) as compared to the current analytical work (red) for the novel geometry with saturated steam at 12 bar .....	130
Fig. 6.9	Burges Mining vane separator design (above) and numerical results (below) for this geometry (black) as compared to the current novel design VS-2 (red) .....	130
Fig. 6.10	Schematic view of the optimized vane separator design (left) and the test module (right).....	131
Fig. 6.11	Experimental efficiencies for VS-1 (triangles) and VS-2 (squares) for varying effective air velocity (closed symbols) and varying liquid mass fraction (open symbols) .....	132
Fig. 6.12	Measured droplet separation efficiencies (squares) and inlet Sauter mean diameters (stars) as a function of effective air velocity (left) and of liquid mass fraction (right) .....	133
Fig. 6.13	Cumulative droplet mass fraction before (blue) and after (red) the vane separator as compared to the model (black), for the measurements at 2% liquid mass fraction (left) and at an effective air velocity of 5.83 m/s (right) .....	133
Fig. 6.14	Experimental Sauter mean diameters at the outlet of VS-1 (triangles) and VS-2 (squares) for varying effective air velocities (left) and varying liquid mass fractions (right).....	134
Fig. 6.15	Pressure drop as a function of effective air velocity (closed symbols) and as a function of liquid mass fraction (open symbols) for VS-1 (triangles) and VS-2 (squares) .....	135

### Appendix Figures

A. Fig. 1	Droplet trajectory in straight section.....	145
A. Fig. 2	Normalized separation efficiency as a function of the gravitational angle $\alpha$ .....	150
A. Fig. 3	Normalized separation efficiency as a function of the gravitational angle $\beta$ .....	150
A. Fig. 4	Normalized separation efficiency as a function of total bend angle $\varphi$ .....	151
A. Fig. 5	Normalized separation efficiency as a function of the number of stages .....	152
A. Fig. 6	Normalized separation efficiency as a function of gas velocity .....	152
A. Fig. 7	Normalized separation efficiency as a function of droplet diameter.....	153
A. Fig. 8	Cumulative droplet mass fractions for the measurements with varying liquid mass fraction .....	157
A. Fig. 9	Cumulative droplet mass fractions for the measurements with varying air velocity .....	158
A. Fig. 10	Cumulative droplet mass fractions for the measurements with varying liquid mass fraction .....	159
A. Fig. 11	Cumulative droplet mass fractions for the measurements with varying air velocity .....	160



## List of tables

Table 1	Vane separator grade efficiencies under the influence of gravity .....	40
Table 2	Representative droplet distribution for PWRs, based on KWU measurements reported by <i>Kolev</i> [34, p. 361] .....	61
Table 3	Limiting liquid film height (by numerical simulation) at various gas velocities for droplet distributions A and B with average droplet diameters of 25 $\mu\text{m}$ and 40 $\mu\text{m}$ respectively .....	69
Table 4	Critical superficial film and gas velocities for water-air systems according to relations by different authors.....	83
Table 5	Film instabilities according to experiments by Swanborn [61, p. 121] .....	85
Table 6	Experimental values of flooding point constants and corresponding flooding velocities [40, p. 122] .....	87
Table 7	Conditions at inception of re-entrainment according to <i>Azzopardi &amp; Sanaulla</i> [3, p. 3560] .....	88
Table 8	Measurement points achieved during the experiments.....	115
Table 9	Sauter mean diameter and range of inlet and outlet droplet size distributions computed from the PDA measurements .....	117
Table 10	Consequences of sub-optimal design of vane separator geometry.....	127
Table 11	Geometrical parameters of novel design .....	128
Table 12	Measurement points for the experiments with the novel design (VS-2).....	132

### Appendix Tables

A. Table 1	Default input parameters .....	149
A. Table 2	Physical parameters of the applied air-water system.....	155



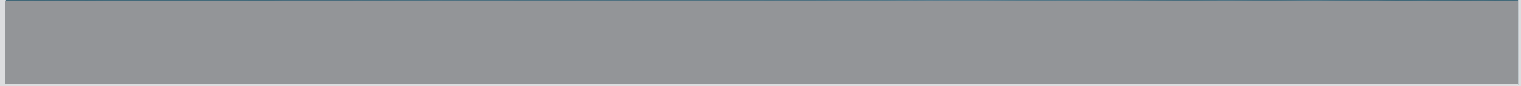
# Bibliography

- [1] ANSYS, Inc. (2010) ANSYS CFX Brochure. <http://www.ansys.com/staticassets/ANSYS/staticassets/resourcelibrary/brochure/ansys-cfx-brochure.pdf>
- [2] ANSYS, inc. (2010) ANSYS Fluent brochure 14.0. <http://www.ansys.com/staticassets/ANSYS/staticassets/resourcelibrary/brochure/ansys-fluent-brochure-14.0.pdf>
- [3] Azzopardi, B. J. and Sanaullah, K. S., *Re-entrainment in wave-plate mist eliminators*, Chemical Engineering Science, vol. 57, pp. 3557-3563, 2002.
- [4] Azzopardi, B. J. (2011) Thermopedia. <http://www.thermopedia.com/content/1108/>
- [5] Bell, C. G. and Strauss, W., *Effectiveness of Vertical Mist Eliminators in a Cross Flow Scrubber*, Journal of the Air Pollution Control Association, vol. 23, no. 11, pp. 967-969, 1973.
- [6] Bournaski, E., *Numerical Simulation of Unsteady Multiphase Pipeline Flow With Virtual Mass Effect*, Int. Journal for Numerical Methods in Engineering, vol. 34, pp. 727-740, 1992.
- [7] Brauer, H., *Grundlagen der Einphasen- und Mehrphasenströmungen*, 1st ed. Aarau und Frankfurt am Main: Sauerländer, 1971.
- [8] Bretherton, F. P., *The motion of rigid particles in a shear flow at low Reynolds number*, Journal of Fluid Mechanics, vol. 14, pp. 284-304, 1962.
- [9] Bürkholz, A., *Die Beschreibung der Partikelabscheidung durch Tragheitskräfte mit Hilfe einer dimensionsanalytisch abgeleiteten Kennzahl*, Chemie-Ingenieur-Technik, vol. 58, pp. 548-556, 1986.
- [10] Bürkholz, A., *Droplet separation*. Weinheim, Germany: Wiley VCH Verlag, 1989.
- [11] Calvert, S., Jashnani, I. L., and Yung, S., *Entrainment Separators for Scrubbers*, Journal of the Air Pollution Control Association, vol. 24, no. 10, pp. 971-975, 1974.
- [12] CHAM Ltd. (2013) PHOENICS - Your Gateway to CFD Success. <http://www.cham.co.uk/default.php>
- [13] Chandesris, M., Serre, G., and Sagaut, P., *A macroscopic turbulence model for flow in porous media suited for channel, pipe and rod bundle flows*, Fourth International Conference on Computational Heat and Mass Transfer, Paris, 2005.
- [14] Crow, C. T. and Pratt, D. T., *Analysis of the flow field in cyclone separators*, Computers and fluids, vol. 2, pp. 249-260, 1974.
- [15] Faxén, H., *Der Widerstand gegen die Bewegung einer starren Kugel in einer Flüssigkeit, die zwischen zwei parallelen ebenen Wänden eingeschlossen ist*, Annalen der Physik, vol. 373, no. 10, pp. 89-119, 1922.
- [16] Fore, L. B., Beus, S. G., and Bauer, R. C., *Interfacial friction in gas-liquid annular flow: analogies to full and transition roughness*, International Journal of Multiphase Flow, vol. 26, pp. 1755-1769, 2000.
- [17] Galletti, C., Brunazzi, E., and Tognotti, L., *A numerical model for gas flow and droplet motion in wave-plate mist eliminators with drainage channels*, Chemical Engineering Science, pp. 5639-5652, 2008.

- [18] Gardner, G. C., *Separation of liquids from gases or vapours*, HTFS Design Report, vol. 46, 1977.
- [19] Ghetti, S., *Investigation of entrainment phenomena in inertial separators (in Italian)*, University of Pisa, Pisa, MS Thesis 2003.
- [20] Gillandt, I., Fritsching, U., and Riehle, C., *Zur mehrphasigen Strömung in einem Zick-Zack-Sichter*, Forschung im Ingenieurwesen - Engineering Research, vol. 62, no. 11/12, pp. 315-321, 1996.
- [21] Gloger, M., *Probleme der Wasserabscheidung in Naßdampfturbinen*, Brennstoff-Wärme-Kraft, vol. 22, pp. 417-460, Nr. 9 1970.
- [22] Hoekstra, A. J., *Gas flow field and collection efficiency of cyclone separators*, Delft University of Technology, Delft, Dissertation ISBN 90-90143341-3, 2000.
- [23] Houghton, H. G. and Radford, W. H., *Measurements on eliminators and the development of a new type for use at high gas velocities*, Transactions of the American Institute of Chemical Engineers, vol. 35, pp. 427-433, 1939.
- [24] Idelchik, I. E., *Handbook of Hydraulic Resistance*, 3rd ed. Mumbai: Jaico Publishing, 2003.
- [25] Ishii, M. and Grolmes, M. A., *Inception Criteria for Droplet Entrainment in Two-Phase Concurrent Film Flow*, American Institute of Chemical Engineers Journal, vol. 21, no. 2, pp. 308-317, 1975.
- [26] Jackson, S. and Calvert, S., *Entrained Particle Collection in Packed Beds*, American Institute of Chemical Engineers Journal, vol. 12, no. 6, pp. 1075-1078, 1966.
- [27] James, P. W., Azzopardi, B. J., Wang, Y., and Hughes, J. P., *A model for liquid film flow and separation in a wave-plate mist eliminator*, Chemical Engineering Research and Design, vol. 83, no. A5, pp. 469-477, 2005.
- [28] Jøsang, A. I., *Numerical and Experimental Studies of Droplet-Gas Flow*, Norwegian University of Science and Technology, Porsgrunn, Dissertation URN:NBN:no-3336, 2002.
- [29] Kall, H., *Entwicklung eines Tropfenabscheiders zur Dampftrocknung in Kernkraftwerken*, Fortschrittberichte der VDI Zeitschriften, vol. 3, no. 51, 1979.
- [30] Kallio, G. A. and Reeks, M. W., *A numerical simulation of particle deposition in turbulent boundary layers*, Int. Journal of Multiphase Flow, vol. 15, no. 3, pp. 433-446, 1989.
- [31] Kolev, N. I., *Multiphase Flow Dynamics, vol. 1 Fundamentals*. Berlin: Springer, 2nd edition, 2011-a.
- [32] Kolev, N. I., *Multiphase flow dynamics, vol. 3 Thermal interactions*. Berlin: Springer, 2nd edition, 2011-c.
- [33] Kolev, N. I., *Multiphase flow dynamics, vol. 4 Turbulence, gas absorption and release, diesel fuel properties*. Berlin: Springer, 2nd edition, 2011-d.
- [34] Kolev, N. I., *Multiphase flow dynamics, vol. 5 Thermal hydraulics*. Berlin: Springer, 2nd edition, 2011-e.
- [35] Kolev, N. I., Koopman, H. K., Khodyachykh, S., Botazolli, P., Mertkaya, B., Meister, M., Tikhomirova, N., Köksoy, Ç., Ertunç, Ö., Lienhart, H., Hedwig, H., Delgado, A., and Hoffmann, W., *The new Siemens vane separator*, Proceedings of the 22th International Conference on Nuclear Engineering (ICONE22-31289), Prague, 2014.
- [36] Koopman, H. K., Köksoy, Ç., Ertunç, Ö., Lienhart, H., Hedwig, H., and Delgado, A., *An analytical model for droplet separation in vane separators and measurements of grade efficiency and pressure drop*, Nuclear Engineering and Design, vol. 276, pp. 98-106, 2014.

- [37] Kowalski, J. E., *Wall and Interfacial Shear Stress in Stratified*, American Institute of Chemical Engineers Journal, vol. 33, no. 2, pp. 274-281, 1987.
- [38] Lang, F. N., Chen, J. Y., and Zhao, G. M., *Study on separation efficiency of a demister vane*, Machine Tool and Hydraulics, vol. 5, pp. 137-140, 2003.
- [39] Lasdon, L. S. and Smith, S., *Solving sparse nonlinear programs using GRG*, ORSA Journal of Computing, vol. 4, no. 1, pp. 2-15, 1992.
- [40] Leber, A., *Transport und Abscheidung von Tropfen im Primärkreis des Hochtemperaturreaktors bei Wasserbruchstörfällen*, Institut für Sicherheitsforschung und Reaktortechnik, Jülich, Dissertation ISSN 0944-2952, 2003.
- [41] Legendre, D. and Magnaudet, J., *The lift force on a spherical bubble in a viscous linear shear flow*, Journal of Fluid Mechanics, vol. 368, pp. 81-126, 1998.
- [42] Li, J., Huang, S., and Wang, X., *Numerical Study of Steam-Water Separators with Wave-type Vanes*, Chin. J. Chem. Eng., vol. 15, no. 4, p. 492–498, 2007.
- [43] Llory, D., Maroteaux, F., Le Coz, J.-F., and Habchi, C., *Liquid film atomization due to sharp edge: separation criterion and droplets characteristics model*, Journal of Fluids Engineering, vol. 124, pp. 565-575, 2002.
- [44] Maxey, M. R. and Riley, J. J., *Equations of motion for a small rigid sphere in a nonuniform flow*, Physics of Fluids, vol. 26, pp. 883-889, 1983.
- [45] McLaughlin, J. B., *Aerosol particle deposition in numerically simulated channel flow*, Physics of Fluids A, vol. 7, pp. 1211-1224, 1989.
- [46] Mertkaya, B., Koopman, H. K., Kolev, N., and Meister, M., *Wet Separator PCT/EP2012/057376*, Apr. 23, 2012.
- [47] Miles, J. W., *The hydrodynamic stability theory of a thin film in uniform shearing motion*, Journal of Fluid Mechanics, vol. 8, no. 4, pp. 593-611, 1960.
- [48] Mugele, R. A. and Evans, H. D., *Droplet Size Distributions in Sprays*, Industrial and Engineering Chemistry, vol. 43, no. 6, pp. 1317-1324, June 1951.
- [49] Nakao, T., Nagase, M., Aoyama, G., and Murase, M., *Development of Simplified Wave-type Vane in BWR Steam Dryer and Assessment of Vane Droplet Removal Characteristics*, Journal of Nuclear Science and Technology, vol. 36, no. 5, pp. 424-432, 1999.
- [50] Ontko, J. S., *Cyclone separator scaling revisited*, Powder Technology, vol. 87, no. 2, pp. 93-104, 1996.
- [51] Owen, I. and Ryley, D. J., *The flow of thin liquid films around corners*, International Journal of Multiphase Flow, vol. 11, pp. 51-62, 1985.
- [52] Phillips, H. W. and Deakin, A. W., *Measurements of the collection efficiency of various demister devices*, Proc. 4th Annual Meeting of Aerosol Society, Loughborough, UK, 1990.
- [53] Regehr, U., *Mechanische Reinigung heterogener Gassysteme mit einem neuartigen Tropfenabscheider*, Chemie-Ingenieur-Technik, vol. 39, pp. 1107-1111, 1967.
- [54] Rosin, P. and Rammler, E., *The Laws Governing the Fineness of Powdered Coal*, Journal of the Institute of Fuel, vol. 7, pp. 29-36, 1933.
- [55] Rubinow, S. I. and Keller, J. B., *The transverse force on a spinning sphere moving in a viscous fluid*, Journal of Fluid Mechanics, vol. 11, pp. 447-459, 1961.

- [56] Saffman, P. G., *The Lift on a Small Sphere in a Slow Shear Flow*, Journal of Fluid Mechanics, vol. 22, pp. 385-400, 1965.
- [57] Saffman, P. G., *Corrigendum to The Lift on a Small Sphere in a Slow Shear Flow*, Journal of Fluid Mechanics, vol. 31, p. 624, 1968.
- [58] Sauter, J., *Die Größenbestimmung der in Gemischnebeln von Verbrennungskraftmaschinen vorhandenen Brennstoffteilchen*, VDI-Forschungsheft Nr. 279, 1926.
- [59] Schiller, L. and Naumann, Z., *Über die grundlegenden Berechnungen bei der Schwerkraftaufbereitung*, Zeitschrift des Vereins Deutsche Ingenieure, vol. 77, p. 318, 1933.
- [60] Sorokin, Yu. L., Popchenkov, I. N., and Burkat, V. S., *Determining the optimum cross section of a venetian-blind separator (translation)*, Chemical and Petroleum Engineering, vol. 2, pp. 781-784, 1966.
- [61] Swanborn, R. A., *A new approach to the design of gas-liquid separators for the oil industry*, Delft University of Technology, Delft, Dissertation TR diss 1672, 1988.
- [62] Taylor, G. I., *Statistical Theory of Turbulence*, Proceedings of the Royal Society of London, vol. 151, No. 873, no. Serie A, Mathematical and Physical Sciences, pp. 421-444, 1935.
- [63] Ushiki, K., Nishizawa, E., Beniko, H., and Inoya, K., *Performance of a Droplet Separator with Multistage Rows of Flat Blades*, Journal of Chemical Engineering of Japan, vol. 15, no. 4, pp. 292-298, 1982.
- [64] Verlaan, C. C. J., *Performance of novel mist eliminators*, Delft University of Technology, Delft, Dissertation ISBN 90-370-0054-1, 1991.
- [65] Wallis, G. B., *One-dimensional two-phase flow*. New York, USA: McGraw-Hill, 1969.
- [66] Wang, Q., Squires, K. D., Chen, M., and McLaughlin, J. B., *On the role of the lift force in turbulence simulations of particle deposition*, Int. Journal of Multiphase Flow, vol. 23, no. 4, pp. 749-763, 1997.
- [67] Wang, Y. and James, P. W., *The calculation of wave-plate demister efficiencies using numerical simulation of the flow field and droplet motion*, Inst. of Chemical Engineers: Trans IChemE, vol. 76, no. A, pp. 980-985, 1998.
- [68] Wang, Y. I. and James, P. W., *Assessment of an Eddy-Interaction Model and its Refinements using Predictions of Droplet Deposition in a Wave-Plate Demister*, Trans IChemE, vol. 77, no. A, pp. 692-698, 1999.
- [69] Wikipedia. (2013) Rankine Cycle. [http://en.wikipedia.org/wiki/Rankine\\_cycle](http://en.wikipedia.org/wiki/Rankine_cycle)
- [70] Wilkinson, D., *Optimizing the design of waveplates for gas-liquid separation*, Proceedings of the Institution of Mechanical Engineers, Part E: Journal of Process Mechanical Engineering, vol. 213, pp. 265-274, 1999.
- [71] Zaichik, L. I., *Estimation of time between particle collisions in turbulent flow (translation from Russian)*, High Temperature, vol. 36, no. 3, 1998.
- [72] Zamora, B. and Kaiser, A. S., *Comparative efficiency evaluations of four types of cooling tower drift eliminator, by numerical investigation*, Chemical Engineering Science, vol. 66, pp. 1232-1245, 2011.
- [73] Zhao, J., Jin, B., and Zhong, Z., *Study of the separation efficiency of a demister vane with response surface methodology*, Journal of Hazardous Materials, vol. 147, pp. 363-369, 2007.



ISBN 978-3-7315-0331-6

ISBN 978-3-7315-0331-6



9 783731 503316 >